Inaugural-Dissertation

zur

Erlangung der Doktorwürde

der

Naturwissenschaftlich-Mathematischen

Gesamtfakultät

der

Ruprecht-Karls-Universität

Heidelberg

vorgelegt von

Dipl.-Physiker Ralf S. Klessen

aus Landau a. d. Isar

Tag der mündlichen Prüfung: 23. Juni 1998

Fragmentation of Molecular Clouds: The Initial Phases of a Stellar Cluster

Gutachter: Priv.-Doz. Dr. Andreas Burkert

Priv.-Doz. Dr. Rainer Spurzem

Zusammenfassung der Arbeit:

In dieser Arbeit betrachten wir die Anfangsphasen der Sternentstehung: die dynamische Entwicklung und Fragmentation von Gebieten im Inneren von Molekülwolken, welche zur Bildung eines gebundenen protostellaren Haufens führen. Wir simulieren diese Prozesse mit Hilfe von SPH ('smoothed particle hydrodynamics') in Verbindung mit der Spezialhardware GRAPE und weisen nach, daß bereits ein einfaches isothermes, selbstgravitierendes Gasmodel in der Lage ist, einen Großteil der Beobachtungsdaten in Sternentstehungsgebieten zu erklären. Die Entwicklung der Modelle folgt aus eine Sequenz statistischer Ereignisse, woraus sich ergibt, daß das dynamische Verhalten unabhängig von der konkreten Wahl der Anfangsbedingungen ist.

Die Wechselwirkung zwischen Gravitation und Gasdruck erzeugt ein komplexes Netzwerk aus Gasklumpen und Filamenten, dessen weitere Entwicklung zur Bildung eines gebundenen, protostellaren Haufens führt. Der Massenzuwachs protostellarer Kerne erfolgt dabei durch Akkretion aus dem umgebenden Gasreservoir, wobei dieser Prozeß stark von direkten N-Körperstößen gestört wird. Es stellt sich heraus, daß die Drehimpulsverteilung der protostellaren Kerne mit dem Ort korreliert ist.
Das Massenspektrum identifizierter Gasklumpen kann durch ein einfaches Potenzgesetz der Form $dN/dM \propto M^{-1.5}$ beschrieben werden, was mit den Beobachtungdaten gut übereinstimmt. Im Gegensatz dazu gilt für protostellare Kerne, daß deren Massen einer logarithmischen Normalverteilung folgen, wobei das Maximum bei der mittleren Jeansmasse des Gesamtsystems liegt. Diese Verteilung kann mit der stellaren Massenfunktion für Mehrfachsysteme verglichen werden, wobei eine Sternentstehungseffizienz von $5-15$ % zu hervorragender Übereinstimmung führt.

Abstract:

Using smoothed particle hydrodynamics in combination with the special-purpose hardware device GRAPE, we numerically investigate the initial phases of the star-formation process. We follow the dynamical evolution and fragmentation of large regions within molecular clouds to form a cluster of protostellar cores. Adopting an isothermal description of self-gravitating gas, we show that even this simple model is able to explain many of the observed features of star-forming regions and identify the processes that dominate the formation and evolution of protostellar cores. The number of protostellar cores that form during the evolution is roughly proportional to the number of Jeans masses contained in the system initially. The overall dynamical behavior of the system is insensitive to the adopted initial conditions, since it evolves through a sequence of highly probabilistic events.

The interplay between self-gravity and gas pressure creates a complex network of clumps, sheets and filaments, and the subsequent evolution leads to the formation of a bound cluster of protostellar cores. These grow in mass via accretion from the available gas reservoir and are subject to highly unpredictable N-body interactions. We find that the angular momenta of protostellar cores are correlated with their location. The mass spectrum of gas clumps can be well approximated by a power-law distribution $dN/dM \propto M^{-1.5}$, comparable to observed molecular clouds. In contrast, the mass spectrum of protostellar cores is best described by a log-normal distribution which peaks roughly at the overall Jeans mass of the system. With the appropriate scaling, this is in excellent agreement with the IMF for multiple stellar systems and suggests a star-formation efficiency which ranges from $5 - 15$ %.

Wir fühlen, daß, selbst wenn alle möglichen
wissenschaftlichen Fragen beantwortet sind,
unsere Lebensprobleme noch gar nicht berührt sind.
Freilich bleibt dann eben keine Frage mehr;
und eben dies ist die Antwort.

(Wittgenstein – Tractatus §6.52)

Contents

Chapter 1

Introduction and Overview

Understanding the processes leading to the formation of stars is one of the fundamental challenges in astronomy. Stars are the dominant sources of radiation for almost all astrophysical objects, ranging from the most distant galaxies down to the bodies found in our solar system reflecting the sunlight. Not only do the properties of stellar systems on all scales depend on how their stars were formed, also the properties of the interstellar medium in galaxies are controlled to a large extent by various feedback effects from stars. Hence, observational studies of star-forming regions and attempts to derive a comprehensive theoretical model for the process of star formation are important for many astrophysical problems.

1.1 Motivation of the Present Study

The recent progress in observational astronomy, especially at infrared and submillimeter wave lengths, has greatly advanced our knowledge of the formation of stellar systems and the evolution of molecular clouds. It now is possible to observe the process of star formation at any evolutionary phase. Studies of the properties and evolution of star-forming regions need to be accompanied by analytical and numerical work to derive a self-consistent picture of the entire process. However, current theoretical models fail to explain the wealth of observational data: analytical models of the star-formation process are restricted to describing the collapse of isolated, idealized objects and much the same applies to numerical studies. Hence, there is a great demand for theoretical work in the field of star formation to reduce that gap between observations and theory.

The general paradigm of star formation is the following: It begins with the formation of molecular cloud complexes in a galaxy and includes their dynamical evolution to the

formation of self-gravitating dense cores. Some of these cores become gravitationally unstable and begin to collapse to form highly-condensed objects in their interior. The central density increases until it exceeds the threshold for nuclear fusion processes to set in. This new source of energy leads to an equilibrium stage: a protostar is born. It is still embedded in its parental gas envelope which continues to fall towards the center. Hence, the object continues to grow in mass via accretion of this gas reservoir. However, conservation of angular momentum prevents the bulk of the material from falling directly onto the central object. Instead, it forms a rotationally supported disk and matter can reach the central star only after the removal of angular momentum through viscous transport phenomena or global disk instabilities. Magnetic fields may play a crucial role at that stage. Parts of the gas that streams towards the center may get expelled in form of a bipolar outflow which is able to pump a considerable amount of energy and momentum into the surrounding protostellar envelope. At the same time, a strong stellar wind and radiation field develop. These effects will eventually blow apart the protostellar cocoon and reveal the star. Furthermore, stars form as members of hierarchically structured cluster. Hence, they interact with each other and modify each others evolution. Stellar feedback processes not only modify a star's immediate vicinity, but may also influence the entire star-forming region. The UV radiation of a few O stars is enough to create a large cavity of ionized gas inside a molecular cloud. The most prominent and best studied example is the Trapezium in the Orion molecular cloud. Statistically, these events limit the life time of an entire cloud complex to $\sim 10^7$ years. On the other hand, stellar feedback processes may compress other parts of a molecular cloud and thus induce a new episode of star-formation. Gas from dissolved clouds replenishes the diffuse phase of the interstellar medium and largely determines its properties. All these processes together participate in the star-formation cycle and the chain of feedback effects makes star formation strongly self-regulated. A comprehensive theory of star formation must take all these processes into account, an apparently unsurmountable task. The formation of individual stars is subject to highly indeterministic statistical events, which make the existence of a deductive theory highly unlikely. However, we may be able to understand the properties of large *ensembles* of stars, say their mass spectrum or kinematical parameters, within the framework of a statistical theory. This results of this dissertation will contribute their share to the development of this theory.

We concentrate our research on the very early stages of the star formation process: on the numerical modeling of the dynamical evolution and fragmentation of molecular clouds leading to the formation of a cluster of protostellar cores. Our scientific goal is to identify the processes that dominate these early phases of the star formation. In the physical regime of interest, molecular gas is approximately isothermal. Thus, our simulations describe the interplay between self-gravity and gas pressure. This creates a complex network of filaments, sheets and knots. The contraction of gravitationally unstable gas

clumps leads to the formation of protostellar cores, which continue to accrete from their surrounding gas envelopes and build up a hierarchically structured and dynamically highly active cluster. We analyze the gas distribution and the properties of the protostellar cluster at any stage of the evolution and compare the numerical results with the observations. Parameters such as mass spectrum, kinematics, spatial distribution and multiplicity of cores can be used to constrain the theoretical model. Despite its simplicity, our isothermal model is able to explain many observational features of young stellar clusters remarkably well, which suggests that gravitational fragmentation and accretion processes dominate the formation and early evolution of stellar clusters and the origin of stellar masses.

Since we cannot resolve the evolution of a molecular cloud as a whole, we concentrate on a smaller *volume* embedded in the interior of a large, stable molecular cloud complex where only the overdense regions are able to contract due to self gravity and assume the molecular cloud is supported on large scales by turbulence and/or other processes. To follow the time evolution of the molecular cloud, we use the numerical technique of smoothed particle hydrodynamics which is intrinsically Lagrangian and can resolve very high density contrasts. To achieve high computational speed, we combine SPH with the special-purpose hardware device GRAPE. Since we wish to describe a region in the interior of a globally-stable molecular cloud we have to prevent overall collapse. This is achieved by applying periodic boundary conditions to the system (see Sec. 3 for technical details).

The second goal of this thesis work is to understand how the formation of protostellar objects and their properties depend on environmental conditions. Hence, within the framework of isothermal models, we perform computations for a wide range of *temperatures* and different sets of *initial density distributions*, typically Gaussian random fluctuations with varying power spectra, to mimic different molecular cloud structure. The results of our large-scale calculations can then be used as more realistic and self-consistent input data for detailed computations of the collapse of *individual* protostellar objects, to gain deeper insight into the late phases of the formation of individual stars.

1.2 Overview of the Present Study

The structure of this thesis is as follows:

Chapter 2 introduces the observational properties of molecular clouds important in the context of star formation. It specifies their physical state and geometrical structure, and elaborates on observed scaling relations. This is followed by a description of the properties of young stellar clusters and of protostellar cores, the direct precursors of individual stars. Then, the chapter sumarizes the current status of analytical and numerical theories of star formation. This part is followed by a discussion of the stellar initial mass function

(IMF) which is one of the most important properties of stellar systems. The chapter ends with the introduction of a statistical model for the IMF.

Chapter 3 presents the mathematical and numerical concepts necessary to conduct the current study. It begins with the equations of hydrodynamics which govern the time evolution of gaseous systems, and analyzes the stability of self-gravitating, isothermal fluids. Since we follow the dynamical evolution of the gas using smoothed particle hydrodynamics (SPH), we introduce the concept of SPH and discuss its abilities and limitations. To achieve high computational performance, this method is combined with the special-purpose hardware device GRAPE. After describing this technique, we finish with a discussion of the scheme to implement periodic boundary conditions in combination with GRAPE.

Chapter 4 discusses the scaling properties of self-gravitating, isothermal gas. Our models are scale-free and their dynamical evolution depends on one global parameter: the dimensionless *temperature* defined as the ratio between internal energy and potential energy. Therefore, our simulations are performed in normalized units. The conversion back into physical units and the scaling to observed star-forming regions are described in the last parts of this chapter.

Chapter 5 specifies the initial conditions adopted for the numerical simulations. At the begin of the dynamical evolution, the gas density follows a Gaussian random fluctuation field which is generated via the Zel'dovich approximation. In this chapter we discuss this approach and its applicability for gaseous systems.

Chapter 6 studies in detail one particular set of models and derives the main results of this dissertation. It analyzes the dynamical evolution of the molecular cloud region we study towards the formation of a dense protostellar cluster. We derive the clump-mass spectrum of the evolving gas and compute the spatial and kinematical properties of the protostellar cluster. Finally, we discuss the implications of this work for a better understanding of the IMF.

Chapter 7 gives a parameter study: it specifies the sensitivity of the behavior of our models on the adopted initial conditions. In detail, we discuss the effect of varying the slope of the power spectrum of the initial fluctuation field and of changing the gas temperature.

Finally, in **Chapter 8** we sumarize our results and suggest further steps towards a general theory of the star formation. We discuss the extension of the current isothermal models of large-scale fragmentation of molecular clouds by including the effects of stellar feedback: radiation, stellar winds and bipolar outflows. Furthermore, it is of great interest to address the question of how dynamical processes in molecular clouds may lead to physical conditions similar to the ones adopted as starting conditions in our models. This leads

into the field of studying interstellar turbulence.

Chapter 2

Observations and Models of the Star Formation Process

All present day star formation takes place in molecular clouds (Blitz, 1993). In order to understand the physical processes leading to the formation of stars, the dynamical evolution and fragmentation properties of molecular clouds are necessary ingredients. Therefore, this chapter begins with a brief introduction into the main features of molecular clouds relevant for the context of the present study. After this, analytical and numerical models of the star-formation process are introduced, followed by a discussion of the different models for the stellar initial mass function.

2.1 Properties of Molecular Clouds

Molecular clouds are huge associations of gas. Their chemical composition is dominated by molecular hydrogen and helium. In the plane of the Milky Way, interstellar gas has been extensively reprocessed by stars, therefore, the metallicity[1] of molecular clouds is approximately solar. This has important consequences for the radiation transport properties and the optical depth of these structures. The presence of elements like carbon, nitrogen, oxygen and of higher order determines the heating and cooling processes in molecular clouds (see e.g. Genzel, 1991). And, equally important, these elements are the physical observables. Radio and submillimeter telescopes mostly concentrate on the rotational transition lines of carbon, oxygen and nitrogen molecules (like CO, NH_3, or H_20). By now, several hundred different molecules have been identified in the interstellar gas. An overview of the application of different molecules as tracers for different physical

[1] In astrophysics, all chemical elements heavier than helium are denoted as metals. The bulk of these elements has been produced in supernova explosions that terminate the life of massive stars.

conditions is given in Fig. 2.1. Further details can be found in the excellent reviews by van Dishoeck et al. (1993) and Genzel (1991).

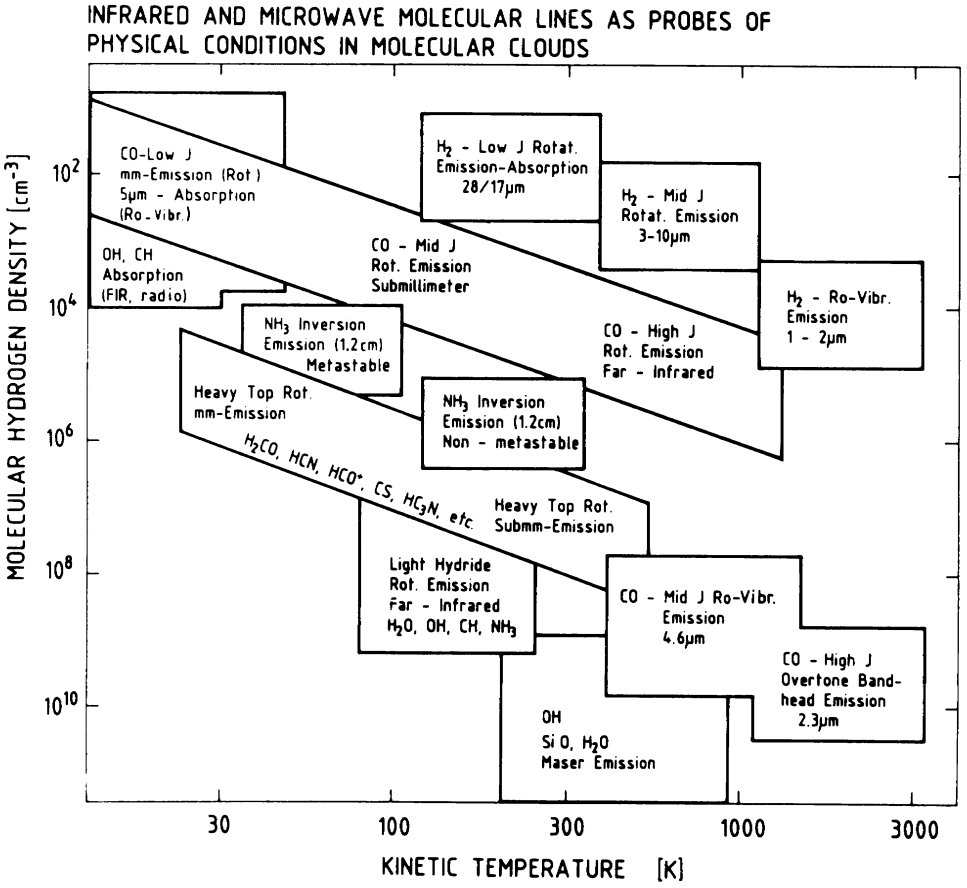

Figure 2.1: Molecular lines as probes of the physical conditions in molecular clouds (from Genzel, 1991).

2.1.1 The Geometrical Structure of Molecular Clouds

From molecular line observations, we know that the structure of molecular clouds is extremely complex. These observations reveal a hierarchy of clumps and filaments on all scales accessible by present day telescopes. Various studies of the mass spectrum of molecular clouds indicate that the spectrum is well described by a power law. Consequently there is no natural mass or size scale for molecular clouds between the observed lower and upper limits. The largest molecular structures considered as "clouds" are the so called giant molecular clouds (GMC). They have masses of typically 10^5 to $10^6\,M_\odot$ and extend over a few tens of parsecs. On the other hand, the smallest observed entities are proto-

stellar cores with masses of a few solar masses or less and sizes of $\lesssim 10^{-2}$ pc. The volume filling factor of dense clumps, even denser subclumps and so on, is very low. It is of the order of 10% or less.

The density structure of molecular clouds is best seen in optically thin spectral lines. The best candidate is ^{13}CO. With the development of very sensitive radio receivers in the 80's it became feasible to map an entire molecular cloud region with high spatial and spectral resolution to obtain quantitative information about the overall density structure. An example of a local giant molecular cloud is given in Fig. 2.2. It is the L1641 cloud in Orion. The maps show the emission from the ^{13}CO (J = 1−0) transition and cover central velocities from $v_{\rm LSR} = 3 - 13\,{\rm km\,s^{-1}}$ in steps of $1\,{\rm km\,s^{-1}}$ (from Bally et al., 1987). In the last panel, the emission integrated over the entire velocity range is shown. It is clearly visible in the maps, that the emission breaks up into clumps and filamentary structure on all resolvable scales and velocity bins. This feature is common to all observed molecular cloud complexes. Like L1641, most GMC's are elongated and are closely aligned with the Galactic plane. Furthermore they show a strong velocity gradient along their major axis which is generally interpreted as rotation. The sense of the angular momentum is typically retrograde with respect to the Galactic rotation (Kutner et al., 1977; Stark & Blitz, 1978).

The hierarchical structure of clumps and filaments spans all observable scales and sizes (see e.g. Falgarone et al., 1992; Falgarone & Phillips, 1996; Wiesemeyer et al., 1997; Wiseman & Ho, 1996). It extends down to individual protostars which are studied by mm-interferometry (Ward-Thompson et al., 1994; Langer et al., 1995; Gueth et al., 1997; Motte et al., 1998). This is illustrated by Fig. 2.3 which shows ^{13}CO, ^{12}CO and C^{18}O maps of a region in the Cygnus OB7 complex at three levels of successively higher resolution (from Falgarone et al., 1992). At each level the molecular cloud appears clumpy and highly structured. When observed with higher resolution, each clump breaks up into a filamentary network of smaller clumps. Unresolved features exist even at the highest resolution. The ensemble of clumps identified in this survey covers a mass range from about $1\,{\rm M_\odot}$ up to a few $100\,{\rm M_\odot}$ and densities $50\,{\rm cm^{-3}} < n({\rm H_2}) < 10^4\,{\rm cm^{-3}}$. These values are typical for all studies of cloud clump structure.

Within the observational margins, the clump mass distribution typically follows a power law of the form

$$\frac{dN}{dm} \propto m^{\alpha}\,, \tag{2.1}$$

with the exponent being in the range $-1.3 < \alpha < -1.8$ (see Tab. 2.1.1). For the remainder of this thesis, a value of $\alpha = -1.5$ will be adopted. The fact that all studies obtain a similar power law is remarkable, and may be the result of turbulent motions acting on

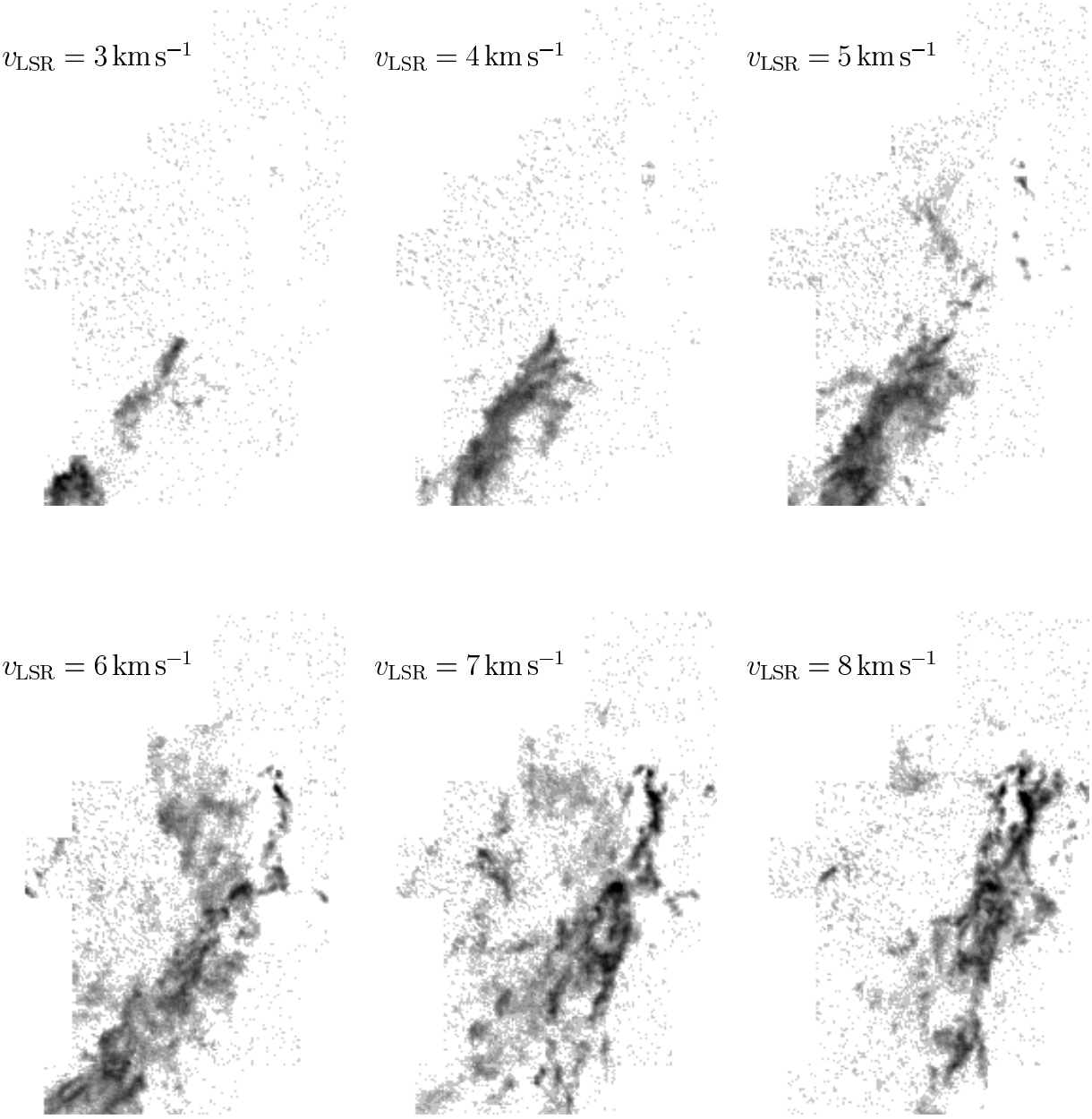

Figure 2.2: The Orion A cloud (L1641) observed in the ^{13}CO (J = 1−0) transition line. Each map shows the integrated emission from a different velocity bin of width $1\,{\rm km\,s^{-1}}$. The LSR velocity of the center of the velocity range is indicated in the upper left corner of each image. The brightness temperature is scaled logarithmically with maximum emission being black. The region covered is roughly $2^\circ \times 5^\circ$ in extent with an angular resolution of about $100''$. Placing L1641 at a distance of 450 pc, this scales to $15 \times 40\,{\rm pc}$. The total amount of molecular gas in this map is $5 \times 10^4\,{\rm M}_\odot$.

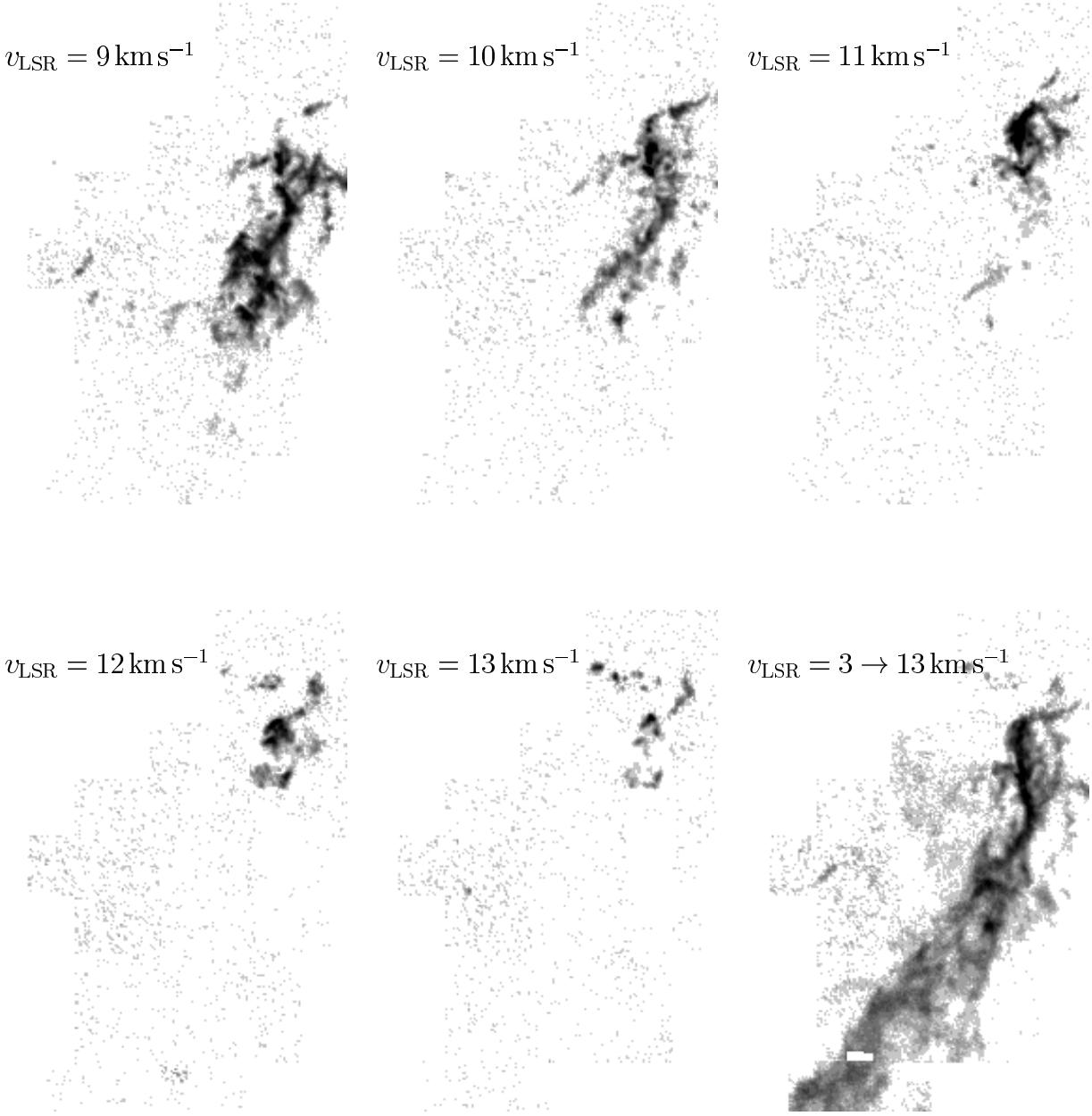

self-gravitating gas. The data for the different clouds are sensitive to different ranges of mass and density, and are obtained from different reduction and analysis techniques. Furthermore, all measurements are determined from fundamentally different sources ranging from very actively star-forming clouds to very cold quiescent ones. Given the uncertainties in determining the slope, it appears reasonable to conclude that there is a universal mass spectrum for the clumps within a molecular cloud, and that the distribution is a power

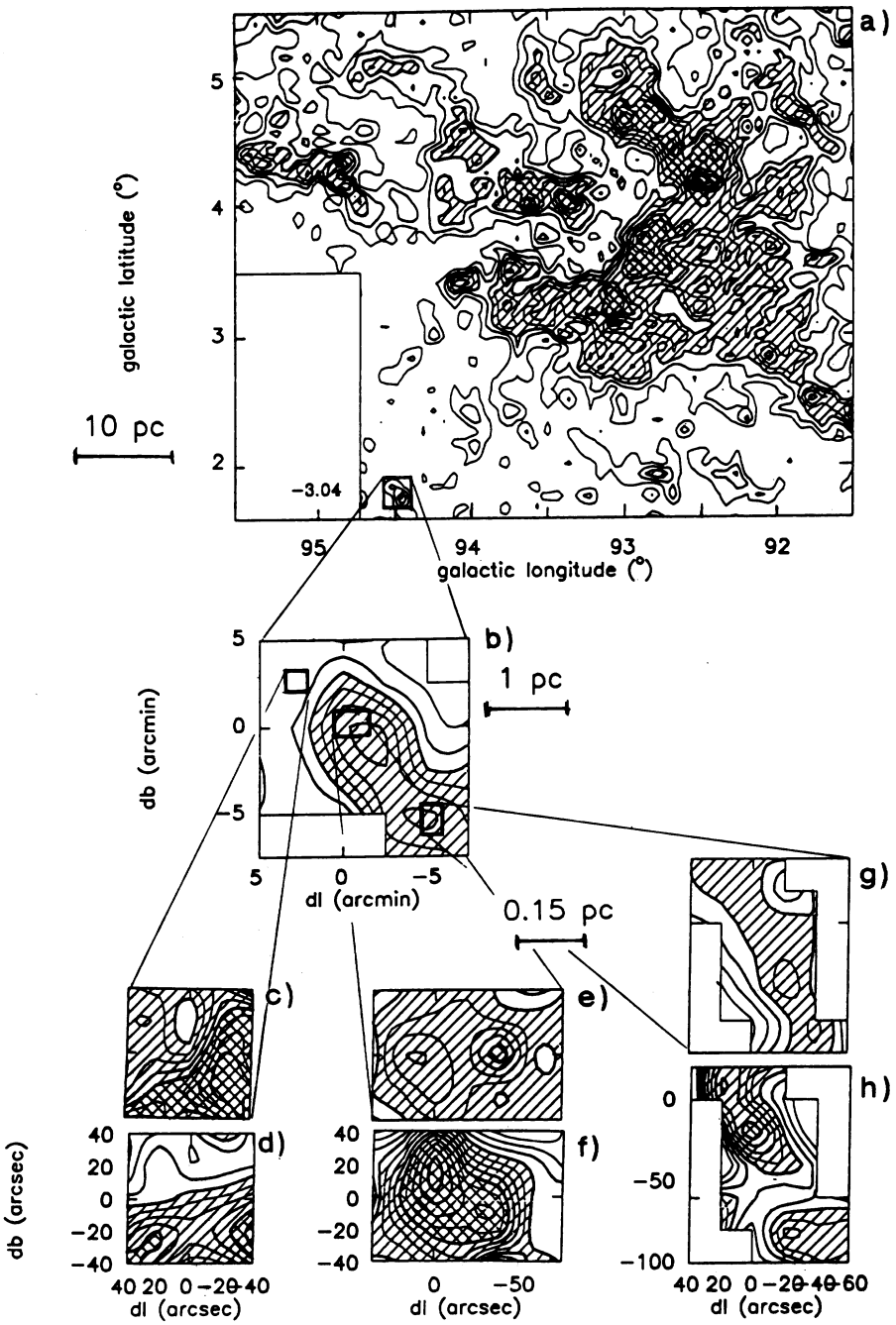

Figure 2.3: Maps of the molecular gas in the Cygnus OB7 complex. (a) Large scale map of the ^{13}CO ($J = 1 - 0$) emission. The first level and the contour spacing are 0.25 K. (b) Map of the same transition line of a sub-region with higher resolution (first contour level and spacing are 0.3 K). Both maps are obtained using the Bordaux telescope. (c) ^{12}CO ($J = 1 - 0$) and (d) ^{13}CO ($J = 1 - 0$) emission from the most transparent part of the field. (e) ^{13}CO ($J = 1 - 0$) and (f) $C^{18}O$ ($J = 1 - 0$) emission from the most opaque field. (g) ^{13}CO ($J = 1 - 0$) and (h) $C^{18}O$ ($J = 1 - 0$) emission from a filamentary region with medium density. The indicated linear sizes are given for a distance to Cygnus OB7 of 750 pc. (The figure is from Falgarone et al., 1992).

Table 2.1: Observed clump mass spectra in molecular clouds

Exponent	Tracer	Source	Reference
-1.7	$C^{18}O$	M17W	Stutzki & Güsten (1990)
-1.6	CS	Orion B	Lada et al. (1991a)
-1.7	^{13}CO	Orion B	Kramer et al. (1998)
-1.3	^{13}CO	Rosette	Williams et al. (1994)
-1.4	^{13}CO	Maddalena	Williams et al. (1994)
-1.3	^{13}CO	Cep OB3	Carr (1987)
-1.6	^{13}CO	Ophiuchus	Nozawa et al. (1991)
-1.7	^{13}CO	Ophiuchus	Loren (1989a)
-1.7	^{13}CO	L1457	Kramer et al. (1998)
-1.6	^{13}CO	L1204	Kramer et al. (1998)
-1.6	^{12}CO	MCLD 126.6+24.5	Kramer et al. (1998)
-1.6	^{13}CO	NGC1499	Kramer et al. (1998)
-1.8	$C^{18}O$	NGC7438	Kramer et al. (1998)
-1.6	^{13}CO	NGC7438	Kramer et al. (1998)
-1.9	$C^{18}O$	Taurus	Onishi et al. (1996)

law within a mass range of three orders of magnitude, i.e. from $1\,M_\odot$ to about $1000\,M_\odot$. Hence, it appears plausible that the physical processes that determine the distribution of clump masses are rather similar from cloud to cloud. And vice versa, clouds that show significant deviation from this universal distribution most likely had different dynamical histories.

There exists an enormous number of studies of molecular cloud structure. For a more detailed introduction into the properties of individual molecular cloud regions, here is a list of useful references: *Cepheus* and *Cassiopeia*: Carr (1987); Grenier et al. (1989); Remy et al. (1997); Yonekura et al. (1997); Yang et al. (1990); Yu et al. (1996), *Cygnus*: Dobashi et al. (1994, 1996); *IC5146*: Lada et al. (1994); Dobashi et al. (1992, 1993); *Lupus*: Nyman et al. (1987); Tachihara et al. (1996); *M17W*: Stutzki & Güsten (1990); *Ophiuchus*: Abergel et al. (1996); Loren (1989a,b); Nozawa et al. (1991); *Orion* and *Monoceros*: Bally et al. (1987); Herrmann et al. (1997); Kramer et al. (1996); Maddalena & Thaddeus (1985); Maddalena et al. (1986); Sakamoto et al. (1994); Tatematsu et al. (1993); *Rosette*: Blitz & Stark (1986); Williams et al. (1995); *Taurus*, *Auriga* and *Perseus*: Hayashi et al. (1994); Hirahara et al. (1992); Kramer & Winnewisser (1991); Mizuno et al. (1995); Nercessian et al. (1988); Ungerechts & Thaddeus (1987); Other clouds: Abraham et al. (1995); Falgarone et al. (1991, 1992); Falgarone & Phillips (1996); Heithausen et al.

(1993); Heithausen (1996); Kramer et al. (1998); Perault et al. (1985). In the outer parts of the Galaxy: Digel et al. (1990).

2.1.2 Temperatures and Line Widths in Molecular Clouds

Molecular clouds are cold. From studying line widths and ratios, the inferred kinetic temperature is typically about 10 K for dark, quiescent clouds and slightly higher for clouds in the proximity of high-mass star-forming regions. For example, the temperature of gas and dust behind the Trapezium cluster in Orion is about 50 K. This higher temperature is due to the heating effects of the UV radiation field from the newly formed O and B stars. However, the interior of the clouds, i.e. the dense cores, are very effectively shielded against radiation and the only heating source that remains are cosmic rays. Therefore, in the presence of nearby star forming regions, one observes a temperature gradient from the outer layers to the inner parts of giant molecular clouds. The temperature in the interior is again approximately 10 K, analogous to dark quiescent clouds (Cernicharo, 1991). This canonical value is the result of the intricate balance between heat input (from cosmic rays) and emission from the most abundant molecular species. Due to the latter, the thermal structure of the gas is related to its density pattern and its chemical abundance. It is therefore remarkable that over a wide range of gas densities and metallicities the equilibrium temperature remains almost constant in a small range around $T \approx 10\,\mathrm{K}$ (Goldsmith & Langer, 1978). This is illustrated in Fig. 2.4 which plots the expected kinetic temperature in dark clouds as function of density for a variety of cooling rates and heating by cosmic rays. It shows that for reasonable chemical composition and densities, the temperature in molecular clouds is roughly constant and the gas can be described to a good approximation by an isothermal equation of state (Eqn. 3.7). This is an important consequence for the numerical simulations presented in this thesis work. However, the approximation of isothermality breaks down when heat can no longer be radiated away efficiently which is the case when the gas density exceeds values of $n(\mathrm{H_2}) \approx 10^{10}\mathrm{cm}^{-3}$. Then the cloud becomes opaque and energy is trapped inside the cloud. The equation of state is then adiabatic with an exponent $\sim 7/5$ being appropriate for molecular hydrogen (see e.g. Tohline, 1982, and references therein).

Giant molecular clouds are gravitationally bound (e.g. Kutner et al., 1977; Elmegreen et al., 1979; Blitz, 1993). Their masses are orders of magnitude larger than the Jeans mass computed from the average density and temperature. Assuming only thermal pressure to oppose gravitational attraction, they should be collapsing and massively forming stars on a free-fall time scale, which is roughly $\tau_{\mathrm{ff}} \approx 10^6$ years. However, that is *not* the case: the typical life time of giant molecular clouds with about 10^7 years is more than ten times larger than the free-fall time scale and the average star forming efficiency with values between 1% and 10% is very low (Blitz & Shu, 1980). The reason is that molecular clouds

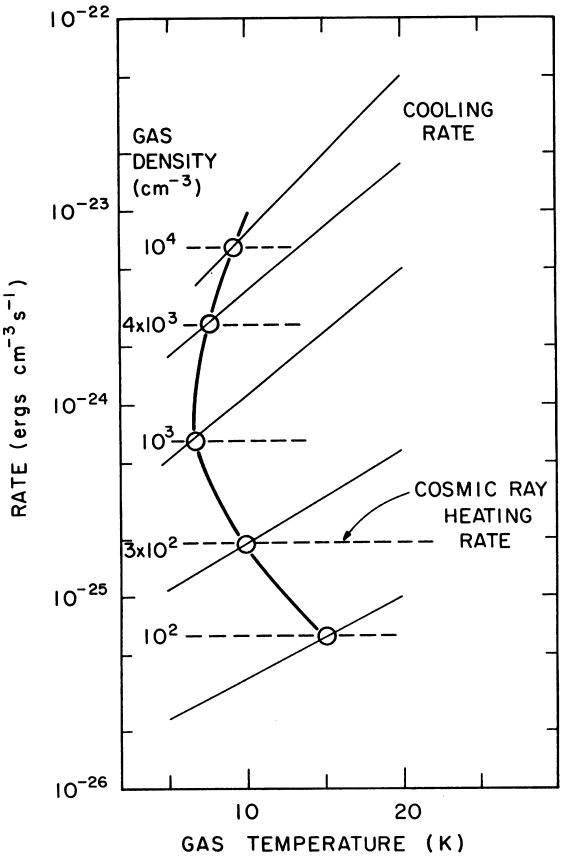

Figure 2.4: Thermal balance between cosmic ray heating and molecular line cooling in an interstellar cloud. The thick line indicates the expected kinetic gas temperature (abscissa) for a particular density. It is determined by the intersection of the heating and cooling curves (ordinate). Only heating by cosmic rays is considered. (The figure is from Goldsmith, 1988).

are stabilized by internal motions which typically are highly supersonic. The observed line widths are *always* wider than implied by the excitation temperature of the molecules. This is interpreted as the result of bulk motion associated with turbulence. Also magnetic fields have long been discussed as stabilizing agent in molecular clouds. However, magnetic fields with average field strength of $10\,\mu$G (Verschuur, 1995a,b; Troland et al., 1996) are not sufficient to stabilize molecular clouds as a whole. Furthermore, magnetic fields are not capable of preventing turbulent velocity fields from decaying quickly (Mac Low et al., 1998). It seems therefore fair to say that the role of magnetic fields in stabilizing giant molecular clouds as a whole is less important. The necessary conclusion is, that turbulence must be constantly driven, because its energy dissipates away too fast to explain the observed cloud life times (for a recent review see Mac Low, 1998). The question about the nature of the source of turbulent energy input is still open. On large scales, Galactic differential rotation introduces shear motions into giant molecular clouds (Fleck, 1981). This energy might cascade down to supply turbulence on smaller scales. Also feedback processes from newly formed stars, bipolar outflows in the late accretion phase, the radiation fields and stellar winds from massive young stars, and finally, the

supernova explosions that terminate the life of massive stars transfer huge amounts of energy and angular momentum into the ambient interstellar medium (e.g. Norman & Silk, 1980; Bertoldi & McKee, 1996). Furthermore, the motion of stars and protostars through the cloud have been considered as possible heating mechanism (e.g. Deiss et al., 1990).

However, the overall velocity dispersion is approximately the same for all molecular clouds, which includes quiescent clouds (either not forming stars at all, like the Maddalena & Thaddeus (1985) cloud, or at very low rate and with small masses, like Taurus), as well as clouds that form stars very actively and with very high masses (like Orion). This fact appears difficult to reconcile with the hypothesis that turbulence is driven from internal sources. Furthermore, molecular clouds have vastly different masses, ranging from giant molecular clouds (with $10^5\,\mathrm{M}_\odot$) down to the very small clouds found at high galactic latitudes (with typical masses of $50\,\mathrm{M}_\odot$, see e.g. Magnani et al., 1985). For all these clouds, the global velocity dispersion is of the same order of magnitude and seems to vary only weakly with galactocentric distance (Clemens, 1985).

For quantification, Tab. 2.2 specifies 'canonical' values for different regions in molecular clouds. It – somehow artificially – distinguishes between giant molecular clouds, that massively form stars, and dark, quiescent clouds, that form stars at very low rates and with low masses. Starting from large complexes, it spans orders of magnitude in size and mass, ranging from individual clouds and their clumpy substructure down to protostellar cores, the gravitationally bound entities that actually form individual stars or binary systems in their interior.

2.1.3 Scaling Relations for Molecular Clouds

Molecular clouds exhibit correlations between various physical properties, such as clump size, velocity dispersion, density and mass. Larson (1981) first noticed, using data of several molecular cloud surveys, that the density ρ and the velocity dispersion σ scale with the cloud size R as

$$\rho \propto R^{\alpha} \tag{2.2.a}$$

$$\sigma \propto R^{\beta}\,, \tag{2.2.b}$$

with α and β being constant scaling exponents. There is a large number of studies of the scaling properties of molecular clouds. The most commonly quoted values of the exponents are $\alpha \approx -1.15 \pm 0.15$ and $\beta \approx 0.4 \pm 0.1$ (e.g. Dame et al., 1986; Myers & Goodman, 1988; Falgarone et al., 1992; Fuller & Myers, 1992; Wood et al., 1994; Caselli & Myers, 1995). However, the validity of these scaling relations is subject of strong

Table 2.2: Physical properties of interstellar clouds

	GIANT MOLECULAR CLOUD	DARK CLOUD
COMPLEX		
Size (pc)	$20-60$	$6-20$
Density ($n(H_2)/cm^3$)	$100-300$	$100-1000$
Mass ($M_\odot$)	10^4-10^6	10^3-10^5
Line width ($km\,s^{-1}$)	$6-15$	$1-3$
Temperature (K)	$7-15$	≈ 10
Examples	W51, W3, M17	Orion-Monoceros, Taurus-Auriga-Perseus complex
CLOUD		
Size (pc)	$3-20$	$1-5$
Density ($n(H_2)/cm^3$)	10^3-10^5	10^2-10^5
Mass ($M_\odot$)	10^3-10^4	$5-500$
Line width ($km\,s^{-1}$)	$4-12$	$0.5-1.5$
Temperature (K)	$10-30$	≈ 10
Examples	L1641, L1630, W33, W3A	B227, L1495, L1529
CLUMPS		
Size (pc)	$\lesssim 0.5-3$	$\lesssim 1$
Density ($n(H_2)/cm^3$)	10^3-10^5	10^3-10^5
Mass ($M_\odot$)	$10-10^3$	$1-100$
Line width ($km\,s^{-1}$)	$1-3$	$0.2-0.5$
Temperature (K)	$10-30$	≈ 10
PROTOSTELLAR CORES		
Size (pc)	$\lesssim 0.1$	
Density ($n(H_2)/cm^3$)	$> 10^6$	
Mass ($M_\odot$)	$0.1-10$	
Line width ($km\,s^{-1}$)	$0.1-1$	
Temperature (K)	$10-100$	
Examples	see Sec. 2.1.5	

This table is adapted from Cernicharo (1991).

controversy and significantly discrepant values have been reported by Carr (1987) or Loren (1989a).

The above 'standard' values can be interpreted in terms of the virial theorem (Larson, 1981; Myers & Goodman, 1988; Caselli & Myers, 1995). For $\alpha = -1$, which implies constant *column* density, a value of $\beta = 0.5$ suggests virial balance between self-gravity and the turbulent velocity dispersion, that is the ratio between kinetic and potential energy is constant with $E_{\rm kin}/|E_{\rm pot}| = \sigma^2 R/(2GM) \approx 1/2$. However, for any arbitrarily chosen value of the density scaling exponent α, a corresponding value of β obeying virial balance can always be found (Vazquez-Semadeni & Gazol, 1995). Under the assumption of virial equilibrium, Larson's relations (Eqn. 2.2) are not independent. In fact, it has been proposed by Kegel (1989) and Scalo (1990) that the density-size relation may be a mere artifact of the limited dynamic range in the observations, and that it may not reflect a real property of interstellar clouds. In particular, in the case of molecular line data, the observations are restricted to column densities large enough that the tracer molecule is shielded against photo-dissociation radiation. With limited integration times, most CO surveys tend to select objects of roughly constant column density, which automatically implies $\rho \propto 1/R$. Surveys that use larger integration times and therefore have larger dynamic range seem to exhibit an increasingly larger scatter in density-size plots, e.g. as seen in the data of Falgarone et al. (1992). Also results from numerical simulations, which are free from observational bias, indicate the same trend (e.g. Vazquez-Semadeni et al., 1997). There are two further concerns: The proportionality between line integrated CO intensity and mass surface density has been reliably established only for extragalactic observations (Dickman et al., 1986). This relationship is only valid for scales larger than a few parsec, at which calibration has been possible. Also it depends on the assumption of local thermodynamic equilibrium and virialization of the gas (e.g. Genzel, 1991). Additionally, for clumps within molecular clouds, the structures identified in CO often do not correspond to those derived from higher-density tracers (e.g. Langer et al., 1995; Bergin et al., 1997; Motte et al., 1998). Altogether, the existence of a unique density-size relation is not well established.

The velocity-size relation does not appear to be so prone of observational artifacts. However, many measurements of molecular clouds do *not* exhibit this correlation (see e.g. Loren, 1989a; Plume et al., 1997). But if it is detected in a molecular cloud, it probably is a real property of the cloud and may be explained by a number of physical mechanisms, ranging from the standard argument of virial equilibrium to the action of interstellar turbulence. In the latter model, the scaling relation is a natural consequence of the characteristic energy spectrum in an ensemble of shocks. Shocks are ubiquitous in supersonic turbulence, which may the dominant agent for stabilizing molecular clouds on large scales (Sec. 2.1.2; see also Fleck, 1996; Vazquez-Semadeni et al., 1997; Mac Low et al., 1998). If the density-size relation (2.2.a) cannot be verified, the standard arguments based on

virial equilibrium between gravity and internal energy cannot be invoked.

In summary, Larson's relations and their interpretation as a result of the virial equilibrium probably apply for dense and strongly self-gravitating clumps. Regions in which the relations are not observed or not well established often show strong evidence of recent perturbations (Loren, 1989a; Caselli & Myers, 1995; Plume et al., 1997) and, hence, are likely not to be in virial equilibrium.

2.1.4 Molecular Clouds as Sites of Star Formation

All giant molecular clouds surveyed within distances less than 3 kpc form stars, except the Maddalena & Thaddeus (1985) cloud. However this cloud may be in a very early evolutionary state, i.e. may have formed just recently. Possible formation mechanisms for molecular cloud complexes involve spiral arm shocks, shear instabilities in the differentially rotating Galactic disk, or Rayleigh-Taylor or thermal instabilities on large scales. Furthermore, they could form in the converging flows of supershells driven by multiple supernovae (for a review see Blitz, 1993). Mooney & Solomon (1988) argue that at least 25% of the molecular clouds in the inner part of Galaxy are *not* forming *massive* stars. However, clouds without O or B star formation may still be forming stars of lower mass in great abundance, like the cloud in Taurus-Auriga. Taking the distance dependent sensitivity limits into account, it appears fair to say that all clouds will form stars at some stages of their evolution.

The star formation process in molecular clouds is fast. Once the collapse of a cloud region sets in, it rapidly forms an entire cluster of stars within 10^6 years or less. This is indicated by the juvenile stars associated with star forming regions which are typically T Tauri stars with ages less than 10^6 years (e.g. Gomez et al., 1992; Greene & Meyer, 1995; Carpenter et al., 1997) or by the small age spread in more evolved stellar clusters (e.g. Hillenbrand, 1997). Once a stellar cluster has formed that contains O or B stars, their radiation fields and stellar winds strongly influence the surrounding molecular cloud: their Strömgren spheres create large cavities of ionized hot gas in the molecular gas distribution and insert energy and momentum into the cloud. This can either trigger a new cycle of star formation in the neighboring cloud regions due to the compression of gas by the induced pressure enhancement, or destroy the molecular cloud as a whole. Using canonical values, a giant molecular cloud may survive the formation of a few O and B stars before their feedback will destroy it completely. This limits the cloud life time to about 10^7 years (Blitz, 1993).

There is considerable debate in the literature, whether there are two distinct modes of star formation, a clustered one and an isolated one, or whether this picture arises solely from observational bias and selection effects. Combining radio data (tracing dense molecular gas) with an IR survey of young stellar objects in the Orion B cloud (L1630), Lada

et al. (1991b) argue that most stars form in dense clusters. They find four pronounced clusters containing 58% – 98% of all young stellar objects in L1630, depending on the correction for field stars. Furthermore, these four clusters are associated with the densest and most massive molecular clumps (Lada, 1992). In contrast, Strom et al. (1993) found in L1641, which is part of the Orion complex as well and several degrees south of L1630, a population of isolated pre-main-sequence stars distributed throughout the cloud. A similar distribution is seen in the molecular cloud in Taurus, which also contains no dense embedded clusters and young stellar objects appear to be evenly distributed throughout the cloud. This dichotomy has led to speculations about two distinct modes of star formation, a clustered and a distributed one. However, this distinction appears quite artificial and the above data sets may not be free of observational bias. The original survey of Lada et al. (1991b) still leaves room for a possible distributed population because of the unknown distribution of field stars. In addition, the observational method to detect young stellar objects has been different in both surveys. The latter issue is addressed in Li et al. (1997) who rederived the results of Lada et al. (1991b). Furthermore, a thorough analysis of the spatial distribution of pre-main-sequence stars in Taurus and several other 'distributed' star forming regions also suggests a clustering tendency (Gomez et al., 1993).

The dichotomy of two different modes of star formation disappears, if one assumes *hierarchical clustering* of the stars analogous to the hierarchical clump structure in the molecular gas they form in. In this picture, stars exhibit clustering properties on all scales considered. The formation of rich clusters is associated with a significant peak in a statistical fluctuation spectrum and the effect of finding O and B stars preferentially in regions of enhanced stellar density is explained as a mere statistical effect. Assuming a universal initial stellar mass function the probability of finding a high-mass star increases linearly with the sample size, i.e. with the total number of stars in the observed region. The picture of a hierarchical or equivalently fractal spatial distribution of stars in star forming regions is also supported by more detailed statistical studies of the distribution of neighboring stars in young stellar clusters (Larson, 1995; Simon, 1997; Bate et al., 1998). Hierarchical clustering seems to be a common feature of all star forming regions. Furthermore, it is a natural outcome of the isothermal fragmentation calculation presented in this thesis. In all our models, the dynamical evolution of self-gravitating gas results in the formation of a hierarchically structured cluster of protostellar cores (see Sec.'s 6 and 7).

2.1.5 Properties of Protostellar Cores

Protostellar cores are the direct precursors of stars. The properties of young stars are thus intimately related to the properties of their parental clumps and it is therefore important to observationally determine the characteristics of condensed cores in molecular clouds. A

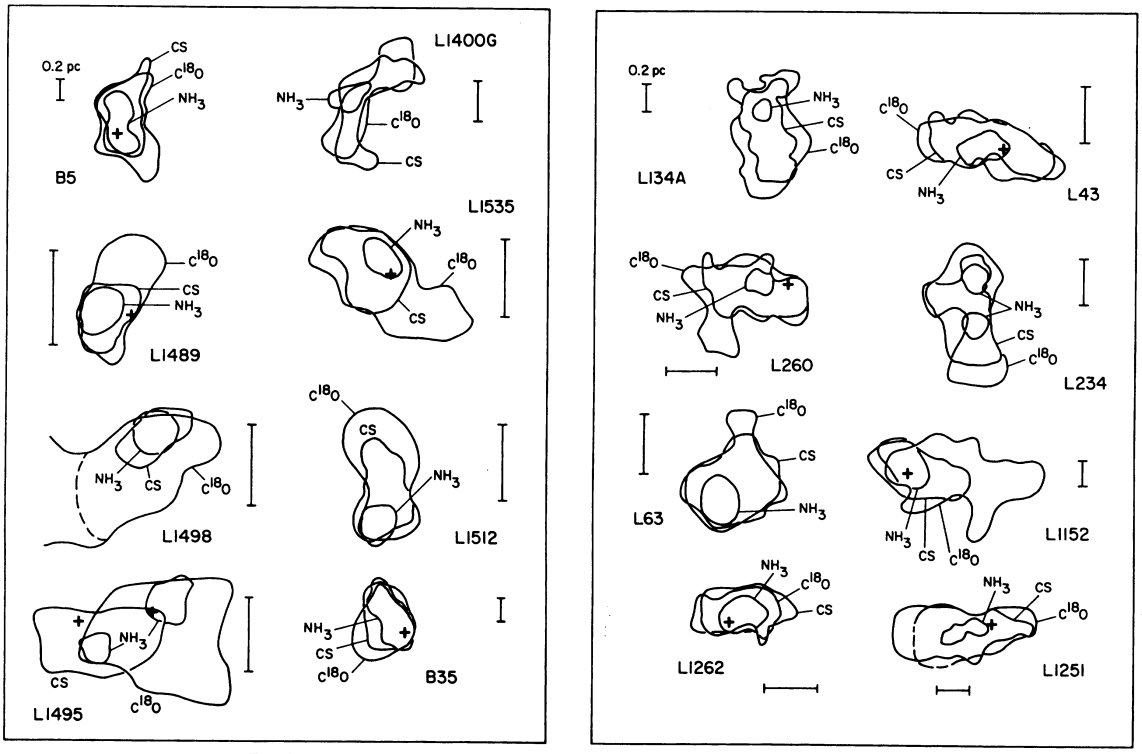

Figure 2.5: Intensity contours at half maximum of 16 dense cores in dark clouds, in the 1.3 cm $(J,k) = (1,1)$ lines of NH_3, in the 3.0 mm $J = 2 \rightarrow 1$ line of CS, and the 2.7 mm $J = 1 \rightarrow 0$ line of $C^{18}O$. A linear scale of 0.2 pc is indicated in each individual map and associated protostars are specified by a cross. The figure is from Myers et al. (1991).

number of such small dense molecular cores have been identified by low angular resolution molecular line surveys of nearby dark clouds (e.g. Benson & Myers, 1989). These cores are thought to be the sites of low-mass star formation. About half of them are associated with low-luminosity IRAS sources and CO outflows, the other half is designated as 'starless' (e.g. Beichman et al., 1986). Those may be in a evolutionary state shortly *before* forming stellar objects in their interior, thus they often are referred to as pre-stellar cores. One of the most notable properties of the sampled cores are their very narrow line widths. These are very close to the line widths expected for thermal broadening alone and, as a result, many of the cores appear approximately gravitationally virialized (see Myers, 1983). They are thought either to be in the very early stage of gravitational collapse or have subsonic turbulence supporting the clump. A comparison of the line widths of cores with embedded protostellar objects (i.e. with associated IRAS sources) and the 'starless' cores reveals a substantial difference. Typically, cores with infrared sources exhibit broader lines, which suggests the presence of a considerable turbulent component not present in 'starless' cores. This may be caused by the central protostar feeding back energy and momentum into its surrounding envelope. Molecular outflows associated with many of the sources

may be direct indication for this process. The first submillimeter continuum maps of dense pre-stellar cores were made by Ward-Thompson et al. (1994); for a recent survey in the ρ-Ophiuchus cloud see Motte et al. (1998). The authors of this high-resolution studies found that 'starless' cores are larger and less centrally condensed than the cores with embedded sources. But both groups appear to have similar masses. Altogether, the 'starless' cores are probable the precursors of class 0 protostellar clumps and may reflect the very early stages of protostellar collapse: a gravitationally bound fragment has formed in a molecular cloud which evolves towards progressively higher degree of central condensation, but has not yet formed a hydrostatic protostar in the center (a class 0 object). The 'starless' cores are observed in the mass range from about $0.1\,M_\odot$ to $10\,M_\odot$. Typical line widths are $0.4\,\mathrm{km\,s^{-1}}$ in NH_3 and $0.6\,\mathrm{km\,s^{-1}}$ in $C^{18}O$ for cores with embedded sources and $0.3\,\mathrm{km\,s^{-1}}$ in NH_3 and $0.5\,\mathrm{km\,s^{-1}}$ in $C^{18}O$ for pre-stellar cores with embedded sources (see e.g. Butner et al., 1995). For comparison, a gas temperature of 10 K corresponds to a thermal line width of $0.16\,\mathrm{km\,s^{-1}}$ for NH_3 and $0.12\,\mathrm{km\,s^{-1}}$ for $C^{18}O$. High-resolution maps suggest that the radial density profiles of the pre-stellar cores on average follow a $1/r^2$-law but are relatively steep towards their edges and flatten out near their centers (Ward-Thompson et al., 1994; Motte et al., 1998). Furthermore, their 2-dimensional shapes deviate quite considerably from spherical symmetry, as illustrated in Fig. 2.5. The cores are elongated with ratios between semi-major and semi-minor axis of about $2-3$; some even appear completely irregular.

2.2 Overview of the Star Formation Process

A self-consistent and comprehensive theory of star formation does not yet exist, and maybe a fully deductive theory capable of predicting the properties of star forming regions from a few basic principles will never exist, because the physical phenomena involved are too complex and too numerous: star formation depends on many processes and many variables which are all interrelated in a delicate way. This and the influence of highly unpredictive and stochastic phenomena make it difficult to treat the complete subject in a deterministic way in the tradition of classical physics.

The process of star formation begins with the formation of molecular cloud complexes in a galaxy and includes their dynamical evolution to the formation of highly self-gravitating dense cores. These may become unstable against collapse and may form a highly condensed object in the interior. The central density increases until it exceeds the threshold for nuclear fusion processes to set in. A new source of energy is available and stops the contraction – a protostar is born. It still is embedded in its parental envelope which continues to fall towards the center. Hence, the central object grows further in mass via accretion of this inflow. However, conservation of angular momentum prevents the

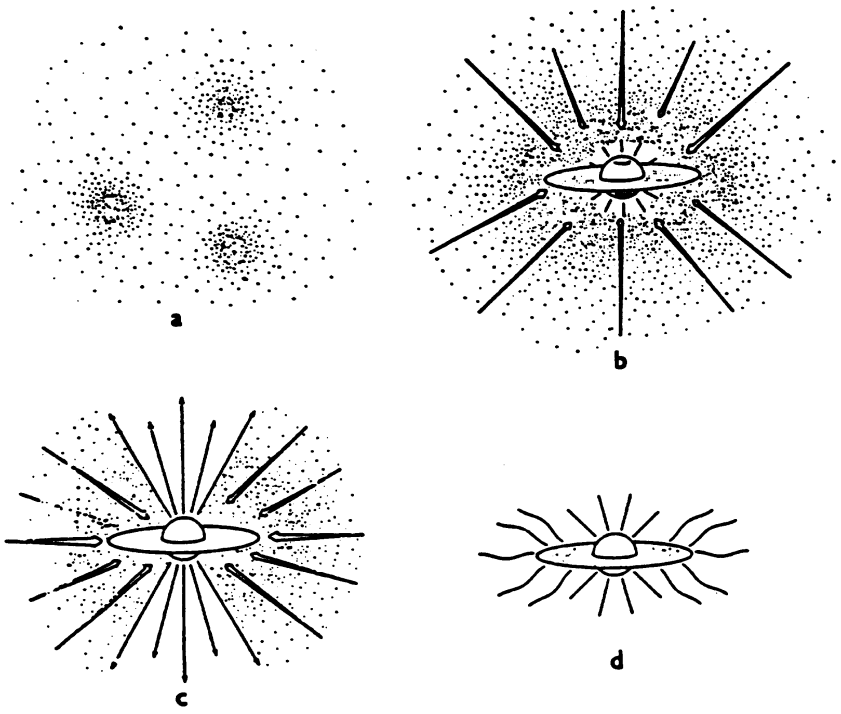

Figure 2.6: The main stages of star formation: (a) Cores form within molecular clouds in areas where self-gravity overwhelms turbulent support. (b) A protostellar object surrounded by an accretion disk forms in the center of the collapsing cloud core. (c) Stellar winds and radiation break out along the rotational axis of the system, create a bipolar outflow and dissolve the protostellar envelope. (d) The envelope has been removed and the infall terminates. The newly formed star is revealed on the main sequence. A circumstellar disk may still exist at that stage, but will disappear on short time scales. The figure is from Shu et al. (1987).

bulk of the material to fall directly onto the central object. It assembles in a rotationally supported disk and matter can only flow towards the star by dissipating momentum through viscous transport phenomena. Magnetic fields may play a crucial role at that stage. Parts of the gas that streams towards the star may get expelled in form of bipolar outflows maybe confined by magnetic field lines. Such a flow is able to pump a considerable amount of energy and momentum into the surrounding protostellar envelope. At the same time, strong stellar winds and strong radiation fields may develop. All effects together will eventually blow the parental gas clump away and reveal the star on the main sequence. These steps of star formation are illustrated in Fig. 2.6. Furthermore, stars form in hierarchical groups, where they interact with each other and modify each others evolution. The binary fraction of young star clusters may be as high as 100%. Stellar feedback processes not only influence their immediate vicinity, they can influence the entire molecular cloud. The UV radiation of a few O stars is enough to ionize a large volume

inside a molecular cloud. Statistically, this limits the life time of giant molecular clouds to $\sim 10^7$ years. On the other hand, stellar feedback may compress parts of a molecular cloud and thus induce a new generation of the star formation cycle. Dissolved clouds replenish the diffuse phase of the ISM and largely determine its properties. All these processes participate in the star formation cycle and that chain of feedback effects makes star formation strongly self-regulated. A comprehensive theory of star formation must take all these processes into account, an apparently unsurmountable task. The formation of individual stars are highly indeterministic statistical events. However, for the description of properties of large *ensembles* of stars, say when studying the IMF, this bears the chance of understanding the process in a probabilistic sense within the framework of a statistical theory (see Sec 2.3).

2.2.1 Analytical Models of Protostellar Collapse

Because of the overall complexity of the problem analytical models for the formation of stars exist only in highly idealized cases. Typically, analytical work concentrates on the collapse of single, isolated spheres and focuses on efforts to find similarity solutions describing the asymptotic evolution of a collapsing cloud core including various physical effects. The two most important solutions represent opposite limiting cases. The first was derived by Larson (1969) and independently by Penston (1969). It describes the asymptotic evolution of the innermost part of an isothermal, freely collapsing spherical cloud towards the development of a central density singularity and has been extended past the singularity by Hunter (1977). The second solution was found by Shu (1977) for the inside-out collapse of an equilibrium singular isothermal sphere that is assumed to have formed by slow quasi-static evolution (say via contraction on the ambipolar diffusion time scale). A comprehensive discussion of the possible similarity solutions for an isothermally collapsing sphere has been presented by Whitworth & Summers (1985). They have shown that there is actually an infinite family of such solutions, where the Larson-Penston and the Shu solutions represent opposite limiting cases and all other possibilities are intermediate between them.

One of the most important quantities in these models is the accretion rate onto the central point mass. In the Shu (1977) solution, the accretion rate onto the protostar is constant in time and equal to $0.975\, c_{\rm s}^3/G$, where $c_{\rm s}$ is the isothermal sound speed and G the gravitational constant. On the other hand, in the Larson-Penston solution, the accretion rate is strongly varying with time. Initially it is very high, with $\dot{m} = 47\, c_{\rm s}^3/G$, but quickly declines and becomes smaller even than the Shu value. Its much higher initial value results from the fact that the protostellar envelope is falling inward at 3.3 times the sound speed rather than at rest, and also because it has a higher density at each radius than the singular isothermal sphere. Numerical simulations give values more

closely resembling the solution of Larson and Penston (see e.g. Hunter, 1977; Foster & Chevalier, 1993).

Since the star formation process involves the action of a large number of physical phenomena, many authors have sought to generalize the simple analytical models. Typically, the effects of magnetic fields and rotation have been examined. The collapse of an unstable magnetized cylinder with conservation of magnetic flux (i.e. with no ambipolar diffusion) has been calculated numerically by Tomisaka (1996). His models form a flattened disk-like structure which becomes increasingly centrally condensed and eventually develops a central singularity in a self-similar way that closely resembles the Larson-Penston solution for unmagnetized spherical collapse. The analogous problem of the collapse of an unstable rotating cylinder with conservation of angular momentum has been addressed most recently by Matsumoto et al. (1997) who also find a similar result: a central disk forms and becomes increasingly centrally condensed, evolving towards a central singularity in an approximately self-similar fashion with superimposed oscillations. In both, the rotating and the magnetized cases, supersonic infall velocities of about twice the sound speed were found. This shows that as long as the cloud was initially unstable to collapse neither rotation nor a magnetic field qualitatively changes the way in which a core collapses towards a central singularity.

Many theoretical discussions of star formation assume that the initial state of protostellar cores is a *stable* equilibrium configuration supported by magnetic fields and evolves only slowly by ambipolar diffusion. In these models, a protostellar core evolves quasi-statically into a state closely resembling a singular isothermal sphere before it becomes magnetically supercritical and begins to collapse from inside out, as is assumed by Shu (1977). This was studied numerically by Basu & Mouschovias (1995) with the result that a singular isothermal sphere is never closely approached, magnetic support is lost at early stages before the cloud becomes very centrally condensed. This is also found in analytic work by Basu (1997) and Safier et al. (1997). Also Whitworth et al. (1996) have given arguments against accepting the Shu (1977) model as a good description of star formation. This model provides no clear way to account for binary or multiple stellar systems with are the most common outcome of the star formation process which requires a more dynamic picture of the protostellar evolution. Altogether, the most successful analytical model of the collapse of protostellar cores appears to the Larson-Penston similarity solution, however idealized it may be.

2.2.2 Numerical Models of Protostellar Collapse

As discussed in the previous section, analytical solutions for the collapse of individual cores exist, but only for highly idealized cases. To study more realistic cases and es-

pecially the formation of binary stars, numerical modeling becomes necessary. Hence, by now the number of publications on protostellar collapse calculations has grown quite large. Simulations including the effects of magnetic fields have been performed by Basu & Mouschovias (1995) and Tomisaka (1996). However, most authors have considered non-magnetic clouds with solar abundance, and typically the collapse has been assumed to be isothermal with a temperature $T \approx 10\,\mathrm{K}$ (see Bonnell & Bastien, 1993; Boss, 1996; Burkert & Bodenheimer, 1996; Di Sigalotti & Klapp, 1996; Monaghan, 1994; Nelson & Papaloizou, 1993; Truelove et al., 1998). Other calculations include radiation transport to account for the heating that occurs once the cloud reaches densities of $n(\mathrm{H_2}) \gtrsim 10^{10}\,\mathrm{cm^{-3}}$ (Boss, 1993; Myhill & Kaula, 1992), or simply assume an adiabatic equation of state once that density is exceeded (Bonnell, 1994; Bate et al., 1995). Others invoke cooling during the collapse (Monaghan & Lattanzio, 1991; Turner et al., 1995; Whitworth et al., 1995) but treat larger volumes and lower densities than that of protostellar cores. If there is a series of papers on the same topic, for the sake of brevity only the latest one has been quoted in the above list of references. For a recent overview see (Burkert et al., 1998).

Typical for all numerical simulations is an almost free-fall collapse with little growth of initial perturbation. This is followed by a phase in which a disk-like equilibrium is reached in the central regions of the cloud because of rotational effects. Fragmentation of the disk into a binary or into a multiple system then occurs. For angular momenta consistent with those observed for cloud cores, a binary or small system of fragments typically forms with eccentric orbits and separations in the range 10 to a few hundred AU. Fragmentation appears independent of the initial density distribution, but is sensitive to the parameters α and β, which are the ratios between internal and gravitational energy and between rotational and gravitational energy, respectively.

The collapse of an isolated protostellar core leading to fragmentation and the formation of a small multiple stellar system is illustrated in Fig. 2.7. It is from a calculation by Burkert et al. (1997) and starts with a uniformly rotating spherical core of mass $1.0\,\mathrm{M_\odot}$ and radius $3.3 \times 10^3\,\mathrm{AU} = 0.016\,\mathrm{pc}$. The initial density distribution is a power law with $\rho \propto 1/r$, where r is the distance from the center, and $\alpha = 0.35$ and $\beta = 0.23$. The initial density field is perturbed by an $m = 2$ mode with an amplitude of 10% and the computation is performed with a finite-difference code with nested subgrids. Figure 2.7a shows the onset of fragmentation in the central region of the core containing about 12% of the total mass. The central density has increased by $\sim 10^4$ and a spiral arm pattern has formed in the disk-like structure which is a consequence of the initial $m = 2$ perturbation. The spiral arms start to fragment and form a triple system which again induces a new spiral pattern in the parts of the disk that lie further out (Fig. 2.7b). The interaction of these outer spiral arms leads to subsequent fragmentation (Fig. 2.7c,d). At the same time, the unstable inner triple system converts into an close inner binary with an outer orbiting companion, which soon merges with one of the components of the outer binary. Clearly

the situation is highly complex and as gas accretion from the infalling envelope continues additional merging of protostellar knots or further subfragmentation is likely to occur. The mass distribution of the fragments is very unequal: the mass of outer companion of the triple system is about one tenth of the mass of the components of the inner binary, which have comparable masses.

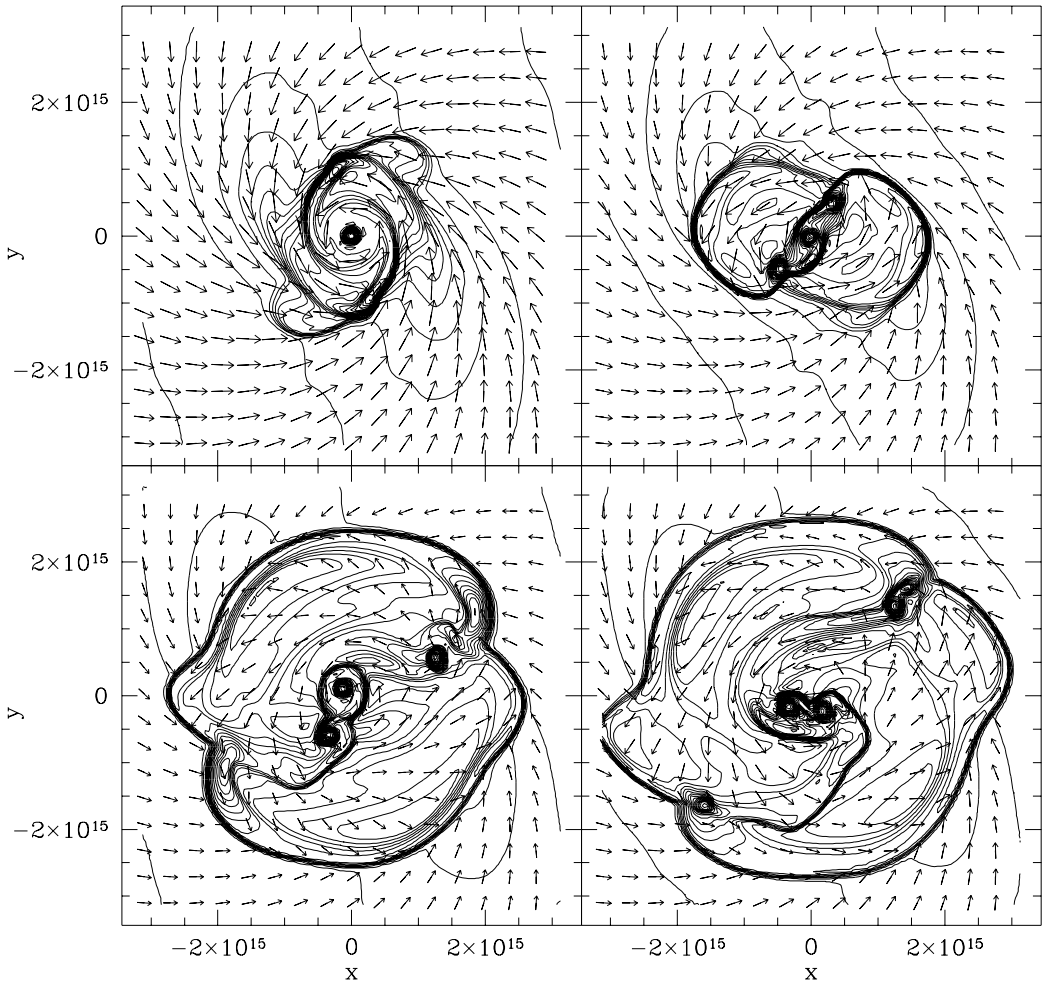

Figure 2.7: Contours of equal density in the equatorial plane at different times of the evolution of a centrally condensed protostellar core with $\alpha = 0.35$ and $\beta = 0.23$. The linear size of the shown region is about 1/20 of the initial cloud radius. Density is scaled logarithmically and velocity vectors are given with length linearly proportional to the speed. For more details see Burkert et al. (1997), where the figure is obtained from.

In summary, the collapse of a rotating protostellar core is likely to produce a multiple system of typically 2 to 5 protostars. Fragmentation occurs only at critical densities which

are about 6 to 8 orders of magnitude larger than the initial values. Hence, fragmentation could be suppressed if the core becomes optically thick before its density passed beyond the critical value. This threshold scales with the core mass m as $1/m^2$, therefore, higher-mass cores are more likely to fragment to form multiple stellar systems than low-mass cores. This may explain why the stellar mass function decreases much faster with increasing mass than the observed mass function of molecular cloud cores. Like the molecular cloud cores on larger scales (see Sec.'s 6 and 7), multiple systems of protostars evolve through N-body encounters while accreting gas from their surrounding. They may merge or trigger further fragmentation. As a result, the outcome of detailed collapse calculations of individual protostellar is unpredictable and can only be determined in a statistical approach.

2.2.3 Numerical Models of Large Scale Collapse

Since most of the numerical work in the field of star formation has concentrated on the collapse of isolated objects, there is a need to extend these studies to larger scales to include the effects of the environment on the evolution and properties of protostellar cores and consequently on the stars that form within. As will be shown in this dissertation, under typical molecular cloud conditions, protostellar cores form from merging gas clumps and strongly interact and perturb each other being immersed in the complex global flow pattern of the cloud. Protostellar cores gain mass through accretion from their parental gas envelopes. If a gas clump contains multiple cores these compete with each other for the available gas reservoir. All these processes determine the masses and kinematical and spatial properties of protostellar cores. Hence, modeling the formation and dynamical evolution of an entire cluster of protostars requires the correct treatment of all these effects.

Previous numerical simulations of the collapse and fragmentation of molecular cloud regions have indeed shown that a large number of condensed objects can form on a dynamical timescale as a result of gravitational fragmentation (e.g. Larson, 1978; Monaghan & Lattanzio, 1991; Keto et al., 1991; Turner et al., 1995; Whitworth et al., 1995). In these studies, the clouds were treated as isolated gaseous spheres which collapse completely onto themselves. Instead, to have the necessary dynamic range and resolution, we study a small region embedded in a large, stable molecular cloud complex where only the overdense regions are able to contract due to self-gravity. We assume periodic boundary conditions to account for the molecular cloud support on large scales by turbulence and/or other processes. Previous numerical models were also strongly constrained by numerical resolution. Larson (1978), for example, used just 150 particles in an SPH-like simulation. Turner et al. (1995) and Whitworth et al. (1995) were the first who addressed star formation on larger scales in detail using high-resolution numerical models. However,

they studied a different problem: fragmentation and star formation in the shocked and rapidly cooling interface of colliding molecular clumps. While clump-clump interactions are expected to be abundant in molecular clouds, the rapid formation of a whole star cluster requires gravitational collapse on a larger scale which contains many clumps and dense filaments.

It is the aim of this dissertation to extend previous studies of the collapse of isolated objects to the regime of the isothermal collapse and fragmentation of a gravitationally unstable *region* embedded in the interior of a molecular cloud. We present numerical models of the dynamical evolution and follow the fragmentation into dense protostellar cores for a large number of different initial gas distributions and different numbers of Jeans masses. The time evolution of the gaseous system is computed using the SPH method with particle numbers ranging from 5×10^4 to 5×10^5. Details of the numerical realization are found in Sec. 3. These calculations may also provide the input data for more detailed, high-resolution collapse calculations of individual cores (Burkert et al., 1998).

2.3 The Initial Stellar Mass Function (IMF)

The initial stellar mass function (IMF) is perhaps the most important result of the star formation process. A detailed knowledge about the distribution of stellar masses is a necessary ingredient for the understanding of many astrophysical phenomena. It is important for the structure and the turbulent dynamics of the interstellar medium, out of which stars form and onto which they directly feed back energy and momentum, but also for the formation and chemical evolution of galaxies as a whole. Unfortunately, the current theory of star formation (see Sec. 2.2) remains unable to derive the IMF from first principles. Most likely, a deterministic analytical formula for the IMF does not exist and instead, realistic models need to be found in the framework of a probabilistic theory of the star formation process. The formation of stars is the outcome of the combination of highly chaotic and indeterministic processes. This picture of the star formation process is strongly supported by the results of this dissertation.

Before introducing the current (competing) statistical models of the IMF, a brief overview about its observational derivation will be given.

2.3.1 The Observed IMF

Gravitationally bound gas spheres are considered to be stars in a classical sense only in a finite mass range. Stellar objects with masses less than about $0.08\,\mathrm{M}_\odot$ cannot produce central temperatures hot enough for the fusion of hydrogen to take place and are called

brown dwarfs (e.g. Burrows et al., 1993; Laughlin & Bodenheimer, 1993). On the other hand, stars with masses greater than about $100\,\mathrm{M}_\odot$ are unstable (e.g. Phillips, 1994). Hence, stars are confined to the mass range

$$0.08 \lesssim m \lesssim 100\,, \tag{2.2}$$

with the dimensionless mass $m \equiv M/(1\mathrm{M}_\odot)$ normalized to solar masses.

It is complicated and laborious to estimate the IMF in our Galaxy empirically. The first such determination from the solar neighborhood (Salpeter, 1955) showed that the number $f(m)$ of stars with masses in the range m to $m+dm$ can be approximated by a power-law relation

$$f(m)dm \propto m^{-\alpha}dm\,, \tag{2.3}$$

with the index $\alpha \approx 2.35$ for stars in the mass range $0.4 \leq m \leq 10$. However, the approximation with one single power-law is overly simplified. Later, Miller & Scalo (1979) introduced a log-normal functional to describe the IMF,

$$\log_{10} f(\log_{10} m) = A - \frac{1}{2(\log_{10}\sigma)^2}\left[\log_{10}\left(\frac{m}{m_0}\right)\right]^2\,. \tag{2.4}$$

Their work has been reinvestigated and improved in a variety of aspects by many authors, for a recent review see Scalo (1998). As illustration, Fig. 2.8 plots the IMF derived from star counts in the solar neighborhood by Scalo (1986) assuming an Galactic disk age of 12×10^9 years. However, the determination by Miller & Scalo (1979) and subsequent studies before the mid 1990's have not taken into account the contamination of star counts by binary and multiple systems. Binary stars can only be resolved and identified as such, if their angular separation exceeds the angular resolution of the telescope used to survey the sky. Otherwise, they are falsely counted as single stars. Neglecting this effect reduces the inferred stellar densities and overestimates the masses of stars. This strongly influences the derived stellar mass distribution and severely underestimates the number of low-mass stars.

For the low-mass end of the IMF, we use the values derived by Kroupa et al. (1990, 1993) for the solar vicinity. Neglecting the effects of binary and multiple systems, Kroupa et al.

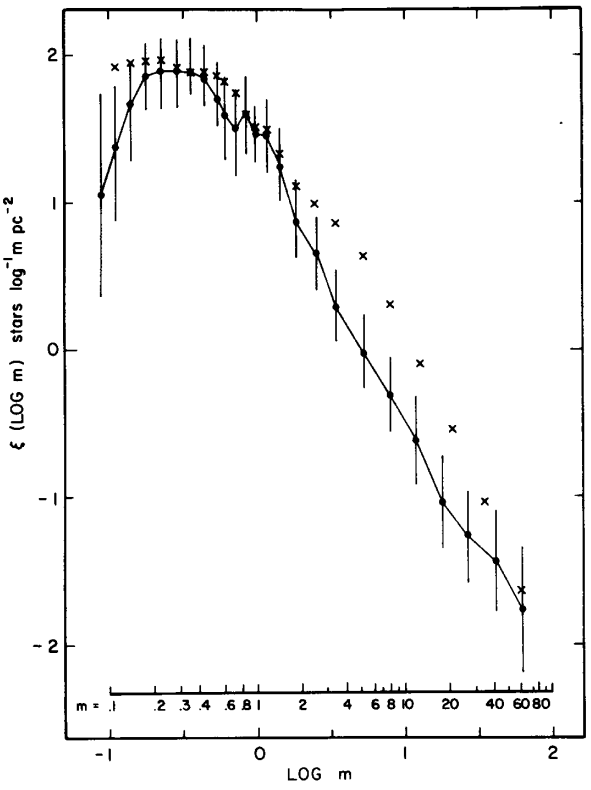

Figure 2.8: Field star IMF derived by Scalo (1986). The data are not corrected for binary contamination and assume a disk age of 12×10^9 years. Crosses represent the IMF obtained by Miller & Scalo (1979).

(1990) derive the following parameters[2] for a log-normal fit:

$$\begin{aligned} m_0 &= 0.23 \\ \sigma &= 0.42 \\ A &= 0.1 \end{aligned} \tag{2.5}$$

This is valid for masses less than a few solar masses. Since the numerical simulations performed for this dissertation cannot resolve close binary stars, this uncorrected mass function is the appropriate one to compare with the computed values and will be referred to as the standard IMF for multiple systems later on (see Sec.'s 6 and 7).

If the effect of unresolved binary and multiple systems is taken into account in an appropriate way, the initial mass function of *single* stars in the solar neighborhood is best fit

[2]Miller & Scalo (1979) derived the log-normal IMF as a quadratic fit to the observed data in $\log m$: $\log_{10} f(\log_{10} m) = a_0 - a_1 \log_{10} m - a_2 (\log_{10} m)^2$. For a disk age of 12×10^9 years, they derive $a_0 = 1.53$, $a_1 = 0.96$ and $a_2 = 0.47$ and for an age of 9×10^9 years, they obtained $a_0 = 1.47$, $a_1 = 1.02$ and $a_2 = 0.44$. The relations between the parameters used in Eqn. 2.4 and by Miller & Scalo (1979) follow as $a_0 = A - 1/2\,(\log_{10} m_0)^2 (\log_{10} \sigma)^{-2}$, $a_1 = -\log_{10} m_0 (\log_{10} \sigma)^{-2}$ and $a_2 = 1/2\,(\log_{10} \sigma)^{-2}$.

by a three-component power-law with the following parameters (Kroupa et al., 1993),

$$f(m) = \begin{cases} 0.035\, m^{-1.3} & \text{for } 0.08 \leq m < 0.5\,, \\ 0.019\, m^{-2.2} & \text{for } 0.5 \leq m < 1.0\,, \\ 0.019\, m^{-2.7} & \text{for } 1.0 \leq m < \infty\,. \end{cases} \tag{2.6}$$

In this formula, especially the exponent for masses $0.08 \leq m < 0.5$ is very uncertain. Depending on the abundance of very low-mass stars the exponent could vary between -0.7 and -1.8.

Outside the solar vicinity, only the intermediate to high-mass parts of the IMF can be determined. There are some indication that the slope of the mass spectrum obtained from field stars may be slightly shallower than the one obtained from observing stellar clusters (Scalo, 1998). The reason for this difference is unknown and somehow surprising, considering the fact that field stars presumably come from dissolved clusters. It is possible that the field star IMF is inaccurate because of incorrect assumptions about past star formation rates and age dependences for the stellar scale height. Both issues are either known or irrelevant for the IMF derived from cluster surveys. On the other hand, these could be subject to failures in detecting low-mass stars due to extinction, crowding or unanticipated pre-main-sequence evolution, which may be modified by collisional effects likely to be important in dense clusters. However, this trend is not at all clear given the different observational methods applied and the uncertainties involved. The IMF may furthermore vary as function of the metallicity or correlated with that as function of Galactic age.

Altogether, the initial stellar mass spectrum has been derived from vastly different regions, from the solar vicinity to dense clusters of newly formed stars. Besides differing in the details as discussed above, all determinations share the same basic features. Therefore, the IMF is ofter considered as being a universal function, common to all star forming regions.

2.3.2 Models for the IMF

The existing models to explain the initial distribution of stellar masses can be divided into two major categories. The first group points out the dominance of the initial conditions for star formation. In this picture, the structural properties of molecular clouds, the mass distribution of Jeans-unstable gas clumps and their spatial and kinematical features, determine the mass of the star that forms inside a gas clump. Assuming a fixed star formation efficiency of individual clumps, there is a one-to-one correspondence between the final star and the molecular cloud structure. The idea that fragmentation of clouds leads directly to the masses of forming stars dates back to Hoyle (1953) and later

Larson (1973). More recently, this has been extended to include the observed fractal and hierarchical structure of molecular clouds (Larson, 1992, 1995). Indeed random sampling from a fractal cloud seems to be able to reproduce the basic features of the observed IMF (Elmegreen, 1997). Price & Podsiadlowski (1995) and Murray & Lin (1996) consider collisional interaction between cloud pieces to make the clump or star mass distribution. Studying different fragmentation schemes, Zinnecker (1984, 1990) shows that whenever a large set of parameters is involved in determining stellar masses, invoking the central limit theorem naturally leads to a log-normal distribution function. This shall be derived in detail in Sec. 2.3.3.

The second group of IMF models incorporate the concept, that the stars themselves may determine their masses. Silk (1995) discusses the IMF for stars that have masses limited by feedback due to both ionization and protostellar outflows. Nakano et al. (1995) describe a model in which stellar masses are sometimes limited by the mass scales of the formative medium and sometimes are limited by stellar feedback. The most detailed model in this category stems from Adams & Fatuzzo (1996) and provides a transformation between the initial conditions in molecular clouds and the final masses of the forming stars. In the limit where many independent physical variable contribute to the stellar masses, applying the central limit theorem leads to a log-normal IMF.

Probably the truth lies in a combination of both categories of models. The structure and dynamical state of molecular clouds are certainly important in determining the properties of protostellar cores that form via gravitational collapse in Jeans unstable gas clumps. However, further physical phenomena come into play to determine which fraction of clump mass will end up in the (multiple) stellar objects in the center. The viscous transport processes in the accretion disk are important, as well as stellar winds or outflows, and in the case of massive stars their radiation field.

Regardless of the detailed physical processes involved, the most important and common feature to all appears to be their statistical nature. Given a set of initial conditions, one is not able to compute the fate of *individual* objects. Only in a probabilistic sense it is possible to determine the evolution of an *ensemble* of objects. The implication is that the star formation process can only be understood within the framework of a statistical theory.

2.3.3 The IMF as a Result of the Central Limit Theorem

In this section, a statistical approach to the calculation of the IMF is adopted. The IMF will be derived in the limit in which a large number of independent physical variables are required to determine the stellar masses.

Consider the case in which the mass M of a star can be expressed as the product of N independent variables x_j

$$M = \prod_{j=1}^{N} x_j \ . \tag{2.7}$$

Taking the logarithm of this equation, the logarithm of the mass is a sum of the random variables,

$$\ln M = \sum_{j=1}^{N} \ln x_j + \text{constant} \ , \tag{2.8}$$

where the constant term includes all quantities that are truly constant, e.g. the gravitational constant G or the gas constant $\mathcal{R}$. The stellar mass is determined by a composite random variable which is the sum of N independent random variables $\ln x_j$. The central limit theorem shows that the distribution of the composite variable always approaches a normal distribution as the number N of variables approaches infinity (Bronstein & Semendjajew, 1987). For the application of the theorem, a transformation into normalized variables ξ_j is useful, which are given by

$$\xi_j \equiv \ln x_j - \langle \ln x_j \rangle \equiv \ln \left(\frac{x_j}{\bar{x}_j} \right) \ . \tag{2.9}$$

The angle brackets denote averages taken over the logarithm of the variables,

$$\ln \bar{x}_j = \langle \ln x_j \rangle = \int_{-\infty}^{\infty} \ln x_j f_j(\ln x_j) d \ln x_j \ , \tag{2.10}$$

here, f_j is the distribution function of the variable x_j.

Due to their definition, the normalized variables ξ_j have zero mean and their dispersions σ_j are given by

$$\sigma_j^2 = \int_{-\infty}^{\infty} \xi_j^2 f_j(\xi_j) d\xi_j \ . \tag{2.11}$$

The composite variable Ξ finally is defined by

$$\Xi \equiv \sum_{j=1}^{N} \xi_j = \sum_{j=1}^{N} \ln \left(\frac{x_j}{\bar{x}_j} \right) \ . \tag{2.12}$$

It also has zero mean and, since the variables are assumed to be independent, its variance Σ is the sum of the dispersions of each variable,

$$\Sigma^2 = \sum_{j=1}^{N} \sigma_j^2 \; . \tag{2.13}$$

A new normalization introduces

$$\hat{\Xi} \equiv \frac{\Xi}{\Sigma} \; , \tag{2.14}$$

which again has zero mean but now unit variance. For $N \to \infty$, the central limit theorem describes its distribution function as being Gaussian,

$$f(\hat{\Xi}) = (2\pi)^{-1/2} \exp(-\frac{1}{2}\hat{\Xi}^2) \; , \tag{2.15}$$

independent of the distribution f_j of the individual variables x_j.

In terms of the variable $\hat{\Xi}$, the mass function (2.7) becomes

$$\ln M = \ln M_0 + \Sigma\hat{\Xi} \; , \tag{2.16}$$

with M_0 being a characteristic mass scale defined by

$$\ln M_0 \equiv \sum_{j=1}^{N} \langle \ln \bar{x}_j \rangle \; . \tag{2.17}$$

Combining the two equations (2.15) and (2.16), we can write the distribution f of stellar masses in the form

$$\ln f(\ln m) = A - \frac{1}{2\Sigma^2} \left[\ln \left(\frac{m}{m_0} \right) \right]^2 \; , \tag{2.18}$$

where A is a constant and where we have normalized all masses to the solar value ($m \equiv M/(1\,\mathrm{M}_\odot)$ and $m_0 \equiv M_0/(1\,\mathrm{M}_\odot)$). This is the log-normal form of the IMF first introduced by Miller & Scalo (1979). It is known, that in the solar vicinity this functional form fits very well the mass distribution of multiple stellar systems with masses less than few solar masses (Sec. 2.3.1). Furthermore, it is well suited to describe the mass distribution of protostellar cores formed in our numerical simulations as the result of the dynamical evolution of isothermal self-gravitating gas (see Sec.'s 6 and 7).

Chapter 3

Mathematical and Numerical Concepts

In this chapter we present a short introduction of the mathematical equations used to describe the time evolution of a fluid (Sec. 3.1). The equations of hydrodynamics interconnect mechanical properties of the system with thermodynamical observables like temperature T (or equivalently internal energy ϵ), density ρ and pressure p. They can be extended for describing gravitational action (via the potential ϕ) or the influence of a magnetic field $\boldsymbol{B}$. First, we derive the complete set of equations, including the equation of state necessary for closure. Following that, the stability of self-gravitating fluids is analyzed, in particular the Jeans criterion for gravitational stability is derived. Then, in Sec.'s 3.3 and 3.4, we specify methods to solve the equations of hydrodynamics numerically for complex systems and introduce the technique of *smoothed particle hydrodynamics* (SPH). We combine this method with the special-purpose hardware device GRAPE which is described in Sec. 3.5. Section 3.6 follows with a description of the method to incorporate periodic boundary conditions into our numerical scheme. Finally, the performance of the method is analyzed in Sec.3.7.

3.1 The Equations of Hydrodynamics

In the framework of classical physics, fluids and gases are large ensembles of interacting particles. The state of the system is generally described by its location in the $6N$-dimensional phase space, where N is the number of particles in the system. The time evolution of the system is identified as its trajectory through phase space. For large ensembles of particles, the exact solution of the problem is an unsurmountable task. In analogy to quantum mechanics, one furthermore needs to adopt a probabilistic point of

view and substitute the exact location of the system in phase space by a N-body probability density. The time evolution is then governed by the equation of motion for the N-body probability distribution $f^{(N)}$. Physical observables are typically associated with one or two-body operators, which require only knowledge of the reduced one or two-body probability density. In general, the reduced n-body probability is derived by integrating out all but n of the N variables of $f^{(N)}$. The equations of motion for this reduced description of the system form a hierarchy of equations, the BBGKY-hierarchy, after Born, Bogoliubov, Green, Kirkwood and Yvon (for a thorough introduction see the excellent textbook of Reichl, 1991; or Landau & Lifshitz, 1983). It is impossible to solve this system of equations without a specific approximation to terminate it, a feature intrinsic to all reduced descriptions.

On the lowest level of the hierarchy, there is the one-body distribution function $f \equiv f^{(1)}(\boldsymbol{q}, \boldsymbol{p}, t)$ in the 6-dimensional phase space. At any time t the function $f(\boldsymbol{q},\boldsymbol{p},t)\, d^3\boldsymbol{q}\, d^3\boldsymbol{p}$ describes the probability of finding a particle in the volume element $d^3\boldsymbol{q}$ at the location $\boldsymbol{q}$ and with momenta in the range $d^3\boldsymbol{p}$ around $\boldsymbol{p}$. The equation of motion for f is called the Boltzmann equation,

$$\begin{aligned} \frac{df}{dt} &\equiv \frac{\partial f}{\partial t} + \dot{\boldsymbol{q}}\nabla_q f + \dot{\boldsymbol{p}}\nabla_p f \\ &= \frac{\partial f}{\partial t} + \boldsymbol{p}\nabla_q f + \boldsymbol{F}\,\nabla_p f = f_{\mathbf{c}}\,. \end{aligned} \tag{3.1}$$

Here, the first line is equivalent to the transition from a comoving (Lagrangian) coordinate system to a spatially fixed one (Eulerian). The second line follows from $\boldsymbol{p} = \dot{\boldsymbol{q}}$ and $\boldsymbol{F} = \dot{\boldsymbol{p}}$. Finally, $f_{\mathbf{c}}$ on the right-hand-side contains the influence of the higher-order contributions from the BBGKY-hierarchy; it is often called the collision term. For "collisionless" systems the "collision" term $f_{\mathbf{c}}$ equals zero; the flow in phase space resembles an incompressible fluid (this is Liouville's theorem for the one-body distribution function f). For realistic systems, solving Boltzmann's equation exactly is still not feasible. However, there are further means to simplify the description of the system: Observable quantities – the thermodynamic observables – are typically *moments* of the Boltzmann equation. For the thermodynamic approximation to be valid, expanding equation (3.1) into moments must yield (locally) well defined and meaningful quantities. This is the case, if the distribution function is a "smoothly" varying function on the scales considered, or stated differently, the averaging scale must be much larger than the mean free path of the gas particles. This is true for the problems considered in this thesis.

However, this approximation breaks down in certain physical regimes. In strong shocks, for example, the scale over which the thermodynamic quantities vary considerably becomes comparable to the mean free path. Therefore, hydrodynamic discontinuities arise requiring extensions (and modifications) of the thermodynamic description. Supersonic

turbulence (for instance in the interstellar medium) is an extreme example for this behavior (Mac Low, 1998). Another example for the invalidity of the hydrodynamic approximation are phase transitions. Here, the correlation length of the particles in the system increases towards infinity, i.e. each gas particle interacts with every other one and the assumption of isolated (uncorrelated) encounters breaks down. Then, computing moments of the Boltzmann equation is no longer meaningful and properties of the system have to be described by a more complex scheme, by the renormalization group theory (Reichl, 1991).

Therefore, applying a thermodynamic description to the interstellar medium and to molecular clouds in particular raises the question about the validity of this approach. Besides the ubiquity of shocks and perhaps closely related with it, the ISM is hierarchically structured or fractal on all scales observed (see Sec. 2.1). Fractal or fully hierarchical systems are *per definitionem* self-similar on *all* scales, which means there is no scale below which the system can be considered smooth and on which the averaging procedure is well defined (for a mathematically sound discussion of fractal behavior see Falconer, 1990). However in real physical systems, the fractal regime does have limits. The upper limit is usually the size of the whole system, e.g. the size of the molecular cloud. And the lower limit typically is the scale on which new physical effects become relevant. In the ISM, this is the scale on which a detailed description of the microphysics involved (non-LTE radiation transfer, the influence of dust grains, etc.) becomes important. Since numerical simulations are not able to reach the resolution necessary to cover the complete fractal regime, it is not clear whether an algorithm based on the thermodynamic description is adequate to describe the ISM. This situation gets even more complicated, if gravity is included. Gravity is not a short range force; its interaction range is infinite. This additionally implies that the system is critical on all scales, and self-gravitating systems behave similar to systems at phase transition (see de Vega et al., 1996b,a). However, since a complete and fully consistent theory for self-gravitating gaseous systems does not exist, this work follows the astrophysical tradition and adopts the thermodynamic approach.

If one assumes that the thermodynamic approximation is valid, then the physical quantities used to describe molecular clouds and the interstellar medium (and its fragmentation and star formation properties) are temperature T (or equivalently internal energy ϵ), density ρ, pressure p, and gravitational potential ϕ. The hydrodynamic equations for a self-gravitating compressible fluid follow as,

$$\frac{d\rho}{dt} = \frac{\partial \rho}{\partial t} + \boldsymbol{v} \cdot \nabla \rho = -\rho \nabla \cdot \boldsymbol{v} \qquad \text{(continuity equation)} \tag{3.2}$$

$$\frac{d\boldsymbol{v}}{dt} = \frac{\partial \boldsymbol{v}}{\partial t} + (\boldsymbol{v} \cdot \nabla)\boldsymbol{v} = -\frac{1}{\rho}\nabla p - \nabla\phi + \eta \nabla^2 \boldsymbol{v} + \left(\zeta + \frac{\eta}{3}\right) \nabla(\nabla \cdot \boldsymbol{v})$$
$$\text{(Navier-Stokes equation)} \tag{3.3}$$

$$\frac{d\epsilon}{dt} = \frac{\partial \epsilon}{\partial t} + \boldsymbol{v} \cdot \nabla \epsilon = T \frac{ds}{dt} - \frac{p}{\rho} \nabla \cdot \boldsymbol{v} \qquad \text{(energy equation)} \tag{3.4}$$

$$\Delta \phi = 4\pi G \rho \qquad \text{(Poisson's equation)} \tag{3.5}$$

$$p = \mathcal{R} \rho T \qquad \text{(equation of state)} \tag{3.6}$$

The continuity equation (3.2) describes the time evolution of the density, which is the 0. moment of the Boltzmann equation. The 1. moment is the velocity of a fluid element, and its motion is determined by Navier-Stokes' equation (3.3). It is the hydrodynamic equivalent to Newton's force law. A fluid element can be accelerated by a pressure gradient (1. term), gravitational (2. term), or viscous forces (3. and 4. term with the two viscosity coefficients η and ζ). In an incompressible fluid any velocity divergence vanishes, $\nabla \cdot \boldsymbol{v} = 0$, and the last term is zero. The energy equation (3.4) follows straight from the thermodynamic relation $d\epsilon = T\,ds - p\,dV = T\,ds + p/\rho^2 d\rho$ (Landau & Lifshitz, 1966). For an adiabatic gas, the first term on the right hand side vanishes. However, there may be heat sources in the system that add energy to a fluid element, or phenomena that remove energy from the gas. Any of those processes can be incorporated into the Tds/dt term. For example, in the interstellar medium, stellar winds or cosmic rays heat the gas, and at the same time the gas radiates away part of its energy and thus cools again. Typically some kind of equilibrium state is reached. A fully self-consistent description of the processes governing the ISM should therefore include a detailed description of radiation transfer. However, for typical densities and temperatures in molecular clouds, i.e. $1\,\mathrm{cm}^{-3} \leq n(\mathrm{H}_2) \leq 10^7\,\mathrm{cm}^{-3}$ and $T \approx 10\,\mathrm{K}$, the gas can cool very efficiently and the opacities in the molecular lines involved are low enough for the medium to be optically thin. Hence, treating the gas isothermally is a good approximation. The gravitational potential and the density are related via Poisson's equation (3.5) and finally, the set of equations has to be closed by the equation of state, which describes the relation between pressure and density. Typical for closure equations, it cannot be derived from within the system, but stems from including additional physical phenomena (for a detailed description see Reichl, 1991; Landau & Lifshitz, 1966, 1983). In the simplest description, we consider the ISM as an ideal gas (Eqn. 3.6). Furthermore, we treat the gas isothermally, since we deal with gas in the regime, where it can cool very effectively. With $c_\mathrm{s} = (\mathcal{R}T)^{1/2}$ being the isothermal sound speed, it then follows

$$p = c_\mathrm{s}^2 \rho\,. \tag{3.7}$$

Observations in molecular clouds furthermore reveal the presence of magnetic fields (see e.g. Goodman et al., 1989; Goodman & Heiles, 1994; Crutcher et al., 1993, 1996; Troland

et al., 1996). This can be accounted for in the above set of equations, first, by adding a magnetic force term to the right hand side of the Navier-Stokes equation (3.3):

$$\boldsymbol{F}_B = -\nabla\frac{B^2}{8\pi} + \frac{1}{4\pi}(\boldsymbol{B}\cdot\nabla)\boldsymbol{B}\,. \tag{3.8}$$

Second, the time evolution of the magnetic field itself has to be taken into account self-consistently. This is done in the Lorentz equation,

$$\frac{\partial \boldsymbol{B}}{\partial t} = \nabla\times(\boldsymbol{v}\times\boldsymbol{B})\,. \tag{3.9}$$

This equation is already a simplification. It neglects Ohmic dissipation and ambipolar diffusion which occur in partially ionized media (for a full treatment see e.g. Shu, 1992, or Mouschovias, 1991).

3.2 Stability of Self-Gravitating Fluids – Jeans Criterion

The first and usually sufficient approach to determine the stability properties of physical fluids is to analyze the linearized set of equations. In general, an equilibrium system is described by a time-independent solution of the Boltzmann equation (3.1), a distribution function $f_0(\boldsymbol{q},\boldsymbol{p})$ with $df_0/dt = 0$. Small perturbations to this equilibrium state can be written as

$$f(\boldsymbol{q},\boldsymbol{p},t) = f_0(\boldsymbol{q},\boldsymbol{p}) + \epsilon f_1(\boldsymbol{q},\boldsymbol{p},t)\,, \tag{3.10}$$

with $\epsilon \ll 1$. This can be substituted into the Boltzmann equation (3.1). The terms independent of ϵ sum to zero because they are the equilibrium solution. In a first order approach, terms of order ϵ^2 and higher are neglected since $\epsilon \ll 1$. What remains is a linearized set of equations governing the time evolution of the perturbation. Deriving a dispersion relation, the properties of growing and decaying modes can be studied.

The linearized set of equations for an isothermal, self-gravitating fluid (see Eqn's. 3.2, 3.3, 3.5 and 3.6) are

$$\frac{\partial\rho_1}{\partial t} + \rho_0\nabla\cdot\boldsymbol{v}_1 = 0\,, \tag{3.11.a}$$

$$\frac{\partial\boldsymbol{v}_1}{\partial t} = -\nabla c_{\rm s}^2\frac{\rho_1}{\rho_0} - \nabla\phi_1\,, \tag{3.11.b}$$

$$\Delta\phi_1 = 4\pi G\rho_1\,. \tag{3.11.c}$$

Here, we have neglected viscosity effects ($\eta = \zeta = 0$). The equilibrium state is characterized by $\rho_0 = \text{const.}$ and $\boldsymbol{v}_0 = 0$. From the definition of the isothermal sound speed (Eqn. 3.7) follows $p_1 = c_\mathrm{s}^2 \rho_1$. Furthermore, we make the ad hoc assumption that Poisson's equation (3.11.c) describes only the relation between the perturbed potential and the perturbed density. In this case, $\phi_0 = 0$ can be chosen. This is the so called Jeans swindle (see e.g. Binney & Tremaine, 1987).

By taking the time derivative of Eqn. 3.11.a and the divergence of Eqn. 3.11.b and by eliminating $\boldsymbol{v}_1$ and ϕ_1, the equations can be combined into a wave equation for the density perturbation ρ_1,

$$\frac{\partial^2 \rho_1}{\partial t^2} - c_\mathrm{s}^2 \nabla^2 \rho_1 - 4\pi G \rho_0 \rho_1 = 0 \,. \tag{3.12}$$

Since the equilibrium state is homogeneous, the coefficients of the partial derivatives in Eqn. 3.12 are independent of position $\boldsymbol{r}$ and time t. The solution of this type of partial differential equation is known to be a superposition of plane waves,

$$\rho_1(\boldsymbol{r}, t) = \int d^3k \, A(\boldsymbol{k}) \mathrm{e}^{i[\boldsymbol{k}\boldsymbol{r} - \omega(k)t]} \,. \tag{3.13}$$

The waves follow the dispersion relation

$$\omega^2 = c_\mathrm{s}^2 k^2 - 4\pi G \rho_0 \,. \tag{3.14}$$

If the density ρ_0 or the wave length $\lambda = 2\pi/k$ are small, the dispersion relation (3.14) reduces to that of a sound wave, $\omega^2 = c_\mathrm{s}^2 k^2$. With increasing wave length or density, the frequency decreases and will eventually become negative. When $\omega^2 < 0$, say $\omega^2 = -\kappa^2$, the time dependence of the solution is proportional to $\exp(\pm\kappa t)$, corresponding to exponential growth or decay. The existence of a growing solution implies that the system is unstable. Hence, from Eqn. 3.14, it follows that modes will collapse for wave numbers

$$k^2 < k_\mathrm{J}^2 \equiv \frac{4\pi G \rho_0}{c_\mathrm{s}^2} \,. \tag{3.15}$$

The critical wave number k_J is called the Jeans wave number. In terms of the wave length, a perturbation is unstable if the wave length exceeds the Jeans length $\lambda_\mathrm{J} = 2\pi/k_\mathrm{J}$, that is, if

$$\lambda^2 > \lambda_\mathrm{J}^2 = \frac{\pi c_\mathrm{s}^2}{G\rho_0}. \tag{3.16}$$

Assuming the perturbation is spherical with diameter $\lambda_{\rm J}$, this corresponds to a critical mass contained inside the perturbed volume. The so called Jeans mass is

$$M_{\rm J} = \frac{4\pi}{3}\rho_0(\frac{1}{2}\lambda_{\rm J})^3 = \frac{1}{6}\pi\rho_0\left(\frac{\pi c_{\rm s}^2}{G\rho_0}\right)^{3/2} . \tag{3.17}$$

For isothermal gases, substituting the sound speed by its dependence on the temperature, $c_{\rm s}^2 = \mathcal{R}T$, the critical mass is

$$M_{\rm J} = \frac{\pi^{5/2}}{6}\left(\frac{\mathcal{R}}{G}\right)^{3/2} \cdot \rho_0^{-1/2}\, T^{3/2} . \tag{3.18}$$

The critical mass for a perturbation to collapse scales as $M_{\rm J} \propto \rho_0^{-1/2}\, T^{3/2}$, i.e. it decreases with increasing density and decreasing temperature. The Jeans instability has a simple physical interpretation. The energy density of a sound wave is positive. However, its gravitational energy is negative, because the enhanced attraction in the compressed regions outweighs the reduced attraction in the dilated regions. The instability sets in at the wave length $\lambda_{\rm J}$ where the net energy density becomes negative. The perturbation will grow allowing the energy to decrease even further. In isothermal gas, there is no mechanism that prevents complete collapse. In reality, however, during the collapse of molecular gas clumps, the opacity increases and at densities of $n({\rm H_2}) \approx 10^{10}\,{\rm cm^{-3}}$ the equation of state becomes adiabatic. The collapse proceeds slower. Finally at very high central densities ($\rho \approx 1\,{\rm g\,cm^{-3}}$) fusion processes set in. This energy source leads to a new equilibrium (e.g. Tohline, 1982).

3.3 Smoothed Particle Hydrodynamics

Using a particle based scheme to solve the equations of hydrodynamics was first introduced by Lucy (1977) and independently by Gingold & Monaghan (1977). Originally proposed as a Monte-Carlo approach to calculate the time evolution of a hydrodynamical system, the formalism of SPH – *smoothed particle hydrodynamics* – is more intuitively understood as an interpolation scheme (Gingold & Monaghan, 1982). This provides better estimates for the errors involved and the convergence properties of the method. It is also the path followed in this brief introduction. Excellent overviews over the method and some of its applications provide the reviews of Benz (1990) and Monaghan (1992).

As derived in Sec. 3.1, hydrodynamical quantities are obtained in an *averaging process* involving scales larger than the local mean-free path of particles in the system. A related approach is facilitated in SPH: The fluid is represented by an ensemble of particles i,

each carrying mass, momentum, and hydrodynamical properties. The technique can therefore be seen as an extension of the pure gravitational N-body system. Besides being characterized by its mass m_i and velocity $\boldsymbol{v}_i$ and its location $\boldsymbol{r}_i$, each particle is associated with a density ρ_i, an internal energy ϵ_i (equivalent to a temperature T_i), and a pressure p_i. The time evolution of the fluid is then represented by the time evolution of the SPH particles. Their behavior is governed by the equation of motion, supplemented by further equations to modify the hydrodynamical properties. Thermodynamical observables are obtained by averaging over an appropriate subset of the SPH particles.

Mathematically, the local averaging process for any quantity $f(\boldsymbol{r})$ can be performed by convolution with an appropriate smoothing function $W(\boldsymbol{r}, \boldsymbol{h})$:

$$\langle f(\boldsymbol{r})\rangle \equiv \int f(\boldsymbol{r'}) W(\boldsymbol{r} - \boldsymbol{r'}, \boldsymbol{h})\, d^3r' \,. \tag{3.19}$$

This function $W(\boldsymbol{r}, \boldsymbol{h})$, often referred to as the *smoothing kernel*, must be normalized, i.e. satisfying

$$\int W(\boldsymbol{r}, \boldsymbol{h})\, d^3r = 1 \tag{3.20}$$

The width of the smoothing function is parametrized by the smoothing vector $\boldsymbol{h}$. It follows for the limit $\boldsymbol{h} \longrightarrow 0$ that

$$\langle f(\boldsymbol{r})\rangle \longrightarrow f(\boldsymbol{r}). \tag{3.21}$$

For $\boldsymbol{h}$ becoming infinitely small, the kernel $W(\boldsymbol{r}, \boldsymbol{h})$ approaches the Dirac delta function $\delta(\boldsymbol{r})$[1]. For simplicity, most authors adopt spherical symmetry in the smoothing and averaging process, i.e. the kernel degrades to an isotropic function of the interparticle distances: $W(\boldsymbol{r}, \boldsymbol{h}) \equiv W(r, h)$ with $r = |\boldsymbol{r}|$ and $h = |\boldsymbol{h}|$. This constrains the achievable resolution, especially when dealing with huge density gradients along a preferred axis like in shocks, or in filamentary and sheetlike structures. Some authors therefore introduced a tensor description of the smoothing method and use anisotropic kernels to account for anisotropies in the particle distribution. Although more complicated, this approach has considerable advantages over the spherical averaging (see e.g. Shapiro et al., 1996). We use SPH in combination with the special hardware device GRAPE which applies spherical smoothing of the gravitational potential and forces (see Sec. 3.5). For consistency, we therefore use the spherical averaging procedure throughout the entire computational scheme.

[1]Dirac's $\delta(\boldsymbol{r})$ is not a function in the sense of classical analysis. It is a mathematical entity exactly *defined* as convolution kernel, i.e. by the sequence of Eqn.'s 3.19, 3.20, and 3.21 in the limit $h \longrightarrow 0$.

The following list describes some useful mathematical identities for the averaged quantities: According to Eqn. 3.21, the kernel function can be seen as an approximation to the delta function for finite h. Hence, the averaged function $\langle f(\boldsymbol{r})\rangle$ can be expanded into a Taylor series for h. If the kernel is an even function, the first order term vanishes and the errors are given by,

$$\langle f(\boldsymbol{r})\rangle = f(\boldsymbol{r}) + \mathcal{O}(h^2). \tag{3.22}$$

For spherical kernels, Eqn. 3.22 reads

$$\langle f(\boldsymbol{r})\rangle = f(\boldsymbol{r}) + K\frac{h^2}{6}\nabla^2 f(\boldsymbol{r}) + \mathcal{O}(h^3), \tag{3.23}$$

with the constant K being independent of h. Approximating $f(\boldsymbol{r})$ by $\langle f(\boldsymbol{r})\rangle$ is therefore of second order in h. Since the term in h^2 is multiplied by the gradient of f, this implies perfect equality for constant or linear functions. Furthermore, for the term in h^2 to be small, the function f should not be discontinuous or having too large gradients over the size of W. This causes problems in the treatment of strong shock fronts.

Within its intrinsic accuracy, the smoothing process itself is a linear function with respect to summation and multiplication,

$$\langle f(\boldsymbol{r}) + g(\boldsymbol{r})\rangle = \langle f(\boldsymbol{r})\rangle + \langle g(\boldsymbol{r})\rangle\,, \tag{3.24.a}$$

$$\langle f(\boldsymbol{r}) \cdot g(\boldsymbol{r})\rangle = \langle f(\boldsymbol{r})\rangle \cdot \langle g(\boldsymbol{r})\rangle\,. \tag{3.24.b}$$

The first equation is an identity following from the linearity of integration with respect to summation, and the second one is true to second order in h. It furthermore follows for the time derivative and the gradient,

$$\frac{d}{dt}\langle f(\boldsymbol{r})\rangle = \left\langle \frac{d}{dt} f(\boldsymbol{r})\right\rangle, \tag{3.25.a}$$

$$\nabla\langle f(\boldsymbol{r})\rangle = \langle \nabla f(\boldsymbol{r})\rangle\,. \tag{3.25.b}$$

The spatial derivative of the physical quantity furthermore can be transformed into a spatial derivative of the kernel function. This is shown by integrating by parts and assuming that the surface term vanishes. If the solution space is extended far enough, either the function f itself or the kernel approaches zero. Thus,

$$\nabla\langle f(\boldsymbol{r})\rangle = \langle \nabla f(\boldsymbol{r})\rangle = \int f(\boldsymbol{r}')\,\nabla W(|\boldsymbol{r}-\boldsymbol{r}'|, h)\,d^3r'\,. \tag{3.26}$$

The basic concept of SPH is a particle representation of the fluid. Hence, the spatial integration in the averaging process transforms into a summation over a fixed number of points. For example, the density at the position of particle i is computed as

$$\langle \rho(\boldsymbol{r}_i) \rangle = \sum_j m_j W(|\boldsymbol{r}_i - \boldsymbol{r}_j|, h) \; . \tag{3.27}$$

In this picture, the mass of each particle is smeared out over the kernel region. The continuous density distribution of the fluid is then obtained by summing over the local contribution of each element. The name "smoothed particle hydrodynamics" derives from this analogy. Equation 3.27 is subject to two distinct interpretations, which are analogous to the meanings of computational gather and scatter operations. The scatter interpretation assumes that each particle has a mass which is smeared out in space according to W and h. The density at the location of particle i is then determined by summing over the contributions from the density profiles of those neighboring particles j, whose smoothing regions overlap with particle i, i.e. one uses h_j in Eqn. 3.27. Alternatively, the gather interpretation regards particles as point markers in the fluid. Local properties (i.e. for particle i) are obtained by sampling all particles within the smoothing region of i and weighting them according to Eqn. 3.27 using h_i. Both viewpoints are indistinguishable, if all particles have the same smoothing length, but lead to different results, if h is spatially variable (see Sec. 3.4.1, or Hernquist & Katz, 1989).

SPH is used, because it is intrinsically Lagrangian: As opposed to mesh-based methods, it does not require a fixed grid to represent fluid properties and calculate spatial derivatives (see e.g. Hockney & Eastwood, 1988). The fluid particles are free to move and – in analogy – constitute their own grid. The method is therefore able to resolve very high density contrasts, by increasing the particle concentration where needed. This it most effective, if the smoothing length is adaptable, as described in Sec. 3.4.1. There is no need for the complex and time-consuming issue of adaptive grid-refinement (Berger & Colella, 1989). However, one weakness compared to grid-based methods is that the analytical convergence behavior is mathematically difficult to assess. Most attempts to address this issue are based on numerical resolution studies and empirical approximations (Steinmetz & Müller, 1993; Balsara, 1995). Another reason for choosing SPH is the possibility to use it in combination with the special-purpose hardware device GRAPE, see Sec. 3.5. This allows calculations at supercomputer level on a normal workstation, and enabled us to do the extensive parameter study presented in this thesis.

3.4 Implementation and Limitation of SPH

After having introduced the general concept of SPH in the last section, we now present a more detailed discussion of the numerical realization. We start with the appropriate choice of the kernel function and the implications of a variable smoothing length (Sec. 3.4.1). Then follows a derivation of the equations of hydrodynamics in terms of the SPH formalism (Sec. 3.4.2), and a discussion of the variable time step scheme used in the code (Sec. 3.4.3). Finally, in Sec. 3.4.4, accretion particles, a special feature to handle highly collapsed objects are described. The code was originally developed by Benz (1990). Then, I. A. Bonnell and more so M. R. Bate modified the scheme by introducing variable time steps and accretion particles. It was then a considerable effort in this thesis to combine the SPH code with the special-purpose hardware device GRAPE and to implement periodic boundary conditions (see Sec.'s 3.5 to 3.7).

3.4.1 Choice of the Kernel Function and Variable Smoothing Length

As discussed in the previous section, we use 1-dimensional, i.e. spherical kernel functions. There are a variety of appropriate functions proposed in the literature, ranging from Gaussian functions (Gingold & Monaghan, 1977), to spline functions of third or higher order and with compact support (e.g Monaghan & Lattanzio, 1985; Monaghan, 1985). These kernels interpolate at least to second order in h, and are always positive in the range of interest. Furthermore all are smooth functions with well defined first derivatives. The spline functions furthermore have the advantage, that there is a clear limit to the number of particles contributing in the averaging process due to their compact support. For the others, one has to implement an artificial cut-off. We use the 3$^{\rm rd}$ order spline introduced by Monaghan (1985). Defining $v = r/h$ it reads,

$$W(\boldsymbol{r},\boldsymbol{h}) \equiv W(r,h) \equiv \frac{1}{\pi h^3} \begin{cases} 1 - \frac{3}{2}v^2 + \frac{3}{4}v^3, & \text{for } 0 \le v \le 1; \\ \frac{1}{4}(2-v)^3, & \text{for } 1 \le v \le 2; \\ 0, & \text{otherwise.} \end{cases} \tag{3.28}$$

One of the main advantages of SPH over grid-based methods is its Lagrangian nature and its ability to resolve high density contrasts. The spatial resolution of SPH is limited by the scale over which forces and physical properties of the fluid are smeared out, i.e. it is determined by the smoothing length h. To make the best use of its spatial flexibility and achieve optimum resolution, one has to allow for variations of this parameter. In high-density regions one needs to decrease h to correctly handle the small-scale kinematics. On the other hand, in low-density regions one has to increase h in order to ensure that

a sufficient number of particles contribute in the averaging process. It has proven useful to determine h such that the number of neighbors always lies in the range from 30 to 70, with the optimum value being about 50.

However, there are several points to consider when allowing for spatial and temporal variations in the smoothing length. First, this introduces additional errors to the scheme. The Taylor expansion of the averaged values, Eqn. 3.23 for spherical symmetric kernel functions, then contains contributions from ∇h (Hernquist & Katz, 1989; Nelson & Papaloizou, 1994). But these are of second and higher order, and the total error is of the same order as the one inherent to the SPH technique. The same is true for the term proportional to $\partial h/\partial t$ occuring in the equations of motion. Second, introducing a spatially varying smoothing length also modifies the gradient of the kernel $W(|\boldsymbol{r}-\boldsymbol{r'}|,h)$ entering Eqn. 3.26. It is

$$\nabla W(|\boldsymbol{r}-\boldsymbol{r'}|,h) = \nabla W(|\boldsymbol{r}-\boldsymbol{r'}|,h)\Big|_{h=\text{const.}} + \frac{\partial}{\partial h} W(|\boldsymbol{r}-\boldsymbol{r'}|,h)\,\nabla h\Big|_{\boldsymbol{r}=\text{const.}}, \quad (3.29)$$

with $h = h(\boldsymbol{r})$. The new term on the right-hand side is proportional to the gradient of the smoothing length. It becomes of importance only if the smoothing length varies on scales less than the smoothing length itself (Evrard, 1988). Since all quantities in SPH are smoothed over this length scale, it is generally neglected. In a typical calculation, this indeed is an adequate approximation, which was numerically confirmed by Nelson & Papaloizou (1994) who extensively studied cases including and neglecting the ∇h-terms in their derivation of the SPH equations.

Third, more important for a code with variable smoothing length is force anti-symmetrisation. When applying the smoothing procedure in the most straightforward way, the mutual forces between two particles i and j are no longer anti-symmetric for different smoothing lengths h_i and h_j. Particle i experiences a different force from particle j than visa versa. Newton's third law is violated and momentum is no longer a conserved quantity. It is therefore necessary to reconstitute the force anti-symmetry. Amongst the several ways to achieve this (for an overview see Monaghan, 1985), we follow Benz (1990) and simply substitute h in all previous equations by the arithmetic average of the smoothing length for all particle pairs,

$$h \longrightarrow h_{ij} = \frac{h_i + h_j}{2}\,. \quad (3.30)$$

Fourth, for variation of the smoothing length one needs criteria how to do this. In our SPH implementation, we modify h such that the number of neighbors roughly remains

constant for each particle. Hence, it is quite natural to couple h to the density ρ via

$$h = h_0 \left(\frac{\rho_0}{\rho}\right)^{1/3}. \tag{3.31}$$

Benz (1990) and Evrard (1988) proposed to use the derivative of Eqn. 3.31 for the time evolution of h,

$$\frac{\mathrm{d}h}{\mathrm{d}t} = -\frac{1}{3}\frac{h}{\rho}\frac{\mathrm{d}\rho}{\mathrm{d}t}\,. \tag{3.32}$$

In combination with the continuity equation this yields

$$\frac{\mathrm{d}h}{\mathrm{d}t} = \frac{1}{3}\,h\,\nabla\cdot\boldsymbol{v}\,. \tag{3.33}$$

The smoothing length is thus evolved similar to any other hydrodynamical quantity. This method works quite well in general and keeps the number of neighbors approximately centered between 30 to 70. However, in the extreme cases, where adapting h according to Eqn. 3.33 exceeds these limits, we enforce them by multiplying h with some appropriate factor. For alternative ways to control the evolution of h see Steinmetz & Müller (1993).

3.4.2 The Fluid Equations in SPH

As described in Sec. 3.3, hydrodynamical quantities are obtained in SPH by an averaging process from an ensemble of fluid particles. When applying a spline kernel with compact support (e.g. Eqn. 3.28) only particles within a finite radius $2h$ contribute to the averaging process. According to Eqn. 3.27 the density at the location $\boldsymbol{r}_i$ of particle i then follows as

$$\rho_i = \sum_{j=1}^{N_i} m_j W(r_{ij}, h_{ij}), \tag{3.34}$$

with $r_{ij} = |\boldsymbol{r}_i - \boldsymbol{r}_j|$, h_{ij} being defined by Eqn. 3.30. N_i is the number of neighbors considered for particle i. Particle i itself is included in the list and contributes to the sum.

In addition to the density, the pressure p_i for each particle must be defined via the equation of state (3.6), which for an isothermal gas is

$$p = c_\mathrm{s}^2 \rho\,.$$

The calculation of the other hydrodynamical quantities requires knowledge of density ρ_i and pressure p_i for each particle i. Therefore, the complete evaluation of the SPH equations is split into two parts. In a first loop over all particles, the values ρ_i and p_i are computed, then in a second one the remaining fluid properties follow.

The motion of the fluid is governed by the Navier-Stokes equation (3.3). Considering only the pressure contributions, it reduces to Euler's equation,

$$\frac{d\boldsymbol{v}}{dt} = \frac{\partial \boldsymbol{v}}{\partial t} + (\boldsymbol{v}\cdot\nabla)\boldsymbol{v} = -\frac{1}{\rho}\nabla p = -\nabla\left(\frac{p}{\rho}\right) - \frac{p}{\rho^2}\nabla\rho. \tag{3.35}$$

The last transformation makes use of the identity $\nabla(p\rho^{-1}) = \rho^{-1}\nabla p - p\rho^{-2}\nabla\rho$. Applying the SPH averaging procedure, this translates into an integral equation, and only the second term on the right hand side remains. In the integration of the first term, the contribution from the surface vanishes, because either the pressure or the kernel itself are assumed to become zero at the integration border. If this is not the case, adequate boundary corrections have to be added. When transformed into a summation over a discrete set of particles, the SPH formulation of Euler's equation is

$$\frac{d\boldsymbol{v}_i}{dt} = -\sum_{j=1}^{N_i} m_j \left(\frac{p_i}{\rho_i^2} + \frac{p_j}{\rho_j^2}\right) \nabla_i W(r_{ij}, h_{ij})\,, \tag{3.36}$$

where ∇_i means the gradient with respect to the coordinates of particle i. The equation is anti-symmetric with respect to i and j and conserves the momentum locally and globally.

So far only the first term on the right-hand side of Eqn. 3.3 has been treated. The next term, the gravitational force, must be computed by summing over the contributions from *all* N particles in the ensemble. Unlike fluid properties, which are defined locally, gravity has infinite range and the gravitational force for particle i is

$$-\nabla\phi_i = -G\sum_{j=1}^{N} \frac{m_j}{r_{ij}^2}\frac{\boldsymbol{r}_{ij}}{r_{ij}}\,, \tag{3.37}$$

with the gravitational constant G and $\boldsymbol{r}_{ij} = \boldsymbol{r}_i - \boldsymbol{r}_j$. Our code allows two choices, the gravitational forces can be computed either by using a TREECODE scheme, or by using the special-purpose hardware device GRAPE. In the first case, the complete set of particles is grouped into a hierarchy of mutual nearest neighbors. At the highest level each particle builds a node together with its nearest neighbor. At the next levels these nodes are grouped together, until at the lowest level only one node remains, containing the whole system. When performing the sum in Eqn. 3.37, contributions from distant particles are grouped together and only the interaction with a complete node is computed. Thus,

the total number of evaluated force terms scales as $\mathcal{O}(N \log N)$. To minimize two body relaxation, the gravitational forces are smoothed using the SPH kernel for consistency. GRAPE on the other hand solves Eqn. 3.37 by direct summation. Each single particle is considered, and the forces are computed via the Plummer law (Eqn. 3.51). Despite performing $\mathcal{O}(N^2)$ operations, using this device with the force calculation hardwired to specifically designed chips leads to a overall speed-up of a factor of 5 to 7 on Ultra Sparc workstations compared to the TREECODE.

The most complicated quantity contributing to Navier-Stokes' equation is the viscosity (the 3. and 4. term in Eqn. 3.3). It parametrizes the physical mechanisms that convert kinetic into internal energy, in heat. An exact treatment and derivation from molecular kinetics is very complex and difficult. Equation. 3.3 is only a first approximation (see Reichl, 1991; Landau & Lifshitz, 1966, 1983). In most astrophysical problems the molecular viscosity is very small and dissipation of kinetic energy should occur only in shocked regions. Therefore, SPH has no explicit treatment of physical viscosity. Nevertheless, one needs to introduce the so called "artificial" viscosity. Besides the effects of numerical diffusivity and dissipation inherent to every discretization of the hydrodynamical equations, in SPH one furthermore needs to prevent particle interpenetration in strong shocks. The only way to enforce this is to spatially smear out the shock interface and introduce terms to allow for dissipation in regions with strong velocity divergence. The standard formulation for the viscous pressures is

$$p_\alpha = \Pi_\alpha \rho^2 = -\alpha \rho \ell c_\mathrm{s} (\nabla \cdot \boldsymbol{v}) \,, \tag{3.38}$$

and

$$p_\beta = \Pi_\beta \rho^2 = -\beta \rho \ell^2 (\nabla \cdot \boldsymbol{v})^2 \,. \tag{3.39}$$

The free parameters α and β control the strength of the viscous terms, and ℓ is the scale over which the shock is smeared out, typical values are $\ell \approx 3h$. Equation 3.38 is a combined shear and bulk viscosity. Its primary purpose is to dampen post-shock oscillations. Equation 3.39 is a second order, von Neumann-Richtmyer viscosity needed to prevent penetration in high Mach number shocks. There exists extensive literature on the limits and capabilities of this formulation of viscosity (Monaghan & Gingold, 1983; Monaghan & Lattanzio, 1985; Benz, 1990; Monaghan, 1992). Typical values for the free parameters are $\alpha \approx 1$ and $\beta \approx 2$ which guarantee adequate treatment of shocked regions (Bate, 1995). The implementation of artificial viscosity for particle i is then

$$F_i^{\mathrm{visc}} = -\sum_{j=1}^{N_i} m_j \Pi_{ij} \nabla_i W(r_{ij}, h_{ij}) \,, \tag{3.40}$$

where the viscosity tensor Π_{ij} is defined by

$$\Pi_{ij} = \begin{cases} (-\alpha \bar{c}_{\rm s} \mu_{ij} + \beta \mu_{ij}^2)/\rho_{ij} & \text{for} \quad \boldsymbol{v}_{ij} \cdot \boldsymbol{r}_{ij} \leq 0\,, \\ 0 & \text{for} \quad \boldsymbol{v}_{ij} \cdot \boldsymbol{r}_{ij} > 0\,. \end{cases} \tag{3.41}$$

Here, $\boldsymbol{r}_{ij} = \boldsymbol{r}_i - \boldsymbol{r}_j$ and $\boldsymbol{v}_{ij} = \boldsymbol{v}_i - \boldsymbol{v}_j$. Furthermore, $\rho_{ij} = (\rho_i + \rho_j)/2$ is the averaged density, $\bar{c}_{\rm s}$ is the mean sound speed at the positions of particles i and j, and

$$\mu_{ij} = \frac{h \boldsymbol{v}_{ij} \cdot \boldsymbol{r}_{ij}}{\boldsymbol{r}_{ij}^2 + 0.01 h^2}\,. \tag{3.42}$$

Altogether, the SPH description of the Navier-Stokes equation is

$$\frac{d\boldsymbol{v}_i}{dt} = -\sum_{j=1}^{N_i} m_j \left(\frac{p_i}{\rho_i^2} + \frac{p_j}{\rho_j^2} + \Pi_{ij} \right) \nabla_i W(r_{ij}, h_{ij}) - \nabla \phi_i\,. \tag{3.43}$$

Finally, if one relaxes the assumption of an isothermal equation of state one has to take the variation of the internal energy into account. For an ideal gas (Eqn. 3.6), the energy conservation takes the form of Eqn. 3.4. In the absence of external heat sources or sinks, and for adiabatic conditions, only the second term on the right-hand side remains. It can easily be translated into the SPH formalism,

$$\frac{d\epsilon_i}{dt} = \frac{p_i}{\rho_i^2} \sum_{j=1}^{N_i} m_j\, \boldsymbol{v}_{ij} \cdot \nabla_i W(r_{ij}, h_{ij})\,, \tag{3.44}$$

which is simple p_i/ρ_i times the divergence of the fluid $\nabla_i \cdot \boldsymbol{v}_i$. In the absence of artificial viscosity this conserves the energy (Benz, 1990).

However, artificial viscosity is needed and leads to heating of the gas in shocks. Viscous terms therefore have to be included in the energy equation. As an example, for a polytropic equation of state, $p = K\rho^\gamma$, with K depending on the entropy s, the specific internal energy of the gas is

$$\epsilon = \frac{K}{\gamma - 1} \rho^{\gamma - 1}\,. \tag{3.45}$$

The change of K due to the artificial viscosity can be derived as (Benz, 1990)

$$\frac{dK}{dt} = \frac{\gamma - 1}{2\rho_i^{\gamma-1}} \sum_{j=1} N_i m_j \Pi_{ij}\, \boldsymbol{v}_{ij} \cdot \nabla_i W(r_{ij}.h_{ij}). \tag{3.46}$$

Altogether, the final SPH formulation of the energy equation 3.4 is

$$\frac{d\epsilon_i}{dt} = \frac{p_i}{\rho_i^2} \sum_{j=1}^{N_i} m_j \boldsymbol{v}_{ij} \cdot \nabla_i W(r_{ij}.h_{ij}) + \frac{1}{2} \sum_{j=1} N_i m_j \Pi_{ij}\, \boldsymbol{v}_{ij} \cdot \nabla_i W(r_{ij}.h_{ij}) + \Gamma_i \,, \quad (3.47)$$

where Γ_i includes the effects of external sources. For $\Gamma_i = 0$, this equation ensures total conservation of the energy in the gas.

3.4.3 Variable Time Steps

The time integration of the SPH equations is performed using a second-order Runge-Kutta-Fehlberg scheme (Benz & Mayor, 1984) with individual time steps for each particle and an adaptive maximum time step.

High-density regions of gas are represented by particles with small separations in SPH. In order to handle their dynamical evolution correctly, one has to allow for very small time steps. On the other hand, in low-density regions the dynamical evolution occurs on much larger time scales, and one could allow for relatively long time steps. Thus, allowing for individual time steps for each particle results in a considerable reduction of the overall computational time (Hernquist & Katz, 1989; Navarro & White, 1993). In the current version of the code, the required time step is calculated individually for each particle. Then, these time steps are binned into multiples of two of the minimum value. This has the advantage, that groups of particles are evolved simultaneously. Furthermore, particles on other time steps may also be advanced at the current time, if they are in smaller time step bins or are synchronized, which means that the current time is a multiple of their larger time step. The efficiency of the force calculation can be increased by calculating the interaction between a synchronized particle pair only once, but assigning the result to both partners.

The time step bins for the particles are determined from the Courant-Friedrichs-Lewy (1928) condition, which is the ratio between a characteristic length scale and a characteristic velocity. The time step must be smaller than the typical time $\delta t_{\rm CFL}$. It basically means that information can only travel a certain fraction of the smoothing length h in one time step and ensures reliable treatment of the kinematical properties. In the context of SPH,

$$\delta t_{\rm CFL} = \frac{0.3\, h}{c_{\rm s} + h|\nabla \cdot \boldsymbol{v}| + 1.2(\alpha c_{\rm s} + \beta h|\nabla \cdot \boldsymbol{v}|)} \,. \quad (3.48)$$

Here, h is the smoothing length, $c_{\rm s}$ is the sound speed, and $\boldsymbol{v}$ is the particle velocity. The two parameters α and β describe again the artificial viscosity. The term involving the

viscosity is only included if necessary, i.e. for $\nabla \cdot \boldsymbol{v} < 0$. Since this criterion is not sufficient to guarantee good resolution during strong compression, there is also a force criterion,

$$\delta t_{\mathrm{F}} = 0.3\sqrt{\frac{h}{|\boldsymbol{F}|}}\,, \tag{3.49}$$

where $\boldsymbol{F}$ is the net acceleration of the particle. In addition, the use of a Runge-Kutta-Fehlberg scheme introduces a third time step criterion. The changes in velocity, acceleration, internal energy and smoothing length of individual particles between two time steps are forced to be less than a given tolerance threshold. This leads to

$$\delta t_{\mathrm{RKF}} = \sqrt{\frac{512\delta t\lambda}{|Q_{\mathrm{new}} - Q_{\mathrm{old}}|}}\,, \tag{3.50}$$

where Q is the physical quantity considered, δt is the current time step, and λ is the given tolerance. The time bin for the particle is then chosen to be the largest one satisfying all three criteria. In this procedure, each particle can at all times move to a smaller time step. However, care must be taken, when increasing the time step. This is only allowed at times that are synchronized with the larger time bin. Otherwise, the integration scheme would fail being of second order.

3.4.4 Accretion Particles

Regions in molecular clouds with masses exceeding the Jeans limit become unstable and collapse. Unless there is an additional source of energy, gas pressure cannot hinder the collapse and the central density grows with ever increasing rate until the whole reservoir is exhausted. If the system is resolved properly, the growth of the density contrast demands an ever decreasing minimum time step. All the computational effort is put into evolving the gas within a few high density peaks, with the result that the calculation grinds to a halt. The evolution of low-density gas cannot be followed despite the large number of iterations done. This happens regardless of the numerical scheme used, and despite the application of individual time steps.

In reality, however, at some late phases of the collapse additional physical effects become important. Conservation of angular momentum enforces the formation of an accretion disk, where matter can only stream toward the center on a viscous time scale. Magnetic fields play an important role and may drive outflows along the spin axis. Finally at the very center, the density might reach the level at which nuclear fusion reactions set in. This new source of energy completely alters the system and establishes a new equilibrium state. A star is born in the central region and blows away the parental cloud (see Chap. 2).

All these effects are not included in our code. For this thesis, we concentrate on the early phases of star formation, on the fragmentation and collapse of molecular clouds in a regime, where the gas can be treated isothermally. Therefore, whenever the density in the central core of a Jeans unstable cloud fragment in our simulation exceeds a certain threshold value, close to the densities for which opacity effects become important and the evolution changes from isothermal to adiabatic, we replace the entire core by one single, non-gaseous, massive 'sink' particle (Bate et al., 1995). This particle has a fixed radius of the order of the Jeans radius of the core, and inherits the combined masses, linear momenta and 'spin' angular momenta of the particles it replaces. It furthermore has the ability to accrete any infalling SPH particle. In this process, the mass of the additional particle, its linear momentum and angular momentum with respect to the sink particle are added to the latter one, thus conserving the overall values. The accreted particle is then removed from the calculation.

By adequately replacing high-density cores and keeping track of their further evolution in a consistent way, the problem of extremely small time steps slowing down the computation is avoided. It is also relatively simple to incorporate this procedure into the SPH scheme, due to the Lagrangian nature of SPH. One needs to find (a) a description of the properties of sink particles and how they accrete gaseous particles, (b) a method to create a sink particle, and (c) define a proper treatment of the boundary conditions between the sink particle and the surrounding SPH gas particles. These issues are discussed in great detail by Bate et al. (1995). Hence, only a brief overview over the method used in our code will be presented here.

(a) Properties of Sink Particles and their Accretion Process:
A sink particle is in principle a regular SPH particle, but tagged to carry additional properties. Sink particles interact with the normal SPH particles and with each other only via gravity. Furthermore, gas particles do not interact with other gas particles on the opposite side of the sink particle, except gravitationally. Sink particles have a predefined radius, typically chosen to be comparable to the Jeans radius of dense cores. Gaseous particles that come close to that accretion radius $r_{\rm acc}$ may be accreted. There are several criteria determining whether the particle will get swallowed or not. First, the particle must be bound to the sink particle. Second, the specific angular momentum of the particle with respect to the sink particle must be less than what is required to move on a circular orbit with radius $r_{\rm acc}$ around the sink particle. These conditions ensure, that particles that come accidentally close to the sink and would normally leave again the accretion region are not accreted. The third criterion is that a SPH particle gets accreted onto the sink particle it is most tightly bound to. If a cluster of sink particles competes for gaseous particles, typically the most massive one wins. If a gas particle is accreted, its mass and linear momentum becomes added to the sink. Also the spin of the sink is updated to account for the angular momentum of the accreted particle. In the individual

time step scheme, particles are only accreted if they have completed their time step.

(b) Sink Particle Creation:
Either sink particles are included in the calculation from the beginning, or are formed dynamically during the collapse. When a regular SPH particle exceeds a certain density threshold (typically a factor of 10^4 higher than the average density), and when its smoothing length is less than half the accretion radius (which ensures that a sink particle is formed from at least ≈ 35 particles), then it is considered to become a sink particle. The following requirements have to be fulfilled: All neighbor particles must be synchronized at the current time, and the sink should only be formed, if these neighboring particles continue to collapse and do not expand again. For this to be true, first, the ratio α between the thermal energy and the gravitational energy of these particles must be $\alpha \leq 1/2$. Second, we require $\alpha + \beta \lesssim 1$, where β is the ratio between the rotational energy and the binding energy. The angular momentum is calculated about the position of the densest particle. Third, the total energy of the particles has to be negative and, finally, also the divergence of the accelerations must be negative. If it were positive, the entire region could be in the process of being tidally disrupted or in expansion after core bounce. In both cases no sink particle should be formed. If all these test are passed, the particle with the highest density gets tagged a sink particle and all its neighbors become accreted according to (a).

(c) Boundary Conditions
Ideally, the formation of sink particles in an SPH simulation should not affect the evolution of gas outside its accretion radius. In practice two effects should be considered: The sink particle is per definition spherically symmetric. The original core of gas particles from which it was created may deviate from this symmetry. In this case, the gravitational potential will be altered by neglecting all multipole moments higher than zero. However, this effect is very small, and it is more important that sink particles introduce a discontinuity into the SPH particle distribution. By accreting particles, they produce holes of the size of their accretion volume. This affects the pressure and viscous forces onto neighboring particles. However, constructing adequate boundary conditions at the 'surface' of the sink particle can correct for these effects (Bate et al., 1995).

As conclusion, introducing sink particles to the SPH method leads to considerable increase of the overall computational performance of a code. It solves the problem of high density regions reducing the time steps by substituting dense cores by one single particle. This replacement does not alter the evolution of the remaining gas particles, which has been shown in extensive tests by Bate et al. (1995). A further point of advantage is, especially for the work described in this thesis, that each sink particle has its own 'identity' and carries properties representing an entire gaseous region. When studying an entire cluster of condensed cores, this is very useful and simplifies the statistical analysis.

3.4.5 The Resolution Limit of SPH

This section summarizes the limitations of the SPH method. As discussed in Sec. 3.3, the advantage of SPH is its Lagrangian nature and its ability to resolve high density contrasts. Particles are free to move and and concentrate in regions of high density. In regions of low density, the particle concentration is decreased. The basic feature of the SPH method is that all relevant quantities are derived in a local averaging process. For this process to lead to reliable results, the number of neighboring particles taken into account should be between 30 and 70, with the optimum value being 50. This fact determines the spatial resolution of the method. To make full use of its Lagrangian nature and resolving power, it is necessary to introduce an adaptive smoothing length (see Sec. 3.4.1). The smoothing length of particles in high density peaks can be chosen small. For particles in voids it has to be large. Naturally, the local spatial resolution depends on the particle number. The more particles are available in the simulation, the smaller is the volume around every particle containing ~ 50 neighbors and the better is the spatial resolution. The spatial resolution is also constrained by the Courant-Friedrichs-Lewy (1928) criterion. It demands that the minimum time stepping in the SPH code is always less than the time required for a sound wave to cross through the minimum smoothing volume (see Sec. 3.4.3). In order to prevent the time stepping required to resolve very high density peaks to become prohibitively small, one has to introduce a minimum smoothing length and thus a minimum resolution. In self-gravitating gaseous systems the minimum resolution is limited by a further constraint. In order to correctly treat the dynamical evolution of high-density peaks, the mass contained within the smoothing volumes of two interacting particles must be less than the local Jeans mass. Otherwise, the stability of the clump against gravitational collapse depends on the detailed implementation of the gravitational force law and on the kernel function used for the simulation, rather than on physical processes. The criterion requires that the minimum Jeans mass that is reached during the calculation must always be greater than approximately twice the number of particles in the SPH kernels, i.e. $M_{\rm J} \gtrsim 100\, m$, with m being the mass of individual particles (see Bate & Burkert, 1997). Within these limitation the SPH method calculates the time evolution of gaseous systems very reliable.

3.5 GRAPE and SPH

In the early 1990's, the first GRAPE boards became available to the scientific community. GRAPE is an acronym for "GRAvity PipE". It is a special-purpose hardware device, which calculates the forces and the potential in the gravitational N-body problem by direct summation on a specifically designed chip with high efficiency (Sugimoto et al., 1990; Ebisuzaki et al., 1993), thus leading to considerable speed-up in computing this type of problems. In the last seven years, GRAPE boards have been used for studying a variety of astrophysical problems, ranging from the evolution of binary black holes (Makino et al., 1993b) up to the formation of galaxy clusters in a cosmological context (Huss et al., 1997).

We use the currently distributed version, GRAPE-3AF, which contains 8 chips on one board and therefore can compute the forces on 8 particles in parallel. The board is connected via a standard VME interface to the host computer, in our case a SUN workstation. C and FORTRAN libraries provide the software interface between the user's program and the board. The computational speed of GRAPE-3AF is approximately 5 Gflops.

The force law is hardwired to be a Plummer law,

$$\boldsymbol{F}_i \;=\; -G\sum_{j=1}^{N}\frac{m_i m_j(\boldsymbol{r}_i-\boldsymbol{r}_j)}{(|\boldsymbol{r}_i-\boldsymbol{r}_j|^2+\epsilon_i^2)^{3/2}}\,. \tag{3.51}$$

Here i is the index of the particle for which the force is calculated and j enumerates the particles which exert the force; ϵ_i is the gravitational smoothing length of particle i; G and m_i and m_j are Newton's constant and the particle masses, respectively. The force calculation is performed via a pipelining technique, as schematically described in Fig. 3.5. First, one needs to store the positions of all particles j in the system into memory on the board. This is done once at the beginning of the force loop. Then, the position of the particle i for which the forces need to be computed is loaded into the GRAPE chip. For each particle pair ij, obtaining the gravitational potential and force involves calculating their distance vector $\boldsymbol{r}_{ij}=\boldsymbol{r}_i-\boldsymbol{r}_j$, its square $r^2=r_{ij}^2+\epsilon^2$, and the two inverse values $1/r$ and $1/r^3$. Then the potential $\phi_{ij}=m_j/r$ and the force $\boldsymbol{F}_{ij}=m_j\boldsymbol{r}_{ij}/r^3$ have to be added to the previous pair-wise values. Altogether, it takes 19 arithmetical operations to perform this calculation. However, it can be done consecutively in a kind of pipeline. For example, while computing the inverse $1/r$ for the pair ij, the square r^2 can be calculated for pair $i(j+1)$, and the distance vector obtained for pair $i(j+2)$, and so forth. Hence, one needs $N+19$ clock cycles to perform the complete force calculation for a single particle i.

To achieve a high speed, concessions in the accuracy of the force calculations had to be made: GRAPE internally works with a 20 bit fixed point number format for particle positions, with a 56 bit fixed point number format for the forces and a 14 bit logarithmic

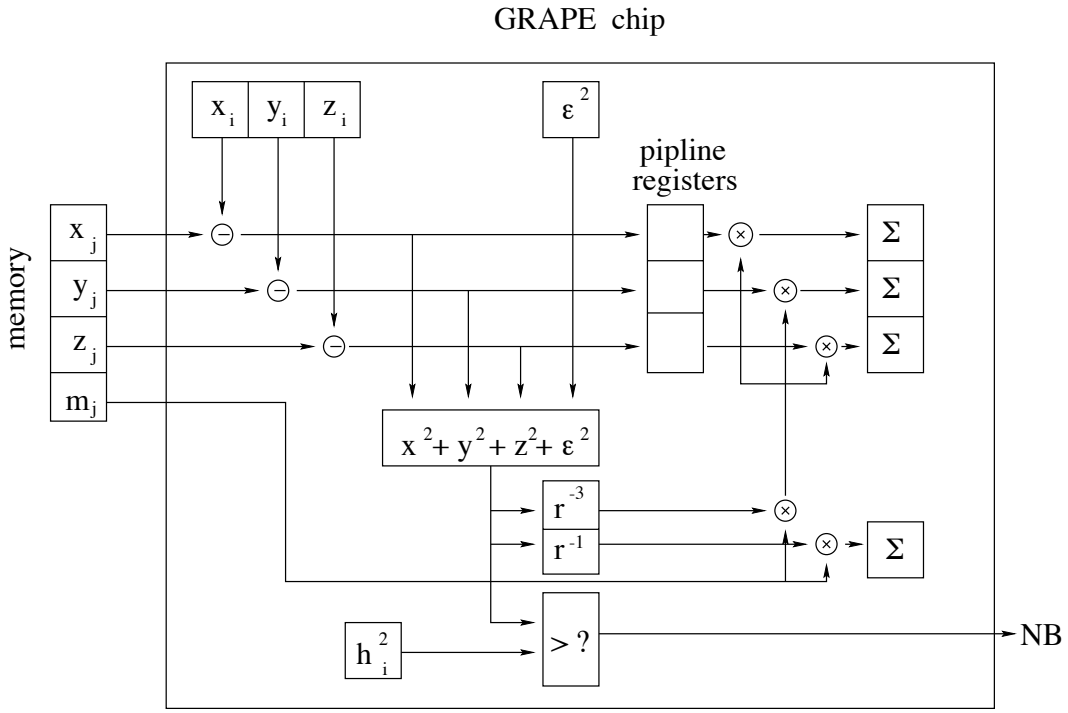

Figure 3.1: Schematic diagram of the arithmetic operations involved to compute the potential and the mutual force of a particle pair ij with GRAPE.

number format for the masses (Okumura et al., 1993). Conversion to and from that internal number representation is handled by the interface software. The number format limits the spatial resolution in a simulation and constrains the force accuracy. However, for collisionless N-body systems, the forces on a single particle typically need not be known better than up to an error of about one percent. In that respect, GRAPE is comparable to the widely used TREECODE schemes (e.g. Barnes & Hut, 1986). In addition to the low-precision GRAPE board, there is a high-precision version available, HARP, (Hermite AcceleratoR Pipeline), which was specifically designed for treatment of collision dominated systems (Makino et al., 1993a).

In addition to integrate the time evolution of an N-body system by direct summation, GRAPE has been incorporated into a TREECODE algorithm (Makino & Funato, 1993) and, more recently, into a P3M code (Brieu et al., 1995). Besides forces and potential, GRAPE also returns the list of neighbours for each particle i within a specified radius h_i. This feature makes it attractive for use in smoothed particle hydrodynamics (Umemura et al., 1993), where gas properties are derived by averaging over a localized ensemble of discrete particles. For particles near the surface of the integration volume, "ghost" particles are created to correctly extend the neighbour search beyond the borders of the computational volume; no forces are computed for these particles. For periodic boundaries, the ghosts

are replicas of particles from the opposite side of the volume. Our SPH code is modified to incorporate GRAPE following the strategy described in Steinmetz (1996). Furthermore we have added the ability to handle periodic boundary conditions (see Sec.'s 3.6 and 3.7).

3.6 Implementing Periodic Boundaries into GRAPE

Due to its restricted force law (Eqn. 3.51), GRAPE cannot treat periodic particle distributions. However, many astrophysical problems require a correct treatment of periodic boundary conditions. Simulating the dynamical evolution and fragmentation in the interior of a molecular cloud, a process that finally leads to the formation of new stars, requires periodic boundaries to prevent the whole object from collapsing to the center. The situation is quite similar in cosmological large-scale structure simulations, where periodic boundaries mimic the homogeneity and isotropy of the initial matter distribution. In the following, we present a method to overcome this limitation and to incorporate fully periodic boundary conditions into an N-body or SPH algorithm using GRAPE. The basic idea is to compute a periodic correction force for each particle on the host computer, applying a particle-mesh (PM) like scheme: We first compute the forces in the isolated system using direct summation on GRAPE, then we assign the particle distribution to a mesh and compute the periodic correction force for each grid point, by convolution with the adequate Green's function in Fourier space. Finally, we add this correction to each particle in the simulation. The corrective Green's function can be constructed as the offset between the periodic solution (calculated via the Ewald (1921) approximation) and the isolated solution on the grid.

Our approach is thus related to the method described in Huss et al. (1997). However, they apply the combined force calculation via a periodic PM scheme and direct summation on GRAPE only to the particle distribution in the center of their simulation volume. In this region, they compute the dynamical evolution of a galaxy cluster with high resolution, whereas the remaining part of the volume is treated by a pure PM scheme and provides the tidal torques for the cluster in the center. For this reason, they do not have to handle possible force misalignment in the border region of the simulation cube. In our situation, studying the evolution and fragmentation in the interior of molecular clouds, we need high resolution and periodicity throughout the *whole* simulation volume. Ensuring numerical stability throughout the complete volume requires additional care in combining both methods, the PM scheme and GRAPE.

We apply the following concept of incorporating periodic boundaries into GRAPE in a general form. We use the Ewald (1921) method to obtain a Green's function that accounts for the correction to potential and force for a system transformed from having vacuum boundary conditions to periodic ones. GRAPE computes the forces and potential for

the isolated system. The Green's function is then used in a PM-like scheme to assign a correction term due to periodicity to each particle in the simulation.

There also has been an attempt to treat periodic boundaries on a special-purpose hardware device, WINE, using the Ewald method hardwired on a special chip (Fukushige et al., 1993). This work has been successful. Fukushige et al. (1996) report the development of the MD-GRAPE, which can handle an arbitrary central force law, including the Ewald method. However, these chips only exist in a experimental version and cannot be bought on the market.

3.6.1 Periodic Force Correction – The Ewald Method

In 1921, P. Ewald suggested a method to compute the forces in a periodic particle distribution (he aimed explicitely to compute the potential in atomic lattices in solids). For a more recent discussion see Hernquist et al. (1991); for applications to large scale structure simulations see Katz et al. (1996), or Davé et al. (1997).

Poisson's equation for a system of N particles, which are infinitely replicated in all directions with period L, is

$$\nabla^2\phi(\boldsymbol{r}) \;=\; 4\pi G\rho(\boldsymbol{r}) \;=\; 4\pi G\sum_{\boldsymbol{n}}\sum_{j=1}^{N} m_j\delta(\boldsymbol{r}-\boldsymbol{r}_j-\boldsymbol{n}L)\;, \tag{3.52}$$

with $\boldsymbol{n}$ being an integer vector. It can be solved in general using an appropriate Green's function $\mathcal{G}$,

$$\phi(\boldsymbol{r}) = -G\sum_{\boldsymbol{n}}\sum_{j=1}^{N} m_j\mathcal{G}(\boldsymbol{r}-\boldsymbol{r}_j-\boldsymbol{n}L) \tag{3.53.a}$$

$$= -\frac{G}{L^3}\sum_{j=1}^{N}\sum_{\boldsymbol{k}}\hat{\mathcal{G}}(\boldsymbol{k})m_j\exp\left[i\boldsymbol{k}(\boldsymbol{r}-\boldsymbol{r}_j)\right], \tag{3.53.b}$$

For the gravitational potential, this Green's function has the form $\mathcal{G}(\boldsymbol{r}) = 1/r$ with $\hat{\mathcal{G}}(\boldsymbol{k}) = 4\pi/k^2$ being its Fourier transform. The sum in Eqn. 3 converges very slowly, which strongly limits its numerical applicability. However, Ewald (1921) realized that convergence can be improved considerably by splitting the Green's function into a short range part $\mathcal{G}_S$ and a long range part $\mathcal{G}_L$ and solving the first in real space and the latter one in Fourier space:

$$\mathcal{G}_S(\boldsymbol{r}) = \frac{1}{r}\mathrm{erfc}(\alpha r) \;\;;\;\; \hat{\mathcal{G}}_S(\boldsymbol{r}) = \frac{4\pi}{k^2}\left[1-\exp\left(-\frac{k^2}{4\alpha^2}\right)\right] \tag{3.54.a}$$

$$\mathcal{G}_L(\boldsymbol{r}) = \frac{1}{r}\mathrm{erf}(\alpha r) \;\; ; \;\; \hat{\mathcal{G}}_L(\boldsymbol{r}) = \frac{4\pi}{k^2}\exp\left(-\frac{k^2}{4\alpha^2}\right) . \tag{3.54.b}$$

Here, α is a scaling factor in units of inverse length and $\mathrm{erf}(x)$ is the error function with $\mathrm{erfc}(x)$ being its complement,

$$\mathrm{erf}(x) \;=\; \frac{2}{\sqrt{\pi}}\int_0^x e^{-\xi^2} d\xi \; . \tag{3.55}$$

With the Green's function split into two parts, $\mathcal{G} = \mathcal{G}_S + \mathcal{G}_L$, the potential reads as $\phi(\boldsymbol{r}) = \phi_S(\boldsymbol{r}) + \phi_L(\boldsymbol{r})$:

$$\begin{aligned}\phi(\boldsymbol{r}) \;=\; -G\sum_{j=1}^{N} m_j \Bigg[& \sum_{\boldsymbol{n}} \frac{\mathrm{erfc}(\alpha|\boldsymbol{r}-\boldsymbol{r}_j-\boldsymbol{n}L|)}{|\boldsymbol{r}-\boldsymbol{r}_j-\boldsymbol{n}L|} - \\ & - \frac{1}{L^3}\sum_{\boldsymbol{k}} \frac{4\pi}{k^2}\exp\left(-\frac{k^2}{4\alpha^2}\right)\cos\left(\boldsymbol{k}(\boldsymbol{r}-\mathbf{r}_j)\right)\Bigg] .\end{aligned} \tag{3.56}$$

Finally, the force (say exerted onto particle i) is

$$\boldsymbol{F}_i \;=\; \boldsymbol{F}(\boldsymbol{r}_i) \;=\; -m_i\nabla\phi(\boldsymbol{r}_i) \;=\; Gm_i\sum_{j\neq i} m_j \boldsymbol{f}(\boldsymbol{r}_i-\boldsymbol{r}_j) \, , \tag{3.57}$$

with

$$\begin{aligned}\boldsymbol{f}(\boldsymbol{r}) \;\equiv\; -\sum_{\boldsymbol{n}} \frac{\boldsymbol{r}-\boldsymbol{n}L}{|\boldsymbol{r}-\boldsymbol{n}L|^3}\Big[& \mathrm{erfc}\left(\alpha|\boldsymbol{r}-\boldsymbol{n}L|\right) + \\ & + \frac{2\alpha}{\sqrt{\pi}}|\boldsymbol{r}-\boldsymbol{n}L|\exp(-\alpha^2|\boldsymbol{r}-\boldsymbol{n}L|^2)\Big] - \\ & - \frac{1}{L^3}\sum_{\boldsymbol{k}} \frac{4\pi\boldsymbol{k}}{k^2}\exp\left(-\frac{k^2}{4\alpha^2}\right)\sin\left(\boldsymbol{k}\boldsymbol{r}\right) \; .\end{aligned} \tag{3.58}$$

To achieve good accuracy with reasonable computational effort, typical values are $\alpha = 2/L$, $|\boldsymbol{r}-\boldsymbol{n}L| < 3.6L$ and $\boldsymbol{k} \equiv 2\pi\boldsymbol{h}/L$ with $\boldsymbol{h}$ being an integer vector with $|\boldsymbol{h}|^2 < 10$ (see e.g. Hernquist et al., 1991; note, the second component in their Eqn. 2.14b is missing a factor $|\boldsymbol{r}-\boldsymbol{n}L|$; it is otherwise identical to our Eqn. 3.58).

For a particle pair with separation $\boldsymbol{r}$, $\boldsymbol{f}(\boldsymbol{r})$ includes the contributions from all L-periodic pairs with identical separation. To obtain the pure periodic *correction* force $\boldsymbol{f}_{\mathrm{cor}}(\boldsymbol{r})$, one has to subtract the direct interaction of the central pair, which leads to

$$\boldsymbol{f}_{\mathrm{cor}}(\boldsymbol{r}) \;\equiv\; \boldsymbol{f}(\boldsymbol{r}) + \frac{\boldsymbol{r}}{|\boldsymbol{r}|^3} \, . \tag{3.59}$$

To obtain the periodic correction for the *potential* of the particle pair, $\phi_{\rm cor}(\boldsymbol{r})$, one proceeds similarly and again subtracts the isolated solution from the Ewald solution (Eqn. 3.56),

$$\phi_{\rm cor}(\boldsymbol{r}) \equiv \phi(\boldsymbol{r}) + \frac{1}{|\boldsymbol{r}|}\,. \tag{3.60}$$

We compute the correction terms $\boldsymbol{f}_{\rm cor}$ and $\phi_{\rm cor}$ for particle pairs on a Cartesian grid covering our whole simulation box, placing particle 1 in the central node and particle 2 on different grid points, and obtain so a table of pairwise force values.

3.6.2 The Particle-Mesh Method

Particle-mesh methods assign particle properties to mesh points, solve the interaction equations on the grid and interpolate the solution back onto the particles (e.g. Hockney & Eastwood, 1988). Typically, the density at each grid point is determined from the particle positions and masses using CIC ("cloud in cell") or TSC ("triangular shaped cloud") schemes, whose assignment functions are triangles or quadratic splines, respectively (again Hockney & Eastwood, 1988, Chap. 5). For the gravitational N-body problem one solves Poisson's equation. Usually this is done in Fourier space, since the differential operation there acts as a simple multiplication. Therefore, the density distribution on the grid is transformed into k-space using FFT and convolved with the appropriate Green's function to solve for the potential. To obtain the forces, we convolve the Fourier transform of the density with the Green's function for the force[2]; separately for the x, y and z-component. Finally, inverse FFT returns the potential and the force at each grid point. The alternative for computing the forces in Fourier space is, to calculate them in real space as gradients of the mesh-defined potential. This would induce additional errors and therefore we prefer the first method.

3.6.3 Combining the PM Method with Direct Summation on GRAPE

In our application of the PM method, we compute the (periodic) *correction* to the force and the potential and add this to the solution for the isolated system, which is obtained via direct summation on GRAPE. This procedure ensures proper treatment of periodic boundary conditions. The Green's function for the PM scheme can be constructed directly

[2]Strictly speaking, a Green's function is the solution of an equation of the type, $\nabla^2\mathcal{G}(\mathrm{r}) = -4\pi\delta(\mathrm{r})$ and its boundary value problem. Green's functions are used to solve Poisson's equation for the potential. Being the gradient of Poisson's equation, the force equation can be solved by the same ansatz.

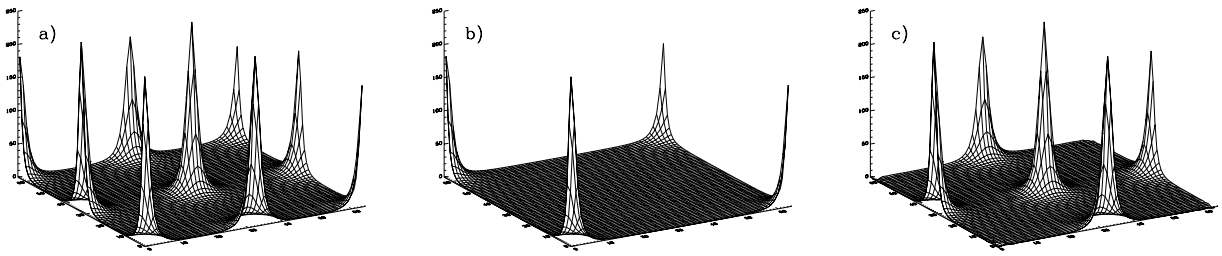

Figure 3.2: Matrix of pairwise forces – x-component F_x; cut through the yz-plane at x=0: a) The periodic contribution (replicated onto the whole grid). b) The isolated solution. c) The difference between both, i.e. the correction term.

in Fourier space (Hockney & Eastwood, 1988). However, for the correction force and potential, this is rather complicated and it is more intuitive and straightforward to proceed in the following way: We obtain the Green's function for each force component as the Fourier transform of the x, y and z-component, respectively, of the mesh-defined pairwise periodic correction force $\boldsymbol{f}_{\rm cor}$, defined in Eqn. 3.59. And for the potential correction, the appropriate Green's function is the Fourier transform of $\phi_{\rm cor}$ in Eqn. 3.60. The *corrective* Green's function is thus the offset between the Green's function for the periodic system $\mathcal{G}_{\rm per}$ and the isolated one $\mathcal{G}_{\rm iso}$,

$$\mathcal{G}_{\rm cor} \; = \; \mathcal{G}_{\rm per} - \mathcal{G}_{\rm iso}. \tag{3.61}$$

Or with other words, $\boldsymbol{f}_{\rm cor}$ and $\phi_{\rm cor}$ *are* the Green's functions with the right properties and only have to be transformed into Fourier space for convolution with the density. Using the Fourier transform of the Ewald forces as periodic Green's function was proposed by A. Huss (private communication) and it is straightforward to extend this for handling the force *correction* by subtracting the isolated solution.

Note, in order to obtain the *isolated* solution in Fourier space, one has to double the linear dimensions of the grid and *zero pad* the additional grid points to avoid contamination from implicitly assumed periodicity (see Press et al., 1989). For example, to solve Poisson's equation for a cubic density field with volume L^3, we have to use a grid of size $(2L)^3$, assign the density field to one octant of the large box and fill the remaining grid points with zero. The Green's function, however, has to be defined on the complete grid, i.e. $\mathcal{G}(\boldsymbol{r}) = 1/|\boldsymbol{r}|$ for the potential, with $-L \leq x, y, z \leq L$. On the other hand, the *periodic* Green's function is defined on the original grid, with $-L/2 \leq x, y, z \leq L/2$. For alignment with the isolated solution, we have to extend the periodic solution into the larger cube. To obtain the right correction Green's function, e.g. for the force, we replicate the table of pairwise Ewald forces (defined on the small cube) into all octants of the large cube. Then, we subtract the isolated force field (defined on the large cube) and transform into Fourier

space. This procedure is illustrated in Fig. 3.2, it plots F_x in the yz-plane at $x = 0$: (a) is the Ewald periodic force computed on a 32-grid and replicated four time into a 64-grid, (b) is the isolated solution defined on the large grid and (c) is the difference, the final correction force. The Green's function finally is the Fourier transform of this force matrix. Convolution with the zero padded density field results in the appropriate force correction. The procedure is analogous for the potential. In practice, it is sufficient to compute the Green's function once at the beginning of a simulation run and store it as a table.

The total force acting on an individual particle during one time step then stems from the particle system inside the simulation cube, computed by direct summation on GRAPE, *plus* the contribution from an infinite set of periodically mirrored systems, computed via the method described above. For smoothed particle hydrodynamics, one also has to add pressure and viscous forces.

We compute the periodic and the isolated solution on a grid, subtract the latter from the first and add the isolated forces calculated with GRAPE. The two isolated solutions cancel out and one can ask the question, and for a system with more or less homogeneous density a pure PM scheme is sufficient. However, the advantage of using GRAPE is evident when computing strongly structured systems. Unlike in PM schemes, the spatial resolution with GRAPE is not limited to a given cell size, but adapts to the density distribution due to its Lagrangian nature. It is limited only by the gravitational smoothing length, or equivalently, by the choice of the minimum time step. Since the potential of strong density peaks is dominated by self-gravity and the influence of periodic boundaries (and thus of the Ewald correction) becomes weak, it is sufficient to compute this correction term on a relatively coarse grid which keeps the additional computational cost low. For a relatively smooth density distribution, a relatively wide mesh is sufficient anyhow. The scheme proposed here unites both, high resolution with GRAPE and the periodicity of a PM scheme. In addition, applying a Courant-Friedrichs-Lewy-like criterion, we typically do not have to compute the FFT at each smallest time step, but can use stored correction values from the previous call. This reduces the computational expense even further.

3.7 Optimization of the Scheme and Performance in Test Cases

The contributions to the total acceleration of one particle are computed by two distinct methods: by direct summation on the GRAPE board for the isolated solution and by applying a particle-mesh scheme for the periodic correction term. Compared to the host computer, the GRAPE chips hereby have only limited numerical accuracy (see Sec. 3.7.1). The spatial resolution of the PM scheme is limited by the number of grid zones and the

choice of the assignment function (Sec. 3.7.2). All this may lead to spurious residuals when combining the forces; some terms may not cancel out completely. This "misalignment" can be minimized by randomly shifting the center of the simulation cube through the periodic particle distribution. Then on average the force residuals cancel out and numerical stability is increased (Sec. 3.7.3).

3.7.1 Gravitational Smoothing Length and Numerical Accuracy of GRAPE

Since GRAPE is used to calculate the force contribution from the isolated system, we also call the board at the start of the simulation, when setting up the force correction table. We subtract the isolated solution from the periodic Ewald solution for each particle pair on a grid. For our test problems and also for calculating the periodic Ewald forces, we use a fixed gravitational smoothing length ϵ throughout the whole computation. As always in collisionless N-body simulations, the choice of ϵ is a trade-off between minimising 2-body relaxation (large ϵ) and spatial resolution (small ϵ). For the simulations presented here, we typically adopt values between $\epsilon = 0.01$ and 0.001, with the total size of the simulation cube being $[-1, +1]^3$. The influence of ϵ is demonstrated in Fig. 3.3. For 32^3 particles which are distributed on a regular grid, it plots the distribution of the normalized residual forces in x-direction, dF_x/F_x. Assuming periodic boundary conditions, this regular particles distribution is – in principle – force free. Residual forces $d\mathbf{F}$ are a spurious result of the calculation scheme. We give relative errors by normalizing the residual force for each particle to the acceleration it would feel without periodic boundaries (i.e. in the isolated system). For all values of $\epsilon \leq 0.001$ the distribution of force errors is homogeneously distributed throughout the volume and determined by the numerical accuracy of the GRAPE chips. For larger ϵ, the force contributions from the two methods become increasingly misaligned and the residual force errors grow.

3.7.2 Grid Resolution and Assignment Function

Another important factor is the resolution of the grid. The more grid zones are used, the smaller are the wave lengths that can be resolved by the PM scheme. However, the number of CPU cycles increases linearly with the number of grid zones. Again one has to find a compromize between accuracy and computational speed, depending on the problem to be solved. The errors furthermore depend on the adopted assignment function. To obtain the force correction, one has to interpolate the particle distribution onto a grid, solve Poisson's equation for the density field to obtain forces and assign these forces back onto the particles. One possibility is to assign all particles to the cell they are located in, the

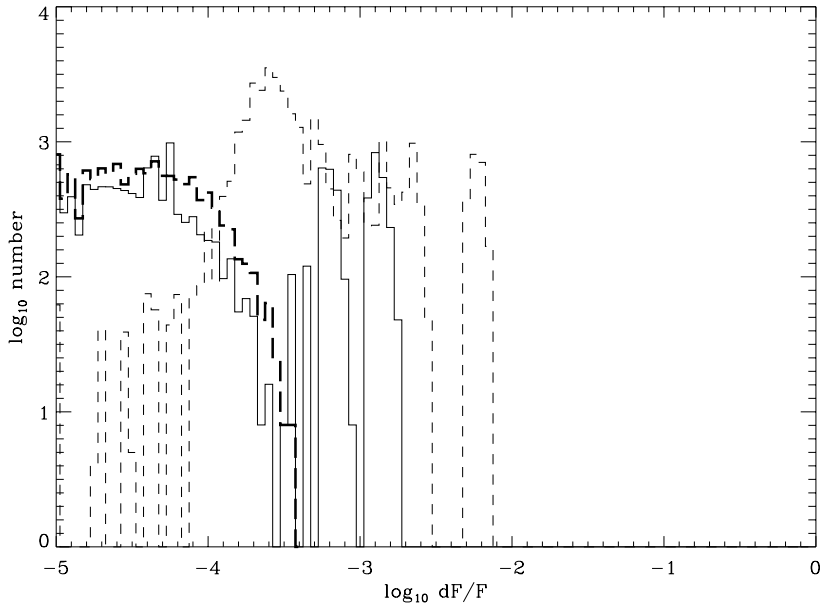

Figure 3.3: Influence of the gravitational smoothing length ϵ. The figure plots histograms of the distribution of the residual force errors in x-direction, dF_x/F_x, for each particle in the simulation. For $\epsilon \leq 0.001$ the force errors are equally distributed throughout the simulated volume and minimal (thick dashed line). The errors grow with increasing ϵ ($\epsilon = 0.005$ – solid line, $\epsilon = 0.01$ dashed line). These force residuals are computed for a distribution of 32^3 particles on a regular grid with periodic boundaries. The force correction is computed on a 64^3-mesh. The particles are centered on grid points to be independent of the assignment scheme.

nearest grid point scheme, NGP. Another way is CIC (cloud in cell), which uses a boxlike cloud shape to distribute each particle into eight neighbouring cells (in three dimensions). TSC (triangular shaped cloud) distributes the particle mass into 27 cells (for more details consult Hockney & Eastwood 1988). For the problems we study here, we consider NGP as too coarse, higher order schemes on the other hand smear out the particle distribution and thus limit the spatial resolution. We adopt the CIC scheme in our calculations. Using CIC, we plot in Fig. 3.4 the normalized residual errors in x-direction, dF_x/F_x, analogous to the previous figure. Again the 32^3 particles are distributed on a regular cubic grid. However, now they have been shifted by $dx = 0.015625$, i.e. half of the cell size of a 64^3-grid, to be able to assess the accuracy of the assignment scheme. As expected for the finer meshes, the interpolation is more precise and the force errors are smaller. As a reference, we have plotted the intrinsic error contribution coming from GRAPE alone (the thick long dashed line). It is computed for minimum smoothing length ϵ and for particles sitting exactly on mesh points. Therefore, this distribution has no mesh-assignment errors. Note that in the general cases, the assignment errors are not evenly distributed amongst the particles; the errors are small and close to zero in the interior of the simulated cube,

whereas particles at the border have errors which are one or two orders of magnitudes larger (dotted and dashed lines in the range $-2 < \log_{10} dF/F < -1$). Note as well, that each grid is in fact a factor of 2^3 larger to account for the zero padding necessary for the isolated solution, i.e. the 64^3-grid is in fact a 128^3-grid.

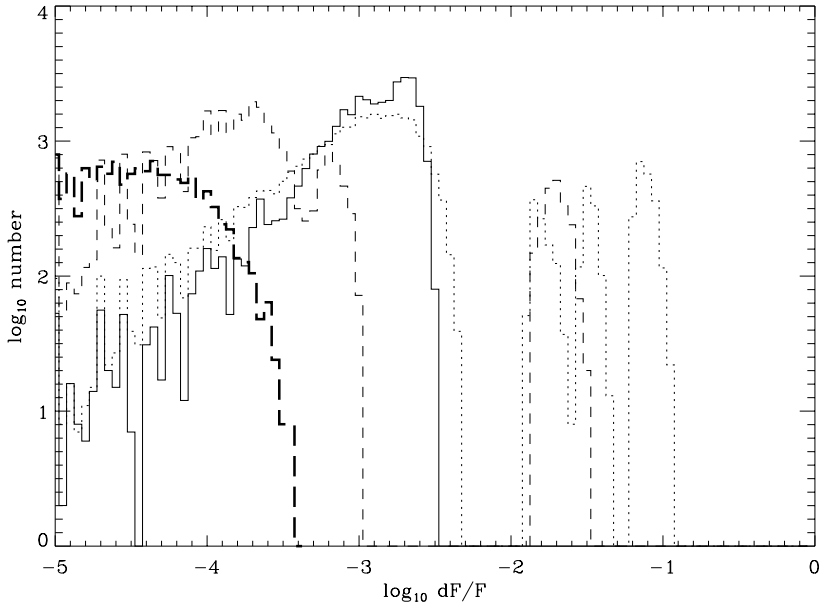

Figure 3.4: Comparison of the normalized residual force errors dF/F for different grid resolutions: 16^3 (dotted line), 32^3 (dashed line) and 64^3 (continuous line). As reference, the error distribution stemming solely from GRAPE is plotted as thick dashed line (analogous to Fig. 3.3).

3.7.3 The Influence of Random Shifts

We can increase the stability of the code by minimizing the influence of the force errors for the border cells. One way to do this is to ensure, that these border cells do not always contain the same group of particles by applying a random shift of the whole simulation area. We can think of our simulation box as a window onto an infinite periodic particle distribution. Since this distribution is infinite and periodic, we are free to choose any region in it, as long as it contains the periodicity of the whole distribution. By randomly shifting the center of the simulation box we prevent the errors made in the border cells to add up coherently for the same particles. On average they cancel out. The stabilizing effect of this method is demonstrated in Fig. 3.5. It compares the time evolution of the average particle displacement (due to force errors) for the standard particle distribution (particles on a regular 32^3 mesh) for the two cases with and without applying random

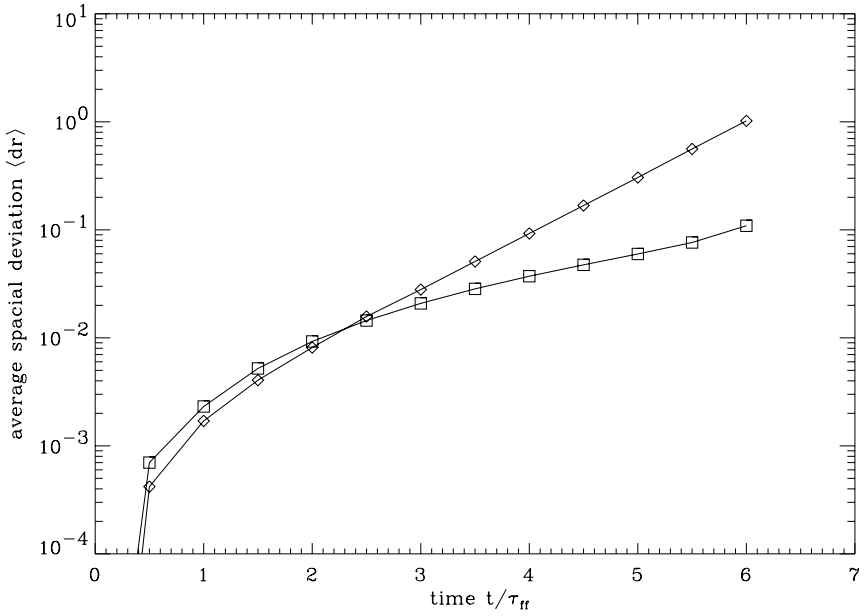

Figure 3.5: Average particle displacement as function of time for the system integrated with (squares) and without (diamonds) random shift.

shift. Clearly, the system computed without shift degrades much faster than the other one. In fact, we plot the pathological case, where the particles are located exactly between two mesh points and therefore the assignment error is maximal. This system collapses due to these errors on a time scale of about 5 free-fall times[3]. For a system where the particles are placed exactly on grid points the assignment errors are minimal. Such a system is more stable without random shift. However, in a physically meaningful context the particles are far from being placed exactly on grid points and random shift is an important tool of stabilizing the code.

3.7.4 Comparison with the Ewald Method

A further test of the performance of this new method is, to compare it with a TREECODE scheme. In this case, the Ewald method can be directly implemented into the force summation, as described by Hernquist et al. (1991). To do so, we distribute 32^3 particles randomly within the simulation cube to get a homogeneous distribution with Poisson fluctuations. We chose the initial kinetic energy to be zero and follow the fragmentation and collapse of the system. In this gravitational N-body system, the random density

[3]The regular infinite system does not collapse; the free-fall time is per default infinite. Here and in the following free-fall time means the time scale on which the an *isolated* simulation cube would collapse.

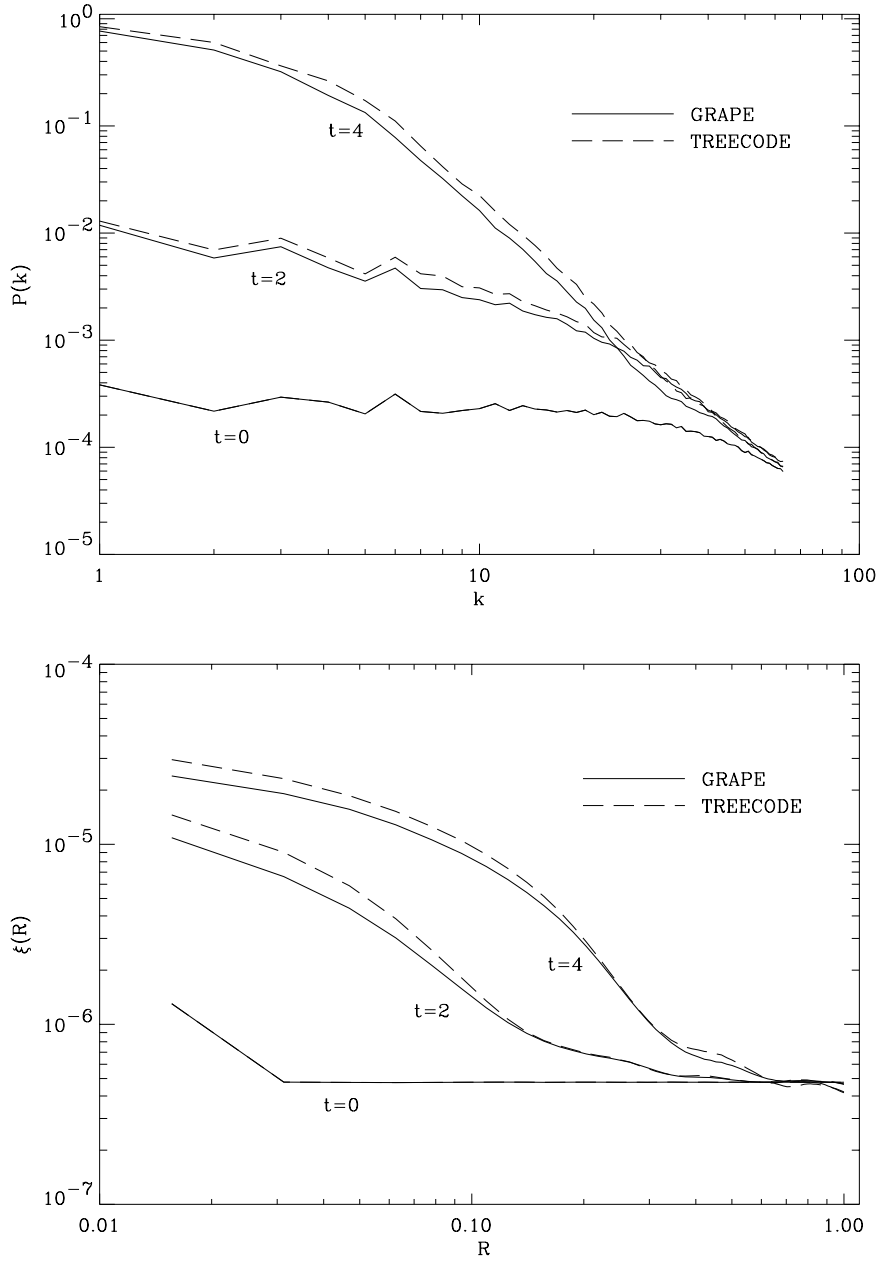

Figure 3.6: Power spectrum $P(k)$ and 2-point correlation function $\xi(R)$ for the collapse of a random fluctuation field in periodic boundaries. The solid lines describe the calculation done with GRAPE and the dashed lines with a TREECODE scheme. Both systems evolve almost identically.

peaks of the initial distribution start to grow and form a network of filaments and knots. These knots finally merge to form one big clump. The evolution of the system with GRAPE and with the TREECODE scheme is compared by plotting the power spectrum

$P(k)$ and the correlation function $\xi(R)$ in Fig. 3.6. Considering the differences in the force calculation method, the evolutions of the two systems agree remarkably well. Only for small to intermediate particle separations, the difference in the force calculation in both schemes leads to a deviation in the correlation and in the power spectrum. However, the computation using the GRAPE hardware is ~ 10 times faster when compared with the TREECODE run on a Sparc Ultra workstation.

3.7.5 Summary

The method described above unites the advantages of GRAPE as being Lagrangian and offering good spatial resolution necessary for treating highly structured density distributions with the advantage of particle-mesh schemes as being intrinsically periodic. The potential of strong density peaks is dominated by the local mass accumulation. In such a region the influence of the global properties of the system is weak and it is therefore sufficient to compute the correction term on relatively coarse grid. This keeps the additional computational cost low. The proposed method has proven to be numerically stable and inexpensive in terms of computer time. Thus the special-purpose hardware device GRAPE can be applied successfully to astrophysical problems that require the correct treatment of periodic boundary conditions.

Chapter 4

Scaling Properties

The numerical models discussed in this thesis describe self-gravitating, isothermal gas. This determines the equation of state and the physical processes invoked. The dynamical evolution of the gas is scale-free and depends only on the ratio between internal and gravitational energy (Sec. 4.1). All calculations are performed and presented in normalized, dimensional units. The conversion between normalized and physical units is introduced in Sec. 4.2. The next section (4.3) describes the appropriate scaling of the simulations to observed star-forming regions. Section 4.4, finally, discusses the conversion of the Jeans mass and the speed of sound, both important quantities determining the dynamical behavior of the system.

4.1 Scaling Properties of Isothermal, Self-Gravitating Gas

For isothermal gas, the energy density is a function of temperature only and the equation of state (3.6) reduces to $p = c_{\rm s}^2 \rho$, with $c_{\rm s}^2$ being the thermal sound speed (Eqn. 3.7). This approximation is valid for physical regimes where the heating and cooling time scales are much less than the dynamical ones. In molecular clouds, this is the case for gas densities $n(\mathrm{H}_2) \lesssim 10^{10}\,\mathrm{cm}^{-3}$, where the gas is optically thin for the dominant cooling processes and energy is radiated away very efficiently (e.g. Tohline, 1982). Average densities in star forming regions typical are in the range $10\,\mathrm{cm}^{-3} < n(\mathrm{H}_2) < 10^5\,\mathrm{cm}^{-3}$ and these are the regions we aim to model. Even when resolving a density contrast of 10^4, the isothermal equation of state is still appropriate throughout the entire simulation.

The self-gravitating, isothermal model studies the interplay between gravity and gas pressure, it is therefore scale free. Besides on the initial conditions, the dynamical evolution

of the system depends only on one parameter, namely the ratio between internal and potential energy. This ratio can be interpreted as dimensionless *temperature*,

$$T \equiv \epsilon_{\rm int}/|\epsilon_{\rm pot}| \,. \tag{4.1}$$

Line widths in molecular clouds are super-thermal, implying the presence of supersonic turbulent motions (Sec. 2.1.2). In case of isotropic turbulence, these non-thermal (turbulent) contributions can be accounted for by setting $\epsilon_{\rm int} = \epsilon_{\rm therm} + \epsilon_{\rm turb} = \gamma \cdot (c_{\rm s}^2 + \sigma_{\rm turb}^2)/2$. This introduces a second parameter which can be absorbed by defining an *effective* temperature, $T_{\rm eff} = T + \sigma_{\rm turb}^2/\mathcal{R}$. The turbulent velocity dispersion is denoted $\sigma_{\rm turb}$ and the factor γ depends on the degree of freedom. In case of anisotropic turbulent motions, the system has (locally) preferred axes and the concept of one single effective temperature is no longer valid.

4.2 Conversion between Normalized and Physical Units

Analogous to the temperature, we adopt dimensionless and normalized units throughout the entire dissertation work. If physical scaling is used, it is always stated explicitely and given in the appropriate units[1]. To distinguish between physical and normalized units, for the remainder of this chapter the latter ones are labeled by a tilde. In the isothermal models, the mass $\tilde{M}$ of the molecular cloud region studied and the length scale $\tilde{L}$ are set to one. The numerically simulated area is a cube $[-\tilde{L}, +\tilde{L}]^3 = [-1, +1]^3$ with periodic boundary conditions. Its volume is $(2\tilde{L})^3 = 8$, therefore, the density of the homogeneous cube is $\tilde{\rho} = \tilde{M}/\tilde{L}^3 = 1/8$. Analogously, the gravitational constant $\tilde{G}$ and the gas constant $\tilde{\mathcal{R}}$ are normalized. In summary,

$$\tilde{M} \equiv \tilde{L} \equiv \tilde{G} \equiv 1 \qquad \text{and} \qquad \tilde{\mathcal{R}} \equiv 1/\gamma \,, \tag{4.2}$$

with $\gamma = 3/2$ for an ideal gas having three degrees of freedom. The following list gives an overview of the definition and the conversion between normalized and physical units of the most important model parameters. Since the model is scale-free, first the physical mass and physical size of the simulated region have to be determined:

- **Mass:** In normalized units, the total mass in the system is *defined* as one: $\tilde{M} \equiv 1$. Physical values are given in solar masses, $M_\odot$. Having determined the physical mass m of the simulated gas, the conversion between both units is fixed as,

$$m\, M_\odot \;\widehat{=}\; 1\, \tilde{M} \,. \tag{4.3}$$

[1]For physical units, a combination of the 'cgs'-system and astrophysical units is used. For values and conversion factors see App. B.

- **Length:** Also the unit length is *defined* as being one, $\tilde{L} \equiv 1$. The physical length unit is parsec, pc. Once the size of the simulated region is chosen as ℓ, the conversion is given as,

$$\ell \text{ pc } \mathrel{\widehat{=}}\ 1\,\tilde{L}\,. \tag{4.4}$$

These choices determine the conversion of dependent quantities and of the independent scaling parameter $\tilde{T}$:

- **Time:** The code time unit $\tilde{t}$ is determined from the normalization (4.2) as $\tilde{t} \equiv \tilde{L}^{3/2}\tilde{M}^{-1/2}\tilde{G}^{-1/2}$. Thus, the conversion into years is

$$1.50 \times 10^7 \text{ yr} \cdot \sqrt{\frac{\ell^3}{m}} \mathrel{\widehat{=}}\ 1\,\tilde{t}\ . \tag{4.5}$$

- **Density:** Density is computed from $\tilde{\rho} \equiv \tilde{M}/\tilde{L}^3$ in the simulation. Plugging in physical values, the conversion follows as

$$6.77 \times 10^{-23}\,\mathrm{g\,cm^{-3}} \cdot \frac{m}{\ell^3} \mathrel{\widehat{=}}\ 1\,\tilde{\rho} \tag{4.6.a}$$

$$40.5 \cdot \frac{1}{\mu} \cdot \mathrm{cm^{-3}} \cdot \frac{m}{\ell^3} \mathrel{\widehat{=}}\ 1\,\tilde{\rho}\,. \tag{4.6.b}$$

The first line gives the mass density. In the last line, the dimensional density $\tilde{\rho}$ corresponds to the number density of H_2-molecules per cm^3. Typically, the interstellar medium has a helium abundance of 10%. Therefore, the mean molecular weight[2] in molecular clouds is $\mu \approx 2.36$. For atomic gas, this value is $\mu \approx 1.30$.

- **Energy:** The energy unit is determined from $\tilde{E} \equiv \tilde{M}\tilde{L}^2\tilde{t}^{-2} \equiv \tilde{M}^2\tilde{G}/\tilde{L}$. The conversion into erg is

$$8.57 \times 10^{40} \text{ erg} \cdot \frac{m^2}{\ell} \mathrel{\widehat{=}}\ 1\,\tilde{E}. \tag{4.7}$$

[2]A helium abundance of 10% implies that the ratio of H atoms to He atoms is 9:1. In atomic gas, the mean mass per particle is therefore $(9\times1+1\times4) : (9+1) = 1.3$. For molecular gas there are two He atoms per nine H_2 molecules. Hence, $\mu = (9 \times 2 + 2 \times 4) : (9 + 2) = 2.36$. However, there is also a dependence on the metallicity of the gas: typically, gas with solar metallicity contains $\sim 2\%$ heavier elements with an atomic number $Z \approx 15$ on average. In this case, $\mu = (22 \times 2 + 5 \times 4 + 1 \times 15) : (22 + 5 + 1) = 2.8$, or in general $\mu = 2.28 + 0.035\,Z$.

- **Specific Energy** and **Energy Density:** The conversion into $\mathrm{erg\,g^{-1}}$ and $\mathrm{erg\,cm^{-3}}$ is

$$4.30 \times 10^7\ \mathrm{erg\,g^{-1}} \cdot \frac{m}{\ell} \ \hat{=}\ 1\,\tilde{E}/\tilde{M} \tag{4.8.a}$$

$$2.91 \times 10^{-15}\ \mathrm{erg\,cm^{-3}} \cdot \frac{m^2}{\ell^4} \ \hat{=}\ 1\,\tilde{E}/\tilde{L}\,. \tag{4.8.b}$$

- **Temperature** and **Internal Energy**: The normalized units are defined such that the internal energy $\tilde{\epsilon}$ and the scale parameter $\tilde{T}$ are *identical*: $\epsilon \equiv T$. Expressed in physical terms, the internal energy per gram is given as $\epsilon = \gamma\ \mathcal{R}/\mu\ T$. With Eqn. 4.8.a and $\gamma = 3/2$ for ideal gas, the physical temperature is

$$0.35\,\mathrm{K} \cdot \mu \cdot \frac{m}{\ell} \ \hat{=}\ 1\,\tilde{T}. \tag{4.9}$$

4.3 Scaling to Observed Star-Forming Regions

Typical quantities to characterize physical regimes in molecular clouds are temperature T and density $n(\mathrm{H_2})$. Canonical values are $T \approx 10\,\mathrm{K}$ and densities between $n(\mathrm{H_2}) \approx 10^2\,\mathrm{cm^{-3}}$ in dark quiescent clouds like Taurus and $n(\mathrm{H_2}) \approx 10^5\,\mathrm{cm^{-3}}$ in dense high-mass star-forming clouds like Orion (see Sec. 2.1).

For a given dimensionless scale parameter $\tilde{T}$, selecting a physical temperature and density determines the size and the mass of the simulated region. Given $\tilde{\rho}$ and $\tilde{T}$, Eqn.'s 4.6.b and 4.9 can be transformed to specify m and ℓ as,

$$m = \sqrt{\left(\frac{40.5\,\mathrm{cm^{-3}}}{n(\mathrm{H_2})} \cdot \tilde{\rho}\right)\left(\frac{T}{0.35\,\mathrm{K}} \cdot \frac{1}{\tilde{T}}\right)^3} \cdot \frac{1}{\mu^2} \quad \text{and} \tag{4.10.a}$$

$$\ell = \sqrt{\left(\frac{40.5\,\mathrm{cm^{-3}}}{n(\mathrm{H_2})} \cdot \tilde{\rho}\right)\left(\frac{T}{0.35\,\mathrm{K}} \cdot \frac{1}{\tilde{T}}\right)} \cdot \frac{1}{\mu}\,. \tag{4.10.b}$$

For molecular clouds with $\mu = 2.36$ and with the average density of the homogeneous distribution being fixed to $\tilde{\rho} = 1/8$ by the normalization (4.2), the mass and size scales are

$$m = 1.95 \sqrt{\frac{1}{n(\mathrm{H_2})}\left(\frac{T}{\tilde{T}}\right)^3} \quad \text{and} \tag{4.11.a}$$

$$\ell = 1.61 \sqrt{\frac{1}{n(\mathrm{H_2})}\frac{T}{\tilde{T}}}\,, \tag{4.11.b}$$

with densities $n(H_2)$ being the number of H_2 molecules per cubic centimeter and the physical temperature T given in Kelvin.

The model discussed in detail in Chap. 6, with dimensionless temperature $\tilde{T} = 0.01$, corresponds in the case of a dark cloud like Taurus, with $n(H_2) \approx 10^2\,\mathrm{cm}^{-3}$ and $T \approx 10\,\mathrm{K}$, to a total mass of $6\,300\,\mathrm{M}_\odot$ and a volume of $(10.4\,\mathrm{pc})^3$. For this scaling, the time unit is equivalent to $t = 2.24 \times 10^6$ years and the average Jeans mass transforms to $M_\mathrm{J} = 28\,\mathrm{M}_\odot$ (see Sec. 4.4). When the model is applied to a dense, massively star-forming cloud with $n(H_2) \approx 10^5\,\mathrm{cm}^{-3}$ and again $T \approx 10\,\mathrm{K}$, similar to the BN region in Orion, the simulated cube translates into a mass of $200\,\mathrm{M}_\odot$ and a size of $(0.32\,\mathrm{pc})^3$. The time unit converts to $t = 7.0 \times 10^4$ years. The mean Jeans mass for the homogeneous distribution is $M_\mathrm{J} = 0.9\,\mathrm{M}_\odot$.

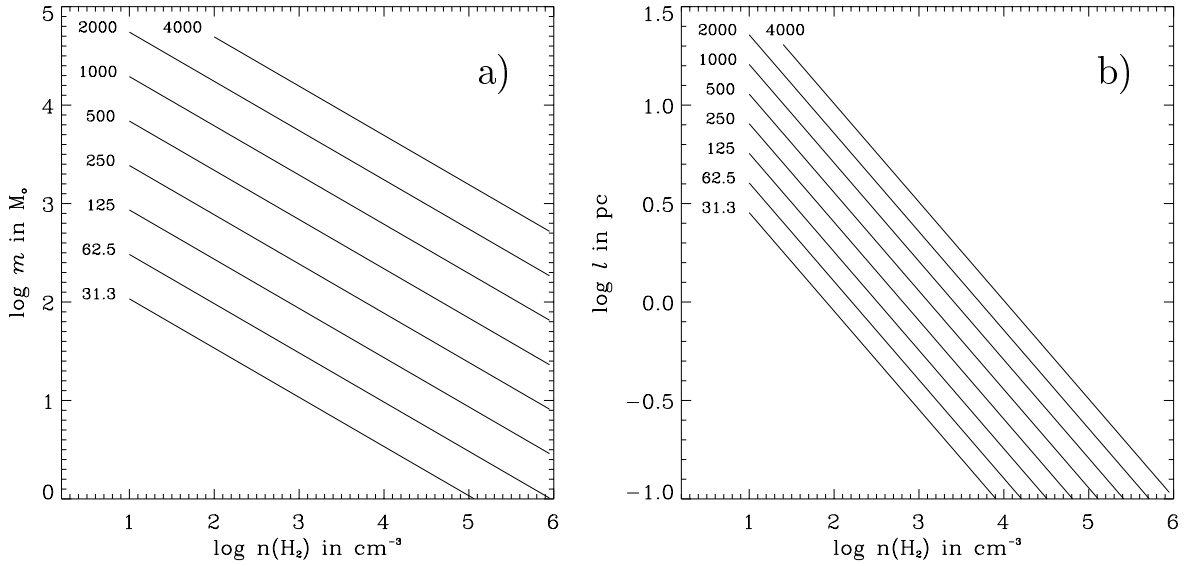

Figure 4.1: Plot of (a) the mass conversion factor m and (b) the physical length scale ℓ as function of average number density $n(H_2)$ in the molecular cloud region to study. The relations are given for different ratios ξ between the physical temperature T in Kelvin and the normalized temperature $\tilde{T}$ adopted for the simulation.

For generalization, Fig. 4.1 specifies the dependence of the physical mass and size of the simulated region on the adopted physical density. The different lines are for different values of the ratio between physical temperature in Kelvin and the dimensionless scaling parameter $\tilde{T}$: $\xi \equiv T(\mathrm{K})/\tilde{T}$. The above values for Taurus and Orion can be directly read off the figure for $\xi = 10/0.01 = 1000$.

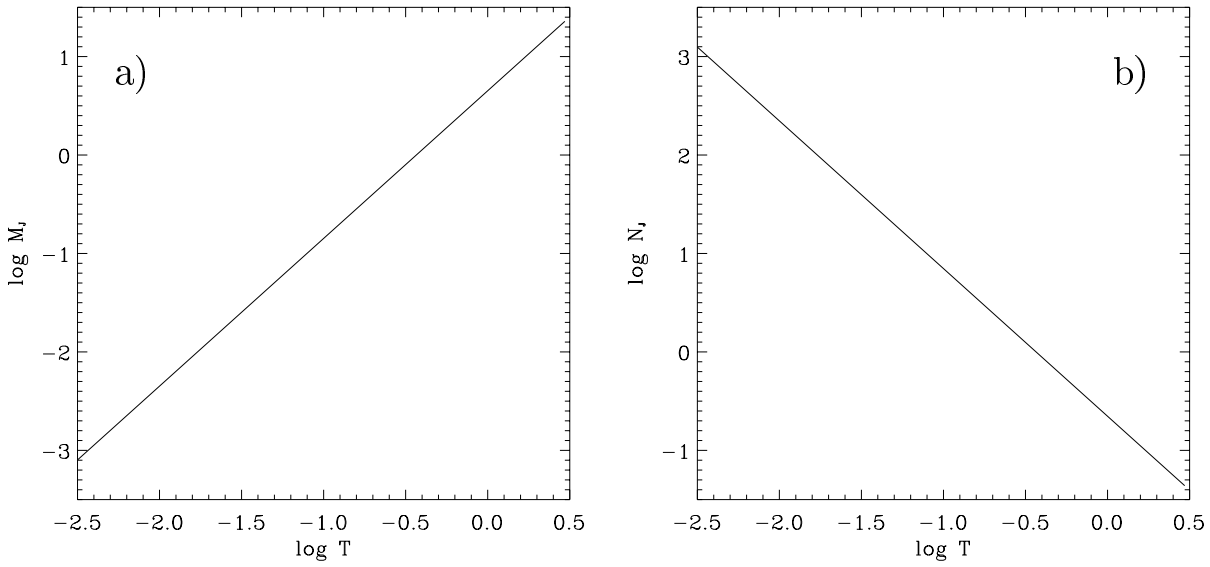

Figure 4.2: Plot of (a) the normalized Jeans mass $M_{\rm J}$ and of (b) the number of Jeans masses $N_{\rm J}$ contained in the simulated volume as function of the scale parameter $\tilde{T}$.

4.4 Jeans Mass and Sound Speed

The dynamical behavior of the system is determined by the scaling parameter $\tilde{T}$. This parameter determines the critical mass for gravitational collapse and can be interpreted in terms of the mean Jeans mass in the system. As derived in Sec. 3.2, the Jeans mass is a function of the temperature $\tilde{T}$ and of the density $\tilde{\rho}$. In normalized units, the mean density $\langle\tilde{\rho}\rangle = 1/8$. Hence, increasing the temperature $\tilde{T}$ implies a larger critical Jeans mass. Since the total mass of the system is defined as $\tilde{M} \equiv 1$, the *number* of Jeans masses modeled in the numerical simulation decreases. On the other hand, decreasing $\tilde{T}$ decreases the Jeans mass and $\tilde{M} = 1$ corresponds to a greater number of Jeans masses. Therefore, for a given density, varying $\tilde{T}$ is equivalent to zooming in or out of the molecular cloud region. A larger $\tilde{T}$ leads to smaller physical mass and size scale of the simulated cube. It acts as a magnifying glass, looking more closely into the evolving volume. Decreasing the scaling parameter $\tilde{T}$ means increasing the mass and volume of the modeled region.

This can be quantified, using Eqn. 3.18, which defines the critical mass for gravitational collapse to set in. The Jeans mass can be expressed in normalized units as

$$M_{\rm J} = 1.6 \cdot \tilde{\rho}^{-1/2}\, \tilde{T}^{3/2}\ . \tag{4.12}$$

With the average density being $\tilde{\rho} = 1/8$, the mean Jeans mass in the computation scales

with temperature $\tilde{T}$ as

$$M_{\rm J} = 4.5 \cdot \tilde{T}^{3/2} \; . \tag{4.13}$$

Figure 4.2 illustrates this relation graphically. On the right hand side, the number of Jeans masses $N_{\rm J}$ contained in the modeled volume is given. Since the total mass is normalized to one, it follows that $N_{\rm J} = 1/M_{\rm J}$. The smaller the scale parameter $\tilde{T}$, the more unstable the system will be against gravitational collapse and the more fragments will form during the dynamical evolution (see Chap. 7).

Again from using Eqn. 3.18, the physical Jeans mass can be expressed in terms of the number density $n(\mathrm{H_2})$ and the temperature T,

$$M_{\rm J} = 49.5\,{\rm M}_\odot \cdot \left(\frac{1}{\mu^2}\right) \cdot n(\mathrm{H_2})^{-1/2}\, T^{3/2} \; . \tag{4.14}$$

With $\mu = 2.36$ being the typical mean molecular weight in molecular clouds, this reads as

$$M_{\rm J} = 8.9\,{\rm M}_\odot \cdot n(\mathrm{H_2})^{-1/2}\, T^{3/2} \; . \tag{4.15}$$

The following table summarizes the critical Jeans mass for different molecular cloud regimes.

	$T = 5\,{\rm K}$	$T = 10\,{\rm K}$	$T = 20\,{\rm K}$	$T = 50\,{\rm K}$	$T = 100\,{\rm K}$
$n(\mathrm{H_2}) = 10\,{\rm cm^{-3}}$	$31.5\,{\rm M}_\odot$	$89.0\,{\rm M}_\odot$	$251.7\,{\rm M}_\odot$	$995.1\,{\rm M}_\odot$	$2814.4\,{\rm M}_\odot$
$n(\mathrm{H_2}) = 10^2\,{\rm cm^{-3}}$	$10.0\,{\rm M}_\odot$	$28.1\,{\rm M}_\odot$	$79.6\,{\rm M}_\odot$	$314.7\,{\rm M}_\odot$	$890.0\,{\rm M}_\odot$
$n(\mathrm{H_2}) = 10^3\,{\rm cm^{-3}}$	$3.1\,{\rm M}_\odot$	$8.9\,{\rm M}_\odot$	$25.2\,{\rm M}_\odot$	$99.5\,{\rm M}_\odot$	$281.4\,{\rm M}_\odot$
$n(\mathrm{H_2}) = 10^4\,{\rm cm^{-3}}$	$1.0\,{\rm M}_\odot$	$2.8\,{\rm M}_\odot$	$8.0\,{\rm M}_\odot$	$31.5\,{\rm M}_\odot$	$89.0\,{\rm M}_\odot$
$n(\mathrm{H_2}) = 10^5\,{\rm cm^{-3}}$	$0.3\,{\rm M}_\odot$	$0.9\,{\rm M}_\odot$	$2.5\,{\rm M}_\odot$	$10.0\,{\rm M}_\odot$	$28.1\,{\rm M}_\odot$
$n(\mathrm{H_2}) = 10^6\,{\rm cm^{-3}}$	$0.1\,{\rm M}_\odot$	$0.3\,{\rm M}_\odot$	$0.8\,{\rm M}_\odot$	$3.1\,{\rm M}_\odot$	$8.9\,{\rm M}_\odot$

Table 4.1: Table of Jeans masses for different physical regimes.

Like the number of Jeans masses $N_{\rm J}$ contained in a region, which determines the dynamical behavior of the system, also the sound speed is an important physical parameter. It determines the time scales on which sound waves can transverse the region. Together with the dynamical time scale it determines the speed at which the system evolves.

In normalized units, the isothermal sound speed is

$$c_{\rm s}^2 = \tilde{\mathcal{R}}\,\tilde{T} = \frac{\tilde{T}}{\gamma}\,. \tag{4.16}$$

For an ideal gas having three degrees of freedom, $\gamma = 3/2$ and the sound speed in normalized units scales as $c_{\rm s} = 0.82 \cdot \tilde{T}^{1/2}$. Since $c_{\rm s} \propto \tilde{T}^{1/2}$, even large variations in the temperature $\tilde{T}$ cause only minor changes in the sound speed. The sound speed in physical units also depends on the mean molecular weight, $c_{\rm s}^2 = \mathcal{R}\,T/\mu$. Using $\mu = 2.36$, Tab. 4.4 gives a list of sound speeds appropriate for molecular clouds.

T:	5 K	10 K	20 K	50 K	100 K	10^4 K
$c_{\rm s}$:	0.13 km s^{-1}	0.19 km s^{-1}	0.27 km s^{-1}	0.42 km s^{-1}	0.60 km s^{-1}	6.0 km s^{-1}

Table 4.2: Table of sound speeds appropriate for molecular clouds.

Chapter 5

Initial Conditions

This chapter introduces the initial conditions adopted for the numerical SPH simulations in this thesis. It describes their statistical properties, the method with which they are generated and its validity. One of the goals of this thesis work is to study the dependence of the dynamical evolution and the fragmentation process in molecular clouds given certain initial cloud properties and to examine how these influence the (proto)stellar cluster that subsequently forms. Therefore, the parameter range that is scanned has to conform with conditions in observed star forming regions. The dynamical evolution in the molecular cloud region is determined by the initial density and velocity distribution. In a self-consistent model, both are related via Poisson's equation (3.5). For the work presented here, we adopt random Gaussian fluctuations for the density field as starting condition for the SPH simulations. We use this approach, because these distributions have well determined statistical properties and can easily be generated by the Zel'dovich approach. Furthermore, their properties are well suited to mimic observed features of molecular clouds.

5.1 Gaussian Random Fields

A Gaussian random field $\rho(\boldsymbol{r})$ is completely characterized by its first two moments, its mean value $\rho_0 \equiv \langle \rho(\boldsymbol{r'}) \rangle_{\boldsymbol{r'}}$ and its standard deviation $S(\boldsymbol{r}) \equiv \langle \rho(\boldsymbol{r'}) \rho^*(\boldsymbol{r'} + \boldsymbol{r}) \rangle_{\boldsymbol{r'}}$, which is equivalent to the power spectrum $P(\boldsymbol{k})$ in Fourier space. All higher moments can be expressed in terms of the 2-point correlation function $S(\boldsymbol{r})$.

It is of advantage to describe the density field $\rho(\boldsymbol{r})$ as a Fourier expansion,

$$\rho(\boldsymbol{r}) = \mathrm{Re} \int \frac{d^3k}{(2\pi)^3} \hat{\rho}(\boldsymbol{k}) \mathrm{e}^{i\boldsymbol{k}\boldsymbol{r}} \,. \tag{5.1}$$

Here, $\hat{\rho}(\boldsymbol{k})$ is the Fourier transform of $\rho(\boldsymbol{r})$. The equivalence between the 2-point correlation function and the power spectrum follows as

$$\begin{aligned}
S(\boldsymbol{r}) &= \langle \rho(\boldsymbol{r'})\rho^*(\boldsymbol{r'}+\boldsymbol{r})\rangle_{\boldsymbol{r'}} \\
&= \int d^3r' \left(\int \frac{d^3k}{(2\pi)^3} \hat{\rho}(\boldsymbol{k}) \mathrm{e}^{i\boldsymbol{k}\boldsymbol{r'}} \right) \left(\int \frac{d^3k'}{(2\pi)^3} \hat{\rho}^*(\boldsymbol{k'}) \mathrm{e}^{-i\boldsymbol{k'}(\boldsymbol{r'}+\boldsymbol{r})} \right) \\
&= \int \frac{d^3k}{(2\pi)^3} \int \frac{d^3k'}{(2\pi)^3} \hat{\rho}(\boldsymbol{k}) \hat{\rho}^*(\boldsymbol{k'}) \int d^3r' \mathrm{e}^{i(\boldsymbol{k}-\boldsymbol{k'})\boldsymbol{r'}} \mathrm{e}^{-i\boldsymbol{k'}\boldsymbol{r}} \\
&= \int \frac{d^3k}{(2\pi)^3} \int \frac{d^3k'}{(2\pi)^3} \hat{\rho}(\boldsymbol{k}) \hat{\rho}^*(\boldsymbol{k'}) \delta(\boldsymbol{k}-\boldsymbol{k'}) \mathrm{e}^{-i\boldsymbol{k'}\boldsymbol{r}} \\
&= \int \frac{d^3k}{(2\pi)^3} |\hat{\rho}(\boldsymbol{k})|^2 \mathrm{e}^{-i\boldsymbol{k}\boldsymbol{r}} \\
&= \int \frac{d^3k}{(2\pi)^3} P(\boldsymbol{k}) \mathrm{e}^{-i\boldsymbol{k}\boldsymbol{r}}. \qquad (5.2)
\end{aligned}$$

Each function is the Fourier transform of the other. For an isotropic fluctuation spectrum $P(k) = P(|\boldsymbol{k}|)$, the 2-point correlation degrades to a function of the distance between two points, $S(r)$. By defining a normalization ρ_0 and power spectrum $P(k)$ in Fourier space, all statistical properties of the field $\rho(\boldsymbol{r})$ are determined.

The values $P(k)$ specify the contribution of waves with wave number k to the statistical fluctuation spectrum. In Gaussian random fields, the phases are arbitrarily chosen from a *uniform* distribution in the interval $[0, 2\pi[$, and the amplitudes for each mode k are randomly drawn from a *Gaussian* distribution with width $P(k)$ centered on zero. Since waves are generated from random processes, only the properties of an *ensemble* of fluctuation fields are determined in a statistical sense. Individual realizations may deviate considerably from this mean value, especially at small wave numbers k, i.e. at long wave lengths, where only a few modes (k_x, k_y, k_z) contribute to a wave number $k = |\boldsymbol{k}|$.

In this thesis, we consider a simple power-law functional form for the fluctuation spectrum, $P(k) \propto k^N$, with $-3 \leq N \leq 0$. For negative N, most power is in large-scale modes. With decreasing N the fluctuation fields becomes increasingly patchy and inhomogeneous. Figure 5.1 compares four different Gaussian random fields with (a) $N = 0$, (b) $N = -1$, (c) $N = -2$ and (d) $N = -3$. The shown images are projections of the 3-dimensional particle distribution into the xy-plane. The increasing degree on inhomogeneity is clearly visible in the sequence.

In Fig. 5.2, (a) the 2-point correlation function $S(r)$ and (b) the power spectrum $P(k)$ for the fields described before are plotted. The dotted function in both plots denotes the

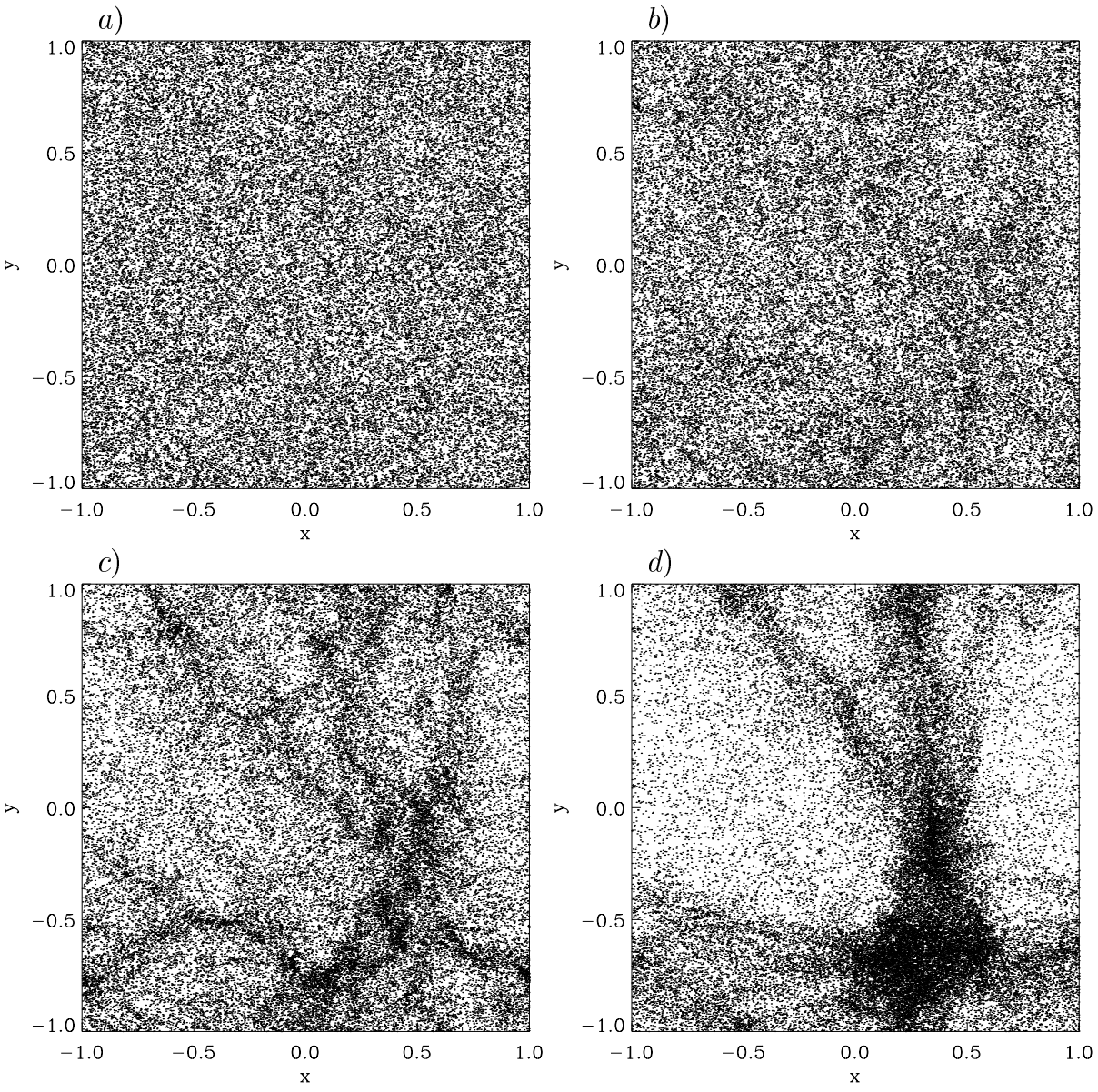

Figure 5.1: Sequence of Gaussian random fields with power spectra $P(k) \propto k^N$ with (a) $N = 0$, (b) $N = -1$, (c) $N = -2$ and (d) $N = -3$. Each distribution consists of 50 000 particles and is projected into the xy-plane. It is created using the Zel'dovich approximation (see Sec. 5.2) with a time interval $t = 2$.

random homogeneous starting distribution; the error bars are given to illustrate the statistical uncertainties for different distances r and wave numbers k. The errors bars apply to all fields in the same way. For the homogeneous field, the two functions are essentially flat. All graphs are normalized such that $S(r) \approx 1$ and $P(k) \approx 1$ for the homogeneous distribution. Comparing the correlation functions $S(r)$ of the different fluctuation fields

shows that with decreasing N the correlation strength and scale grows. Furthermore, it reproduces the power spectra $P(k)$ that have been used to generate the fields initially. Note, that for large wave numbers, the spectra become flat. With particle numbers of 50 000, the typical interparticle distance becomes larger than the wave lengths of modes with $k \gtrsim 30$. For these wave numbers one basically measures white noise, which results in a flat spectrum.

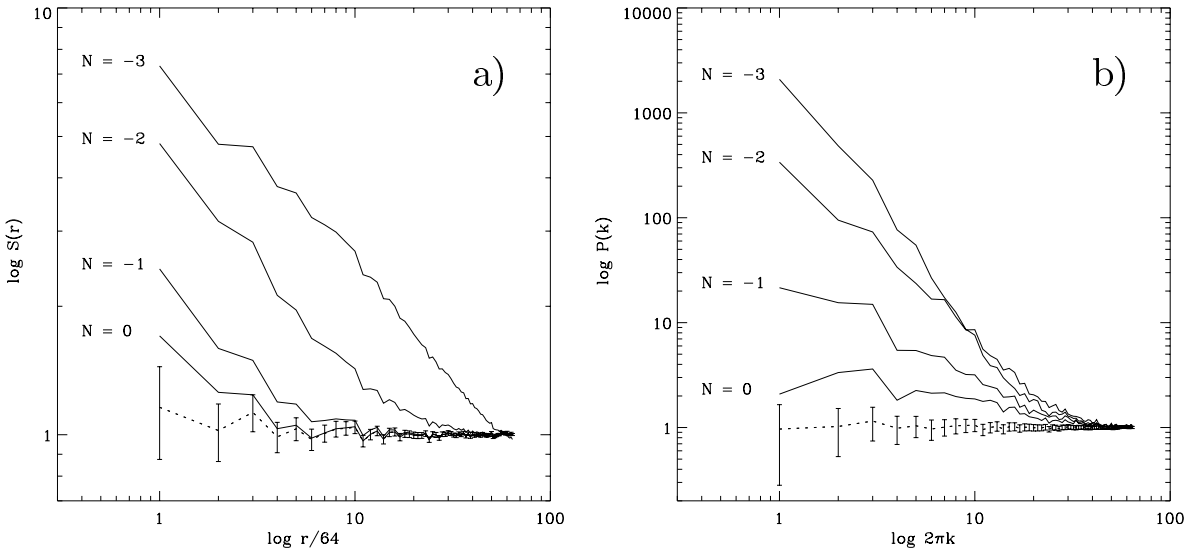

Figure 5.2: (a) 2-point correlation function $S(r)$ and (b) power spectrum $P(k)$ of the density fields discussed before. To compute the functions, the cube has been subdivided into $(128)^3$ cells. The random homogeneous starting distribution is plotted with dotted lines. The statistical errors for different distances r and wave numbers k apply to all fields equally. All other fields are characterized by the index N of the power spectrum they are generated from.

The next figure 5.3 shows the probability distribution functions (pdf) for the four density fields introduced in the previous figure. As reference, the density histogram for a random homogeneous field is denoted by the dotted curve. It is a narrow Gaussian that peaks at the mean density (dashed vertical line). This distribution is starting condition for the Zel'dovich shift (see Sec. 5.2). As expected from looking at Fig. 5.1, the density distribution gets broader with decreasing power-law index N and the deviations from the (Gaussian) starting distribution become more extreme. In the non-linear regime, i.e. for density contrasts $\delta\rho \gtrsim 1$, the structure is dominated by dense peaks and large voids. Complementary to specifying density histograms (pdf's) is plotting the spatial distribution of densities. In the SPH formalism, each particle carries a density which is derived via the averaging process over all neighboring particles within one smoothing radius (see Sec. 3.3), and intimately reflects the spatial structure of the particle distribution. Fig. 5.4, which plots the density of each particle in the previously discussed distributions as function of

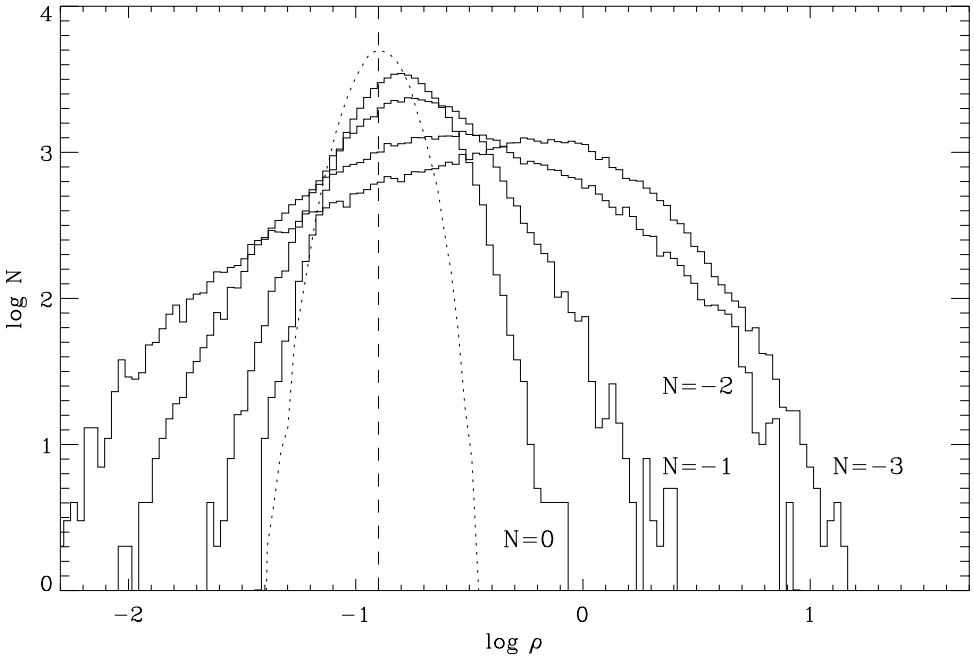

Figure 5.3: Probability distribution function (pdf) for the four density fields in Fig. 5.1. The dotted line denotes the random homogeneous field that is the starting distribution for the Zel'dovich shifts. Its density distribution is a Gaussian and peaks at a value of 1/8 which is the average density in the homogeneous cube (dashed vertical line). In the non-linear regime considerable deviations from the (Gaussian) initial pdf occur.

its location along the x-axis, describes the distribution and shapes of high density peaks more clearly than Fig. 5.1. Furthermore, the density contrasts $\delta\rho = (\rho - \rho_0)/\rho_0$ resulting from the Zel'dovich shifts can be directly measured from the plot. As reference, the initial mean density is indicated by the straight line at $\rho = 1/8$. The density contrasts range from $\delta\rho \lesssim 5$ for $N = 0$ to $\delta\rho \lesssim 100$ for $N = -3$.

5.2 The Zel'dovich Approximation

In 1970, Zel'dovich proposed for cosmological simulations a method to extrapolate the linear theory into the non-linear regime. For a idealized, self-gravitating and pressure-free continuous medium, the dynamics can be expressed in terms of a function $f(\boldsymbol{r}_0, t)$. Its value is the position $\boldsymbol{r}$ of a fluid element at time t, whose original position was $\boldsymbol{r}_0$ at $t = 0$: $\boldsymbol{r}(t) = \boldsymbol{f}(\boldsymbol{r}_0, t)$. If the original density field was $\rho(\boldsymbol{r}_0)$, then the density field at t is given

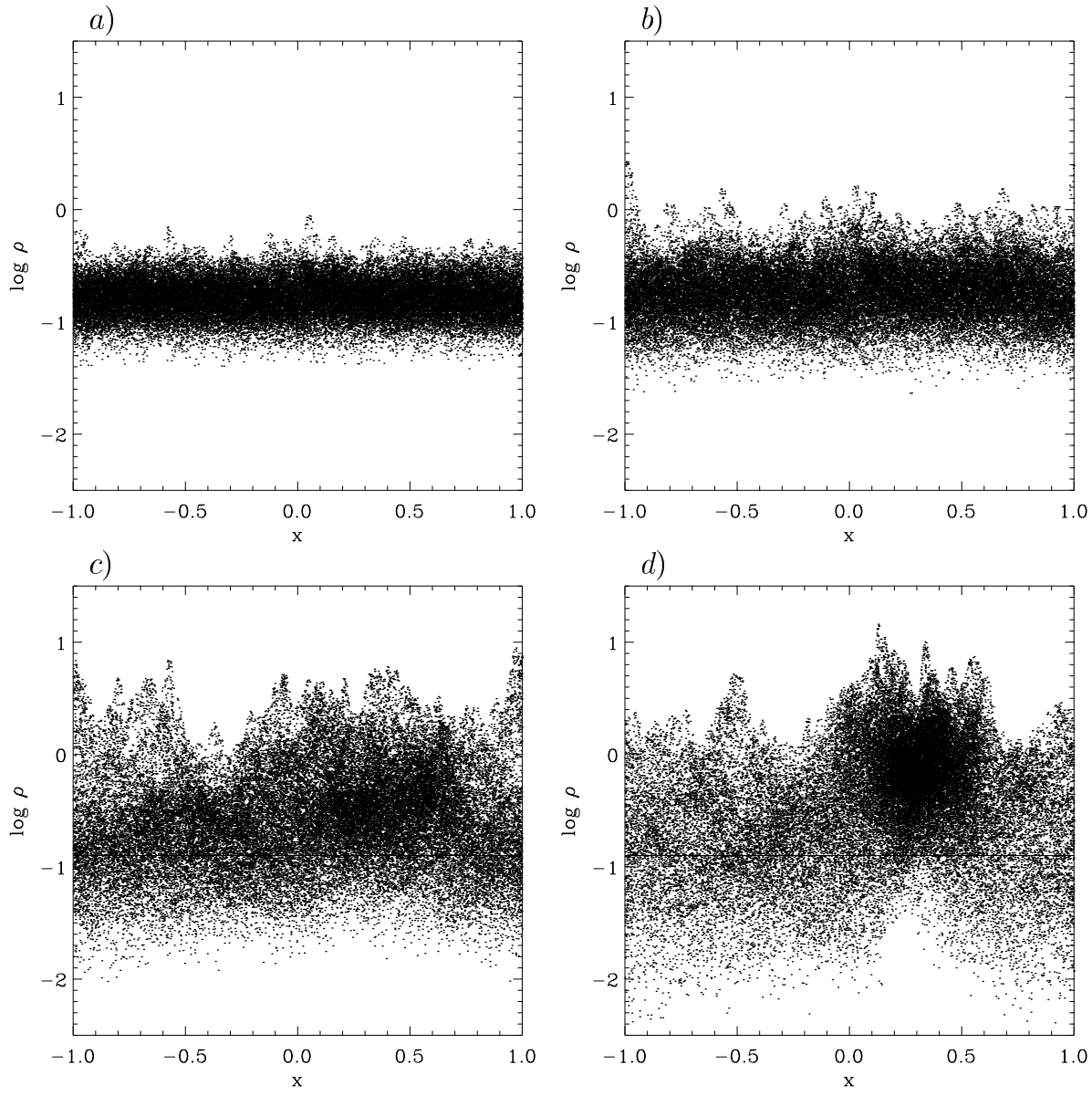

Figure 5.4: Density ρ of each particle as function of its location along the x-axis. (a) – (d) denote the particle distributions described before. The figure illustrates the density contrast $\delta\rho = (\rho - \rho_0)/\rho_0$ for each particle. As orientation, the average density previous to the Zel'dovich shift, $\rho_0 = 1/8$, is plotted by a straight line.

by

$$\rho(\boldsymbol{r}, t) = \frac{\rho(\boldsymbol{r}_0)}{|\det f_{i,j}[\boldsymbol{r}_0(\boldsymbol{r}, t)]|} \; . \tag{5.3}$$

Here, $f_{i,j}$ denotes the partial derivative of the i-th component of $\boldsymbol{f}$ in r_j. The time evolution of $f(\boldsymbol{r}_0, t)$ is given by the Poisson equation (3.5). The linearized equation then follows as

$$\boldsymbol{r}(t) = f(\boldsymbol{r}_0, t) = \boldsymbol{r}_0 + \boldsymbol{v}(\boldsymbol{r}_0)\, t \;, \tag{5.4}$$

with $\nabla_{r_o} \cdot \boldsymbol{v}(\boldsymbol{r}_0) \propto \rho(\boldsymbol{r}_0)$. This assumes that the velocity field is rotation-free, because then the existence of a potential $\phi(\boldsymbol{r}_0)$ with $\boldsymbol{v}(\boldsymbol{r}_0) \equiv \nabla_{r_0}\phi(\boldsymbol{r}_0)$ is guaranteed and is connected to the density field via $\Delta_{r_o}\phi(\boldsymbol{r}_0) \propto \rho(\boldsymbol{r}_0)$.

Zel'dovich (1970) suggested to use this method to extrapolate the field into the non-linear regime, i.e. into regions where the density contrast exceeds one. It is not clear, in how far this is mathematically and physically appropriate. For $|\det f_{i,j}|$ being very small or zero, the inclusion of pressure forces becomes important and prevents infinite densities. If trajectories along which $|\det f_{i,j}|$ vanishes are followed, the density decreases again. At the same time the solution is no longer unique. However, for practical purposes the appropriate choice of the shift time t can minimize these problems and the Zel'dovich (1970) approximation is valid, as will be shown in the next section. The method is well suited for advancing the system in one large time interval without solving the complete set of equations and computing the time evolution of individual particles by integrating over many small time steps.

When computing random Gaussian fields, the method is applied as follows: One chooses a power spectrum $P(k)$ and computes a *hypothetical* density field by determining the phases and amplitudes of all contributing modes in Fourier space (according to Sec. 5.1). This field is transformed back into real space and Poisson's equation (3.5) is solved in order to obtain the velocities which would generate the density field self-consistently. Starting from a homogeneous initial distribution, this velocity field is used to advance the particles in the system in one single large time step. As illustration, Fig. 5.5 plots the 2-dimensional projection of a homogeneous starting condition (a) and of the system after the Zel'dovich shift has been applied for various shift intervals t (b – h). Note that the method assumes periodic boundary conditions. Therefore, the images have to be seen periodically replicated in all directions.

5.3 Validity of the Zel'dovich Approach

In this section, the validity of the Zel'dovich approximation and its parameter dependence is discussed. This is done by comparing the state of systems which have been generated using the Zel'dovich method with different sets of parameters t and N. Furthermore,

these distributions are compared with systems that have been advanced in time using the full SPH formalism.

First, the influence of the shift interval t in the Zel'dovich approximation shall be examined. As discussed in the previous section, each particle is advanced in one large time step via Eqn. 5.4. If particles move along trajectories on which $|\det f_{i,j}|$ vanishes, the solution is no longer unique, i.e. different paths may lead to the same location. For converging flows, the density increases before reaching the singularity in $|\det f_{i,j}|$ and decreases afterwards, particles have 'interpenetrated'. This is unphysical. Depending on the size and the strength of individual fluctuations, the time interval t to reach this point may differ. Assuming comparable amplitudes, for small perturbations t will be short and for large-scale modes t will be longer. This has to be taken into account when determining the optimum choice of the shift interval t. The effect of varying t is addressed in Fig. 5.5 which shows a sequence of particle distributions generated by the Zel'dovich method from a power spectrum $P(k) \propto k^{-2}$ with $0 \leq t \leq 30$. The homogeneous starting field is identical to a shift of $t = 0$. With increasing t the density contrast starts to grow and the distribution becomes more structured. However, at $t \approx 3$ the small-scale fluctuations begin to disperse and the density contrast starts to diminish. At $t \approx 30$ the system appears homogeneous again. The same is true for different slopes N of the power spectrum. Figure 5.5i illustrates the dependence of the average (open circles) and maximum (solid circles) particle density on the time shift t graphically. The dashed line denotes the average density of the homogeneous cube.

Figure 5.6 describes the influence of different shift intervals t on (a) the 2-point correlation function $S(r)$ and on (b) the measured power spectrum $P(k)$. In analogy to the above, the correlation strength and length increase with shift interval t for systems generated with $t \lesssim 3$ and decrease again for larger shifts. Similar conclusions apply to the power spectrum. For $t \gtrsim 2$ the initial slope of $N = -2$ is best reproduced. Shorter shifts t do not establish the mode spectrum sufficiently, the spectrum is too flat. Longer intervals produce overshooting on small scales, i.e. perturbations with short wave lengths are smeared out, whereas large modes are still amplified. Therefore the spectrum gets steeper. For $t > 10$, overshooting occurs for the largest modes as well and the entire power spectrum flattens again.

Finally, we compare systems which have been generated by the Zel'dovich method with systems that have been advanced in time entirely with SPH. The Zel'dovich shift generates fluctuations on all scales, since only gravitational forces are considered. Large perturbations are Jeans unstable and start to collapse. Most small ones are Jeans stable and pressure forces smear them out in the subsequent evolution with the SPH method. However, also some low-mass fluctuations may have been generated with sufficiently high density to be gravitationally unstable, since the Jeans mass is inversely proportional to

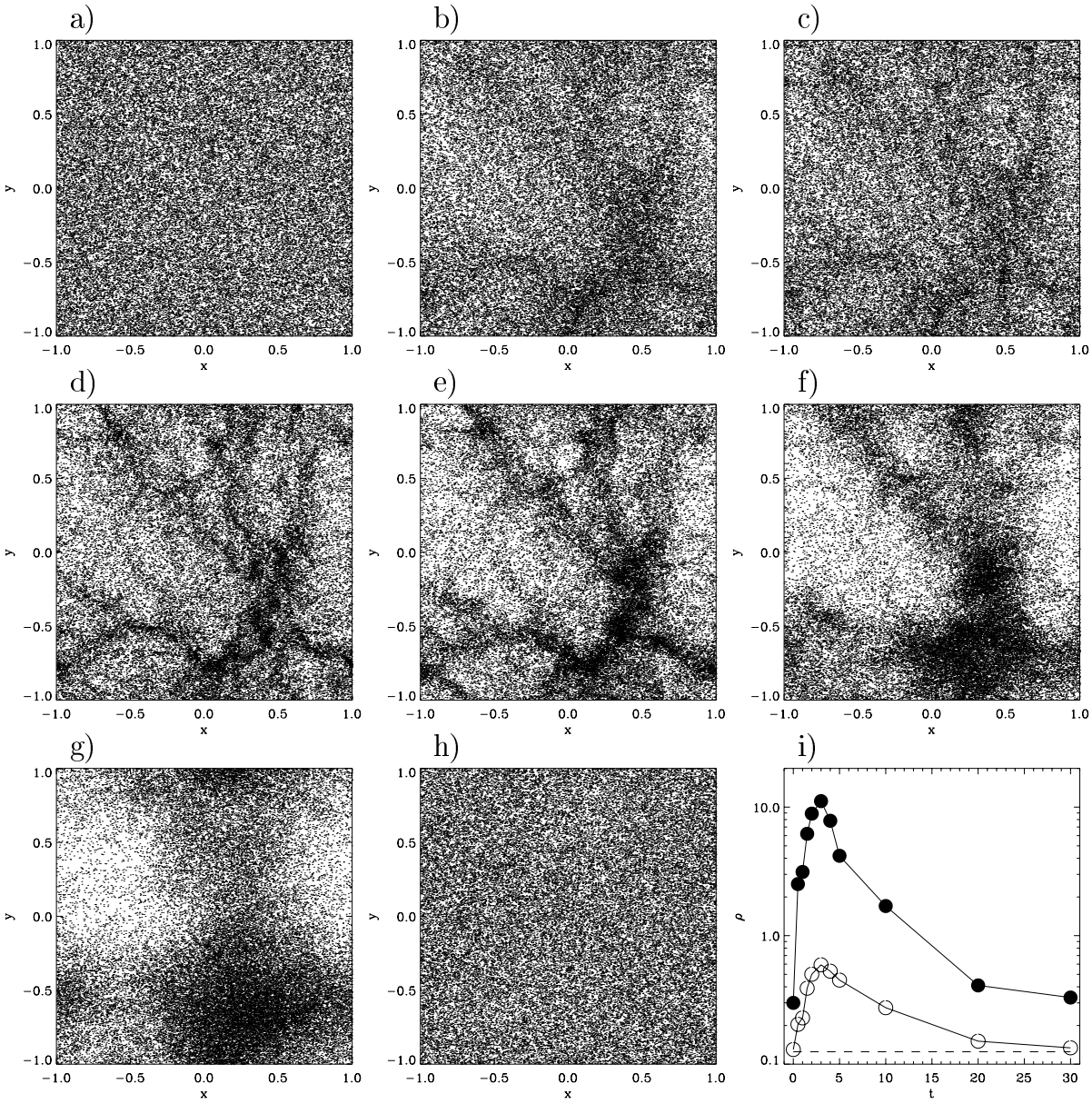

Figure 5.5: Projections of the particle distribution generated by the Zel'dovich method from a power spectrum $P(k) \propto k^{-2}$. (a) Homogeneous starting distribution. The distribution after applying the Zel'dovich method with (b) $t = 1/2$, (c) $t = 1$, (d) $t = 2$, (e) $t = 3$, (f) $t = 5$, (g) $t = 10$, and (h) $t = 30$. (i) The dependence of the average and maximum particle density on the time shift t is plotted in open and filled circles, respectively. The dashed line denotes the average density of the homogeneous cube.

the square root of the density, $M_{\rm J} \propto \rho^{-1/2}$. These clumps will collapse as well. Furthermore, while flowing towards a common center of gravity small clumps may merge to form more massive clumps, which again may exceed the Jeans limit. The probability for that to happen depends on the time scale for the collapse and dispersal of individual clumps

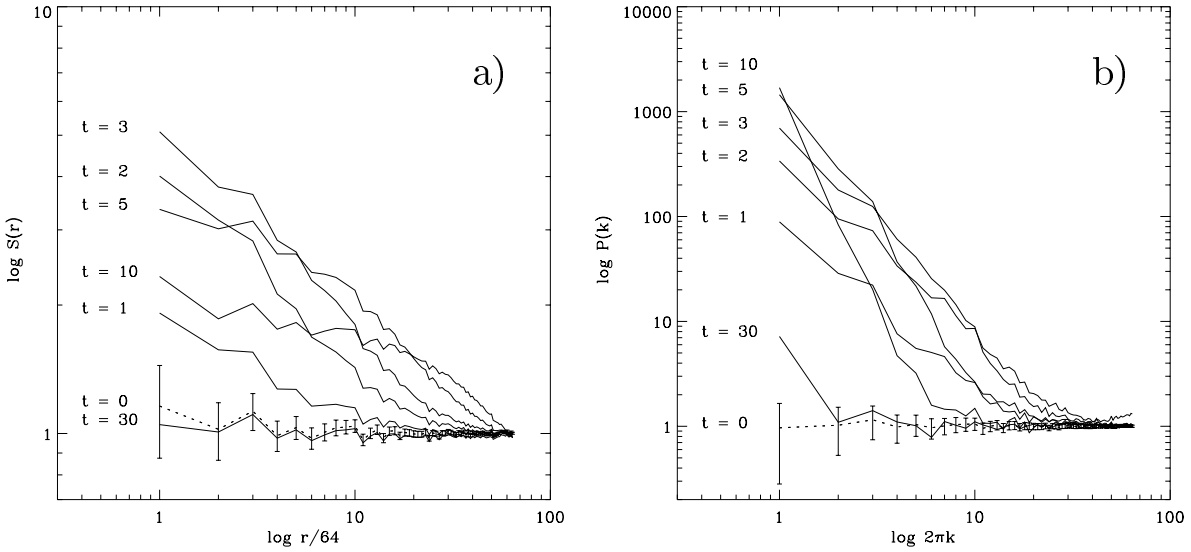

Figure 5.6: (a) 2-point correlation function $S(r)$ and (b) power spectrum $P(k)$ for different shift intervals t, analogous to Fig. 5.2.

relative to the time scale for clumps to merge or fragment. The dynamical evolution of the entire system is extremely complex and can only be determined in a statistical sense.

If we advance the system from the homogeneous state with the full SPH formalism, we compute the self-consistent velocity field for a hypothetical fluctuation field, as for the Zel'dovich method, but use the velocities as input for the SPH simulation instead of doing one Zel'dovich shift. Pressure forces are included from the beginning and small perturbations have no possibility to grow unless their mass exceeds the Jeans limit of the homogeneous system, which is determined by the mean density. Therefore, only high mass clumps can form. This is different from the Zel'dovich case, where perturbations are created on all scales and also some low-mass clumps may have large enough densities such that their local Jeans mass is smaller than the clump mass. Therefore, slightly smaller and more fragments are expected in systems that have been generated using the Zel'dovich method. The detailed discrimination of two systems subtly depends on the desired inhomogeneity and density contrast in the system, i.e. on the choice of N and t. These small-scale differences decrease, the more homogeneous the distribution and the smaller the Zel'dovich shift is chosen. On large scales, the statistical properties are not affected regardless of the choice of N and t.

This is exemplified, using a distribution of 50 000 particles with a power spectrum $P(k) \propto k^{-2}$. The temperature is $T = 0.01$ and hence the simulation cube contains roughly 222 Jeans masses computed from the average density of the homogeneous starting condition (see Sec. 4.4). Figure 5.7 shows snapshots of the time evolution of the system initially generated applying a Zel'dovich shift with $t = 2$ and subsequently advanced with SPH. On

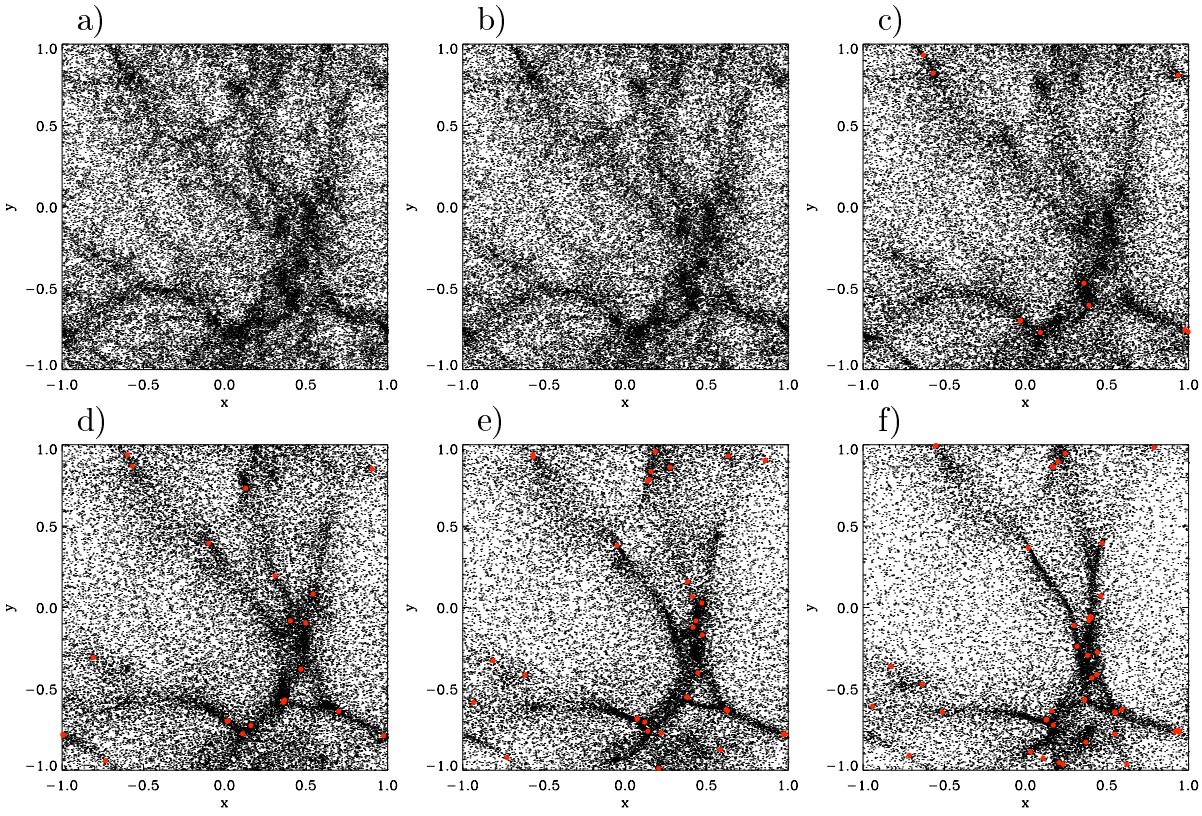

Figure 5.7: Snapshots of the evolution of a system generated by the Zel'dovich method from a power spectrum $P(k) \propto k^{-2}$ and shift interval $t = 2$. After applying the Zel'dovich shift, the subsequent evolution is calculated using SPH. The figures show projections of the 3-dimensional distribution into the xy-plane in intervals of $\Delta t = 0.3$: (a) initially at $t = 0.0$, (b) at $t = 0.3$, (c) at $t = 0.6$, (d) at $t = 0.9$, (e) at $t = 1.2$, and (f) at $t = 1.5$. Time is measured from the begin of the SPH simulation.

the other hand, Fig. 5.8 describes the evolution of the system that was evolved from the homogeneous state using SPH without applying the Zel'dovich method. Confirming the above considerations, the large-scale behavior of the two systems is very similar, whereas differences on small scales occur. The distribution initially evolved with the Zel'dovich approximation is patchier at comparable times[1]. However, with the progression of the SPH calculation the higher degree of irregularity is reduced. Small perturbations are smoothed by pressure.

In summary, the Zel'dovich approximation is very well suited to generate fluctuation fields with well defined statistical properties determined by the power spectrum $P(k)$. With the appropriate choice of the shift interval t, every spectrum can be generated.

[1]Note, that time is measured from the begin of the evolution with SPH. To compare both systems at equal times, the Zel'dovich shift interval $t = 2$ has to be added to the numbers in Fig. 5.7.

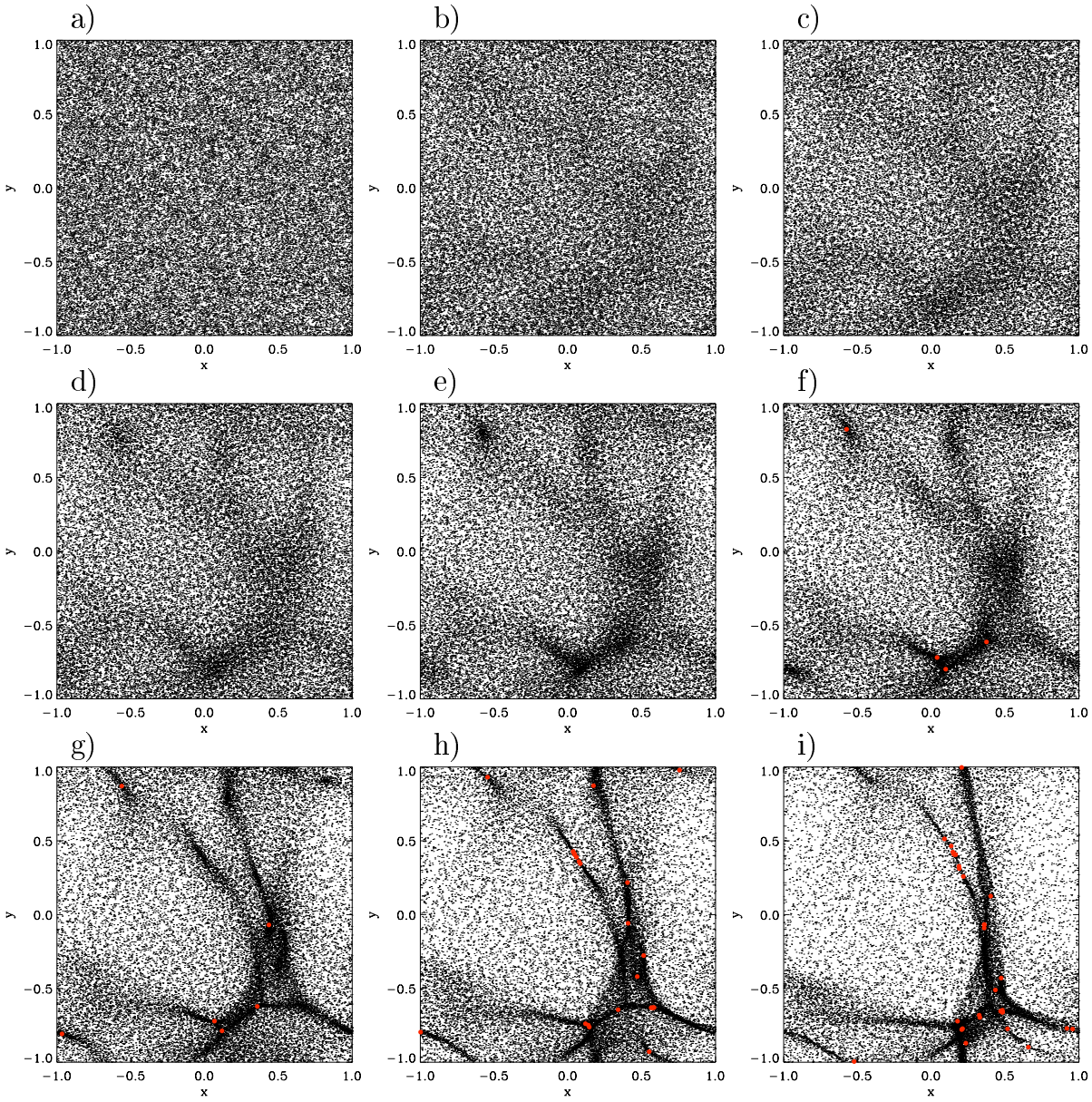

Figure 5.8: Analogous to Fig. 5.7, but describing a system that is entirely evolved in time using SPH. No Zel'dovich shift is applied. The system is projected into the xy-plane at (a) $t = 0.0$, showing the homogeneous starting condition, at (b) $t = 1.0$, (c) $t = 1.7$, (d)$t = 2.0$, (e) $t = 2.3$, (f) at $t = 2.6$, (g) at $t = 2.9$, (h) at $t = 3.2$, and (i) at $t = 3.5$. Again, time is measured from the begin of the SPH simulation.

When applying the Zel'dovich method to gaseous systems, one has to take the effect of neglecting pressure forces into account. On small scales, deviations from the fully self-consistent time evolution may occur which can influence the detailed dynamical behavior of the system. These deviations cannot be described in the context of Gaussian random fields; they cannot be accounted for in this simple statistical theory. However, for the

purpose of this thesis we want to follow the evolution of density fields that have well defined and reproducable statistical properties, therefore applying the Zel'dovich method is fully appropriate.

Chapter 6

A Case Study: $T = 0.01$ and $P(k) \propto 1/k^2$

This chapter discusses in detail the time evolution of *one* particular set of models, thereby introducing the statistical tools used to analyze all simulations. It concentrates on computations with a dimensionless temperature $T = 0.01$ and an initial fluctuation spectrum of $P(k) \propto 1/k^2$. We present results from nine different statistical realizations of that initial conditions, using different particle numbers to address the issue of numerical resolution: six models with 50 000 SPH particles, two with 200 000 and one with 500 000 particles, respectively. Their properties are summarized in Tab. 6.1. The results and conclusions derived for these calculations will be compared in Chap. 7 with models which have deviating initial conditions.

The quantities derived and analyzed in the current chapter include, the clumping properties of the gas at various stages of its dynamical evolution, the kinematical and spatial properties of the protostellar cluster that forms as the system advances in time and the mass spectrum of protostellar cores. We discusse the boundedness of the cluster and the rotational properties of protostellar cores. Finally we speculate about the implications of our results for understanding the IMF. We compare the numerically calculated core mass spectrum with the IMF for multiple stellar systems and derive constraints for the overall star-formation efficiency.

6.1 Model Properties and Initial Conditions

The nine models discussed in this chapter have a temperature $T = 0.01$ and are generated from a power law $P(k) \propto 1/k^2$ using the Zel'dovich approximation (see Sec. 5). The

Table 6.1: The models described in this chapter: $T = 0.01$ and $P(k) \propto 1/k^2$.

Temperature	Exponent[a]	Particles	Initial[b]	Zel'dovich[c]	Identification
$T = 0.01$	$N = 2$	50000	random	$\delta t = 2.0$	T01N2-A
$T = 0.01$	$N = 2$	50000	random	$\delta t = 2.0$	T01N2-B
$T = 0.01$	$N = 2$	50000	random	$\delta t = 2.0$	T01N2-C
$T = 0.01$	$N = 2$	50000	random	$\delta t = 2.0$	T01N2-D
$T = 0.01$	$N = 2$	50000	random	$\delta t = 1.0$	T01N2-E
$T = 0.01$	$N = 2$	50000	grid	$\delta t = 2.0$	T01N2-F
$T = 0.01$	$N = 2$	200000	random	$\delta t = 2.0$	T01N2-G
$T = 0.01$	$N = 2$	200000	random	$\delta t = 1.5$	T01N2-H
$T = 0.01$	$N = 2$	500000	random	$\delta t = 1.5$	T01N2-I

[a]Exponent of the power law, $P(k) \propto 1/k^N$. [b]Initial distribution for the Zel'dovich shift. A homogeneous random distribution is denoted by 'random', whereas 'grid' means that the particles have initially been placed on a regular grid. [c]Shift interval δt for the Zel'dovich approach.

projection into the xy-plane of the initial particle distribution in each model at the start of the dynamical evolution with SPH is presented in Fig. 6.1.

The global statistical properties of all nine models are identical, all reproduce the implied power law $P(k) \propto 1/k^2$. However, each realization is different since varying sets of random numbers are used to generate the fluctuation spectrum. This variance is more important on large scales (or equivalently at small wave numbers k) since only few modes contribute to the power spectrum. Statistical deviations of individual modes more strongly influence the average values. The visual appearance of each particle distribution is therefore dominated by the effect of statistical variance on large-scales; every initial density field looks different.

All but one model assume a random uniform particle distribution before applying the Zel'dovich shift. Placing particles randomly into a given volume produces an overall distribution that is homogeneous on large scales, but is subject to statistical fluctuations on small scales which introduce white noise into the correlation function. The scale at which this effect becomes important is of the order of the mean interparticle distance. These undesired small-scale fluctuations may influence the fragmentation behavior of the gas. However, with the adopted temperature, the mass of small-scale regions of enhanced density is much less than the local Jeans mass. Therefore, these fluctuations are quickly damped and dynamically unimportant. As alternative to the random distribution, in model T01N2-F particles are placed on a regular grid before applying the Zel'dovich approximation. This distribution is force-free and has exactly uniform density. On the

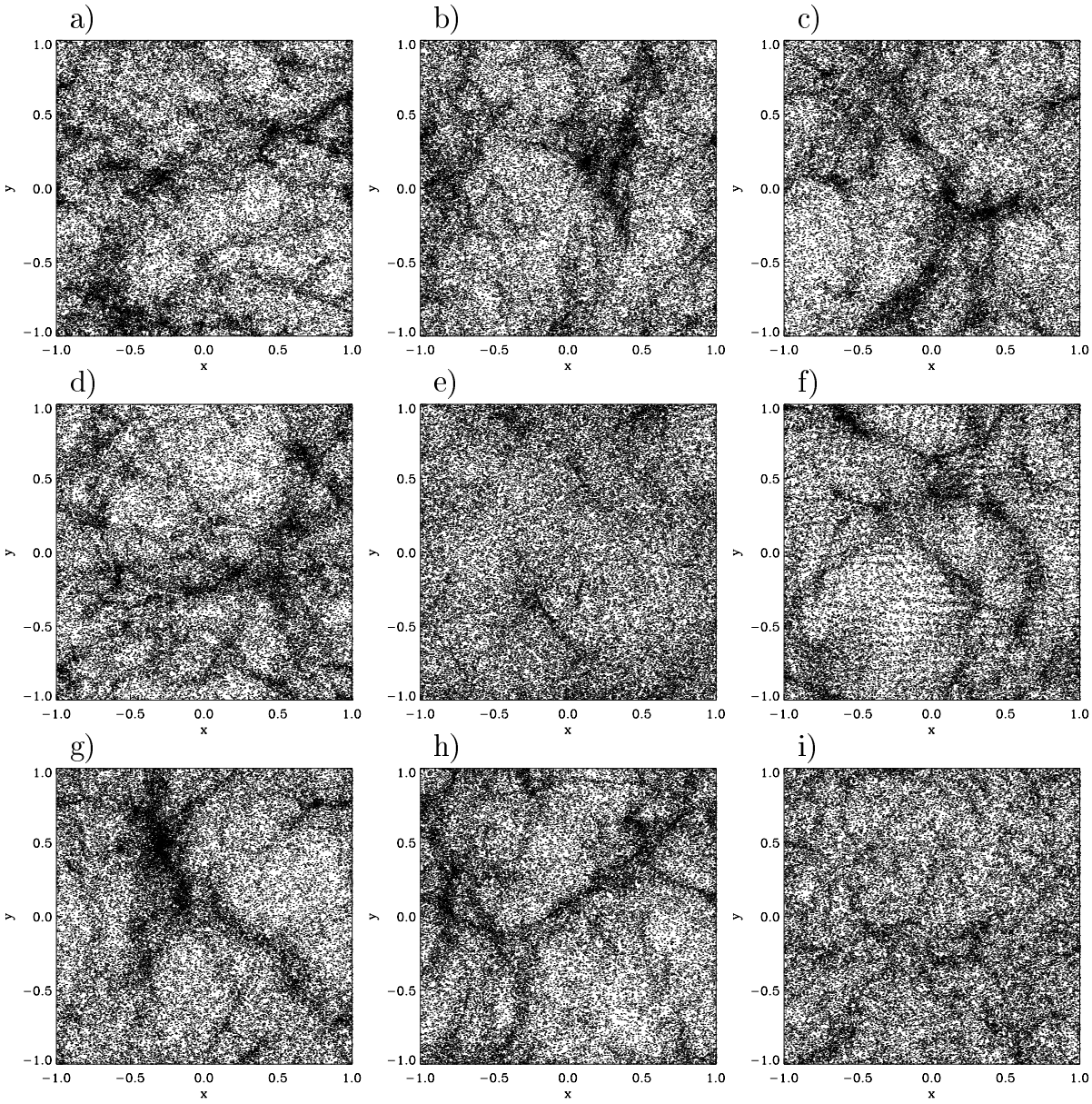

Figure 6.1: Initial particle distribution for the nine SPH simulations with $T = 0.01$ and $P(k) \propto 1/k^2$ projected into the xy-plane. The six models with 50 000 particles: a) T01N2-A, b) T01N2-B, c) T01N2-C, d) T01N2-D, e) T01N2-E, f) T01N2-F. Models with 200 000 particles: g) T01N2-G, h) T01N2-H. The high-resolution model with 500 000 particles: i) T01N2-I. Every figure contains 50 000 particles. In case of a larger total number, the plotted particles are selected randomly. Model T01N2-F (f) is generated from particles placed on a grid, which is still visible in the figure. All other ones use random uniform particle distributions. The Zel'dovich shift applied to generate model T01N2-E is $\delta t = 1.0$, the shift for models T01N2-H and T01N2-I is $\delta t = 1.5$. Otherwise, $\delta t = 2.0$ is used. Therefore these distributions exhibit more structure and larger density contrasts. For a summary see Tab. 6.1.

other hand, the grid has preferred axes which introduce anisotropies in the neighbor list of each particle. This fact may again influence the small-scale behavior. On larger scales, the system is increasingly isotropic and this effect becomes negligible. In the hydrodynamical evolution phase, after the Zel'dovich shift, traces of the grid are quickly erased. Comparing the dynamical evolution, the model with the particles placed on a grid is statistically indistinguishable from the models generated from a random distribution, which we use as standard.

As discussed in Sec. 5, the Zel'dovich shift interval δt determines the density contrast in the particle distribution. Typically, larger δt leads to higher peak densities, which may influence the fragmentation behavior of the system. On the other hand, smaller δt implies that a larger fraction of the total time evolution of the gas has to be computed with the SPH method and pressure forces, which are not included in the Zel'dovich approximation, have more time to act on the gas. In general, δt should be chosen small enough so that the subsequent evolution is not dependent on the choice of δt which is indeed the case for $\delta t \lesssim 2.0$ as is shown in Sec. 5.3. To address this issue again and to examine how a variation of the Zel'dovich shift interval influences the properties of the protostellar cluster that forms during the dynamical evolution and collapse of the gas, two models are generated with smaller shift intervals δt: model T01N2-E with $\delta t = 1.0$, and model T01N2-H together with the high-resolution model T01N2-I having $\delta t = 1.5$. Within the statistical variance between different models, this effect is negligible.

Most simulations introduced in this chapter use 50 000 SPH particles. To address the issue of numerical resolution and how the particle number in the simulation effects the dynamical evolution and fragmentation of the gas, we performed computations with four times (T01N2-G and T01N2-H) and ten times more particles (model T01N2-I). As long as the minimum Jeans mass in the system is larger than about hundred particle masses (see Sec. 3.4.5) the dynamical behavior of the system is well resolved and the results do not depend on the particle number.

6.2 Time Evolution

This section discusses the time evolution of the simulations with $T = 0.01$ and a power-law index $N = 2$. As discussed in Chap. 4, a dimensionless temperature $T = 0.01$ corresponds to 222 Jeans masses in the computed volume. This number determines the dynamical behavior of the system. The gravitational energy outweighs the internal energy by far and the system is highly unstable to gravitational collapse and fragmentation. As a result, typically about sixty collapsed cores form during the dynamical evolution. The complete time evolution is illustrated in Fig. 6.2. Representative for all nine models with $T = 0.01$ and $N = 2$, it shows snapshots of the model T01N2-A at twelve different stages of its

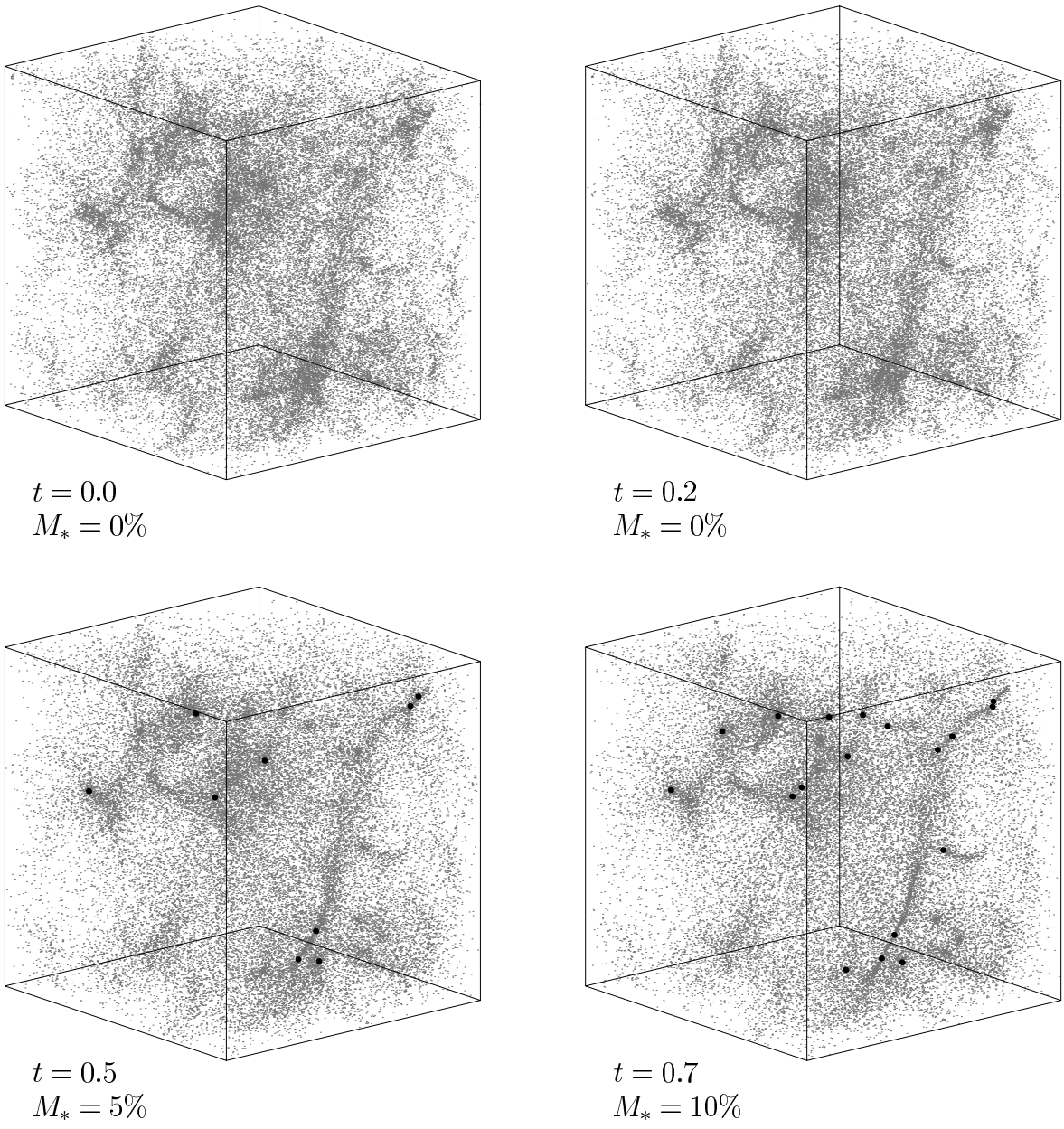

Figure 6.2: Snapshots of the model T01N2-A at $t = 0.0$ (initial condition at the start of the SPH simulation), at $t = 0.2$, at $t = 0.5$ and at $t = 0.7$. During the dynamical evolution, small-scale fluctuations are damped, whereas Jeans unstable clumps start to collapse. At $t = 0.5$, the first compact cores ('sink particles' in terms of the SPH code) have formed in the centers of the densest clumps and have accreted 5% of the total gas mass. At $t = 0.7$ the protostellar cores altogether gained 10% of the available mass. Gas particles are plotted by small dots and collapsed cores are denoted by thick dots. Note that the figures do not give information about the smoothing volume of individual particles. Its size is such that it contains typically 50 neighbor particles.

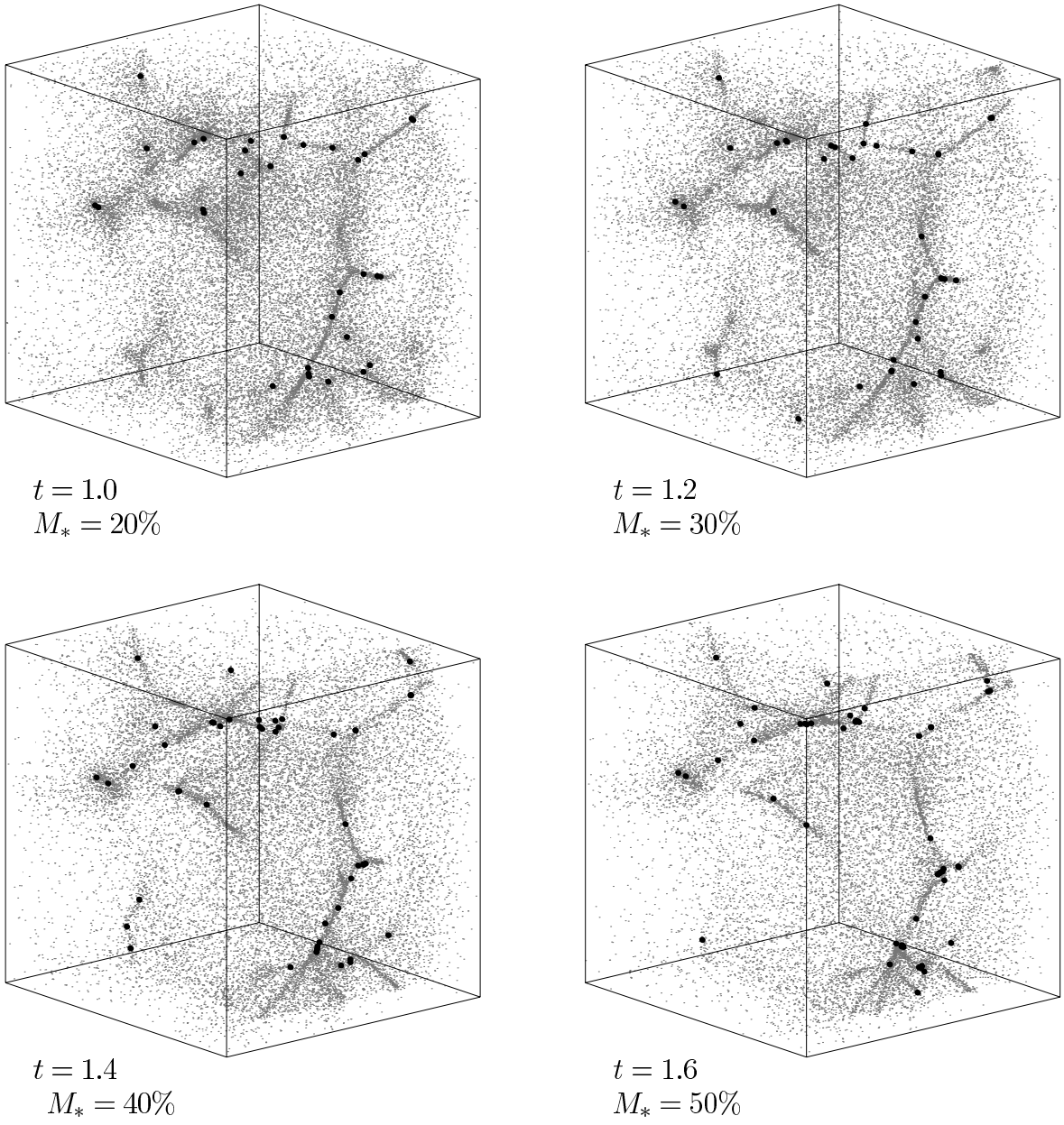

Figure 6.2 — continued: Snapshots of the model T01N2-A at $t = 1.0$, $t = 1.2$, $t = 1.4$ and $t = 1.6$. The total gas mass accreted onto protostellar cores is $M_* = 20\%$, $M_* = 30\%$, $M_* = 40\%$ and $M_* = 50\%$, respectively.

dynamical evolution. Note that the cube has to be seen periodically replicated in all directions. With the start of the SPH simulation, pressure forces begin to act on the gas and smear out small-scale fluctuations which are Jeans stable. On the other hand, large

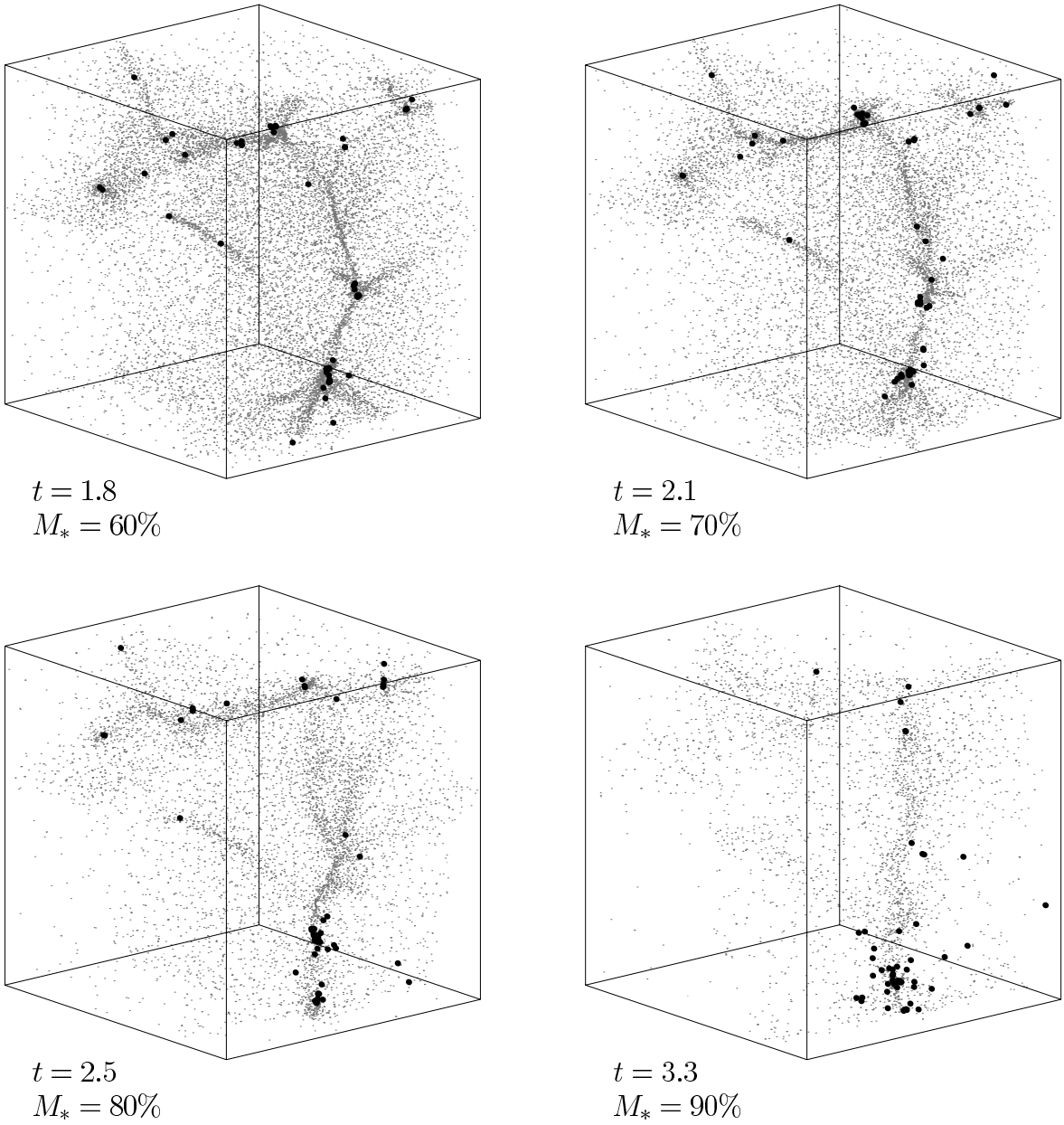

Figure 6.2 — continued: Snapshots of the model T01N2-A at $t = 1.8$, $t = 2.1$, $t = 2.5$ and $t = 3.3$. The total gas mass accreted onto protostellar cores is $M_* = 60\%$, $M_* = 70\%$, $M_* = 80\%$ and $M_* = 90\%$, respectively.

modes are unstable against gravitational collapse and start to contract. At $t \approx 0.4$ the first highly-condensed cores form in the centers of the most massive and densest Jeans-unstable gas clumps and are replaced by sink particles (see Sec. 3.4.4). Soon, clumps of

lower initial mass and density follow. The density threshold for the formation of sink particles is chosen to be $\rho_c = 5000$ and the diameter of sink particles is 1/100 of the linear size of the simulated cube. It is visible in Fig. 6.2 that the system evolves into a network of intersecting sheets and filaments. The gas density is highest along filaments and at their intersections. These are the locations where dense cores form predominantly and soon a hierarchically-structured cluster of accreting protostellar cores is built up. Whereas the overall dynamical evolution of the system is initially dominated by hydrodynamical effects (all the mass is in the gas phase), the later evolution is increasingly determined by the gravitational N-body interaction between protostellar cores and between cores and their environment because more and more gas is accreted onto dense cores. These only interact with each other gravitationally. The final result is a bound dense cluster of protostars. After a few cluster crossing times, core motions have been randomized by close encounters and the protostars have lost knowledge of their initial conditions. The dynamical evolution of the entire system is extremely complex. Its influence on the properties of individual protostars shall be discussed in Sec. 6.4.

At this stage it is necessary to draw attention to one caveat: The gas in the models is treated isothermal. This implies that there exists no feedback mechanism which may prevent the complete collapse. During the dynamical evolution of the system, *all* the gas finally becomes accreted onto protostellar cores: the global core-formation efficiency[1], defined by the percentage of gas that is converted into dense cores, is of order unity. This is unphysical and not observed in star-forming regions (see Sec. 2.1.4). At some stage during the protostellar evolution phase, feedback processes from nascending stars inside protostellar cores or from already existing massive stars in their vicinity must become relevant and terminate the accretion onto cores and protostars. These effects cannot be treated in an isothermal model. However, the early (isothermal) phases of the dynamical evolution and collapse in molecular clouds are well described. The time at which these assumptions break down is difficult to estimate. We are therefore hesitant to interpret the models beyond the phase at which more than $\sim 60\,\%$ of the gas has been accreted onto protostellar cores.

In Fig. 6.3, four stages of the evolution of the high-resolution model T01N2-I are presented. Figure 6.3 plots the system initially, at time $t = 1.4$, when 10% of the gas is condensed into protostellar cores, at 2.0 and at $t = 2.8$. At those times, the mass in protostellar cores has grown to 30% and 60% of the total mass in the system, respectively. Instead of placing individual SPH particles, Fig. 6.3 plots the distribution of the gas density. The density field is scaled logarithmically with darker areas denoting higher densities. Hence, dark dots identify the location of dense collapsed cores. When comparing the time scales for core formation and subsequent accretion with the previous model, the different Zel'dovich

[1]We use the word core-formation efficiency to distinguish from the commonly quoted star-formation efficiency. Both are connected via the ability and effectiveness of *individual* cores to form stars.

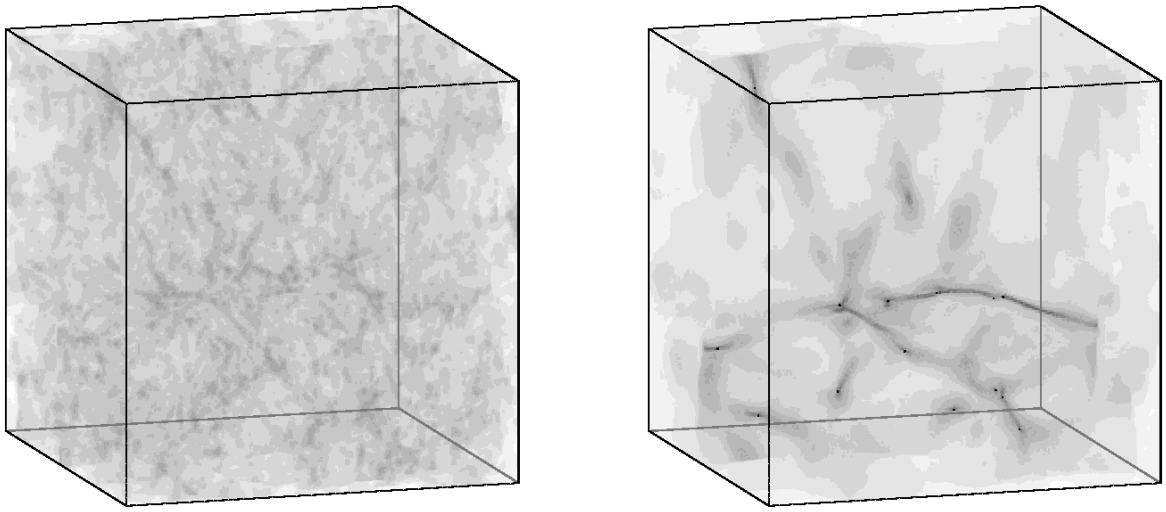

$t = 0.0$
$M_* = 0\%$

$t = 1.5$
$M_* = 10\%$

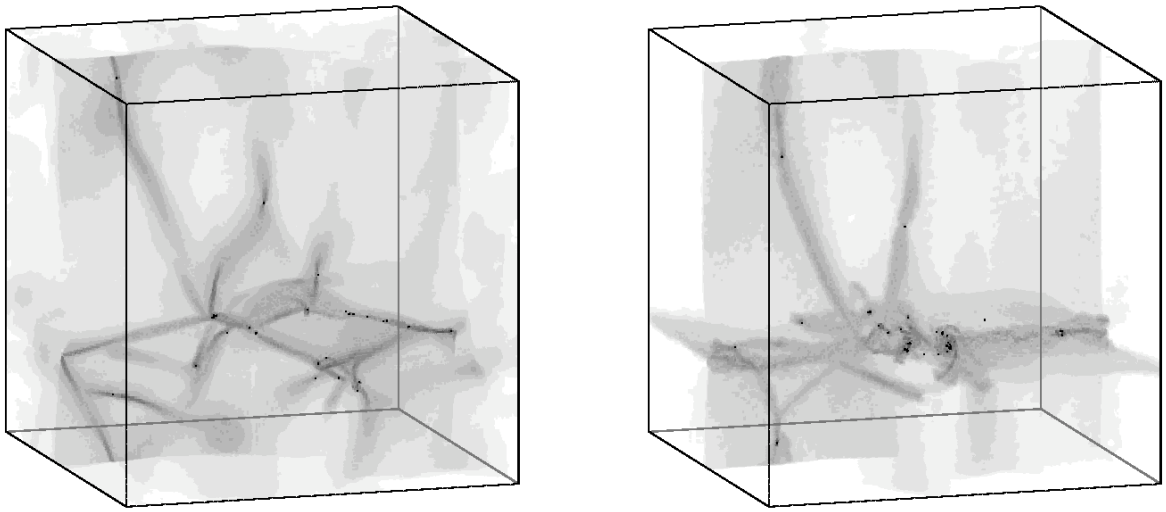

$t = 2.0$
$M_* = 30\%$

$t = 2.8$
$M_* = 60\%$

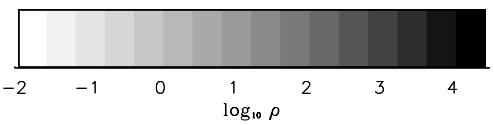

Figure 6.3: Density distribution of the high-resolution model T01N2-I at four different times: Initially, at $t = 1.5$, at $t = 2.0$, and at $t = 2.8$. The total mass fraction accreted onto protostellar cores is denoted by M_*. The location of protostellar cores is denoted by black dots and the density is scaled logarithmically.

shift intervals have to be taken into account. In the high-resolution calculation T01N2-I it is chosen to be $\delta t = 1.5$ instead of $\delta t = 2.0$ for model T01N2-A. Furthermore, the adopted accretion radius of sink particles in the code was reduced by a factor of two, it is 1/200 of the linear size of the simulation box. This delays the formation and accretion onto sink particles by $\Delta t \approx 0.3$. Altogether, the state of the system where the mass fraction accumulated in collapsed cores exceeds a certain percentage is reached later by $\Delta t \approx 0.8$ in simulation T01N2-I. Besides this timing issue, the dynamical behavior of the system is very similar, again a cluster of protostellar cores develops which grows in mass by accretion from its surrounding gas reservoir.

6.3 Clumping Properties of the Evolving Gas

As is discussed in Sec. 2.1.1, the structure of molecular clouds is extremely complex and observations reveal a network of intersecting filaments and clumps on all scales. Molecular clouds may be fractal and various studies of the mass spectrum of molecular clouds and of the gas clumps inside of clouds indicate that their distribution may be approximated by a power law of the form $dN/dm \propto m^{\alpha}$ with exponent $\alpha \approx -1.5$ (see Tab. 2.1.1). This universal clump mass spectrum is an important constraint and test for the modeling of molecular cloud evolution. Numerical simulations *must* be able to reproduce this structural feature of observed clouds. In the isothermal gas model presented in this thesis, the power-law clump mass spectrum is a result of the interaction between gravity and gas pressure. The dynamical evolution of strongly self-gravitating gas naturally leads to a hierarchical density structure with a power-law mass distribution. This is discussed in detail in Sec. 6.3.1, followed by a study of the statistical properties of individual clumps in Sec. 6.3.2.

6.3.1 Clump Mass Spectrum

Figures 6.4 and 6.5 characterize the distribution of clumps and of condensed cores at four different stages of the dynamical evolution of the isothermal models T01N2-A and T01N2-I, namely initially and when 10%, 30% and 60% of the available gas has been accreted onto protostellar cores. For each of these times the upper panels compare the mass distribution of detected gas clumps (thin line) with the observed clump mass distribution $dN/dm \propto m^{-1.5}$, which translates into a slope of -0.5 when plotting $\log_{10} N$ versus $\log_{10} m$ (dashed line). To identify individual clumps, we have developed a clump-finding algorithm similar to that of Williams et al. (1994), but based on the framework of SPH. For details see App. A. The thick line depicts the mass distribution of condensed protostellar cores that have formed within the more massive gas clumps (a detailed analysis of this process

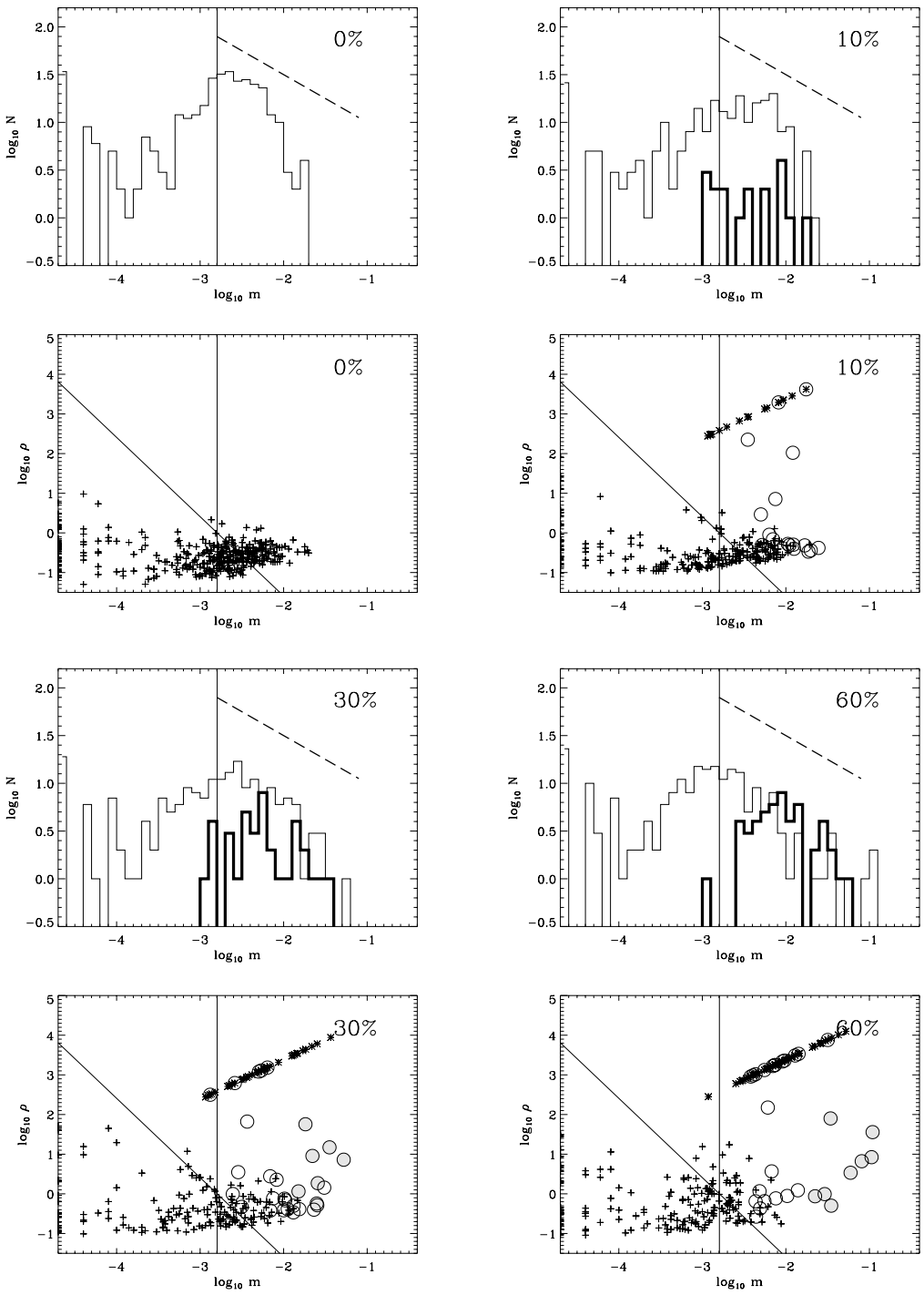

Figure 6.4: Properties of identified clumps and condensed cores in the standard simulation T01N2-A at times $t = 0.0$, 0.7, 1.2 and 1.8, when 0%, 10%, 30% and 60% of the total gas mass is collapsed onto protostellar cores. For each point in time the upper panel shows the distribution of gas clump masses (thin lines) and core masses (thick lines). The lower panel shows the location of each identified clump in a density–mass diagram. A detailed explanation is given in the main text.

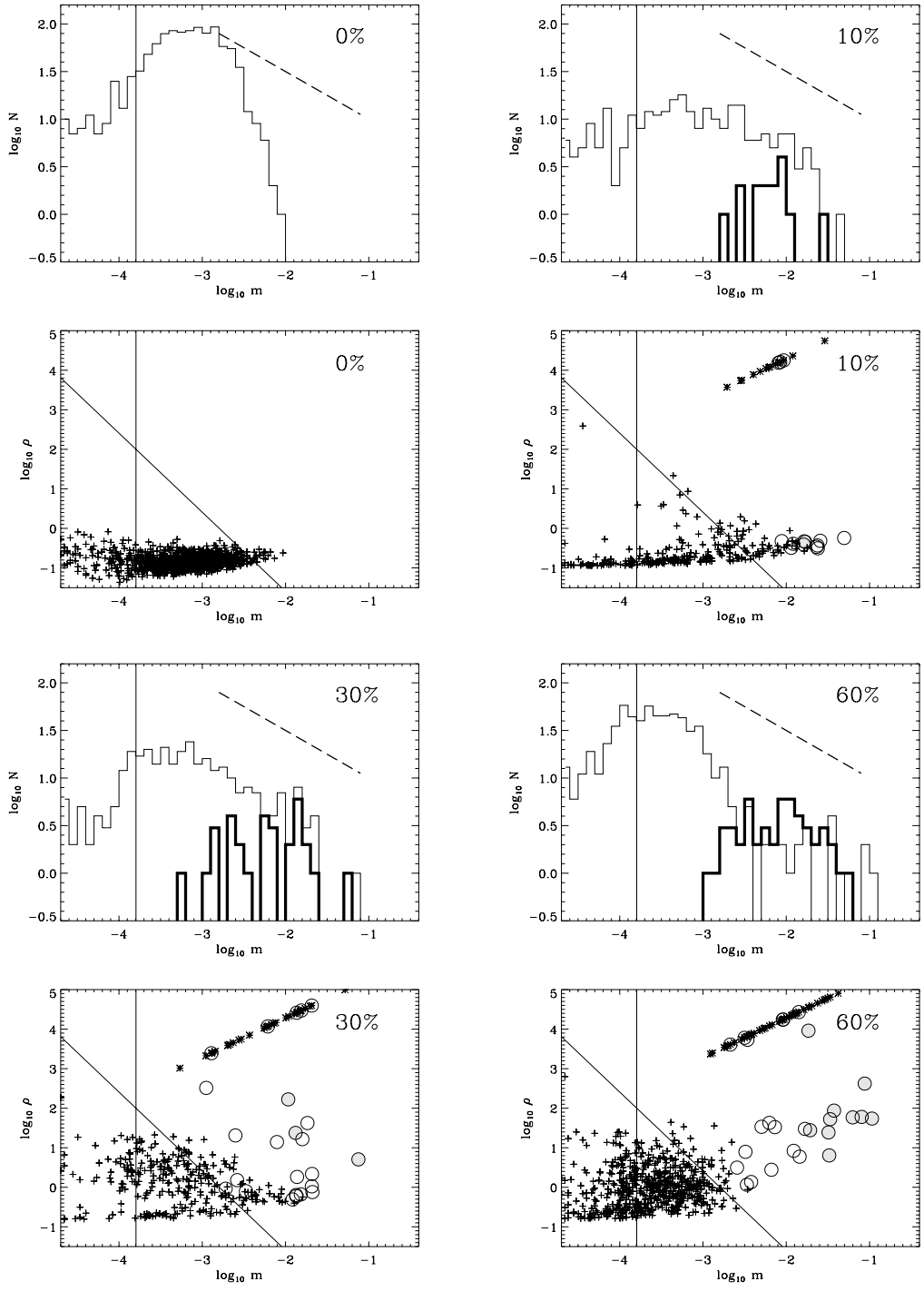

Figure 6.5: Properties of identified clumps and condensed cores in the high-resolution simulation T01N2-I at times $t = 0.0$, 1.5, 2.0 and 2.8, i.e. when 0%, 10%, 30% and 60% of the total gas mass is collapsed onto protostellar cores. The notation is analogous to Fig. 6.4. Note, however, that model T01N2-I uses ten times more particles. Therefore the mass resolution is better by one order of magnitude.

is given in Sec. 6.4). The lower panels show the position of each gas clump in a mass–density diagram. Clumps containing one single core are denoted by open circles, those with multiple cores by filled circles. The unresolved cores are plotted as stars with the density of cores being defined as the core mass divided by the volume within the fixed accretion radius. Therefore, they all fall along a straight line with slope 1/3. The isothermal Jeans mass as function of density is indicated by the diagonal line which separates the diagram into two regions. Clumps that lie to the right of the line exceed their Jeans mass and are due to collapse, whereas clumps to the left are stabilized by gas pressure. The vertical line indicates the SPH resolution limit (Sec. 3.4.5). Clumps to the right of this line are well resolved, objects to the left are ill-defined and may be spurious results of the clump find algorithm. Note that Fig. 6.5 describes the high-resolution simulation and therefore the mass resolution is better by one order of magnitude.

The clumping properties in both simulations, the standard model T01N2-A and the high-resolution model T01N2-I, are remarkable similar, regardless of the fact that model T01N2-I consists of ten times more particles. This suggests that the dominant dynamical processes are well treated and resolved. In both simulations, the clump spectrum of the initial gas distribution *cannot* be described by a simple power-law, it reflects the structural properties of the Gaussian random field from which the initial conditions are generated. The linear approach is not able to generate a hierarchical structure on all scales. This requires considerable non-linear gravitational evolution to take place. Hence, in the subsequent self-consistent dynamical evolution with SPH, the clump distribution quickly achieves a universal mass distribution with a power-law slope which is in excellent agreement with the observed exponent $\alpha \approx -1.5$ (dashed line). The core distribution, on the other hand, deviates significantly from a power-law distribution for smaller masses. Note, that the relative underabundance of low-mass cores with respect to low-mass clumps is not a resolution effect (see the vertical thin lines). Whereas some cores in model T01N2-A may be only marginally resolved, clearly all are well resolved in the high-resolution case T01N2-I. Considerable deviations from a simple power-law spectrum of clump masses occur again in the very late phases of the evolution when most material is accreted onto dense cores and the gas reservoir becomes depleted significantly. Then, huge voids of very low density open up and the entire system resembles more strongly a (proto)star cluster than a molecular cloud. Within these two extrema of the isothermal gas evolution, from the linear initial gas distribution to the final star cluster, the complex interplay between gravity and gas pressure naturally creates a hierarchical structure best described by a simple power-law.

The lower panels in Fig.'s 6.4 and 6.5 indicate that initially only very few high-mass clumps exist which exceed the local Jeans mass. The average density of clumps is close to the mean density $\langle\rho\rangle = 1/8$. These clumps will collapse rapidly and form the first condensed cores in their central region (see also Sec. 6.4). On the other hand, the whole

gas distribution evolves, clumps begin to stream towards a common center of gravity, and a complex network of intersecting sheets and filaments builds up. At the intersections of filaments clumps are likely to merge and may form larger clumps. The density grows and once enough mass is accumulated, the new clumps will undergo rapid collapse to form new protostellar cores. Therefore, with progression of time the number of Jeans-unstable clumps and subsequently of protostellar cores increases, populating a larger region to the right of the diagonal line. If clumps merge which already contain protostellar cores, the new more massive clump suddenly contains multiple cores in its interior. Within this protostellar cluster, cores now compete with each other for the surrounding gas envelope. This competitive accretion and the direct gravitational interaction between the members of the cluster has important consequences for the further evolution. It influences the mass growth of individual cores and thus determines the final mass spectrum (more details are discussed in Sec. 6.4). These unpredictable probabilistic phenomena are responsible for the difference between the distribution of clump masses and of core masses. Whereas gas clumps only evolve according to the laws of hydrodynamics, cores are subject to direct gravitational interaction, they behave like an N-body system. This inevitably alters their mass distribution. The mass spectrum of protostellar cores is well approximated by a log-normal functional form, being comparable to the stellar IMF. A detailed comparison is discussed in Sec. 6.5.

6.3.2 Properties of Individual Clumps

Whereas the previous section discussed global features of the clump and core distribution, this section looks in detail into the properties of individual clumps. This is important if one wants to study the collapse and fragmentation of single clumps with very high resolution. As indicated before, the simulations presented here are no longer able to resolve the collapse and sub-fragmentation of protostellar cores once they have been substituted by sink particles in our code (a detailed description of how this is handled is given in Sec. 3.4.4). To study this subsequent evolution, a new simulation just concentrating on the collapse of one single core becomes necessary (see Sec. 2.2.2). To connect the final stages of the larger-scale simulations discussed here and the initial conditions for detailed collapse calculations, statistical knowledge about the properties of individual cores is necessary. Important parameters entering individual collapse scenarios are the mass distribution of clumps (this was discussed in the previous section), their density structure (this is discussed in this section) and their rotational properties (the angular momentum evolution of cores will be examined in Sec. 6.4.3). However, gas clumps are never in isolation, the progenitors of protostellar cores interact with each other and may merge or fragment. This has very important consequences for the mass spectrum, the spatial distribution and the geometrical shape of clumps and cores. In a very crude

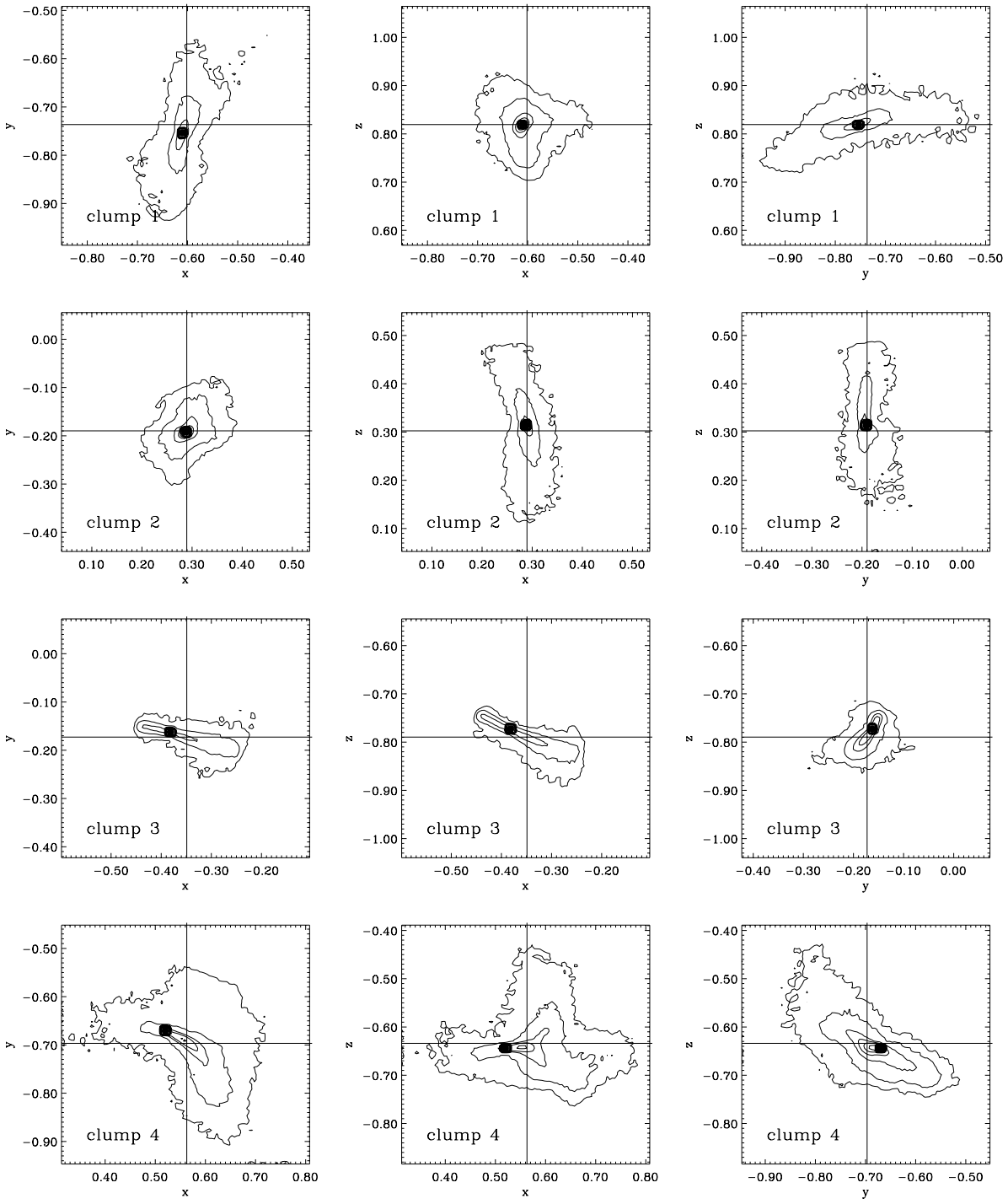

Figure 6.6: Typical shapes of identified clumps in the high-resolution model T01N2-I at time $t = 1.2$, i.e. when four collapsed cores have formed and accreted 1% of the total gas mass. This first part of the figure projects the clumps containing the four protostellar cores into the xy-, xz- and yz-plane. Density is scaled logarithmically. Two contour lines span one decade ($\log_{10} \Delta\rho = 1/2$) with the lowest contour level being $10^{1/2}$ above the mean density $\langle\rho\rangle = 1/8$. The black dots indicate the positions of the dense protostellar cores.

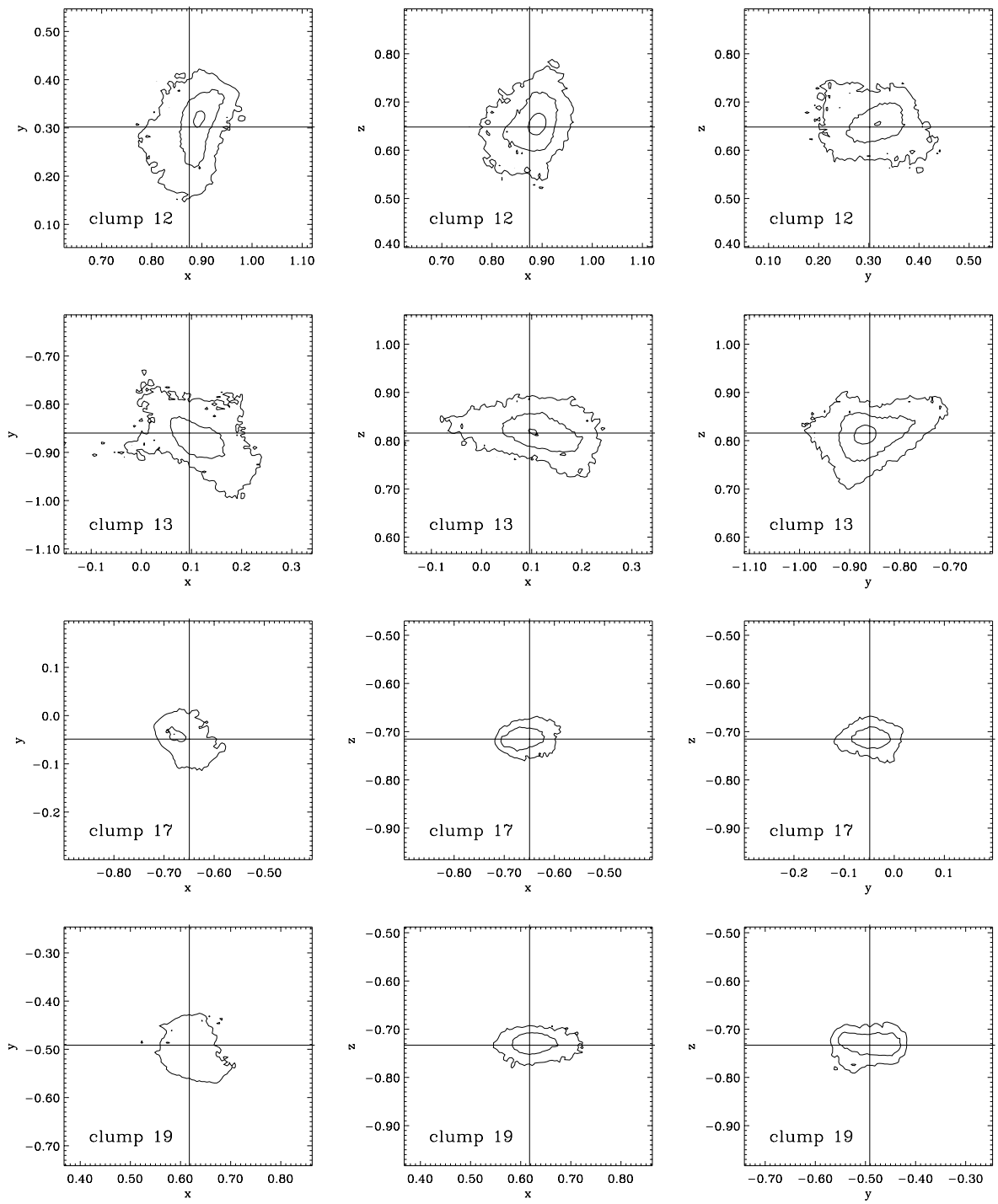

Figure 6.6 — continued: Typical shapes of identified clumps in the high-resolution model T01N2-I at time $t = 1.2$. This second part of the figure shows contour plots of clumps that have not yet collapsed to high enough densities to contain dense cores. Note that clumps are numbered accoring to their peak density. The plot is centered on the center-of-mass of each clump, as indicated by the two intersecting lines.

fashion this is included in the collapse calculation of single, isolated cores by assuming some kind of external perturbation, e.g. random noise or an $m = 2$ mode (see Sec. 2.2).

Typically, the overall density distribution of identified clumps in our simulations follows a power law and the density increases from the outer regions inwards to the central part as $\rho(r) \propto 1/r^2$. For clumps that contain collapsed cores, this gradient continues towards the central protostellar object. However, for clumps that have not yet formed a collapsed core in their center, the central density gradient becomes flat. This is in accordance with the theory for isothermal collapse (see Sec. 2.2) and with the observational data for dense cores in dark molecular clouds (see Sec. 2.1.5). However, the clumps generally are highly distorted and are by no means spherical. Typically they are triaxial with high axis ratios. Depending on the projection angle, they often appear extremely elongated, being part of a filamentary structure which may be identified as chain of connected elongated individual clumps. Also more complicated shapes are common which may result from recent clump mergers at the intersections of filaments. A selection of clump shapes is presented in Fig. 6.6 which plots the contour lines for eight high-density clumps in simulation T01N2-I at time $t = 1.2$ projected into the xy-, xz- and yz-plane. At this state of the dynamical evolution, four collapsed cores have formed which accreted 1% of the total gas mass. This time is most appropriate to determine clump properties, because the system has already undergone substantial evolution (the power-law clump spectrum is well established) but is not yet influenced by the dynamical interaction between dense protostellar cores. Their mass is negligible and there are no clumps with multiple cores yet. The clumps that already formed dense cores in their interior are plotted in the first part of the figure, the second part describes clumps whose central densities are not yet high enough to be identified as condensed core. The clumps are numbered according to their peak density, i.e. clump #1 has the highest central density. The density contours are spaced logarithmically with two contour levels spanning one decade, $\log_{10} \Delta\rho = 1/2$. The lowest contour is therefore by a factor of $10^{1/2}$ above the mean density $\langle\rho\rangle = 1/8$. The black dots indicate the positions of the dense protostellar cores. Note the similarity to the appearance of observed dense (pre-stellar) clumps (Fig. 2.5). It is clearly visible that the clumps are very elongated. The ratios between the semi-major and the semi-minor axis measured at the second contour level are typically between 2:1 and 4:1. However, there may be significant deviations from simple triaxial shapes, see e.g. clump #4 which is located at the intersection of two filaments. This clump is distorted by infalling material along the filaments and appears 'y'-shaped when projected into the xz-plane. As a general trend, high contour levels typically are regular and smooth, because they are mostly influenced by self-gravity. On the other hand, the lowest level is strongly influenced by environmental effects. Hence, it appears patchy and irregular. The location of the condensed core within a clump is not necessarily identical with the center-of-mass of the clump. This is due to the irregular shape of the clump caused by dynamical evolu-

tion. All these properties of the clumps identified in the numerical simulations are in good agreement with the features of observed clumps (see Sec. 2.1.5), suggesting that gravity and gas pressure are dominant agents in shaping molecular cloud structure.

6.4 The Formation and Properties of Protostellar Clusters

The location and the time at which protostellar cores form, is determined by the dynamical evolution of their parental gas clouds. Besides collapsing individually, clumps stream towards a common center of attraction, where they may merge with each other or undergo further fragmentation. As can be seen in Fig.'s 6.2 and 6.3, isothermal models evolve into a network of intersecting sheets and filaments. The gas density is highest along filaments and at their intersections. These are the locations where dense cores form predominantly. The time of their formation in the centers of unstable clumps depends strongly on the relation between the timescales for individual collapse, streaming motion along filaments, merging and sub-fragmentation. Individual clumps may become Jeans unstable and start to collapse to form condensed cores in their centers. While collapsing, these clumps also interact with each other. When clumps merge, the larger new clump continues to collapse, but contains now a *multiple* system of cores in its center. Now sharing a common environment, these cores compete with each other for the limited reservoir of gas in their surrounding (see e.g. Price & Podsiadlowski, 1995; Bonnell et al., 1997). Furthermore, the protostellar cores interact gravitationally with each other. As in dense stellar clusters, close encounters lead to the formation of unstable triple or higher order systems and alter the orbital parameters of the cluster members. As a result, a considerable fraction of protostellar cores get expelled from their parental clump. Suddenly bereft of the massive gas inflow from their collapsing surrounding, they effectively stop accreting and their final mass is determined. Ejected objects can travel quite far and resemble the weak line T Tauri stars found via X-ray observation in the vicinities of star-forming molecular clouds (e.g. Neuhäuser et al., 1995; Wichmann et al., 1997). All these effects act together to shape the formation and accretion history of individual cores and determine the kinematical and spatial properties of the entire cluster of protostars.

6.4.1 Formation and Growth of Protostellar Cores

As stated before, the formation and accretion history of protostellar cores is extremely complex and influenced by a variety of effects. As illustration, we specify in Fig. 6.7 the accretion history for a number of selected protostellar cores (a) from model T01N2-A and

(b) from model T01N2-I. The objects are numbered chronologically according to their time of formation. Model T01N2-A forms altogether 60 cores and model T01N2-I 55. The figure reveals the following trends:

(a) The cores which form first tend to have the largest final masses. They emerge from the initial clumps with the largest masses and highest densities which are identified with the most significant peaks in the fluctuation field. Jeans unstable clumps with these qualities have very short collapse time scales. Hence, these clumps are the first ones in the simulation to satisfy in their central region the conditions to convert a dense group of SPH particles into a single sink particle (see Sec. 3.4.4). These first sink particles are likely to swallow a mass large fraction of their parental clumps before the dynamical evolution of their environment changes the clump properties too much, i.e. before the clumps get dispersed or merge with other clumps. If a clump which already contains a core merges with a non-collapsed gas clump, for example when streaming along a filament towards a common center of attraction, then also the new clump is likely to become completely accreted onto the protostellar core. Since the first cores form in the highest-density regions more or less independent of each other, their mass growth rate is dominated by the matter originating from their vicinity.

(b) On the other hand, matter that contracts into dense cores at later times (say $t \gtrsim 2$) has already undergone considerable dynamical evolution. Clumps that were initially not massive enough to collapse onto themselves follow the large-scale flow towards the global minimum of the gravitational potential. They stream along filaments and may merge at the intersections. Once enough mass is accumulated, they undergo rapid collapse and build up a new protostellar core. This accumulation procedure needs time. It forms cores predominantly in the late stages of the dynamical evolution. In a closed system, the available gas is already depleted considerably. Therefore, their average mass is very small. The final masses of the protostellar cores for the high-resolution model T01N2-I (i.e. at the time when 90% of the available gas mass has been accreted) are plotted in Fig. 6.8.

Another aspect of the accretion process onto individual cores is discussed in Fig. 6.9. For the (a) first nine cores and for the (b) last nine cores that form in the high-resolution model T01N2-I, it plots the initial (at $t = 0.0$) distances between the accreted SPH particles and the particle that gets converted into the sink particle during the course of the simulation. This defines a volume from which particles accrete onto protostellar cores. As indicated above, the cores in Fig. 6.9a accrete most particles and the bulk of their final mass from their vicinity, i.e. from a distances less than ~ 0.5. With the total size of the simulated cube being 2^3, this corresponds to roughly 1/64 of the total volume. In the case, the material would be randomly sampled from a homogeneous cube of size 2^3, the most material would come from a distance of ~ 1.3. On the other hand, the cores in

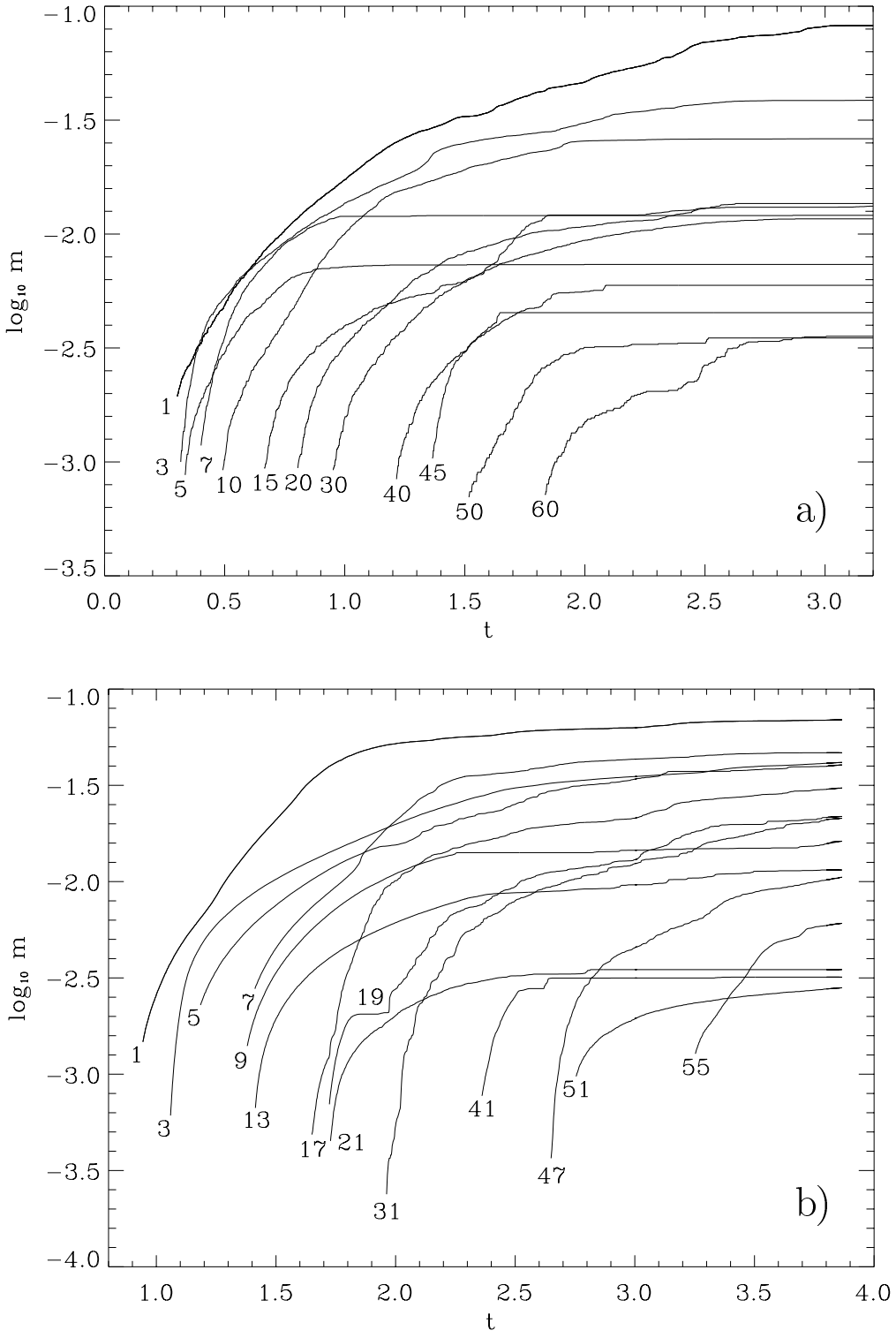

Figure 6.7: Formation and accretion history of selected protostellar cores in the simulations (a) T001N2-A and (b) T01N2-I. The numbers reflect the order of their formation.

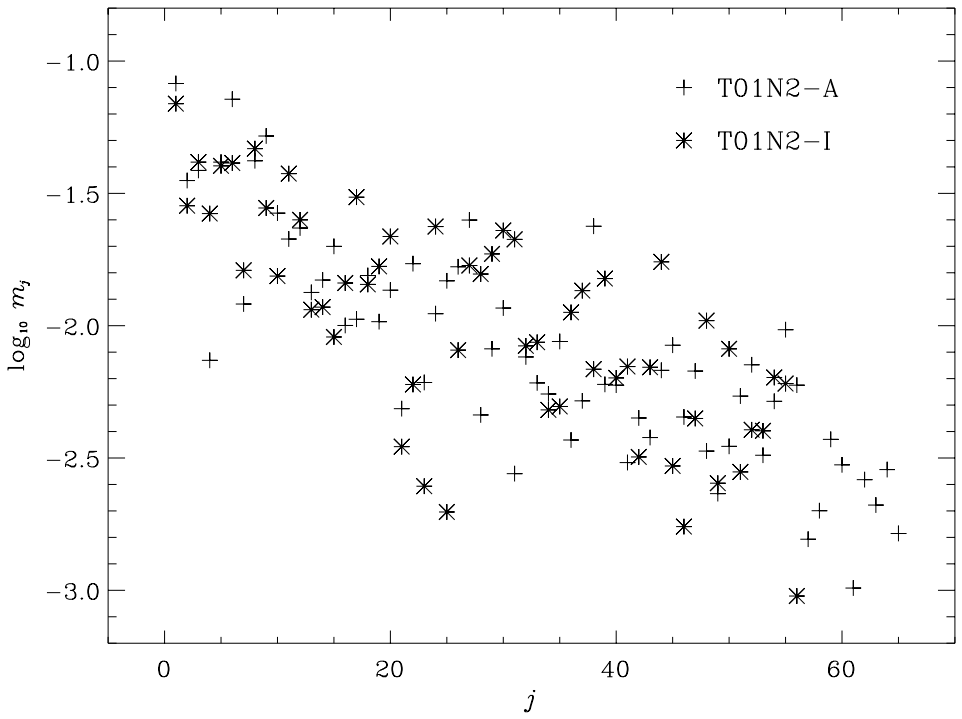

Figure 6.8: Final masses m_j of the protostellar cores j in the standard model T01N2-A (crosses) and in the high-resolution model T01N2-I (stars). Again the numbers reflect the order of their formation.

Fig. 6.9b are much smaller (note the diffent scale at the ordinate) and consist of matter that originates from a larger volume, much closer to the value for random sampling. This indicates that these clumps accrete from matter that already has undergone considerable dynamical evolution and is well mixed.

Further information about the processes determining the formation of and accretion onto dense cores is given in Fig. 6.10. It plots the contributions from individual clumps to the final mass of selected cores. As a general trend, cores that form very early can accrete a large fraction of their parental and neighboring clumps before clump interaction and merging becomes important. On the other hand, matter that builds up protostellar cores at the late stages of the dynamical evolution has participated in large-scale motions and successive clump merging. It is well mixed and the initial clump assignment is no longer significant. Furthermore, the competition amongst groups of cores in the interior of multiple merged clumps for the accretion from the surrounding gas reservoir becomes more important with the progression of time. This phenomenon also contributes to the distribution of available gas mass onto a larger number of cores. Therefore, the fraction $\langle f_j \rangle$ of material of individual clumps that gets accreted onto the cores decreases again with time. Since the cores that form early gain most of their mass rapid-Ely and from their vicinity, $\langle f_j \rangle$ is larger than the values for cores that form later form well mixed

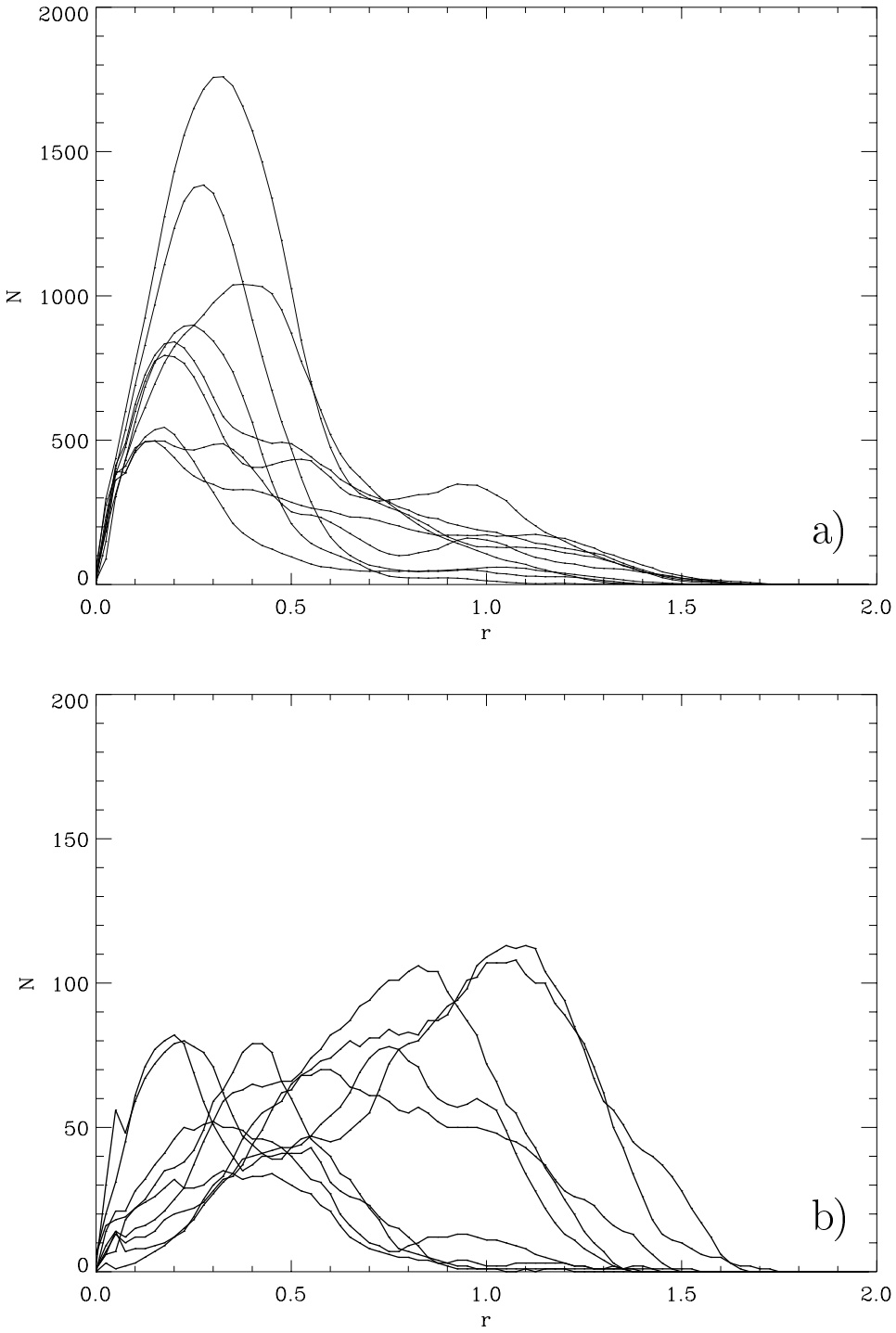

Figure 6.9: Initial distance distribution of matter that gets accreted onto protostellar cores. For (a) the first nine cores to form and for (b) the last nine ones, the number N of SPH particles that get accreted onto a condensed core are plotted as function of their initial distance r to the particle that is converted into the accreting core particle (see Sec. 3.4.4). The cores that form first accrete more mass than the later ones and this mass is accumulated from a smaller volume.

material.

6.4.2 The Importance of Dynamical Interaction

Besides the effects discussed in the previous section, the growth rate of protostellar masses is strongly affected by the dynamical interaction between the cores themselves. This phenomenon is closely related to the competitive accretion of multiple cores within one common gas envelope (Price & Podsiadlowski, 1995; Bonnell et al., 1997) and becomes important when clumps merge that already contain dense cores. In the protostellar cluster in the center of the larger merged clump, protostellar cores interact gravitationally with each other. As in dense stellar clusters, close encounters may lead to the formation of unstable triple or higher-order systems and alter the orbital parameters of cluster members. During the decay of unstable subsystems, protostellar cores can get accelerated to very high velocities and may leave the cluster. During this process, the less massive cores are more likely to become ejected. Protostellar cores that get expelled from their parental clump are suddenly bereft of the massive gas inflow from their still collapsing surrounding. They effectively stop accreting and their final mass is determined. The dynamical interaction between cores is an important agent in shaping the mass distribution.

For example, looking at the accretion history of protostellar cores in the standard model, Fig. 6.7a, it is evident that core #5 stops accreting at $t \approx 0.8$, long before the overall gas reservoir is depleted. The same applies to core #7 at $t \approx 0.9$. In both cases, the objects were involved in a 3-body encounter that resulted in the expulsion from their gas rich parental clumps. Fig. 6.11 depicts the trajectories of the cores #3, #5, #11, #31, and #46. At $t \approx 0.3$ core #3 forms within an overdense region and slightly later cores #5 and #11 form in its vicinity from other Jeans-unstable density fluctuations. Their parental gas clumps merge and the whole systems flows towards a local minimum of the gravitational potential. The three cores soon build an unstable triple system, continuing to accrete from the converging gas flow they are embedded in (the detailed trajectories are shown in Fig. 6.11b, note the larger scale). At $t \approx 0.8$, core #5 is expelled and the remaining two cores form a wide binary, which at $t \approx 1.6$ suddenly hardens due to the gravitational encounter with core #46 (see Fig. 6.11c). Also this hard binary is transient, the interaction with core #31 pumps energy in its orbit, and in the subsequent evolution, the orbital period increases further during the encounter with a dense gas filament whose tidal influence finally disrupts the binary at $t \approx 2.4$. At that time, accretion stops.

Also the high-resolution simulation is subject to these unpredictable and chaotic kinematical effects. In Fig. 6.7b, at $t \approx 1.8$, core #19 stops accreting. It is expelled from a dense clump at the intersection of two massive filaments by a triple interaction with cores #1 and #17. However, it still is bound to the gas knot which grows in mass due to continuous

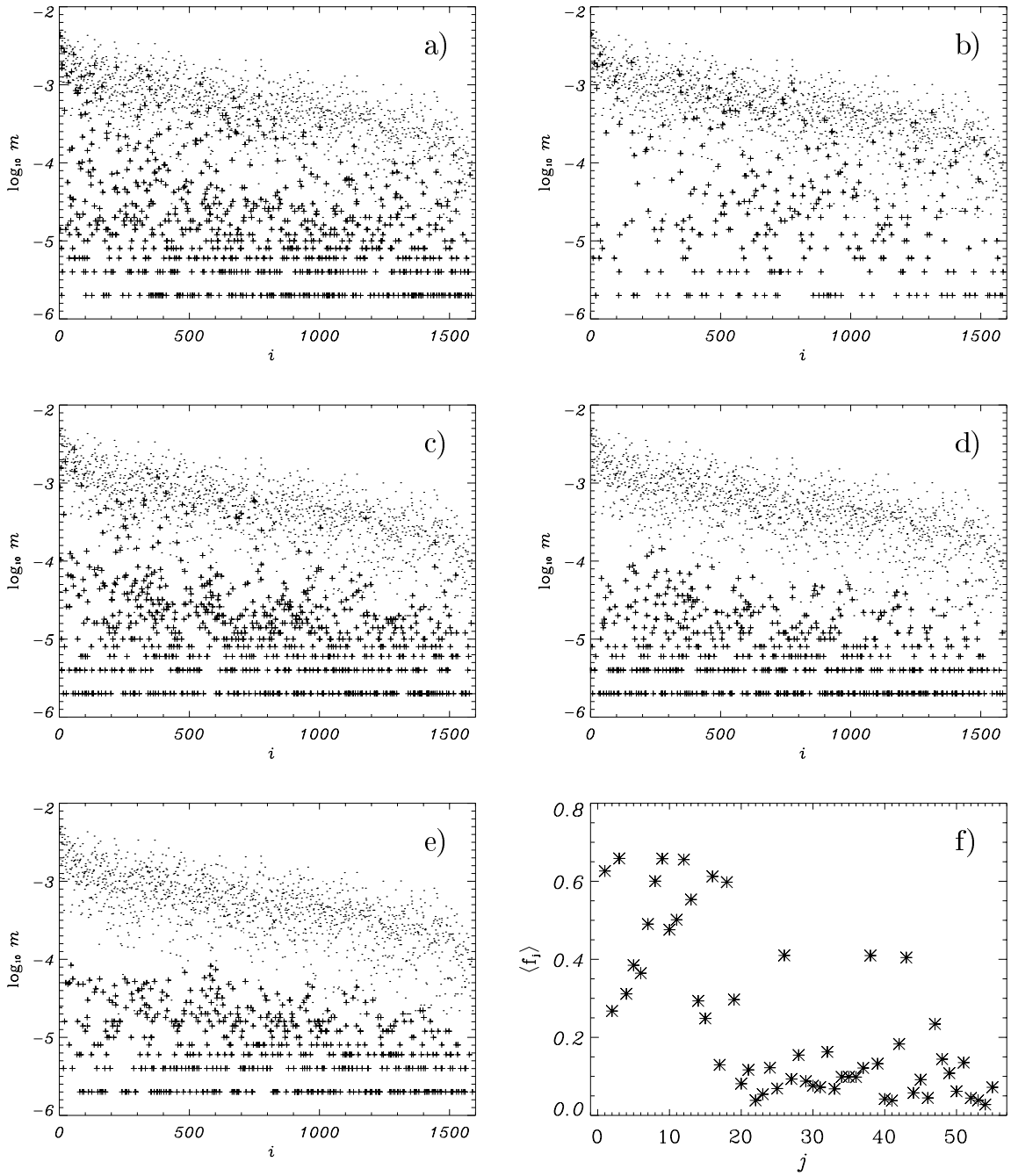

Figure 6.10: Contribution m_i of individual clumps i identified in the initial density field to the final mass of core particles j, denoted by crosses: for (a) core $j = 1$, (b) core $j = 2$, (c) core $j = 10$, (d) core $j = 40$ and (e) core $j = 55$. The total mass of the gas clumps i is indicated by dots. Plot (f) gives the mass-weighted mean of the fraction of clump material $\langle f_j \rangle$ that gets accreted onto individual cores j. Cores that form early tend to accrete nearby clumps more completely, whereas material that builds up cores at later stages has already undergone sufficient dynamical evolution to be well mixed. The initial association with certain clumps becomes irrelevant.

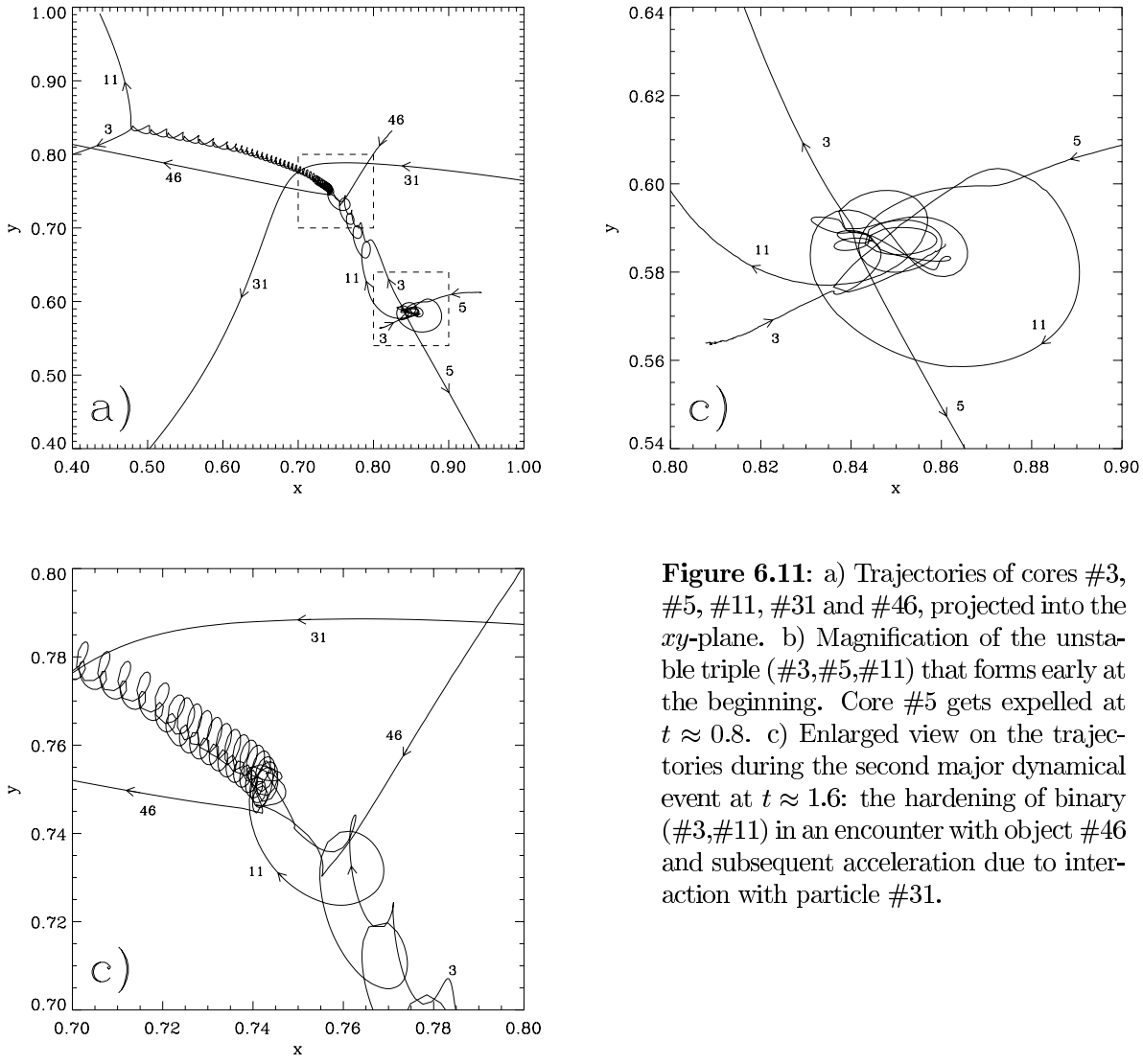

Figure 6.11: a) Trajectories of cores #3, #5, #11, #31 and #46, projected into the xy-plane. b) Magnification of the unstable triple (#3,#5,#11) that forms early at the beginning. Core #5 gets expelled at $t \approx 0.8$. c) Enlarged view on the trajectories during the second major dynamical event at $t \approx 1.6$: the hardening of binary (#3,#11) in an encounter with object #46 and subsequent acceleration due to interaction with particle #31.

infall. It falls back onto the clump of gas and resumes accreting at $t \approx 2.0$. Cores #9 and #41 are also expelled from their parental clumps but, unlike core #17, their accretion is terminated completely. These dynamical interactions between protostellar cores influence their mass distribution significantly. In reality, ejected protostars may travel quite far and could cause the extended distribution of weak-line T Tauri stars found via X-ray observations in the vicinities of star-forming molecular clouds (e.g. see Neuhäuser et al., 1995; Sterzik et al., 1995; Krautter et al., 1997; Wichmann et al., 1996, 1997).

6.4.3 Rotational Properties of Protostellar Cores

A very important parameter for the further collapse and possible sub-fragmentation of individual protostellar cores is their rotational. If a rotating gas clump begins to collapse, the conservation of angular momentum prevents material from the envelope to directly accrete onto the central protostar. Only the inner part of the clump is able to immediately fall onto the star, the bulk of the infalling envelope accumulates in a rotationally supported disk around the central object. Angular momentum is removed outward on the viscosity time scale $\tau_{\rm vis}$ (see Sec. 2.2). Only the viscous transport processes within the accretion disk or global instabilities are able to transfer matter further towards the central star. The time scale $\tau_{\rm vis}$ on which viscous transport takes place is typically by a factor of $10 - 100$ larger than the rotational time scale, which is comparable to the free-fall time scale $\tau_{\rm ff}$ (see e.g. Pringle, 1981).

These processes take place deep inside the protostellar cores, hence they cannot be resolved by our numerical scheme. However, we can keep track of the the total angular momentum accreted onto each condensed core in our simulation. Figure 6.12 plots the time evolution of the angular momentum vector $\boldsymbol{L}$ of all protostellar cores in the high-resolution model T01N2-I. The left panel describes the evolution of each individual component of the vector. The right panel plots the distribution of L_x, L_y and L_z at the end of the simulation at $t = 3.9$. For comparison, we overlay the final distribution (at $t = 5.6$) of the angular momenta of the cores in the standard model T01N2-A with dashed lines. Both distributions are statistically indistinguishable. From the plots, we see that the evolution of the angular momentum of individual cores can be very complex and intimately reflects the rotational properties of the environment they are embedded in: the angular momentum of the protostellar core is determined by the angular momentum of the clump it forms in. Clumps that merge at the intersection of two filaments can accumulated considerable angular momentum which is transfered onto the core by accretion. The angular momentum vector of cores may even change its sign if material is accreted which rotates counterclockwise with respect to the core.

The distribution of the absolute values of angular momenta $|\boldsymbol{L}|$ of the protostellar cores in simulation T01N2-I is plotted in Fig. 6.13a. It gives these values at $t = 2.8$ (solid line), i.e. when 60% of the gas is converted into dense cores, and at the final stage, $t = 3.9$ (dashed line). As already indicated in Fig. 6.12, the angular momenta are very broadly distributed and peak at $\sim 10^{-5}$. Note again that these values are given in dimensionless units with length and mass scales set to one. Figure 6.13b plots the distribution of the specific angular momenta $|\boldsymbol{L}|/m$ of the cores, again at $t = 2.8$ (solid line) and at $t = 3.9$ (dashed line). The mass dependence of $|\boldsymbol{L}|/m$ is specified in Fig. 6.13c. There are no massive cores with low specific angular momentum. However, there is no clear correlation between both quantities.

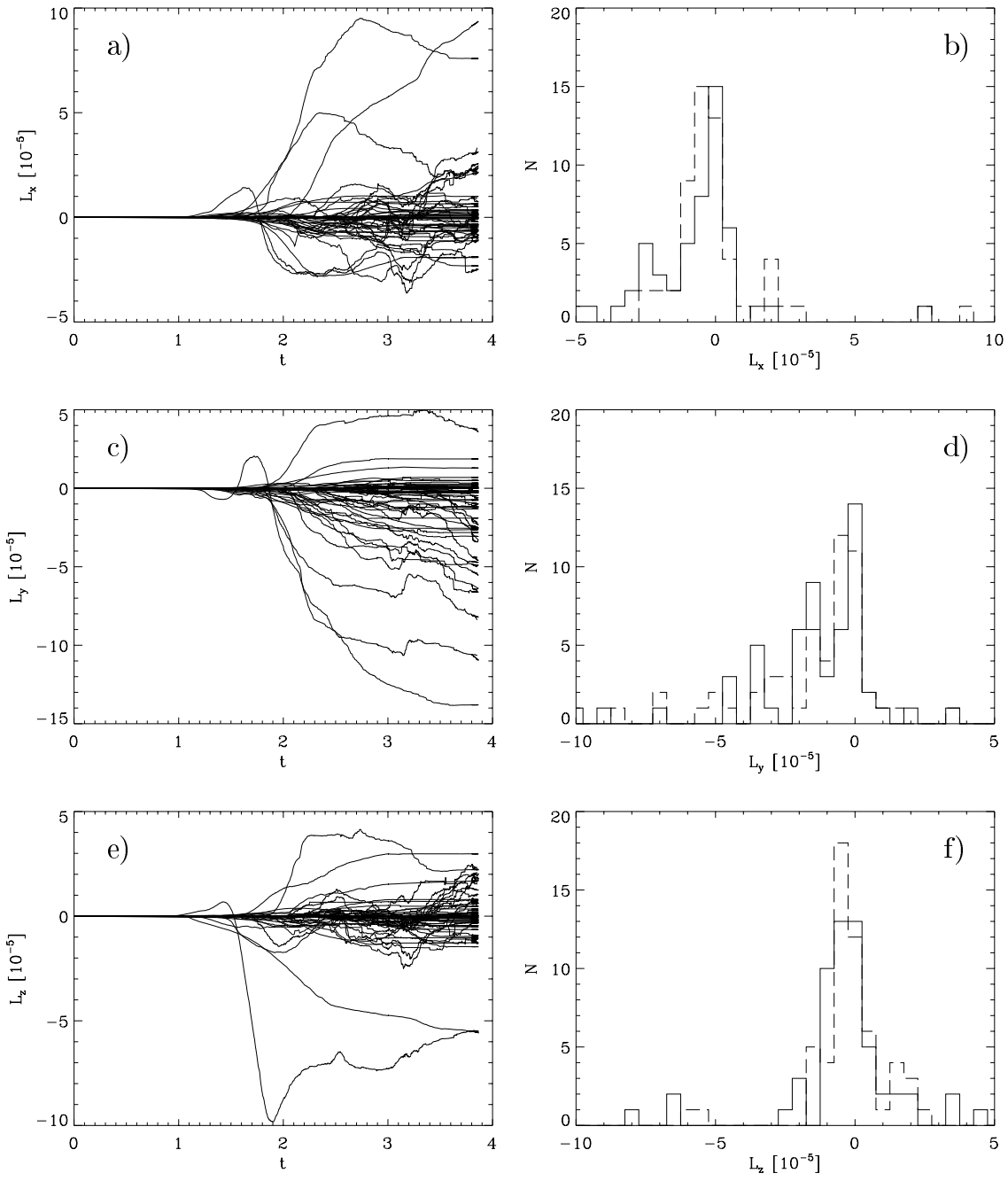

Figure 6.12: Time evolution of the angular momentum $\boldsymbol{L}$ of protostellar cores. The left column plots (a) the x-component L_x, (c) the y-component L_y and (e) the z-component L_z of each condensed core in the high-resolution simulation T01N2-I as function of time t. The right column plots the distribution of every component at the end of the SPH simulation, i.e. at $t = 3.9$ for model T01N2-I (solid lines) and also for the standard model T01N2-A at $t = 5.6$ (dashed lines): (b) L_x, (d) L_y and (f) L_z.

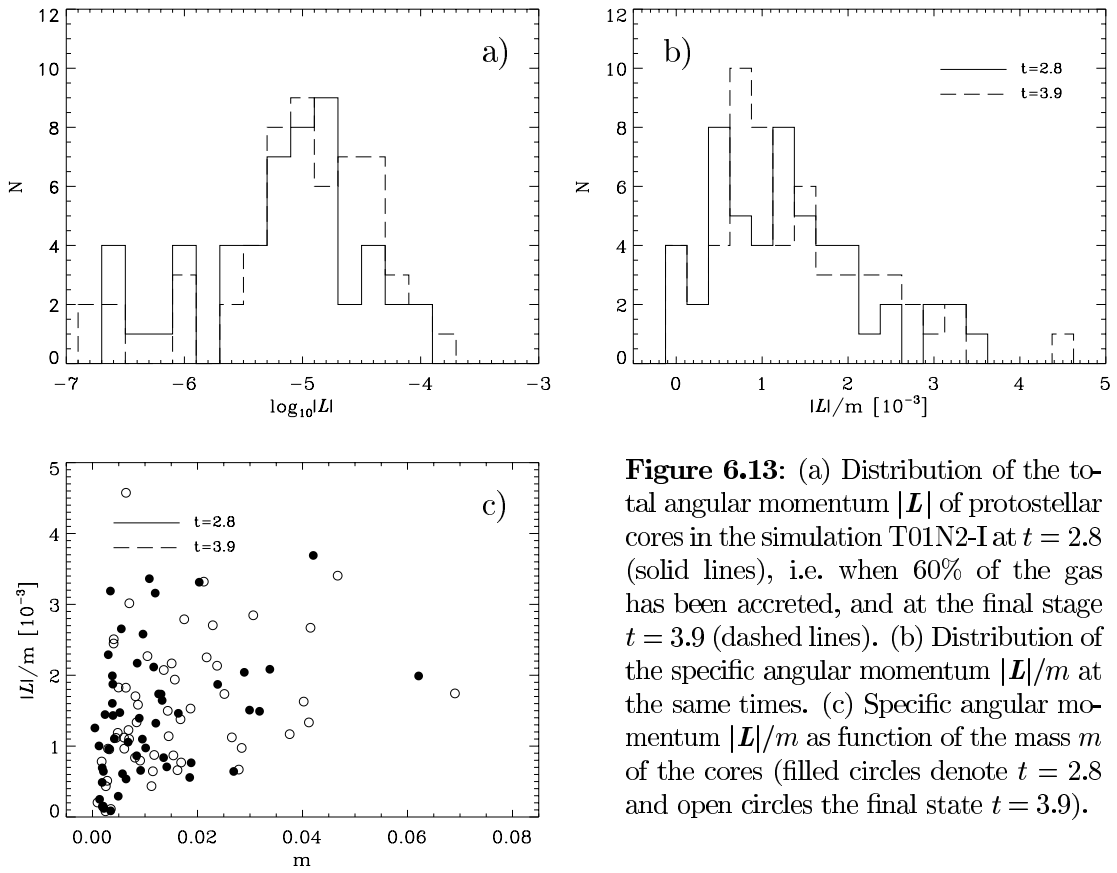

Figure 6.13: (a) Distribution of the total angular momentum $|\boldsymbol{L}|$ of protostellar cores in the simulation T01N2-I at $t = 2.8$ (solid lines), i.e. when 60% of the gas has been accreted, and at the final stage $t = 3.9$ (dashed lines). (b) Distribution of the specific angular momentum $|\boldsymbol{L}|/m$ at the same times. (c) Specific angular momentum $|\boldsymbol{L}|/m$ as function of the mass m of the cores (filled circles denote $t = 2.8$ and open circles the final state $t = 3.9$).

When looking at the spatial distribution of the angular momentum vectors of protostellar cores, there is a correlation between the location and the orientation. As is visible in Fig. 6.14, the angular momentum vectors of cores that form in the same region tend to be aligned. These cores form from gas that has similar global flow patterns. When clumps follow the same flow and also when clumps stream towards each other, they tend to have comparable rotational properties. Furthermore, in clumps which contain multiple cores as the result of merging, all cores accrete from the same environment with a certain angular momentum. As a result, the rotational properties of these cores tend to be similar. In some star-forming regions, molecular outflows from young stellar objects indeed appear to be correlated and aligned (e.g. in the northern part of the L1641 cloud, see Fig. 14 in the review article by Reipurth, 1989). Assuming that the protostellar outflows are associated with the rotational properties of the protostellar object they emerge from, this implies a correlation between the angular momenta of the protostellar cores similar to the one found in our numerical models. On the other hand, in other regions no correlation is found at all. Taking all together, the observational data are not conclusive.

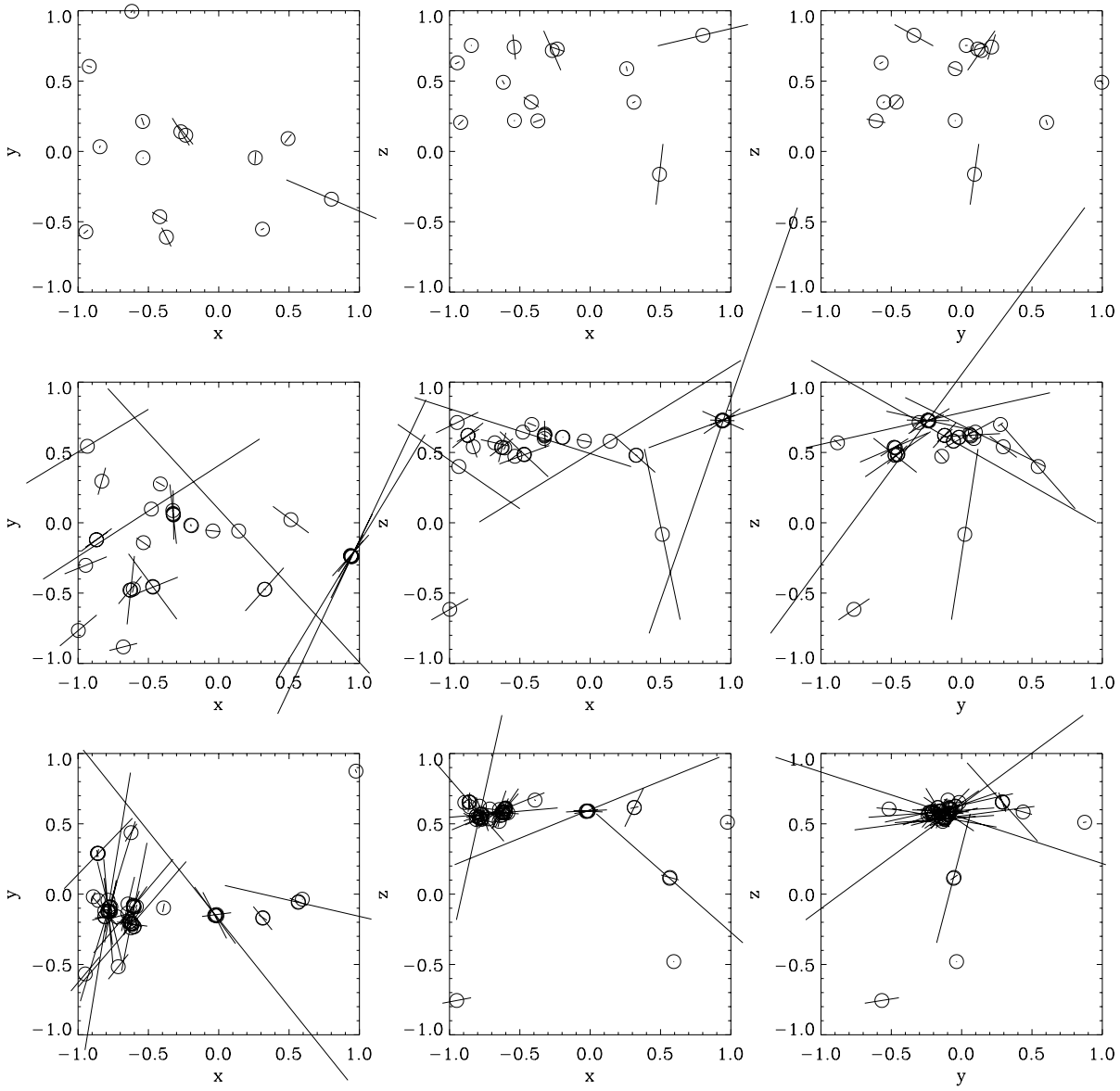

Figure 6.14: Projection of the angular momenta $\boldsymbol{L}$ of protostellar cores in simulation T01N2-I into the xy-, xz- and yz-plane at $t = 1.5$ (upper panel), $t = 2.0$ (middle panel) and $t = 2.8$ (lower panel), i.e. when 10%, 30% and 60%, respectively, of the gas mass is accreted onto the cores. The length of the lines is proportional to $|\boldsymbol{L}|$; note that for better legibility the scaling factor in the bottom row is reduced by a factor of 1/3 compared to the upper two panels.

6.4.4 Clustering Properties of Protostellar Cores

When studying the spatial properties of (proto)stellar clusters, the typical statistical quantity derived from observational data is the 2-point correlation function of the cluster or equivalently the mean surface density of companion stars ξ as function of separation r.

Larson (1995) found that in the Taurus star-forming region the mean surface density of companions follows a power law as function of separation with a break in the slope at the transition from the binary to the large-scale clustering regime. This analysis has also been applied to other star-forming regions (Simon, 1997; Bate et al., 1998). Larson identified the transition separation with the typical Jeans length in the molecular cloud. For Taurus this may be true, but is is probably a coincidence; in Orion this conclusion fails. In general, it can be shown that the transition separation depends on the volume density of stars, the extent of the star-forming regions along the line-of-sight, the volume-filling nature of the stellar distribution and on the details of the binary distribution (Bate et al., 1998). Additionally, the transition separation evolves in time due to dynamical interactions amongst the cluster members. Note that the 2-point correlation function is not unique. It cannot differentiate between hierarchical (fractal) and non-hierarchical structure, and different stellar distributions may lead to the same 2-point correlation function. Therefore, the analysis of the spatial distribution by eye is very important for a meaningful interpretation of ξ. Alternatively, to obtain quantitative results, the calculation of higher-order correlation functions may be useful, which is common in studying the large-scale structure of the universe (Peebles, 1993). Unfortunately, the stellar distributions in star-forming regions typically have been analyzed in terms of correlation functions only to the lowest order. Hence, in the comparison with observational data we also restrict our analysis of the spatial distribution of protostars in our models to calculating the lowest-order correlation function.

Figure 6.15 plots the mean surface density of companions ξ as function of separation r for the protostellar cluster that forms in the standard model T01N2-A at five different times of its evolution. At each point in time, the left panel gives the spatial distribution of the protostellar clusters projected in the xy, xz- and yz-plane. The resulting functions ξ for each projection are shown in the right panel. Figure 6.16 gives the same information for the high-resolution simulation T01N2-I. The two figures reveal the following trend: The first cores form relatively homogeneously distributed with large separations and a small binary fraction. Note, that if altogether 50 protostellar cores would form and if they were distributed randomly throughout the entire region, the projected number of companions per unit area would $50/4 = 12.5$. The value of the plateau of the mean surface density of companions describing the large-scale clustering at separation between 0.1 and 0.5 is approximately of this order. At the intersections of filaments clumps which already contain one or more cores may merge, forming larger clumps which subsequently contain a cluster of cores. As a result of this process, in Fig. 6.15b one sees several small aggregates distributed throughout the simulated volume. Within these small, dense clusters close encounters between protostars are very frequent and dominate the dynamical evolution (see Sec. 6.4.2). Binary and higher-order multiple systems form and determine the function ξ at very small separations. During the progression of the evolution, the small

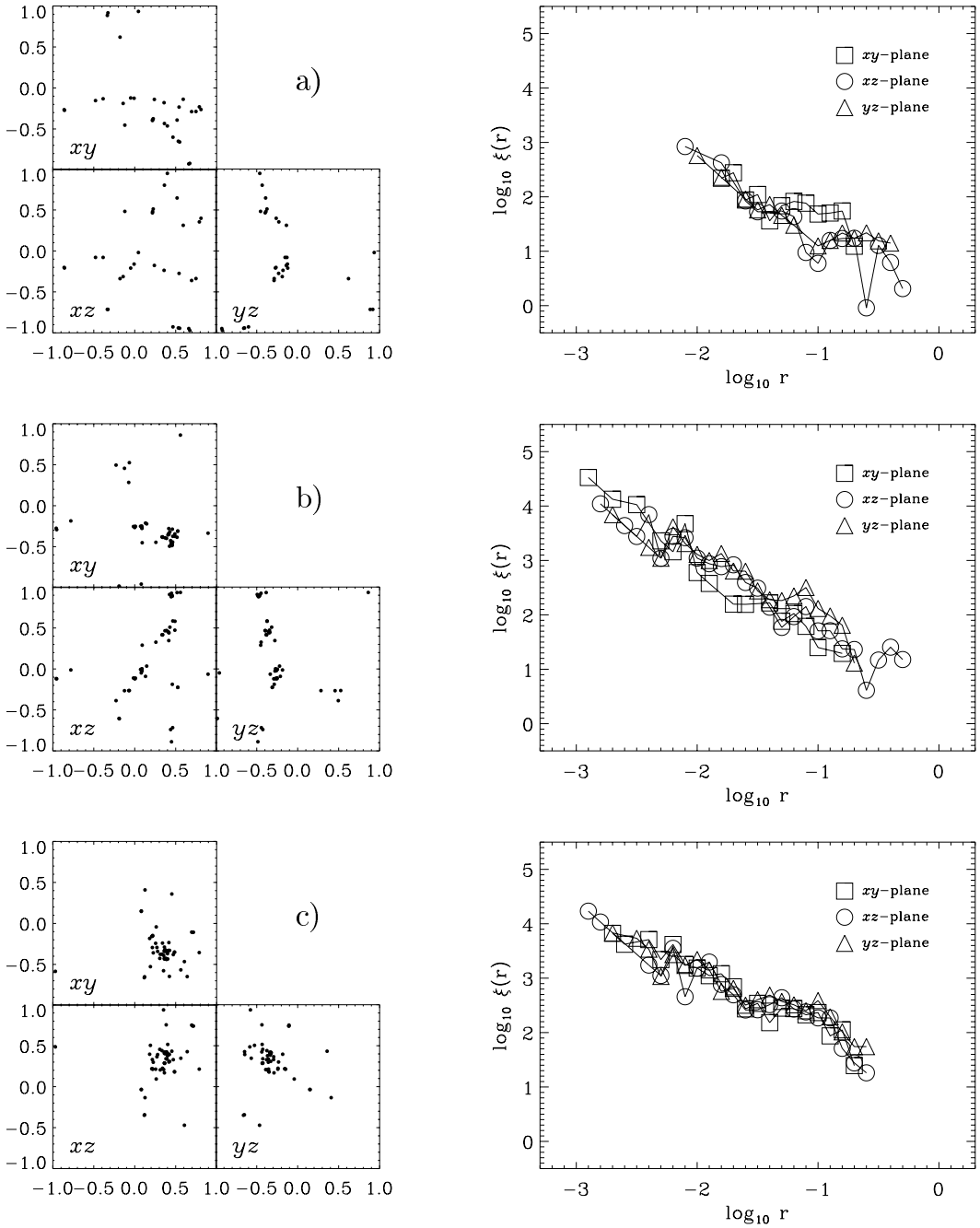

Figure 6.15: Clustering properties of the protostellar cluster. The left panel plots the location of protostellar cores projected into the xy-, the xz- and yz-plane, respectively, for the model T01N2-A at (a) $t = 1.0$, (b) $t = 2.0$ and (c) $t = 3.0$. The right panel shows the projected mean surface density of companions ξ for protostellar cores as function of separation r. (The figure is continued on the next page.)

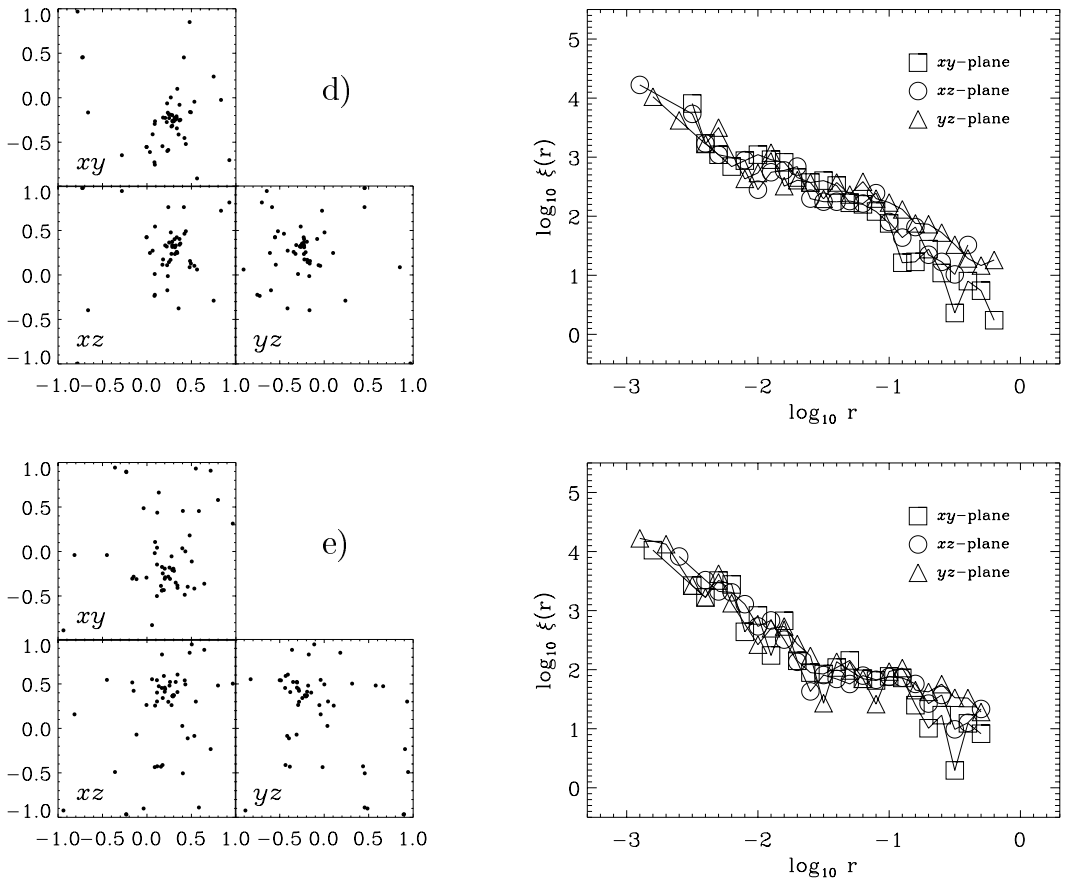

Figure 6.15 — continued: Projection of the location of protostellar cores in model T01N2-A into the xy-, the xz- and yz-plane, respectively (left panel) at (d) $t = 4.0$ and (e) $t = 5.0$. Projected mean surface density of companions ξ as function of separation r (right panel).

protostellar aggregates follow the streaming motion of their surrounding gas envelopes and merge, thereby forming a single bound cluster (see Fig. 6.15c), the protostellar system has reached a state of minimum spatial extent. At that stage about 90% of the available gas has been accreted and the subsequent evolution of the cluster is almost entirely determined by gravitational interaction. It behaves like a pure N-body system: it expands again and rapidly develops the core/halo structure typical for collision-dominated self-gravitating N-body systems (see e.g. Binney & Tremaine, 1987). This process is expedited by the fact that cores which have been accelerated to high velocities by close encounters with hard binaries cannot leave the simulation box due to the periodic boundary conditions. Once they have trespassed the boundaries of the cube, they are reinserted at the opposite side with the same velocity and may again interact with other cluster members to transfer energy to more slowly moving cores. In reality they would be ejected from the cluster and leave the star-forming cloud. At these late stages of the evolution, a clear change

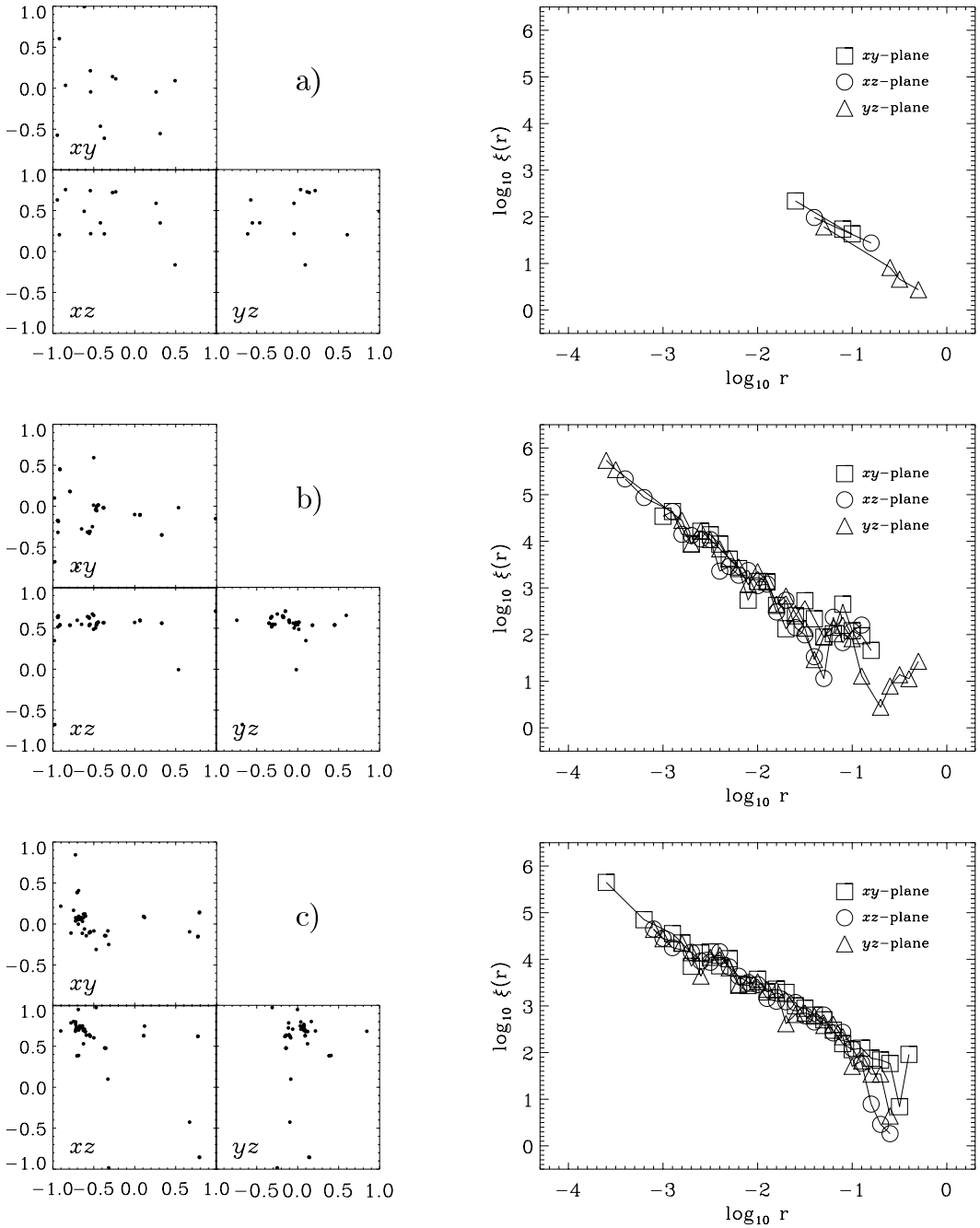

Figure 6.16: Clustering properties if the protostellar cluster in the high-resolution model T01N2-I. Again, the left panel plots the location of protostellar cores projected into the xy-, the xz- and yz-plane, respectively, at (a) $t = 1.5$, (b) $t = 2.5$ and (c) $t = 3.5$. The right panel shows the projected mean surface density of companions ξ for protostellar cores as function of separation r.

in the slope of the function ξ can be seen at the break between the binary regime and the large-scale clustering (see Fig. 6.15e). This trend is not so clearly visible in Fig. 6.16. However, this model was not evolved far enough in time. Furthermore, due to the larger particle number in simulation T01N2-I, the gravitational softening and the smoothing radius are smaller by a factor of $\gtrsim 2$ and the cluster becomes more compact. The break between the binary and the clustering regime will occur at somewhat smaller separations and higher densities.

Like in observed stellar clusters, the mean surface density of binary companions on average decreases with separation as $1/r^2$. This behavior is a result of the distribution of binary separations being approximately flat in logarithm. Duquennoy & Mayor (1991) analyzed a sample of nearby G-dwarfs and found that the distribution of orbital periods of binary stars in their sample follows approximately a broad Gaussian with a peak at $\sim 10^{4.8}$ days[1]. We have shown in Fig. 6.13 that also in our models the logarithmic distribution of angular momenta is relatively flat and very broad as well, spanning at least three orders of magnitude. If we assume that rotating protostellar cores typically break up into binary systems (see Sec. 2.2) we also would expect the distribution of orbital periods to be very broad without significant peaks. Similar to the mass distribution which also is very broad and relatively flat (see Sec. 6.5), this may follow as the result of the stochastical processes which determine the formation and evolution of protostellar cores, and therefore the distribution of their angular momenta as well. However, we cannot follow the detailed evolution and subfragmentation of individual condensed cores and this picture may be highly speculative. For the same reason, our model is not able to describe the formation of close binaries. The binary systems of protostellar cores in our simulations could only correspond to the very wide binaries in the observed distribution.

6.4.5 Boundedness of Protostellar Clusters

In every simulation described in this chapter, the dynamical evolution of the gas results in the formation of a dense cluster of protostars (see Fig.'s 6.2 and 6.3, and the left panels of Fig.'s 6.15 and 6.16). These clusters are bound throughout their entire evolution.

[1]The sample of Duquennoy & Mayor (1991) comprises 164 G-dwarfs or equivalently 82 binary systems. The distribution of orbital periods P can be approximated by a broad Gaussian-type relation, $f(\log_{10}) \propto \exp\left[-1/2\,(\log_{10} P - \langle\log_{10} P\rangle)^2/\sigma^2_{\log_{10} P}\right]$, which centers at $\langle\log_{10} P\rangle = 4.8$ and has a width of $\sigma_{\log_{10} P} = 2.3$. The period P is given in days. The mass ratio q between secondary and primary star in each system is $q \approx 0.2$. Since the typical mass of G-dwarfs is $\sim 1\,\mathrm{M}_\odot$, Keplers 3rd law implies that an orbital period of $P = 10^{4.8}$ days corresponds to semi-major axis of ~ 32 AU. From the broad distribution of orbital periods (in $\log_{10} P$) follows immediately a broad distribution of binary separations $\log_{10} r$, which to the lowest order can be approximated as being flat, i.e. $dN/d\log_{10} r = K$. Then, $dN = K/r\ dr$ is the number of binary companions with separations in the range r to $r + dr$ and the mean surface density of companions in the 2-dimensional projection follows as $\xi(r) = N^{-1} dN/(2\pi r dr) = N^{-1} K/(2\pi r^2) \propto 1/r^2$.

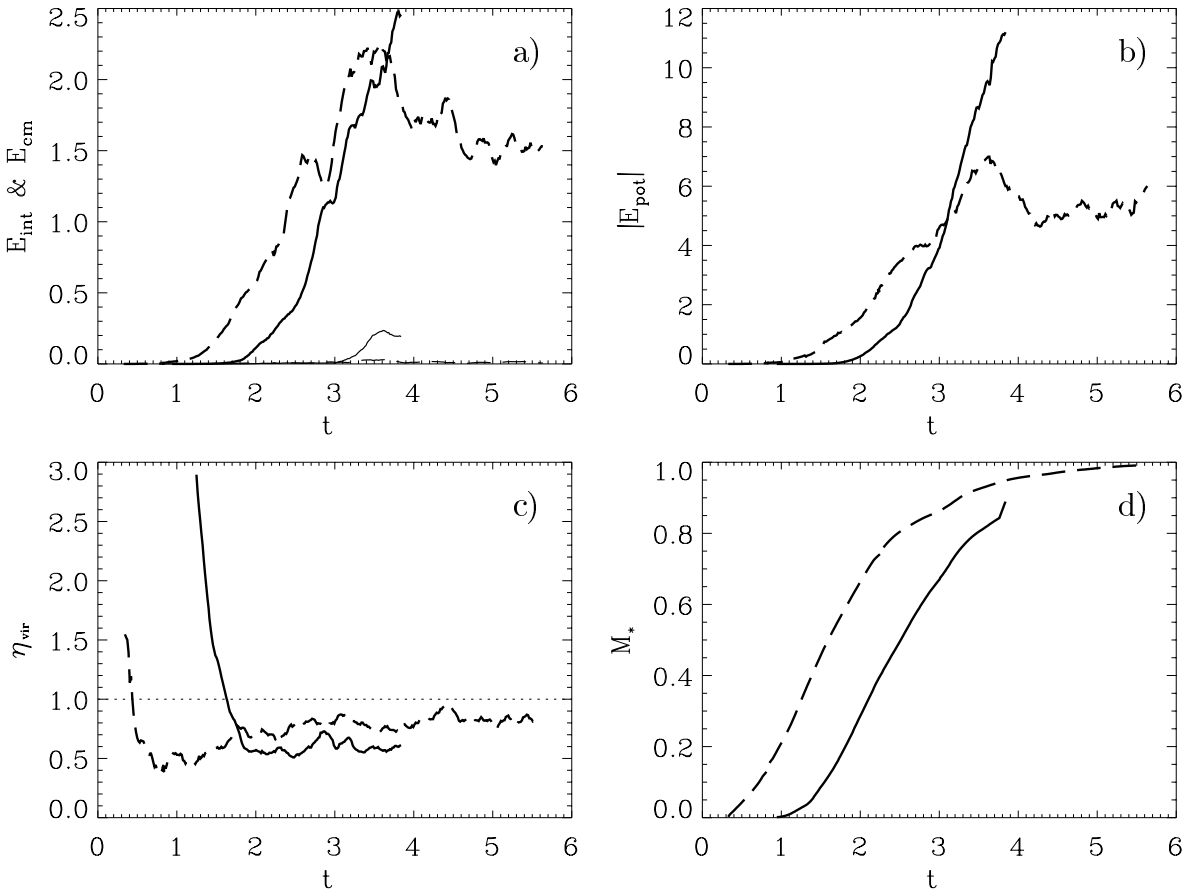

Figure 6.17: For the protostellar clusters that form in model T01N2-A (dashed lines) and model T01N2-I (solid lines): Time evolution of (a) the total kinetic energy, subdivided into the contribution from random motions $E_{\rm int}$ (thick lines) and from the center-of-mass motion $E_{\rm cm}$ (thin lines at the bottom of the plot), (b) the potential energy $E_{\rm pot}$, (c) the virial coefficient $\eta_{\rm vir} \equiv 2E_{\rm int}/|E_{\rm pot}|$, and (d) the cumulative mass $M_{\rm tot}$ of the cluster.

To specify this in more detail, Fig. 6.17a plots for the protostellar clusters forming in simulation T01N2-A (dashed lines) and T01N2-I (solid lines) the time evolution of the total kinetic energy subdivided into the contribution from the internal velocity dispersion (thick line) and from the center-of-mass motion (thin line). The kinetic energy is almost entirely dominated by the internal random motions of the cluster members. In Fig. 6.17b, the evolution of the potential energy is given. The cluster in the high-resolution model T01N2-I (solid lines) is still in its contraction phase when the simulation stops at $t = 3.9$. The cluster in T01N2-A does evolve further, it develops the typical core/halo structure of collisional N-body systems. The global virial coefficient $\eta_{\rm vir} \equiv 2E_{\rm int}/|E_{\rm pot}|$ is plotted in Fig. 6.17c. Once the clusters has formed it always is marginally bound, i.e. $\eta_{\rm vir} \lesssim 1$. These conclusions do not change when taking into account only the cores that lie within the half-mass radius of the clusters. The cumulative mass of the clusters is given in Fig. 6.17d.

During the formation of the cluster, the conversion of gas into dense protostellar cores is such that the decrease of potential energy is always more or less balanced by the increase of kinetic energy, even at very early times when the gravitational potential is strongly dominated by the gas. If the gas suddenly were removed, the cluster of protostellar cores would still remain bound. This is an intrinsic feature of the larger-scale isothermal collapse. The 3-dimensional velocity dispersion and the line-of-sight velocity dispersion of the two clusters at any time of their evolution are described in Fig.6.18, again the dashed line denotes model T01N-A and the solid line model T01N1-I. The line-of-sight velocity dispersion of young stellar clusters is an important observable containing information about their dynamical state and future evolution. The fact that in our models the line-of-sight measurements along the different axes are almost identical to each other indicates again that the cluster is kinematically well mixed and isotropic. When scaled to low-density star-forming regions like Taurus, a dimensionless value of $\sigma = 1$ corresponds to $2.2\,\mathrm{km\,s^{-1}}$. In the case of a high-density region, this corresponds to $3.0\,\mathrm{km\,s^{-1}}$ (see Chap. 4). The values calculated from our simulations are in agreement with the measurements in Taurus and in the Trapezium cluster in Orion which both have comparable velocity dispersions of $\sigma \approx 2.5\,\mathrm{km\,s^{-1}}$ (for Taurus see Frink et al. 1997, and for Orion Jones & Walker 1988). However, for very high core-formation efficiencies, say when more than 60% of the gas has been converted into condensed cores, the derived velocity dispersions appear to be too high. This may be used to constrain the core-formation efficiency in our models.

6.5 Implications for the IMF

In this section, the time evolution and the properties of the mass distribution of protostellar cores in our simulations and their relation to the initial stellar mass function are discussed. As analyzed in the previous sections, protostellar cores form in the centers of Jeans-unstable massive gas clumps and grow in mass via competitive accretion. This process is strongly influenced by the presence of unpredictable dynamical events which determine the shape of the mass spectrum. In Fig. 6.5 the mass distribution of identified gas clumps and protostellar cores in the high-resolution model T01N2-I has been introduced at four different stages of the dynamical evolution of the system, i.e. initially and when 10%, 30% and 60% of the available gas has been converted into condensed cores. Whereas the mass spectrum of gas clumps is best described by a power-law function, the distribution of core masses follows a Gaussian. Again for the high-resolution model, Fig. 6.19 concentrates on protostellar cores only and plots their mass distribution at times when the cluster of cores has accreted a total mass fraction of (a) $M_* = 5\%$, (b) 15%, (c) 30%, (d) 45%, (e) 60%, and (f) 85%. Spanning two orders of magnitude, the mass distribution of protostellar cores is very broad and peaks approximately at the overall Jeans mass of the system, $\langle M_\mathrm{J} \rangle = 1/222 = 10^{-2.3}$ (see Chap. 4).

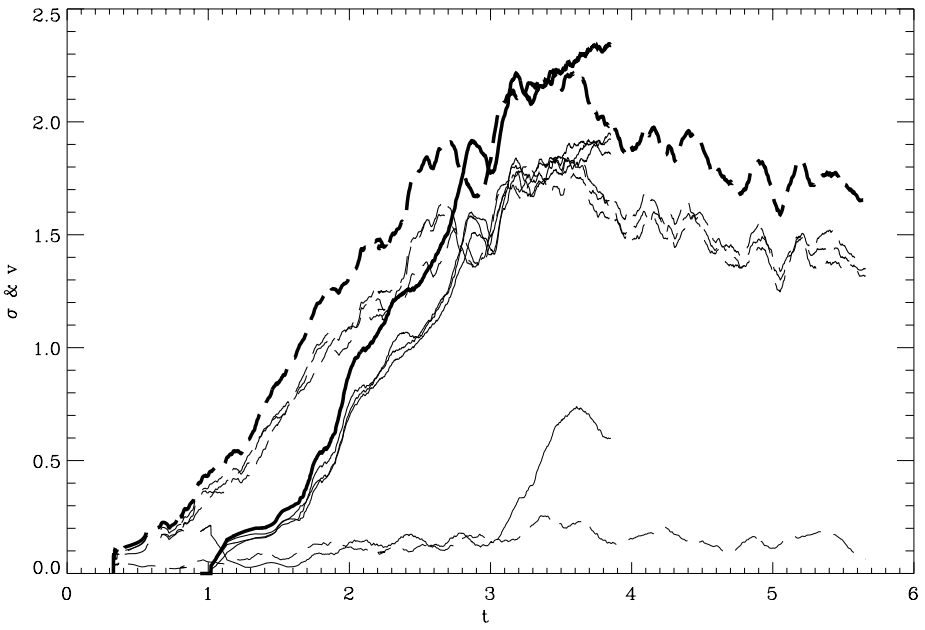

Figure 6.18: Time evolution of the total (3-dimensional) velocity dispersion σ (thick lines), of the line-of-sight velocity dispersion along the x-, y- and z-axis (thin lines) and of the center-of-mass velocity (thin lines at low velocities) of the protostellar cluster that forms during the dynamical evolution of the standard model T01N2-A (dashed curves) and the high-resolution model T01N2-I (solid curves).

This is somewhat surprising, given the complexity of the overall dynamical evolution. The Jeans mass is a function of density and may vary strongly for different clumps. In a statistical sense, the system retains 'knowledge' of its (initial) average properties: the 'typical' core mass is identical with the 'typical' Jeans mass. In the initial conditions the density contrast is relatively small, there was no time for non-linear growth. Hence, the gravitationally unstable clumps (in Fig.'s 6.4 or 6.5 these are located to the right of the tilted line indicating the Jeans limit as function of density) all have densities comparable to the mean density of the system, i.e. their Jeans mass is $\sim \langle M_{\rm J} \rangle$. These clumps form the first generation of cores which will become very massive and populate the upper end of the mass spectrum. At later stages, smaller clumps may have gained densities high enough to become Jeans unstable. They too begin to collapse and due to their small masses they will form cores preferably at the low-mass part of the spectrum. As long as there is enough gaseous material available, the growth rate of already existing cores to larger masses and the formation rate of new low-mass cores are comparable and the mass distribution evolves symmetrically (Fig. 6.19a – e). However, at very late stages of the evolution, the distribution gets skewed towards higher masses which is an effect of the depletion of the gas reservoir. There is still mass available for accretion, but it is not sufficient to form new cores (see Fig. 6.19a – f). The fact that the total gas reservoir is

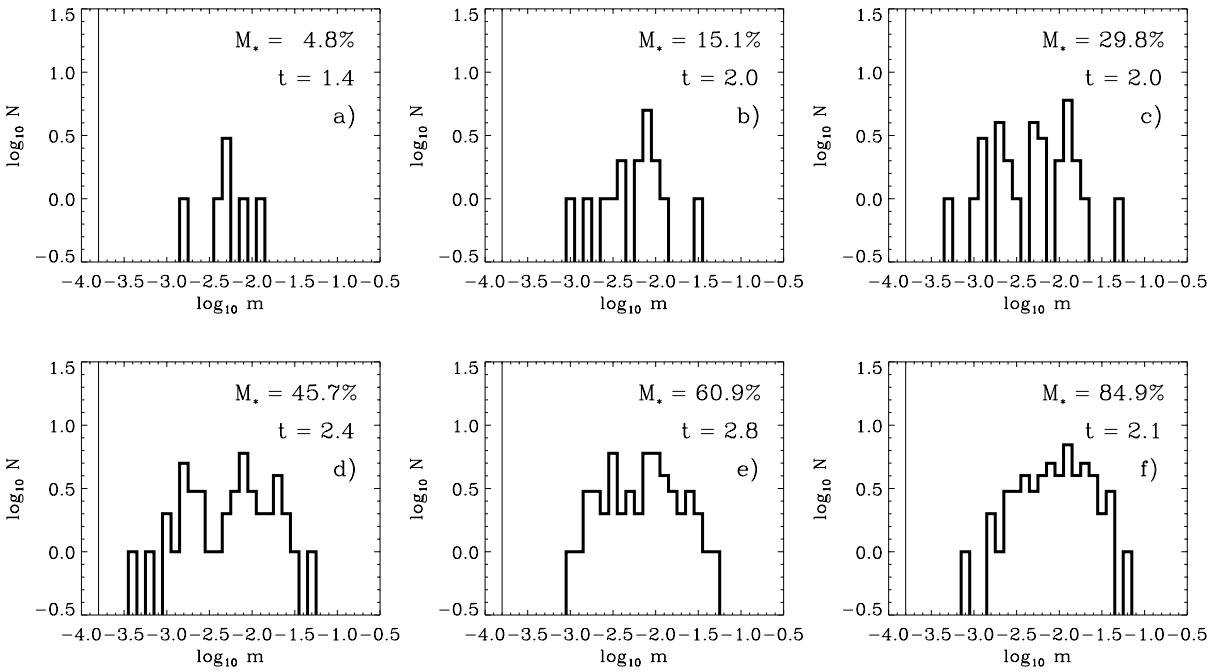

Figure 6.19: Mass distribution of protostellar cores in the high-resolution model T01N2-I at different stages of the dynamical evolution. In the upper right corner of each plot, the time t and the fraction of the total gas mass converted into protostellar cores M_* is indicated. Analogous to Fig. 6.3, the vertical line indicates the resolution limit of the simulation.

limited not only modifies the shape of the distribution, it also influences its peak value. At early stages, the median core mass is slightly below the average Jeans mass, at late stages it lies above (see also Tab. 6.2). Competitive accretion and the dynamical interaction of protostellar cores as members of dense clusters (see Sec. 6.4.2) do not alter the shape of the mass distribution, but may widen it further.

Figure 6.20 presents the mass spectra of protostellar cores for *all* simulations discussed in this chapter (see Tab. 6.1) at the time at which roughly 60% of the gas is accumulated in protostellar cores. The distributions are very similar and the variations in widths and centroid are small. Since the data for observed protostellar cores are not sufficiently accurate to determinate their mass distribution[2], we have to go one step further and compare the core mass spectrum with the initial mass function of stars (IMF) when applying the results of our simulations to star-forming regions. The present simulations cannot resolve the conversion of individual protostellar cores into stars. Since detailed collapse simulations show that perturbed cores tend to break up into multiple systems (typically binaries, see Sec. 2.2.2), we can only make predictions about the mass function of

[2]One of the most detailed determinations of the masses of pre-stellar cores is by Motte et al. (1998), who studied a sample of ~ 60 objects in the ρ-Ophiuchus cloud (see their Fig. 5).

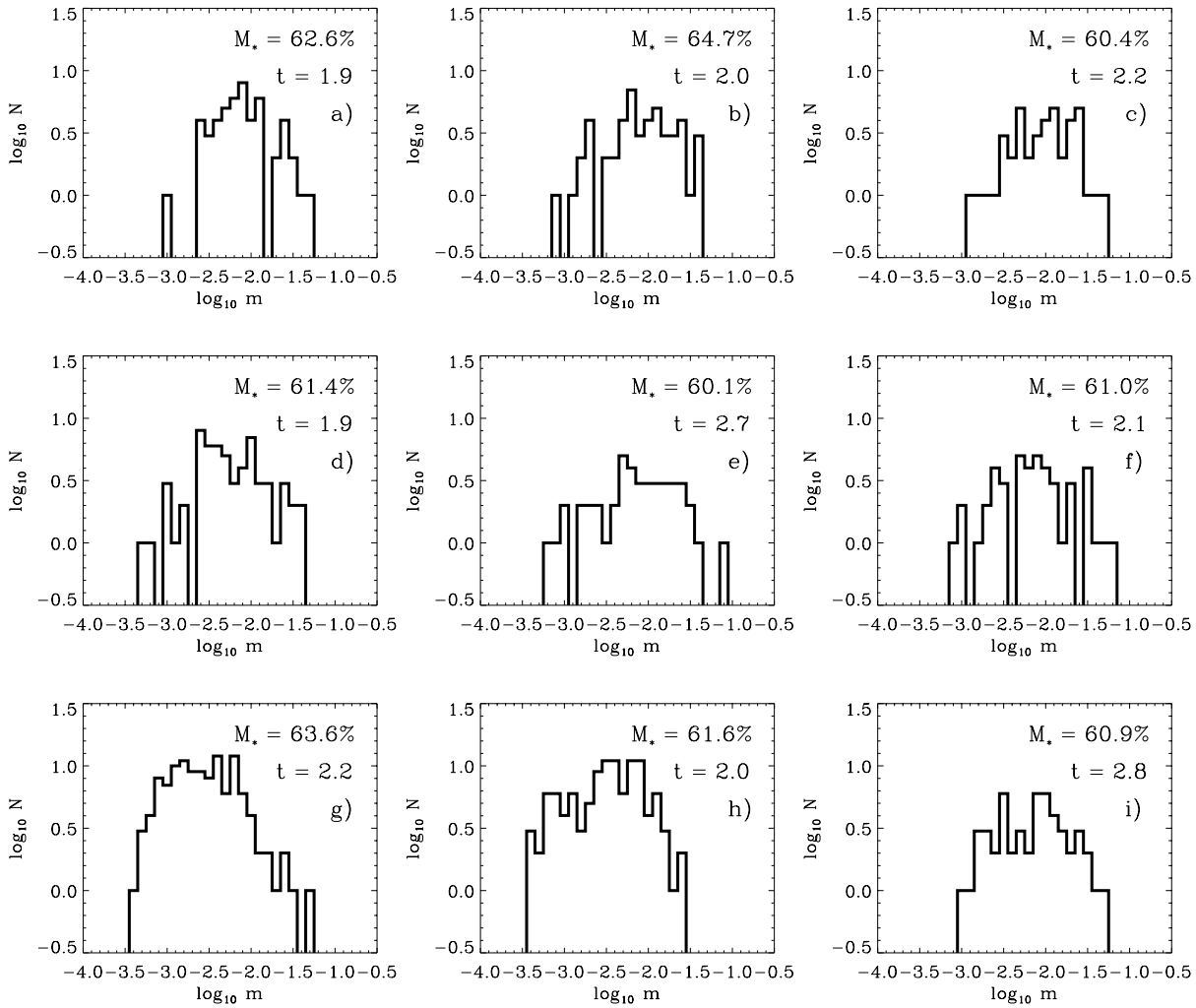

Figure 6.20: Distribution of protostellar core masses for all models described in this chapter (Tab. 6.1) at the stage when roughly 60% of the gas mass is accumulated in condensed cores: (a) corresponds to model T01N2-A, (b) to model T01N2-B, and so forth.

multiple systems. We adopt the IMF for multiple stellar systems (i.e. without corrections for binary stars and higher-order systems) from Kroupa et al. (1990) – see Sec. 2.3, Eqn.'s 2.4 and 2.5 – which we compare with our numerically obtained core mass distribution. For this comparison, we assume that the mass of the multiple stellar system that forms within a condensed core is roughly proportional to the core mass, $m_{\rm star} = \eta_{\rm core \rightarrow star} \times m_{\rm core}$, where $\eta_{\rm core \rightarrow star}$ is the core star-formation efficiency. Its value is determined by the subfragmentation of cores, the physical processes in the accretion disk, and the subsequent dispersion of the protostellar envelope through the action of stellar radiation, winds and outflows (e.g. Adams & Fatuzzo, 1996). Besides through internal evolution, $\eta_{\rm core \rightarrow star}$ may

also be influenced by environmental effects, e.g. by the UV radiation of nearby massive O or B stars. Taking the best-fitting log-normal functional form of Kroupa et al. (1990) with the peak of the distribution located at $m_0 = 0.23\,\mathrm{M}_\odot$ and the width being $\sigma = 0.42\,\mathrm{M}_\odot$ we can estimate the core star-formation efficiency $\eta_{\mathrm{core}\rightarrow\mathrm{star}}$ for our numerical models. In order to do this, we have to determine a physical scaling for the simulations. Since we are interested in a mass scale, we determine the Jeans mass M_J. The Jeans mass in 'typical' star-forming molecular clouds is roughly $1\,\mathrm{M}_\odot$, which for example corresponds to a density of $n(\mathrm{H_2}) = 10^5\,\mathrm{cm}^{-3}$ and a temperature of $T = 11$ K, assuming a mean molecular weight $\mu = 2.26$ (see Chap. 4). For a given Jeans mass, we obtain the peak of the core mass spectrum by fitting a log-normal function to the distribution, i.e. we calculate the centroid and the width of the appropriate Gaussian in $\log_{10} m$. The correct core star-formation efficiency $\eta_{\mathrm{core}\rightarrow\mathrm{star}}$ is the factor necessary for the peak of this distribution to overlap with the observed distribution derived by Kroupa et al. (1990).

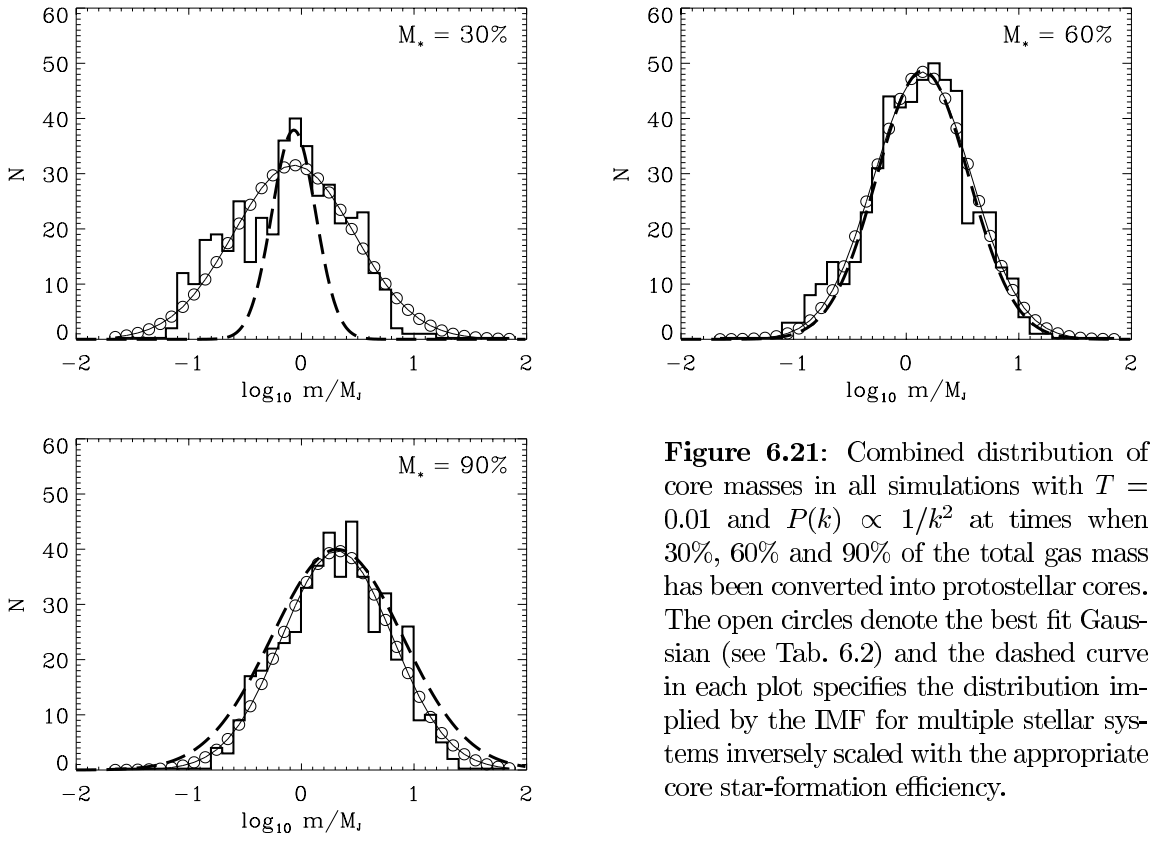

Figure 6.21: Combined distribution of core masses in all simulations with $T = 0.01$ and $P(k) \propto 1/k^2$ at times when 30%, 60% and 90% of the total gas mass has been converted into protostellar cores. The open circles denote the best fit Gaussian (see Tab. 6.2) and the dashed curve in each plot specifies the distribution implied by the IMF for multiple stellar systems inversely scaled with the appropriate core star-formation efficiency.

To allow for a statistically significant comparison with observational data, before applying the above scheme we merge together the mass spectra of all nine models with $T = 0.01$ and $P(k) \propto 1/k^2$. This is done in Fig. 6.21 at three stages of the evolution, when the frac-

tion of mass in protostellar cores is $M_* = 30\%$, $M_* = 60\%$, and $M_* = 90\%$, respectively. The histogram in each plot shows the combined distribution of all protostellar cores at the appropriate times. The masses on the abscissa are scaled logarithmically, whereas the ordinate is scaled linearly. Denoted by open circles are the best-fit Gaussian functions. The optimal values for the location of the center and the width are specified in Tab. 6.2. Using a χ^2-estimator for the quality of the fit (last line of Tab. 6.2), the Gaussian fit function for the $M_* = 30\%$ mass distribution has to be rejected on the basis of the commonly used 95% significance level, whereas at the later stages of the dynamical evolution the core mass spectrum is well approximated by a Gaussian. We convert the log-normal

		Optimum fit parameters					
	KTG90	$M_* = 30\%$		$M_* = 60\%$		$M_* = 90\%$	
a) $\log_{10} m_0$		−0.068		0.147		0.319	
b) $\log_{10} \sigma$		0.537		0.435		0.491	
c) $\eta_{\mathrm{core}\to\mathrm{star}}$		*0.27*		*0.16*		*0.11*	
		$\times 1$	$\times\eta_{\mathrm{core}\to\mathrm{star}}$	$\times 1$	$\times\eta_{\mathrm{core}\to\mathrm{star}}$	$\times 1$	$\times\eta_{\mathrm{core}\to\mathrm{star}}$
d) μ in $\mathrm{M}_\odot$	**0.23**	0.86	**0.23**	1.40	**0.23**	2.08	**0.23**
e) σ in $\mathrm{M}_\odot$	**0.42**	3.44	**0.93**	2.72	**0.44**	3.03	**0.34**
f) $P(>\chi^2)$		$< 10^{-6}$		0.22		0.15	

Table 6.2: Estimated values for the core star-formation efficiency and parameters of the optimum Gaussian fits for the combined core mass distribution in Fig. 6.21: (a) The locations of the centroids and (b) of the full width at half maximum of the Gaussian fit curves given in units *normalized* to the average Jeans mass of the system. (c) Core star-formation efficiency $\eta_{\mathrm{core}\to\mathrm{star}}$ necessary for the peaks of the observed IMF for multiple stellar systems (from Kroupa et al., 1990) and the best-fit Gaussian curve to agree, assuming a *physical* Jeans mass of $M_\mathrm{J} = 1\,\mathrm{M}_\odot$. (d) Peak location and (e) width of the Gaussian fit curves converted in solar masses (again assuming $M_\mathrm{J} = 1\,\mathrm{M}_\odot$). The column denoted KTG90 lists the values from (Kroupa et al., 1990). For each of the simulated distributions, the column denoted by '$\times 1$' gives values for the *core* mass spectrum itself and the column indicated by '$\times\eta_{\mathrm{core}\to\mathrm{star}}$' the corresponding (multiple) *stellar* mass spectrum adopting the appropriate core star-formation efficiency $\times\eta_{\mathrm{core}\to\mathrm{star}}$. The quantities emphasized by bold face have to be compared with each other. Finally, (f) specifies the quality of the Gaussian fit for the numerically obtained core mass spectrum. Using a χ^2-test, the quantity $P(>\chi^2)$ specifies the probability to obtain fit residuals $\chi^2 = \sum_i \chi_i^2$ larger than the computed value, assuming that the errors follow a normal distribution. The very low probability for the case $M_* = 30\%$ indicates that the distribution is very badly described by a simple Gaussian curve. However, at later stages of the dynamical evolution the high values $P(>\chi^2)$ suggest an excellent agreement.

IMF for multiple systems (Kroupa et al., 1990) into a mass distribution of protostellar cores (dashed lines), by scaling with the inverse of the appropriate core star formation efficiency $\eta_{\rm core\rightarrow star}$ such that its peak agrees with the numerical distribution (denoted by open circles): $m \longrightarrow \eta^{-1}_{\rm core\rightarrow star} \times m$ and $\sigma \longrightarrow \eta^{-1}_{\rm core\rightarrow star} \times \sigma$. For the distribution $M_* = 30\%$, the numerically calculated mass distribution is clearly wider than the mass spectrum implied by the observed IMF. However, for $M_* = 60\%$, the agreement in width is excellent: assuming the appropriate efficiency, the numerically calculated core spectrum would convert into a stellar mass spectrum that is indistinguishable form the observed one. For the case $M_* = 90\%$, this procedure would lead to a stellar mass spectrum that is slightly too narrow in width. However, given the uncertainties involved in obtaining the IMF (see Sec. 2.3) this deviation is too small to be significant. In summary, at their late evolutionary stages our models of self-gravitating isothermal gas predict a universal initial mass function with a log-normal functional form which agrees well with the observational data.

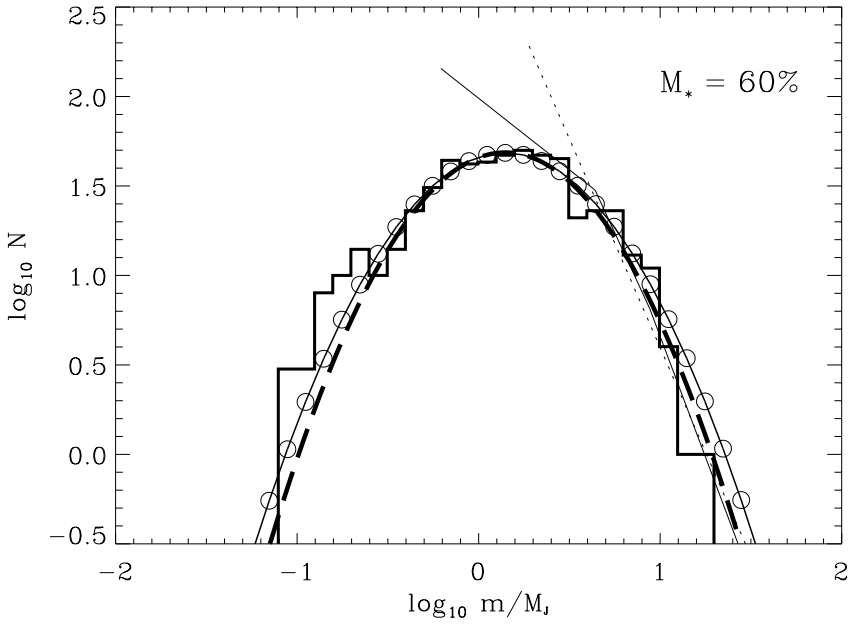

Figure 6.22: Comparison of the cumulated core mass spectrum at the stage $M_* \approx 60\%$ with different observationally based models for the IMF. Masses are scaled to the overall Jeans mass of the system. The open circles denote the best-fit Gaussian curve. It agrees very well with the core mass spectrum implied by the observed IMF of multiple stellar systems using $\eta_{\rm core\rightarrow star} = 0.16$. For comparison, the IMF for single stars (Kroupa et al., 1993) is given by the thin solid line, and the Salpeter (1955) IMF by the thin dotted line. These functions are scaled such that they fit the high-mass end of the mass distribution.

The best fit is reached at stages of the evolution at which roughly $M_* \approx 60\%$, i.e. for a core-formation efficiency $\eta_{\rm gas\rightarrow core} = 0.6$. This is described in detail in Fig. 6.22, which

shows the distribution $\log_{10} N(\log_{10} m)$ and overlays the best-fit Gaussian curve (open circles) and the core mass spectrum implied by the observed IMF of multiple stellar systems using $\eta_{\rm core\rightarrow star} = 0.16$. As reference, also values for the multiple power-law IMF for single stars (Kroupa et al. 1993; solid thin line) and the mass function from Salpeter (1955) (dotted thin line) are given. These curves are scaled such that they fit the high-mass end of the distribution. As expected, neither of the latter two mass functions agrees with the numerically obtained distribution.

As discussed in Sec. 2.3, the star formation process probably can only be understood in the frame work of a probabilistic theory, where a sequence of statistical events may naturally lead to a log-normal IMF. Since the final mass distribution of protostellar cores in our self-gravitating, isothermal models is a consequence of the chaotic kinematical evolution during the accretion phase, our simulations strongly support this hypothesis.

For a physical Jeans mass $M_{\rm J} = 1\,{\rm M}_\odot$, our dynamical models of isothermal, self-gravitating gas predict an overall star-formation efficiency $\eta_{\rm tot} = \eta_{\rm gas\rightarrow core} \times \eta_{\rm core\rightarrow star}$ of roughly 10%. For $M_* = 60\%$ we obtain $\eta_{\rm tot} = 0.16 \times 0.6 = 0.096$ and for $M_* = 90\%$ follows $\eta_{\rm tot} = 0.11 \times 0.9 = 0.099$. If we assume different values for the physical Jeans mass, the efficiencies have to be scaled accordingly. For example, in regions with $M_{\rm J} = 0.5\,{\rm M}_\odot$ the overall star-formation efficiency would be twice as large ($\eta_{\rm tot} \approx 0.2$) and for clouds with $M_{\rm J} = 2\,{\rm M}_\odot$ we obtain $\eta_{\rm tot} \approx 0.05$. These values agree well with observationally derived numbers and with theoretical derivations. Adams & Fatuzzo (1996) for example, predict efficiencies $\eta_{\rm tot} \approx 0.07$ (see also Sec. 2.3).

6.6 Summary

In this chapter, results from altogether nine isothermal SPH simulations with $T = 0.01$ and initial fluctuation spectra $P(k) \propto 1/k^2$ have been presented. In every model for the dynamical evolution and fragmentation of molecular clouds, the interplay between self-gravity and gas pressure leads to the formation of a complex network of filaments and clumps, some of which are gravitationally unstable and collapse to form protostellar cores. Gravitational action alone can produce clump-mass spectra and clump shapes that agree well with the observed data. Once protostellar cores have formed, they grow in mass via accretion from their gaseous environment and build up a hierarchically structured cluster. The evolution of this cluster and the properties of individual cores are determined by highly unpredictable statistical events. In the calculations presented here, we find several trends. The protostellar cores that form first are generally formed in the clumps with the highest initial density, and tend to have the highest final masses. Cores that form later, form from gas that was initially in low-density clumps or distributed gas which streamed towards a common center of gravity where enough mass could accumulate to exceed

the Jeans limit. Overlaid on these general trends are dynamical interactions between individual cores which can terminate the accretion onto a core by ejecting it from its parental clump, thus setting its final mass.

The excellent agreement between the numerically-calculated mass function and the observed IMF for multiple stellar systems predicts an overall star-formation efficiency of about 10% and suggests that gravitational fragmentation and accretion processes dominate the origin of stellar masses. It strongly supports the hypothesis that the stellar initial mass function is resulting from a sequence of statistical events which may naturally lead to a log-normal IMF (see Sec. 2.3). Using numerical simulations, it is possible to identify some of the underlying processes which contribute to the form of the stellar initial mass function.

Chapter 7

A Parameter Study

One of the goals of this dissertation is to understand how the formation of protostellar clusters is influenced by environmental and initial conditions. To address this issue, we perform computations for a large number of different initial density distributions (Sec. 7.1) and a wide range of temperatures (Sec. 7.2). Within the framework of isothermal gas physics, these are the parameters that determine the dynamical behavior of the system. The results of this parameter study are sumarized in Sec. 7.3.

7.1 Dependence on the Power Spectrum

In this section we analyze the dependence of the fragmentation of a region inside a molecular cloud and of the properties of the protostellar cluster that forms during the dynamical evolution on the choice of the initial fluctuation spectrum $P(k) \propto 1/k^N$. Again for models with $T = 0.01$ which contain 222 Jeans masses, we compare the evolution of the system for different values of N, ranging from $N = 0$ which means that fluctuations of all wave lengths k have statistically the same amplitude, to the very steep power spectrum $N = 3$ which implies strong dominance of the large-scale modes. For $N = 0$, the initial density distribution looks quite homogeneous, whereas it is strongly biased towards having one dominant density peak in the case of $N = 3$. Additionally, for $N = 1$ we study the case of a truncated spectrum where fluctuations on scales $k < 4$ have been removed. For a comparison of the initial density fields with different power spectra see Fig. 7.1. The parameters of all models discussed in this section are listed in Tab. 7.1.

Table 7.1: Models with $T = 0.01$ and different initial power spectra $P(k) \propto 1/k^N$ with $N = 0$, 1, 2, or 3.

Temperature	Exponent	Particles	Initial[a]	Zel'dovich[b]	Identification
$T = 0.01$	$N = 0$	200000	random	$\delta t = 1.5$	T01N0-A
$T = 0.01$	$N = 1$	200000	random	$\delta t = 1.5$	T01N1-B
$T = 0.01$	$N = 1$[c]	500000	random	$\delta t = 1.0$	T01N1-C
$T = 0.01$	$N = 2$[d]	200000	random	$\delta t = 1.5$	T01N2-H
$T = 0.01$	$N = 2$[d]	500000	random	$\delta t = 1.5$	T01N2-I
$T = 0.01$	$N = 3$	200000	random	$\delta t = 1.5$	T01N3-A

[a]Initial distribution for the Zel'dovich shift. A homogeneous random distribution is denoted by 'random'. [b]Shift interval δt for the Zel'dovich approach. [c]The fluctuation spectrum used to generate model T01N1-C has been truncated at small wave numbers, i.e. the initial density field contains no large-scale fluctuations. The wave length of the largest mode is 1/4 of the linear size of the volume (it contains modes with $4 \leq k \leq 32$). [d]For a complete list of simulations with $T = 0.01$ and $N = 2$ see Tab. 6.1. Here, only the two models used for this chapter are listed.

7.1.1 Dependence on the Slope of the Power Spectrum

To generate the initial density distribution for all models, we use the Zel'dovich approximation as discussed in Sec. 5. The fluctuation spectrum is chosen to be a power law $P(k) \propto 1/k^N$. Hence, the main parameter that determines the statistical properties of the initial distribution is the slope N of the fluctuation spectrum.

To examine how the variation of the slope of the initial fluctuation spectrum influences the dynamical evolution of the gas system, we generated four models with almost identical properties, but with different N: models T01N0-A, T01N1-B, T01N2-H and T01N3-A consist of 200 000 SPH particles and have been generated via the Zel'dovich method from the same initial random particle distribution applying the same shift interval $\delta t = 1.5$. However, their fluctuation spectra have slopes in Fourier space $N = 0$, $N = 1$, $N = 2$ and $N = 3$, respectively. The similarity between models T01N0-A, T01N1-B and T01N3-A is even closer. To exclude the variance effects inevitable when comparing different realizations of a fluctuation field with given statistical properties, we apply the same set of random numbers to generate the fluctuation spectrum for these three models . This means, that individual modes k in each of the three fields have identical *phases*. However, they differ in *amplitude*, since these are drawn from Gaussians with different width $P(k) \propto 1/k^N$, where $N = 0$, 1 or 3, respectively. For this reason, at comparable stages of their dynamical evolution, the three models look remarkably similar. On the other hand, for the generation of the initial particle distribution in model T01N2-H, a different set

of random numbers has been used and statistical variance leads to a different appearance. This can be seen in Fig. 7.1, which plots the 3-dimensional particle distribution for each model at different stages of the dynamical evolution. The first row denotes model T01N0-A, the second row model T01N1-B, the third one model T01N2-H and finally the fourth row model T01N3-A. Each column in the figure shows the distributions at comparable evolutionary phases, typically characterized by the mass fraction M_* accreted onto protostellar cores, as indicated at the top of each column. The first column shows the initial density distribution, the second column describes the state of the system when the maximum density contrast has reached half the value necessary for a collapsing object to be identified as protostellar core (i.e. to be converted into a sink particle – see Sec. 3.4.4), the third column shows the system when 2% of the gas mass is contained in condensed cores, and so forth.

As described earlier, the steeper the slope N of the fluctuation spectrum, the more structure has the system and the higher is its degree of inhomogeneity. The density fields of the models with $N \gtrsim 2$ are dominated by the largest-scale modes. On the other hand, for $N \lesssim 1$, fluctuations on smaller scales have sufficient amplitudes to compensate the large-scale fluctuations when the whole spectrum is added up. As a result, model T01N0-A appears more or less homogeneous and smooth initially, and its maximum density contrast is small, $\delta\rho \lesssim 3$ (with a Zel'dovich shift interval $\delta t = 1.5$). On the other extreme, the initial particle distribution of model T01N3-A is highly structured and dominated by one large and massive high-density region in the center[1]. With $\delta t = 1.5$, its maximum density contrast is very large, $\delta\rho \gtrsim 50$. The models T01N1-B with $N = 1$ and T01N2-H with $N = 2$ lie in between these extreme cases (compare also with Fig.'s 5.3 and 5.4)

Since models which are generated from fluctuation spectra with steep power-law slope are strongly structured and since their initial conditions contain already high density contrasts, their subsequent dynamical evolution with SPH, using the full set of hydrodynamical equations, proceeds faster than for models which are initially more homogeneous. This can be seen when looking at the times at which each snapshot in Fig. 7.1 is taken as indicated at the lower left corner of each cube. In the case of model T01N0-A, the dynamical evolution requires a time interval $t \approx 2.4$ to create the first condensed core. For model T01N1-B, this is the case at $t \approx 1.5$ and for T01N2-H at $t \approx 0.9$. In model T01N3-A, the central region of the dominant fluctuation initially has already a sufficiently high density so that immediately after the start of the evolution with SPH it begins to collapse and rapidly[2]forms a protostellar core within $t = 0.1$. For this reason the second column contains no entry for model T01N3-A: the formation time of the first protostellar

[1]As allowed by the periodic boundary conditions, the cube has been shifted such that it is centered on the region of highest density.

[2]Note again that the free-fall time scales with density as $\tau_{\rm ff} \propto \rho^{-1/2}$. A difference in initial density contrast of ~ 100 translates into a time difference of ~ 10.

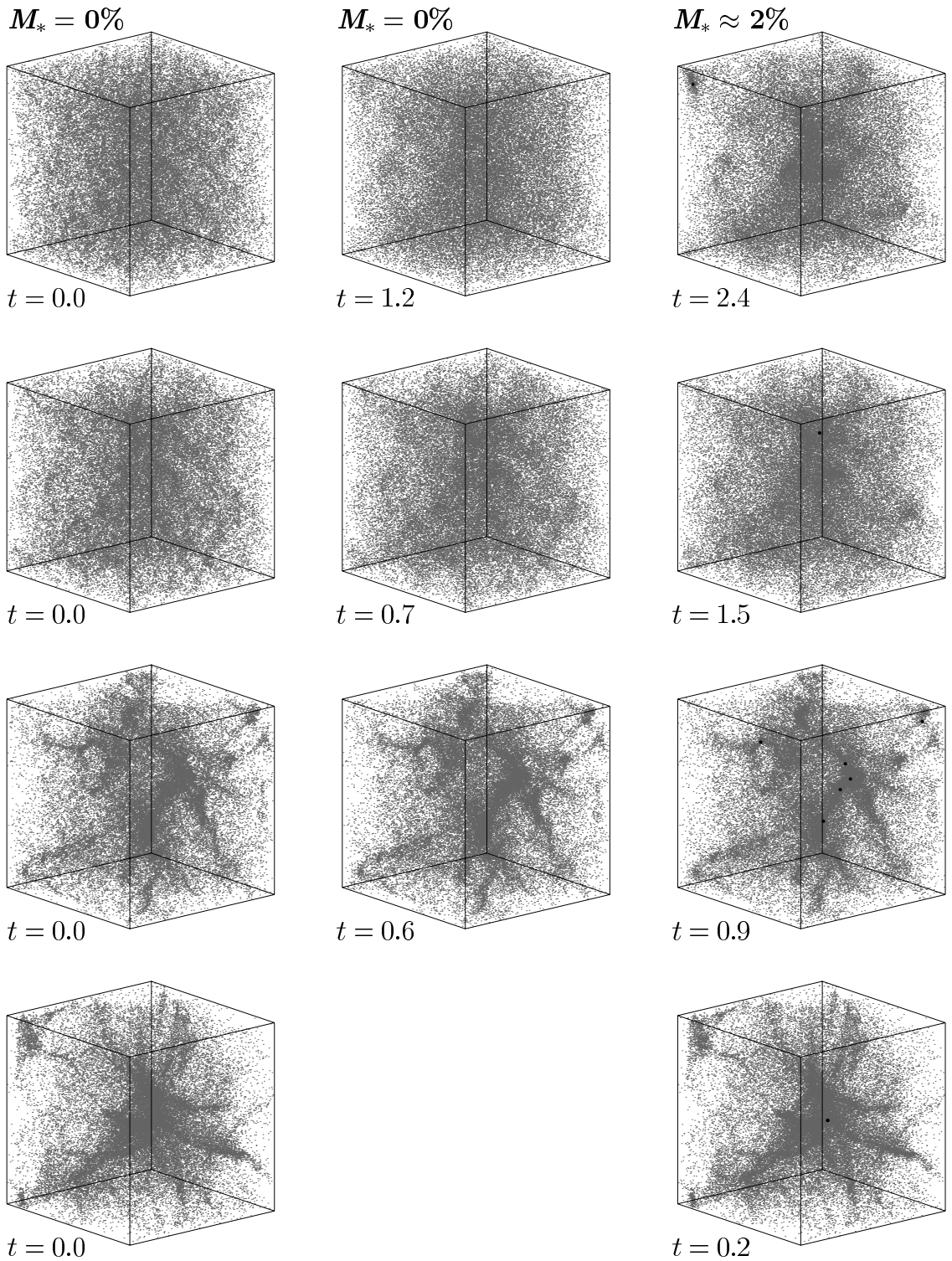

Figure 7.1: Comparison of the time evolution of four models with different initial power spectra $P(k) \propto 1/k^N$, initially (first column), after the first protostellar cores have formed (second column) and when $M_* \approx 2\,\%$ of the gas is converted into condensed cores. The first row plots model T01N0-A with $N = 0$, the second row model T01N1-B with $N = 1$, the third row model T01N2-G with $N = 2$, the fourth row model T01N3-A with $N = 3$.

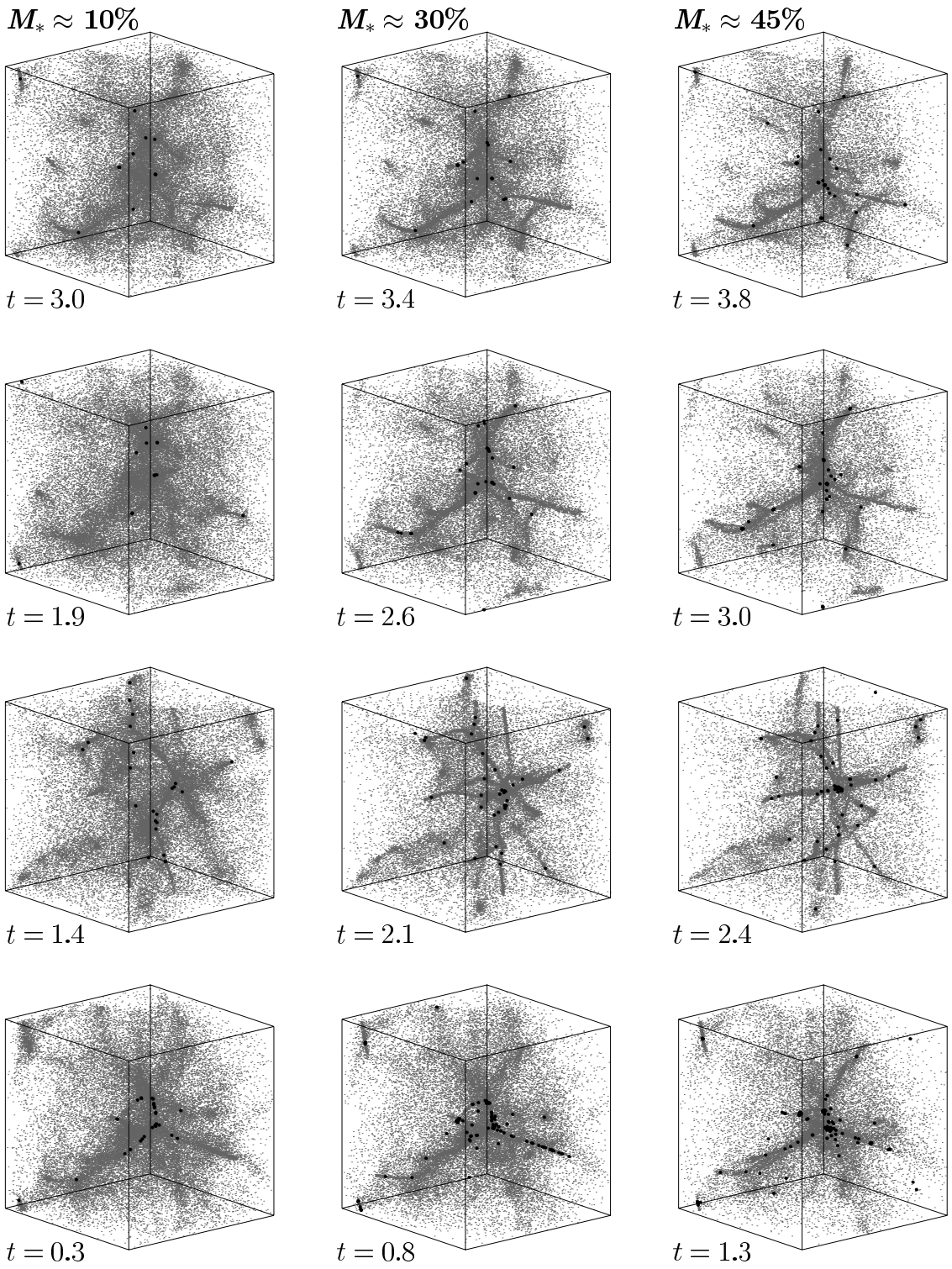

Figure 7.1 — continued: Comparison of the time evolution of four models with different initial power spectra $P(k) \propto 1/k^N$: the distribution is plotted when $M_* \approx 10\,\%$ (first column), when $M_* \approx 30\,\%$ (center column) and when $M_* \approx 45\,\%$ of the available gas is accreted onto protostellar cores.

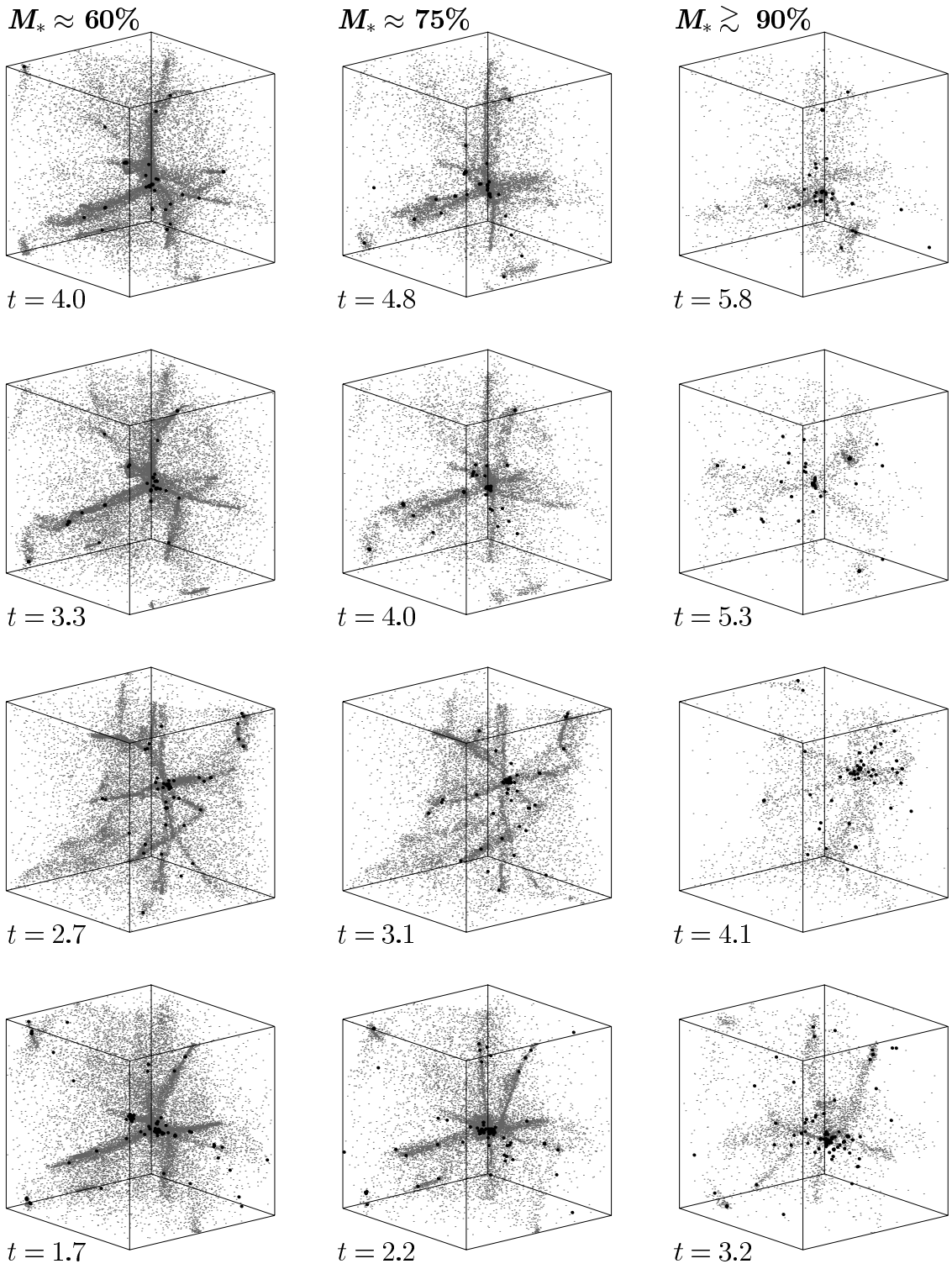

Figure 7.1 — continued: Comparison of the time evolution of four models with different initial power spectra $P(k) \propto 1/k^N$: the distribution is plotted when $M_* \approx 60\,\%$ (first column), when $M_* \approx 75\,\%$ (center column) and when $M_* \gtrsim 90\,\%$ of the available gas is accreted onto protostellar cores.

core in the simulation is shorter than the interval adopted for writing the state of the system onto disk.

This sequence of evolutionary delays relative to the fastest developing model, T01N3-A, remains approximately constant throughout the entire simulation. When comparing similar evolutionary stages as defined by the total mass fraction converted into protostellar cores, M_*, model T01N0-A lags behind by $\Delta t \approx 2.5$, model T01N1-B by $\Delta t \approx 1.5$ and model T01N2-H by $\Delta t \approx 1$. These time delays are the result of the different time intervals necessary for the large-scale modes to reach a certain density level. This is different for different values of N when applying the Zel'dovich method with a fixed shift interval δt (see Fig. 5.3 in Sec. 5). For $N = 0$, the density of the bulk of matter in the large-scale modes is close to the average density in the system: $\langle\rho\rangle \approx 1/8$. Deviations from homogeneity are small. Models with $N = 3$, on the other hand, contain large regions with $\rho \gg 1/8$, this cannot be compensated by voids which have $\rho \lesssim 1/8$. Therefore, most matter is in a density regime $\langle\rho\rangle > 1/8$, and the system reaches a given evolutionary stage earlier than the previous one. The fact that a large fraction of mass has relatively high densities initially also affects the total number of protostellar cores that form during the evolution. Since the local Jeans mass of individual gas clumps decreases with density (see Eqn. 3.18), the number of (small-scale) density fluctuations whose mass exceeds the local Jeans limit is larger in the case where they are superposed onto a large-scale mode of increased background density. In the case in which fluctuations rise from a homogeneous background of low density, this number is low. In summary, the larger the initial density contrast of the large-scale mode, the more condensed cores one expects. Indeed, in our simulations the model with the steepest fluctuation spectrum T01N3-A has formed 130 sinks altogether, roughly three times more than model T01N0-A which has a flat fluctuation spectrum and forms 45 protostellar cores. For comparison, model T01N1-B forms 49 and model T01N2-H 59 cores.

However, besides these details, the overall dynamical evolution of all models is remarkable *similar*. They all form a cluster of protostellar cores which grows in mass via competitive accretion from the common gas reservoir, as discussed in detail in the last chapter. Also the mass distribution of identified gas clumps and protostellar cores at various stages of the evolution are very similar. This can be seen in Fig. 7.2, which plots the number of gas clumps (thin lines) and of protostellar cores (thick lines) as function of their mass. Individual masses are scaled relative to the Jeans mass of the homogeneous cube which is $M_\mathrm{J} = 1/222$. Analogous to Fig. 7.1, each row denotes an individual model (from $N = 0$ to $N = 3$) and each column indicates a certain stage of the evolution characterized by the mass fraction contained in protostellar cores. The vertical line denotes the SPH resolution limit, below which a local Jeans mass is not resolved properly (see Sec. 3.4.5). The dashed line indicates the observed slope of the clump-mass spectrum $dN/dm \propto m^{-1.5}$ (see Sec.2.1.1).

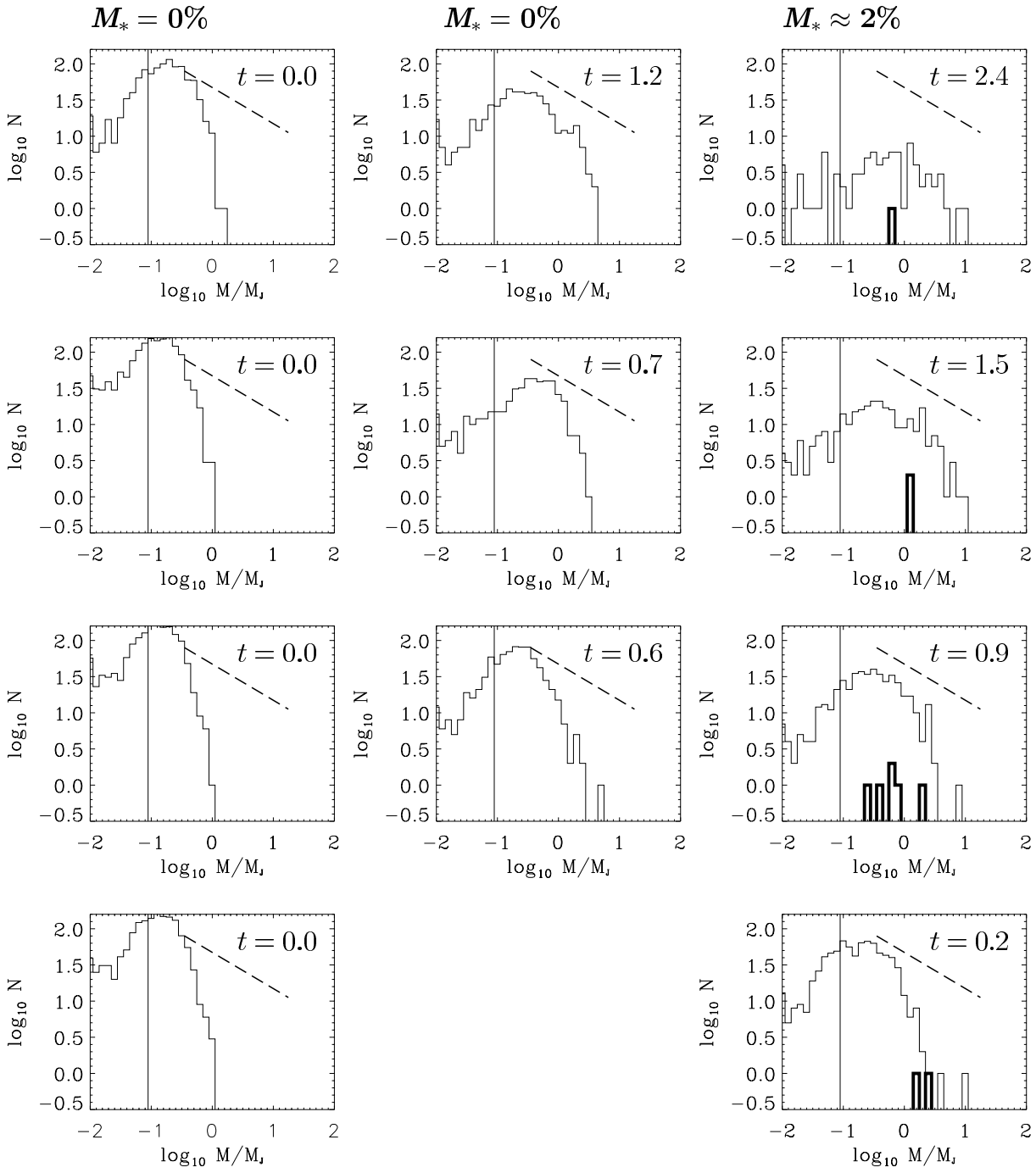

Figure 7.2: Mass spectrum of gaseous clumps (thin lines) and protostellar cores (thick) lines in models T01N0-A (first row), T01N1-B (second row), T01N2-I (third row), and T01N3-A (fourth row). Each column describes a different evolutionary stage of the models as indicated by the fraction of mass converted into condensed cores M_*. The time is indicated separately in each plot. The horizontal line indicates the spatial resolution limit which constrains the clump-mass resolution: if the Jeans mass of a clump falls below that value its time evolution is no longer treated properly.

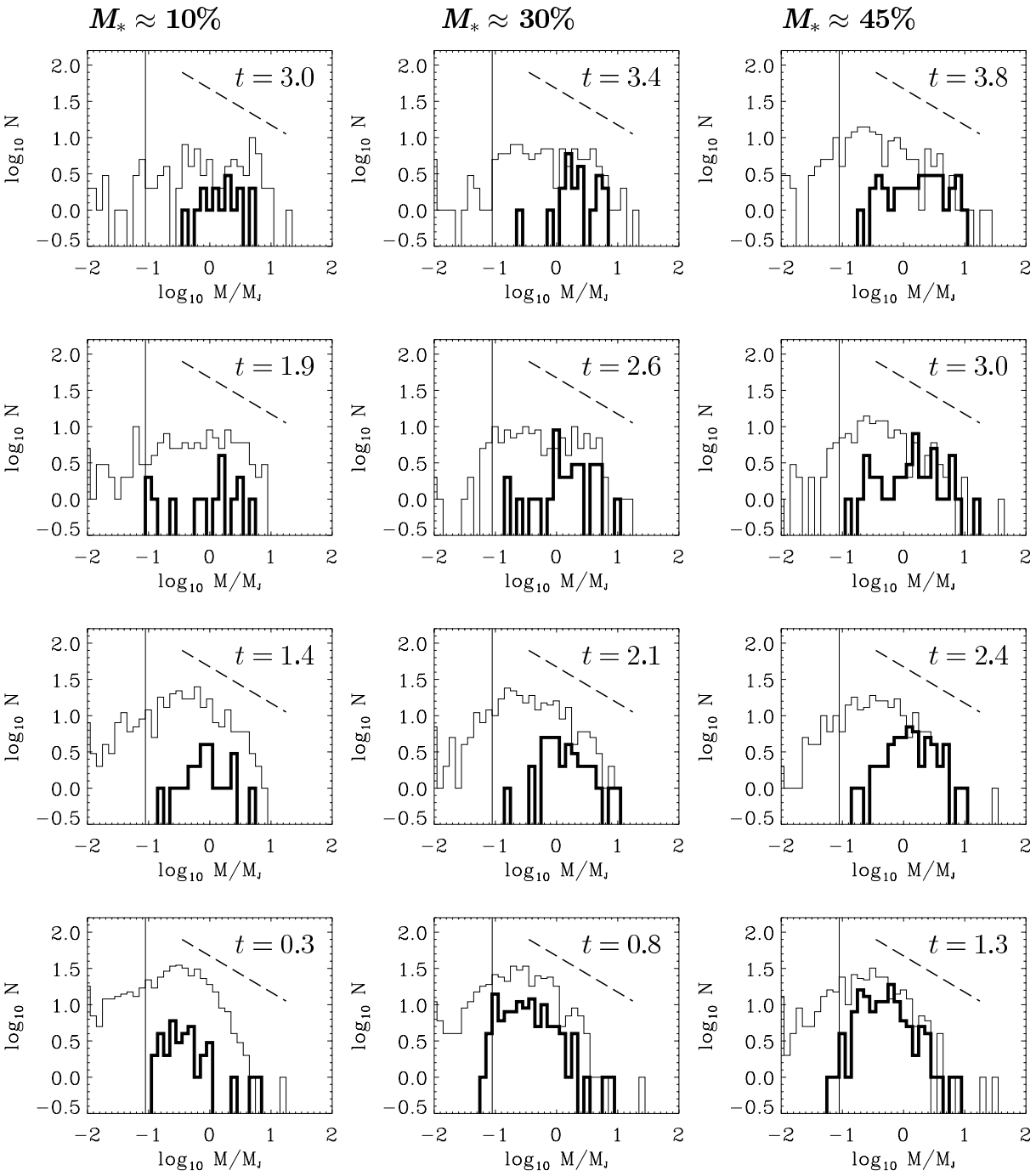

Figure 7.2 — continued: Mass spectrum of gaseous clumps (thin lines) and protostellar cores (thick) lines in models T01N0-A (first row), T01N1-B (second row), T01N2-I (third row), and T01N3-A (fourth row) at phases of the evolution when $M_* \approx 10\%$, $M_* \approx 30\%$, and $M_* \approx 45\%$.

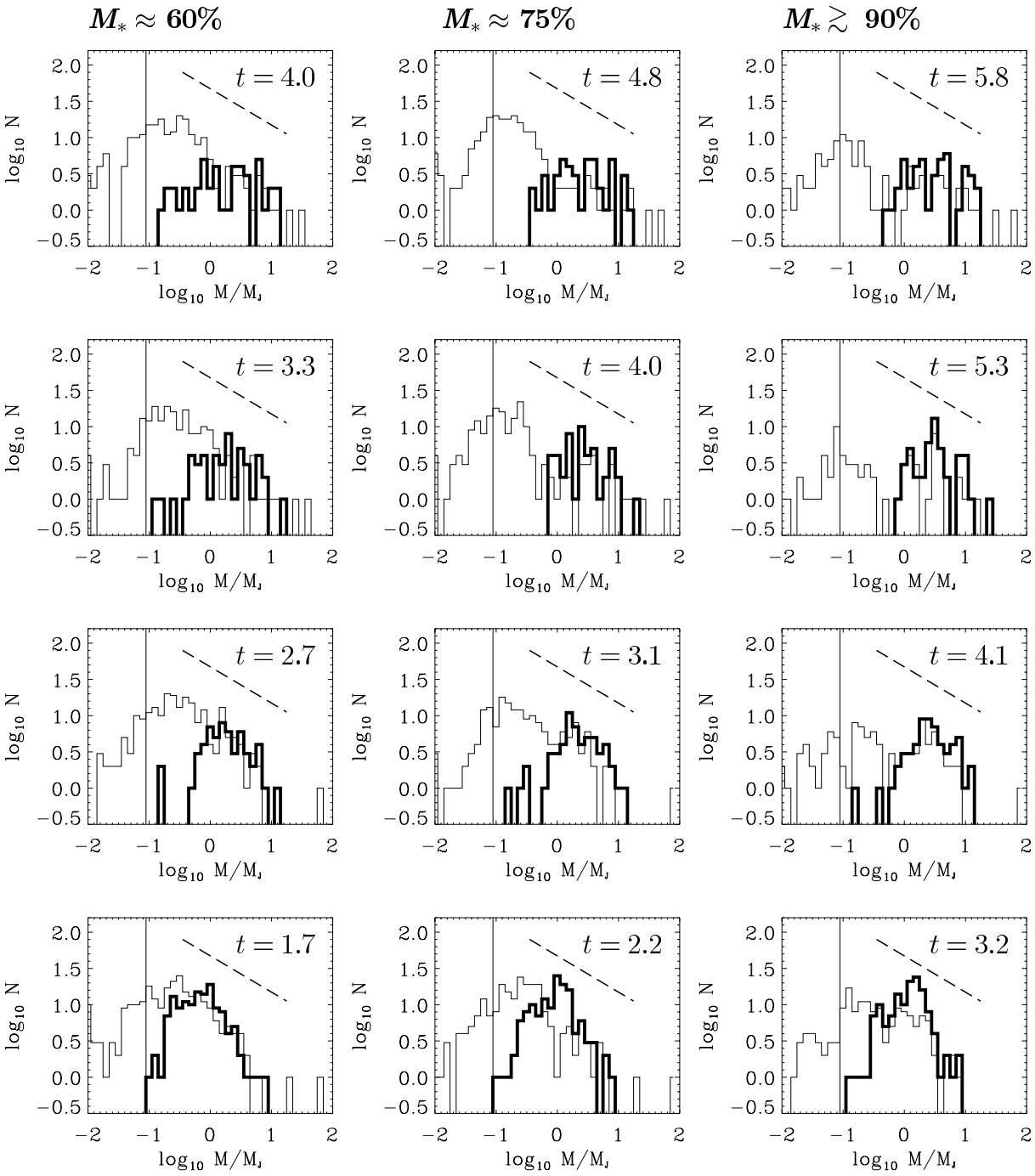

Figure 7.2 — continued: Mass spectrum of gaseous clumps (thin lines) and protostellar cores (thick) lines in models T01N0-A (first row), T01N1-B (second row), T01N2-I (third row), and T01N3-A (fourth row) at evolutionary phases when $M_* \approx 60\%$, $M_* \approx 75\%$, and $M_* \gtrsim 90\%$.

Clearly, the initial conditions fail to reproduce the observed clump-mass distribution. Our clump-finding algorithm detects the initial Gaussian fluctuation spectrum and the clump spectra for the different models appear identical since the algorithm is biased towards small scale fluctuations: if a variety of small-scale peaks are superposed on a large-scale mode, it breaks the latter one up into the contributions of the smaller fluctuations. The large mode is identified only if it is sufficiently 'smooth', i.e. if it cannot be identified as the sum of an ensemble of smaller clumps. For details on the clump-finding scheme see App. A. However, gas pressure causes the desintegration of small clumps with masses below a Jeans mass, and as soon as the system begins to evolve in time, gravitational attraction leads to clump merging thus creating clumps with increasingly larger mass. As a result, for models T01N0-A and T01N1-B, the clump spectrum becomes approximately flat in the interval $M_* \approx 1\%$ to $M_* \approx 30\%$. At later stages, additional low-mass clumps are identified which may result from irregularities or sub-fragmentation in the converging gas flows at the intersection of two filaments along which gas streams towards a common center of attraction. At very late stages of the evolution, when almost all mass is contained in protostellar cores, fitting a single power-law slope to the mass spectrum becomes completely meaningless. Since the models T01N2-H and T01N3-A pass through all evolutionary stages at earlier times, self-gravity and gas pressure have less time to shape the clump-mass spectrum. Therefore, these system contain more low-mass clumps compared to the other two and their clump-mass spectrum is on average steeper. Again at late stages the distribution can no longer be fitted by a simple power law. In summary, the clump-mass spectrum of self-gravitating isothermal gas evolves in time and exhibits a well defined power-law behavior only during a limited period of its dynamical evolution. This fact may explain the variety of different slopes that are quoted for observed clump-mass spectra and the uncertainty in their determination (see e.g. Tab. 2.1.1).

In agreement with the results of Sec. 6, the mass distribution of protostellar cores is very broad and peaks roughly at the mean Jeans mass of the system. As discussed in Sec. 6.4.1, this results from the fact that the formation of new low-mass protostellar cores and the accretion onto already existing ones are approximately in balance; they populate the low-mass and high-mass side of the distribution more or less equally. The peak of the distribution moves away from the Jeans mass only at late stages of the evolution, when the formation of new cores has stopped, but the already existing ones are still able to grow in mass. This effect is largest for model T01N0-A, since it forms the lowest total number of condensed cores. Model T01N3-A builds up three times more cores. Therefore, each protostellar core is on average three times lighter than in the other cases and the distribution peaks at smaller masses. Only towards the end of the simulation, when almost all gas is accreted onto the protostellar cores the peak reaches values of the average Jeans mass.

Figure 7.3 specifies the energy and kinematical properties of the protostellar cluster that

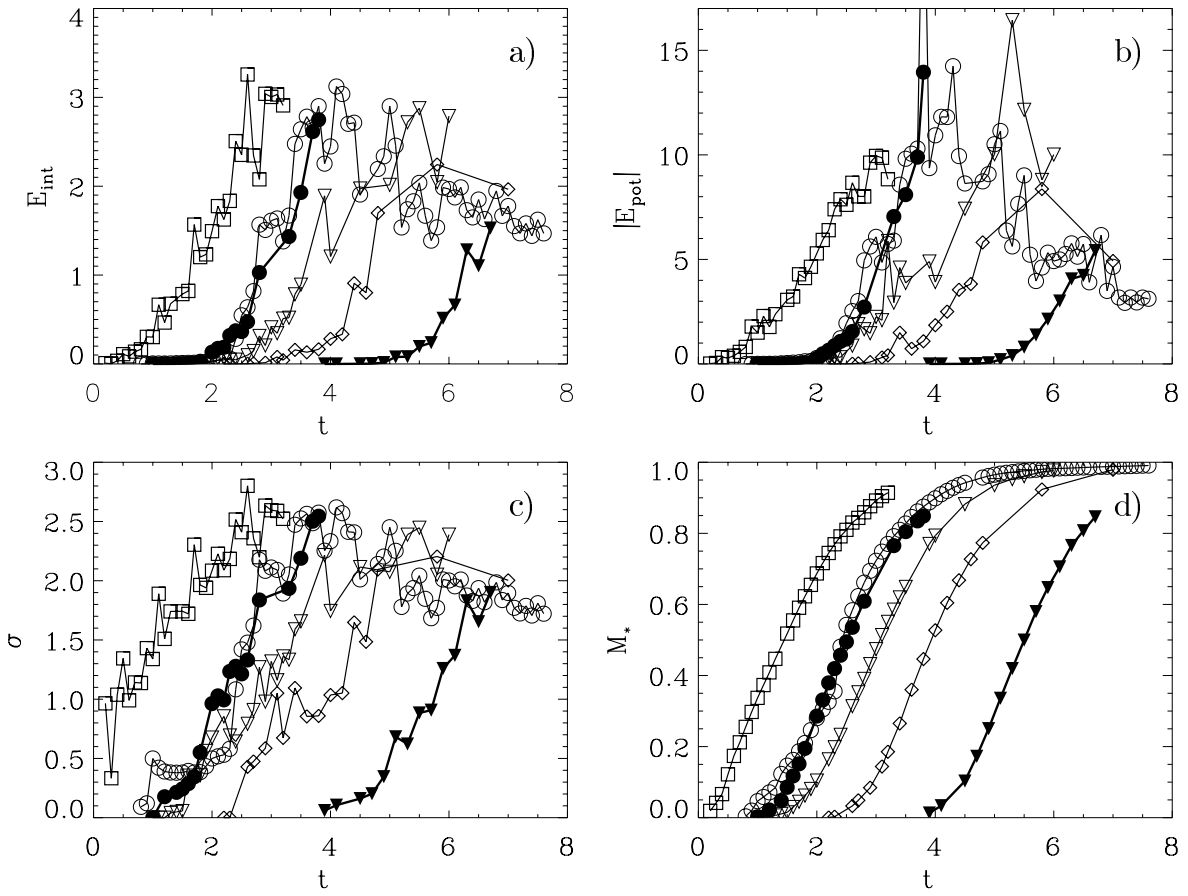

Figure 7.3: Time evolution of (a) the kinetic energy in random motions $E_{\rm int}$, (b) the potential energy $E_{\rm pot}$, (c) the velocity dispersion σ, and (d) the cumulative mass M_* in condensed cores for the protostellar clusters that form during the dynamical evolution of the models with different initial power-law fluctuation spectra $P(k) \propto 1/k^N$. The open diamonds denote model T01N0-A with $N = 0$. There are two models with $N = 1$: T01N1-B which is denoted by the open triangles and the high-resolution model T01N1-C which is plotted with filled triangles (its initial fluctuation spectrum is truncated and contains only modes with $k \geq 4$). The circles denote models with $N = 2$: T01N2-H (open circles) and the high-resolution model T01N2-I (closed circles). Finally, model T01N3-A with the steepest spectrum, $N = 3$, is characterized by open squares.

forms in each of the above models. First, it plots the time evolution of the kinetic energy of the random motions of the protostellar cores, $E_{\rm int} = 1/2 \sum_i m_i (\boldsymbol{v}_i - \boldsymbol{v}_{\rm cm})^2$, where m_i and $\boldsymbol{v}_i$ are the masses and velocities of individual cores i, and $\boldsymbol{v}_{\rm cm} = \sum_i m_i \boldsymbol{v}_i / M_*$ is the center-of-mass velocity of the protostellar cluster. Second, the potential energy of the cluster is given: $E_{\rm pot} = \sum_{ij} G m_i m_j / r_{ij}$, where the gravitational constant $G \equiv 1$, and $r_{ij} = |\boldsymbol{r}_i - \boldsymbol{r}_j|$ is the distance between two cores i and j. Each pair-wise potential is counted once. Third, the velocity dispersion[3] σ and finally the total mass accumulated

[3]Note, that here we follow the observers and define the velocity dispersion as $\sigma^2 = \sum_i (\boldsymbol{v}_i - \boldsymbol{v}_{\rm cm})^2$.

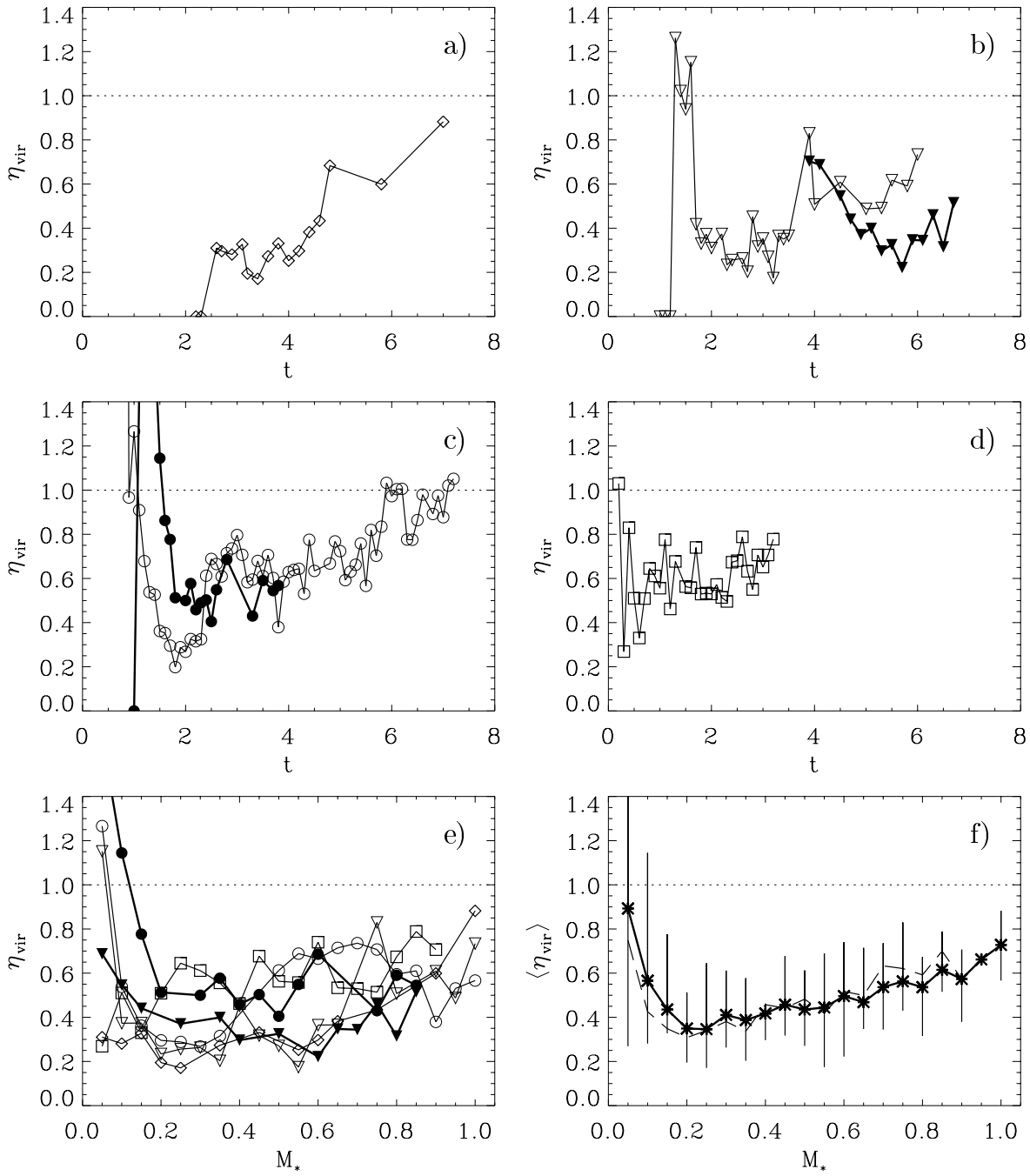

Figure 7.4: Time evolution of the virial coefficient $\eta_{\rm vir}$: (a) for model T01N0-A, (b) for models T01N1-B and T01N1-C, (c) for models T01N2-H and T01N2-I, and (d) for model T01N3-A. The correspondence between each plotting symbol and model is analogous to Fig. 7.3. Plot of $\eta_{\rm vir}$ as function of the total mass fraction M_* accreted onto protostellar cores (e) for each model individually and (f) averaged over all models (thick solid line with error bars indicating the statistical deviations) and averaged over the four models with 200000 particles (dashed line).

Theoretically, σ should be mass weighted: $\sum_i m_i(\boldsymbol{v}_i - \boldsymbol{v}_{\rm cm})^2/M_*$.

in protostellar cores $M_* = \sum_i m_i$ are specified. In Fig. 7.3 and also in Fig. 7.4, open diamonds denote model T01N0-A with $N = 0$ and triangles the models with $N = 1$: T01N1-B (open symbols) and the high-resolution model T01N1-C (filled symbols), whose initial fluctuation spectrum has been truncated at large scales, i.e. contains only modes with $4 \leq k$. The two models with $N = 2$, T01N2-H and T01N2-I are plotted with open and filled circles, respectively. Finally, the model with the steepest initial fluctuation spectrum ($N = 3$) is given by open squares. From Fig. 7.3, one immediately can read off the time delay between identical evolutionary stages for models due to the different values of N. Furthermore, one sees that the evolution of the energetical and kinematical properties of the cluster in model T01N2-H and T01N2-I is almost identical, independent of their different particle number: both systems are well resolved. The delay between model T01N1-B and T01N1-C is due to the truncation of the fluctuation spectrum of the latter, which will be discussed in Sec. 7.1.2.

Figure 7.4, specifies the time evolution of the virial coefficient, $\eta_{\rm vir} = 2E_{\rm int}/|E_{\rm pot}|$, for each of the models. A value $\eta_{\rm vir} = 1$ suggests the cluster is in virial equilibrium; $\eta_{\rm vir} < 1$ indicates that gravitational attraction outweighs kinetic energy and the cluster is contracting. In the opposite case, $\eta_{\rm vir} > 1$, the cluster as a whole will be expanding. To compare the virial coefficient of each model at comparable evolutionary stages, Fig.7.4e plots $\eta_{\rm vir}$ as function of the total fraction of gas converted into protostellar cores M_*. Finally, Fig. 7.4f specifies the average value and its uncertainty. The scatter at early times or equivalently at very low values of M_* is due to low number of protostellar cores at that stage of the evolution and the fact that these first cores typically are well dispersed throughout the entire volume. In the subsequent evolution, the number of protostellar cores increases, and altogether the cores follow the global gas flow pattern towards the common center of gravity. There, a dense protostellar cluster builds up. Analogous to the results of Sec. 6, the protostellar clusters are bound, typically with moderately low values of $\eta_{\rm vir}$ indicating that their kinematical evolution is strongly influenced by the presence of gas that has not yet accreted onto protostellar cores: the conversion of gas into dense cores is such that the overall gain of potential energy is more or less balanced by the increase of kinetic energy. However, this ratio slowly increases with time due to the decrease of the available gas reservoir, as is best visible in Fig. 7.4f. Once the gas reservoir is completely depleted, the clusters behave like collision-dominated N-body systems and quickly develop the typical core/halo structure, approaching $\eta_{\rm vir} \approx 1$. The overall velocity dispersion σ and the energies $E_{\rm int}$ and $|E_{\rm pot}|$ decrease again (see model T01N2-H; and compare with Sec. 6.4.4). The situation is even more complicated, when the conversion of cores into individual stars is considered. Whereas the cluster of protostellar cores is a bound entity, this may no longer be true for the subsequent stellar cluster. If the star-formation efficiency of cores is very low ($10 - 20\%$, as indicated by the results of Sec. 6), a large fraction of the gas from protostellar cores gets lost and will not end up in stars. If the conversion of protostellar

cores into stars and the accompanying mass-loss occur rapidely, the resulting star cluster retains the velocity dispersion of the protostellar, but its potential well becomes shallower since the cluster has lost a considerable fraction of the mass. This may be sufficient for the cluster to dissolve. Only, if the mass loss takes place gradually, the system may have time to adjust to the change and remain bound. Therefore, even if the cluster of protostars is bound, we cannot predict the dynamical evolution of the resulting stellar cluster without detailed knowledge of the mass loss process.

7.1.2 Dependence on the Wave Number

The initial conditions for the SPH simulations depend on the slope of the initial fluctuation spectrum. Furthermore, they depend on the number of modes that contribute to the overall fluctuation field. The models discussed so far are all generated such that the entire spectrum of modes is activated, i.e. fluctuations range from waves with $k = 1$, where the wave length is equal to the total size of the considered volume, down to $k = 32$, where the wave fits 32 times into the cube. For steep power spectra, the overall appearance of the fluctuation field is strongly dominated by the presence of the large-scale modes (see Fig. 7.1). To relax this constraint, we generate a model with $N = 1$ using the Zel'dovich method with shift time $\delta t = 1.0$ and a fluctuation spectrum which is truncated for modes $k < 4$. Since the largest active mode is $k = 4$, when neglecting the fluctuations present from generating a homogeneous random field, this increases the periodicity by a factor of four: the density distribution is equivalent to generating a fluctuation field on a sub-cube of size $(L/2)^3$ and replicating it 64 times to fill in the entire volume. However, as exerted by the periodic boundary conditions for the whole volume, the real periodicity is on the scale $2L$ and the intrinsic periodicity present in the initial distribution quickly disappears during the dynamical evolution. The time evolution of the system is displayed in Fig. 7.5, which shows the particle distribution at different stages of the dynamical evolution characterized by the total mass fraction M_* accumulated in protostellar cores. Since the Zel'dovich shift interval is relatively small and the initial fluctuation field lacks the presence of large-scale modes, the particle distribution appears very smooth and homogeneous. Its evolution is most comparable to model T01N0-A, which also is very homogeneous and smooth at the beginning of the evolution. The initial density contrast in model T01N1-C is even less than in model T01N0-A, which implies that it needs even longer to reach comparable evolutionary stages, e.g. it takes $t \approx 3.9$ to form the first highly-collapsed protostellar object. However, as in all other models, a bound cluster of protostellar cores builds up whose mass distribution is very broad, spanning two orders of magnitude, and peaks slightly above the mean Jeans mass as defined for a completely homogeneous distribution; the mass spectrum of protostellar cores is indistinguishable from the one of model T01N0-A.

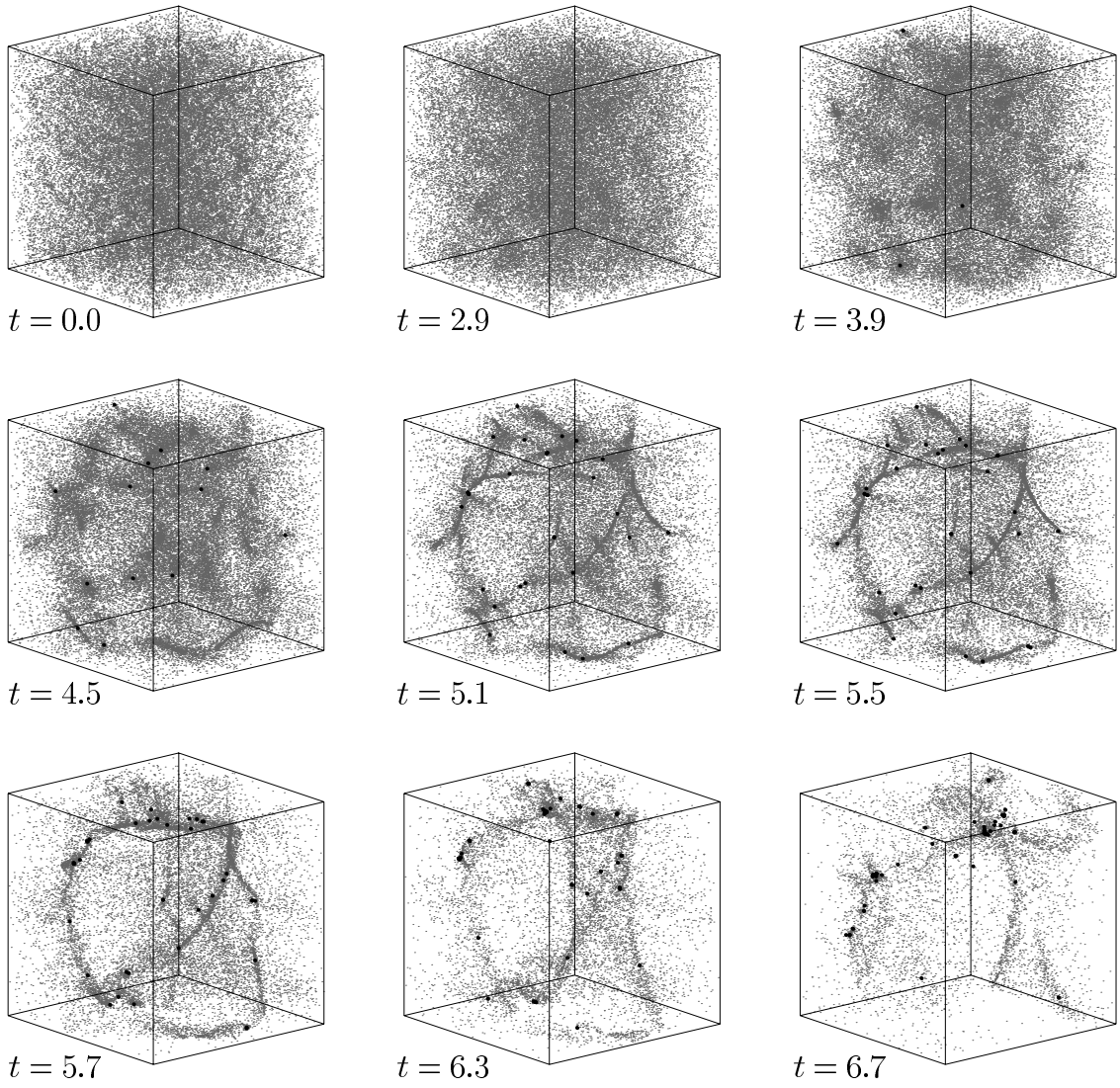

Figure 7.5: Time evolution of model T01N1-C. It contains 500 000 SPH particles and the initial distribution is generated from a fluctuation spectrum with $N = 1$ which is truncated for modes $k < 4$. The snapshots correspond to the following stages of the dynamical evolution: $t = 0.0$ – initial particle distribution, $t = 2.9$ – the maximum density contrast has reached half the value required to identify compact objects as protostellar cores, $t = 3.9$ – the first protostellar cores have formed and contain altogether $M_* = 2\%$ of the total gas mass, $t = 4.5$ – $M_* = 10\%$, $t = 5.1$ – $M_* = 30\%$, $t = 5.5$ – $M_* = 50\%$, $t = 5.7$ – $M_* = 60\%$, $t = 6.3$ – $M_* = 75\%$, and $t = 6.7$ – $M_* = 85\%$. For legibility, only every tenth non-accreted gas particle is displayed (small gray dots). Protostellar cores are denoted by large dark dots.

In summary, removing the large-scale modes is equivalent to flattening the overall spectral slope. The details depend on the slope of the initial spectrum and the wave number up to which fluctuations are deactivated. For example, removing all modes with $k < 4$ in a model with $N = 1$ produces a system that behaves like a model with $N = 0$.

Table 7.2: Models with initial power spectra $P(k) \propto 1/k^N$, where $N = 0$ and $N = 2$, but different temperatures T.

Temperature	Exponent	Particles	Initial[a]	Zel'dovich[b]	Identification
$T = 0.010$	$N = 1$	50 000	random	$\delta t = 1.5$	T01N1-A
$T = 0.025$	$N = 1$	50 000	random	$\delta t = 1.5$	T025N1-A
$T = 0.075$	$N = 1$	50 000	random	$\delta t = 1.5$	T075N1-A
$T = 0.100$	$N = 1$	50 000	random	$\delta t = 1.0$	T10N1-A
$T = 0.500$	$N = 1$	50 000	random	$\delta t = 1.0$	T50N1-A
$T = 0.010$	$N = 2$	50 000	random	$\delta t = 2.0$	T01N2-A
$T = 0.025$	$N = 2$	50 000	random	$\delta t = 1.5$	T025N2-A
$T = 0.050$	$N = 2$	50 000	random	$\delta t = 1.5$	T075N2-A
$T = 0.250$	$N = 2$	50 000	random	$\delta t = 1.5$	T10N2-A
$T = 0.500$	$N = 2$	50 000	random	$\delta t = 1.5$	T50N2-A

[a]Initial distribution for the Zel'dovich shift. A homogeneous random distribution is denoted by 'random', whereas 'grid' means that the particles have initially been placed on a regular grid. [b]Shift interval δt for the Zel'dovich approach.

7.2 Dependence on the Temperature

For a given density, the Jeans mass is a function of temperature only (Eqn. 3.18). Therefore, changing the temperature in an isothermal model is equivalent to modifying the number of Jeans masses contained in the simulated volume. Since isothermal models are scale-free, increasing the dimensionless temperature but keeping the physical gas temperature constant (say at 10K) can also be seen as zooming in more closely onto a physical region of interest and decreasing the temperature is equivalent to studying a larger volume of molecular cloud material. This means, for example the behavior of a system with a temperature of $T = 0.04$ should be comparable to the evolution within a sub-volume of a model with $T = 0.01$ which is eight times smaller that the entire box, say in one octant of the simulation cube. However, this neglects the presence of large-scale modes. As we see in all simulations, the growth of the largest possible mode determines the final matter distribution: there always is *one* global minimum of the potential, towards which the bulk of matter flows. The final outcome of the dynamical evolution is always the formation of *one* protostellar cluster. Basically, this is the result of the given periodicity of the simulated cube. The (periodic) boundary conditions for a model with high temperature are not identical to the boundary conditions for a subregion within a model with lower temperature, which contains a comparable number of Jeans masses. The more the evolution of the system depends on the boundary conditions, the stronger are the deviations

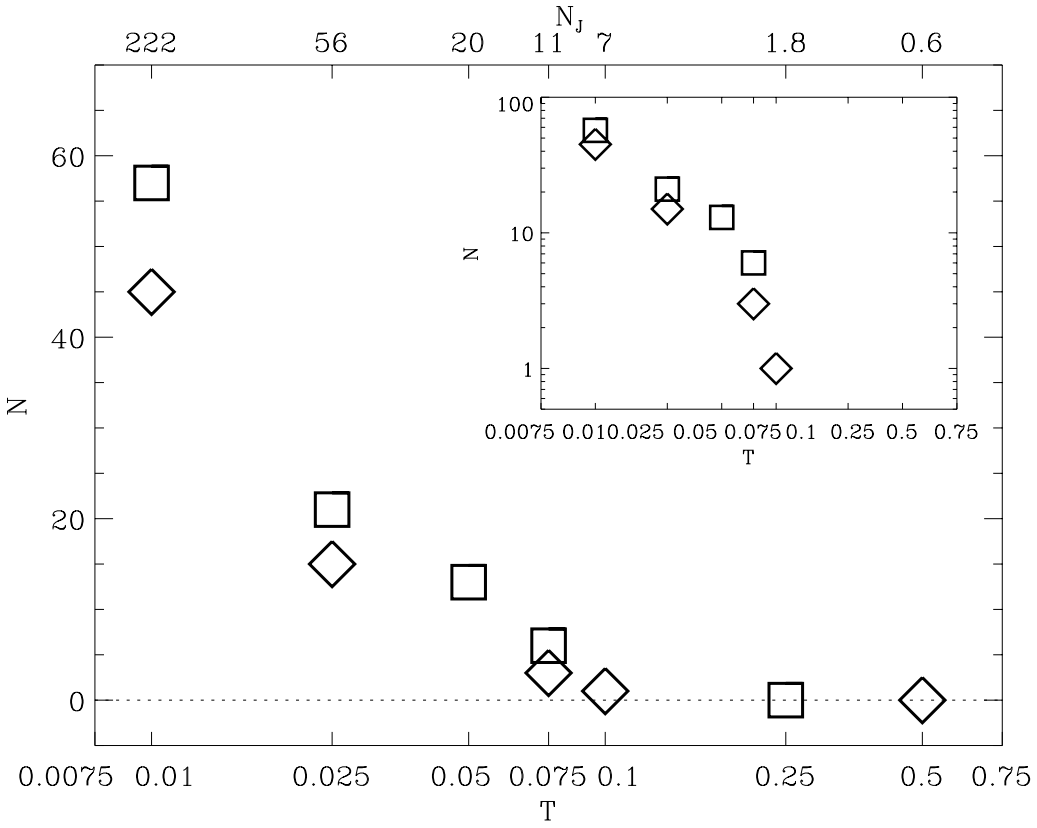

Figure 7.6: Total number N of protostellar cores that form during the dynamical evolution of the isothermal models listed in Tab. 7.2 as function of the temperature T. Open diamonds denote the set of models with $N = 1$ and open squares denote models with $N = 2$; temperatures are given on a logarithmic scale. The upper axis indicates the number of Jeans masses $N_{\rm J}$ contained in the considered volume corresponding the temperature. The inlay gives N scaled logarithmically to indicate that the number of protostellar cores declines with increasing temperature roughly proportional to $T^{-3/2}$.

between both models and the less meaningful is a detailed comparison. Properties of the system that are strongly influenced by large-scale flows and are the result of considerable dynamical evolution, e.g. the spatial properties of the forming protostellar clusters, are vastly different, whereas properties that are less sensitive to this processes, say the overall slope of the clump-mass spectrum, are be quite similar. The latter is the result of the interplay of non-linear gravitational action and gas pressure whenever it occurs.

To quantify the above, we have performed a number of simulations with varying temperature, see Tab. 7.2. All models contained 50 000 particles and can be divided into two groups with initial slope of the power spectrum $N = 1$ and $N = 2$. The covered temperatures range from $T = 0.01$, corresponding to 222 Jeans masses in the simulation, to $T = 0.5$, which means the Jeans mass is larger than the mass contained in the cube. With the above caveats in mind, consider Fig. 7.6. It specifies the total number N of pro-

tostellar cores that form during the dynamical evolution as function of the temperature T (lower abscissa) of equivalently the number $N_{\rm J}$ of Jeans masses in the system (upper abscissa). The temperature is scaled logarithmically. To indicate the power-law behavior of the dependence of N on T, the inlay repeats the plot but with N scaled logarithmically as well. No fluctuations in models with temperatures $T \gtrsim 0.25$ are massive enough to exceed the Jeans limit, they are quickly smeared out by pressure and the system reaches a state of maximum homogeneity. Collapse takes place for models with lower temperatures and the number of protostellar cores scales roughly linearly with the number of Jeans masses in the system $N \propto N_{\rm J}$ or equivalently $N \propto T^{-3/2}$; typically one core forms per every 4 to 5 Jeans masses.

7.3 Summary

The dynamical evolution and fragmentation of self-gravitating isothermal gas is relatively *insensitive* to the adopted initial configurations. It is determined by the interplay between self-gravity and gas pressure. For strongly self-gravitating systems, this leads to the formation of a network of intersecting filaments and clumps. Some clumps may become Jeans unstable and collapse individually to form protostellar cores. Their subsequent dynamical evolution and mass growth is dominated by highly statistical events which quickly wipe out the memory of the initial configuration. The evolution of isothermal models depends mainly on *one* global parameter: the *gas temperature*, or equivalently the ratio between gravitational and internal energy. Therefore, the evolution of all models with identical temperatures is very similar, regardless of the initial conditions.

Variations of the temperature are equivalent to changing the number of Jeans masses treated in the system. Converted to physical conditions in molecular clouds which typically have (physical) temperature of ~ 10K, this is equivalent to zooming in or out onto different regions of the cloud. Hence, the number of protostellar cores that form during the course of the evolution is roughly proportional to the number of Jeans masses contained in the system.

Chapter 8

Summary and Future Prospects

In this dissertation we discussed the dynamical evolution and fragmentation of molecular clouds. We studied the interplay between gravity and gas pressure and showed that even the simple isothermal model of self-gravitating gas is able to explain many of the observed features of star-forming regions. Within the framework of these isothermal models, we identified the processes that dominate the formation and evolution of (proto)stellar clusters and determined their properties. Furthermore, varying the gas temperature and initial density distribution, we addressed the issue of how sensitively the dynamical behavior of the gas depends on environmental and initial conditions. We sumarize our results in Sec. 8.1 and, starting from the current paradigm, in Sec. 8.2 we suggest further steps to deepen our knowledge of the star-formation process.

8.1 Summary

Our simulations show that, in general, the formation of a cluster of condensed cores and protostars through gravitational collapse and fragmentation of a molecular cloud region is extremely complex. The dynamical evolution of molecular gas is determined by the interplay between self-gravity and gas pressure. This creates an intricate network of filaments, sheets and dense clumps. Some clumps will become gravitationally unstable and undergo rapid collapse. While contracting individually to form protostellar cores in their interior, gas clumps stream towards a common center of attraction: the dynamical evolution of molecular clouds involves processes acting on largely different time scales. While following the large-scale flow pattern, gas clumps can undergo further fragmentation or merge at the intersections of filaments. At that stage, the central regions of some clumps will have already collapsed to sufficiently high densities to be identified as protostellar cores. These cores rapidly grow in mass via accretion from their parental gas envelope.

In the case of clumps merging, the newly formed merged clump may contain a multiple system of protostellar cores which subsequently compete with each other for accretion from the same limited and rapidly changing reservoir of contracting gas in which they are embedded. Since the cores are dragged along with the global gas flow, quickly a dense cluster of accreting protostellar cores builds up. Analogous to dense stellar clusters, its dynamical evolution is subject to the complex gravitational interaction between the cluster members: close encounters occur frequently and will drastically alter the orbital parameters of cores. This leads to the formation of unstable triple or higher-order systems, and consequently a considerable fraction of protostellar cores becomes expelled from the cloud. These cores effectively stop accreting and their final mass is determined.

The presence of unpredictable dynamical events in the overall gas flow and the evolution of the nascending protostellar cluster very efficiently erases the memory of the initial fluctuation spectrum. For this reason, we cannot predict the detailed evolution of individual objects from knowing the initial status of the system. Only the properties of an *ensemble* of protostellar cores, for example their kinematics and mass distribution, can be determined in a probabilistic sense. A comprehensive theory of star formation needs to be a *statistical theory*. Some first attempts to formulate a statistical model of the star-formation process appear very promising (see Sec. 2.3) and are supported by the results of our numerical study. Taken together, our simulations strongly suggest that gravitational fragmentation and accretion processes dominate the early phases of star formation.

We extend the above overview by giving a detailed list of the features and results of our calculations derived from the comparison of our numerical models with specific observational properties of molecular clouds and young stellar clusters:

- **Scaling Properties of Isothermal Gas:** In the physical regime we study, molecular gas can be well approximated as being isothermal. The dynamical behavior of self-gravitating isothermal gas is entirely determined by *one* scale parameter: the dimensionless *temperature* as defined by the ratio between internal energy and potential energy. To apply our models to observed star-forming regions, they have to be scaled to physical units. This is derived in Sec. 4.

- **Clump mass spectrum:** During the central phase of the dynamical evolution, our simulations of self-gravitating isothermal gas are able to reproduce the observed power-law clump-mass spectrum of molecular clouds. This is due to the progression of non-linear gravitational attraction and the disintegration of small clumps by gas pressure. The observed spectrum is best fit at times between the formation of the first condensed objects to the time when depletion of the gas reservoir becomes considerable. Neither the initial Gaussian fluctuation spectrum, nor the final stages of the evolution when most of the gas is condensed into protostellar cores, give a

clump-mass distribution with the observed features. This is discussed in Sec. 6.3.1. The masses of protostellar cores, however, follow a log-normal distribution.

- **The Shapes of Individual Clumps:** Dense Jeans-unstable gas clumps are the precursors of protostellar cores. As being part of a complex network of filaments, individual clumps are typically very elongated objects with ratios between semi-major and semi-minor axis of 2:1 to 4:1. However, in many cases (especially at the intersection of two filaments) they may be quite irregularly shaped. These features are in agreement with observed dense pre-stellar cores in dark clouds (see Sec. 6.3.2).

- **Formation and Growth of Protostellar Cores:** As stated above, the formation and growth of protostellar cores is subject to a progression of statistical events. However, we can identify the following trends in our models: (a) The protostellar cores that form first are generally formed in the clumps with the highest initial density, and tend to have the highest final masses. They accrete the bulk of their final mass from their close vicinity. (b) On the other hand, matter that forms cores at later times has already undergone considerable dynamical evolution; these cores form from gas that was initially in widely distributed low-density clumps. Along filaments, they stream towards a common center of gravity and may merge at the intersections. Once enough mass is accumulated, these clumps undergo rapid collapse and build up new protostellar cores. The cores which form a late stages tend to have very low final masses.

- **Competitive Accretion and the Importance of Dynamical Interaction:** Once a gas clump becomes Jeans unstable it collapses and forms a condensed core. This core grows in mass via accretion from the infalling envelope. Merging may lead to clumps that contain multiple cores. These compete with each other for the material of a common gas reservoir. The succession of clump mergers leads to the formation of an embedded, dense protostellar cluster, whose dynamical behavior is dominated by close encounters between cluster members. Competitive accretion and collisional dynamics determine the kinematical and spatial properties of the cluster and the mass distribution of protostellar cores.

- **Rotational Properties of Protostellar Cores:** The rotation of a protostellar core is an important parameter for its late collapse phase. It determines the stability of the accretion disk and its tendency for subfragmentation. Within the complex network of intersecting filaments and dense clumps, the clumps can gain angular momentum from tidal torque and shear which is transferred onto the embedded cores. Since the angular momentum is gained from large-scale motion, the orientation of the spin vectors of individual protostellar cores is correlated with their location (see Sec. 6.4.3). A similar correlation is often found in observed star-forming regions

between the orientation of the molecular outflows from young stellar objects and their location. However, the observational data are not conclusive.

- **Clustering Properties of Protostellar Cores:** The time evolution of a highly Jeans-unstable region within a molecular cloud leads to the formation of a dense cluster of protostellar cores. The final dynamical state of the system closely resembles the properties of observed stellar clusters: it exhibits the typical core/halo structure of collision-dominated N-body systems, and when calculating its 2-point correlation function, or equivalently the mean surface density of companions as function of separation, one can clearly distinguish between the binary regime and the large-scale clustering regime (see Sec. 6.4.4).

- **Boundedness of Protostellar Clusters:** The clusters of protostellar cores in our simulations form as bound entities: the conversion of gas into condensed cores is such that the decrease of potential energy is always balanced by the increase of kinetic energy (Sec.'s 6.4.5 and 7.1.1). Whereas the protostellar cluster is bound, this may not be true for the resulting stellar cluster. Its kinematical properties depend strongly on the details of the conversion of individual cores into stars: on the speed and the overall efficiency of the process. However, this cannot be treated in our simulations and needs to be addressed in detailed calculations of individual core collapse.

- **Mass Spectrum of Protostellar Cores — The Star Formation Efficiency and Implications for the IMF:** The distribution of stellar masses is one of the most important properties of the star-formation process. Any comprehensive model of star formation must be able to derive this quantity or at least address this issue. In our isothermal models the masses of protostellar cores are the result of a sequence of unpredictable statistical events. In a natural way this leads to a *log-normal* mass spectrum which peaks roughly at the average Jeans mass of the sytem.

  Detailed collapse calculations show that perturbed rotating cores tend to break up into multiple stellar systems, which cannot be resolved in the larger-scale simulations presented here. Therefore, we have to compare the numerical mass function of protostellar cores with the IMF derived for multiple stellar systems. The latter is well approximated by a log-normal mass spectrum centered on $m_0 = 0.23\,\mathrm{M}_\odot$ with width $\sigma = 0.42\,\mathrm{M}_\odot$ (see Sec. 2.3). When we scale our isothermal models to typical Jeans masses of $M_\mathrm{J} \approx 1\,\mathrm{M}_\odot$, the numerically calculated mass function and the IMF are in excellent agreement, if we assume a efficiency of $\eta_{\mathrm{gas}\to\mathrm{core}} \gtrsim 0.6$ for the conversion of molecular gas into dense protostellar cores and additionally an efficiency of $\eta_{\mathrm{core}\to\mathrm{star}} \approx 0.15$ for the conversion of individual cores into stars. Altogether we predict a total star-formation efficiency $\eta_\mathrm{tot} \equiv \eta_{\mathrm{gas}\to\mathrm{core}} \times \eta_{\mathrm{core}\to\mathrm{star}}$ which is of the order of 10%.

- **Dependence on the Initial Conditions:** The dynamical evolution of self-gravitating isothermal gas is determined by a sequence of unpredictable statistical events. Therefore, these systems quickly lose memory of their initial density distribution and the global behavior is relatively insensitive to the properties of the initial density distribution. Systems with different slopes of the initial fluctuation spectrum evolve very similarly. The major difference is the time at which the systems pass through comparable stages of the evolution after the start of the SPH simulation (Sec. 7.1).

- **Dependence on the Temperature:** Our isothermal models of self-gravitating gas are scale-free. Their dynamical evolution is determined by the dimensionless temperature defined as the ratio between internal and potential energy. This specifies the number of Jeans masses contained in the simulated volume, and hence the degree of instability towards gravitational collapse. From varying the temperature, we find that the number of collapsed objects (protostellar cores) is roughly proportional to the number of Jeans masses contained in the simulation (Sec. 7.2).

At this stage it is necessary to add some caveats. Our approach to the dynamical evolution of molecular clouds involves very simple physics: we treat the gas isothermally and include self-gravity. For the physical regime we are interested in, this is certainly a very good approximation. However, at some stages of the evolution, additional physical phenomena may become important.

(a) The collapse process leads to gas densities at which energy can no longer be radiated away efficiently, so the gas heats up and the equation of state becomes adiabatic. We do not include this effect, since it will happen 'inside' the condensed cores that form during the dynamical evolution of the system we study and we cannot properly resolve that stage of the evolution anyway. Furthermore, at the very late stages of protostellar accretion, when stars remove their parental gas cocoon, additional physical phenomena will become important. These processes determine the efficiency $\eta_{\mathrm{core}\rightarrow\mathrm{star}}$ for the conversion of individual protostellar cores into stars, which we have to determine indirectly in our models. For a direct derivation, detailed collapse calculations of individual cores including all physical effects are necessary.

(b) Furthermore, our approach does not include the effects of magnetic fields. As is known from polarisation measurements and observations of the Zeeman effect, magnetic fields are present in molecular clouds. Contrary to the common belief, recent studies have shown that magnetic fields are not capable of stabilizing molecular clouds on large scales. Not only do the observational data suggest that the typical field strength is not sufficient to prevent global collapse, but also magnetic fields are unable to prevent turbulent velocity fields from decaying quickly. Therefore, they have been neglected in the current study. However, magnetic fields may play an crucial role in the late phases

of protostellar accretion, for example bipolar outflows may be intimately related with magnetic phenomena. At the level at which we identify protostellar cores in our models, magnetic fields may already start to modify their further collapse behavior. We cannot resolve this. Additionally and more important, magnetic fields may be a necessary agent for distributing energy and momentum from stellar feedback throughout a molecular cloud. This will become important when studying interstellar turbulence.

(c) In star-forming regions feedback processes from newly formed stars may be important for an additional reason. Bipolar outflows, winds and the radiation from young stars are able to deposit large amounts of energy and momentum into the surrounding molecular cloud. These processes may remove the remaining gas of an entire protostellar cluster and terminate the mass accretion of all cores together. Hence, this effect may strongly influence the time scale and efficiency of star formation. On the other hand, stellar feedback processes may compress large regions of a molecular cloud material to make them Jeans supercritical. This may induce a new cycle of star formation. The inclusion and correct treatment of these phenomena in the current models are the next steps towards a better understanding and more complete theory of star formation.

8.2 Future Prospects

The caveats listed on the previous page immediately lead to the next steps to improve the current numerical models of the early stages of the star-formation process. This involves the inclusion and proper treatment of stellar feedback processes and attempts to better understand of the phenomenon of interstellar turbulence.

8.2.1 Introduction of Stellar Feedback Processes

As discussed extensively in this dissertation, the self-gravitating, isothermal fragmentation model is able to treat the most dominant physical phenomena of the early formation phases of protostellar cores correctly. However, in the late stages of accretion, feedback processes from the young stellar object in the center become important, since stellar wind and radiation finally will blow away the protostellar envelope as the star approaches the main sequence. This is an important effect for determining the efficiency with which protostellar cores are converted into stars. Furthermore, feedback processes from massive stars strongly influence the environment and are able to modify the global properties of star-forming regions. Their winds and bipolar outflows deposit momentum and energy into the interstellar medium, while strong UV radiation is capable of creating extended ionized regions. A famous and well-studied example of a star forming region in which

these effects are important is the Trapezium Cluster in Orion, a very dense, young stellar cluster.

Therefore, to improve the current description of the early phases of young stellar clusters, feedback effects and energy input from young stars need to be taken into account. Radiation transfer processes have already been successfully incorporated into the numerical models (see Kessel & Burkert, 1998). The immediate next step is thus the introduction of stellar winds and outflows. With this more elaborate physical description we will be able to derive star-formation efficiencies and time scales in a more realistic and quantitative way, and be one step closer towards a general *statistical* theory of star formation.

8.2.2 Turbulence in Molecular Clouds

There are further important aspects of stellar feedback. The observed supersonic linewidths in molecular clouds strongly suggest that the clouds are stabilized against global collapse by turbulent internal motions. Since turbulent energy dissipates away too fast to explain the observed cloud life times, it must be constantly driven. Stellar winds and bipolar outflows are obvious candidates for turbulent energy input, as they influence their surrounding over large distances. Including these effects in the numerical scheme will make this hypothesis testable, and will enable us to discriminate between this and other possible sources of turbulent energy, such as large-scale shear (see Sec. 2.1.2).

Studying interstellar turbulence is essential for understanding the global parameters of molecular clouds, e.g. their life times, their spatial and velocity structure, and their ability to form stars. One of the key questions untouched in the current work is about the physical processes which produce to the initial conditions adopted for the collapse and fragmentation simulations presented in this dissertation. In other words, what will cause a sufficiently large region within a molecular cloud complex suddenly to become Jeans supercritical and form a cluster of stars. One possible scenario involves stellar feedback processes as indicated before: stars may deposit energy and momentum into a moleclular cloud region to compress it to densities high enough for the entire region to become Jeans unstable. Another possibility involves the supersonic turbulence ubiquitous on all scales in molecular clouds. The action of highly supersonic converging shocks may again create a region of molecular cloud material with high enough density to form a cluster of stars. Since we expect stellar feedback phenomena to drive turbulent motions in molecular clouds, both scenarios may be closely interrelated. Certainly from studying the properties and sources of interstellar turbulence, we will gain important insight into the overall process of star formation.

Appendix A

The Clump Finding Method

This appendix describes the method used to identify the clumping properties of the numerical calculations. It is applies a scheme similar to the one introduced by Williams et al. (1994), but is fully integrated into the SPH formalism.

In SPH, the densities ρ_i of individual particles i are obtained in a local averaging process over a list of neighbors within distances less than twice the smoothing length h_i (see Sec. 3.3). To identify clumps, the resulting 3-dimensional density field is subdivided into ten bins equally spaced in the logarithm of the density. Starting with the highest density level, the particles are sorted by decreasing density, i.e. the first particle in the list is the one with the highest density. Going through this list, for each particle i it is checked whether the particles in its neighbor list are already assigned to a clump. If this not the case, then particle i is assigned to a new gas clump, together with all particles in its neighbor list. Then all further particles at that level which are connected to the particles of the new clump by means of overlapping smoothing volumes are identified and assigned to the same clump. The assigned particles are finally removed from the density list. On the other hand, does the neighbor list of the tested particle i already contain contribution from identified clumps, then the particle i will be assigned to that clump that contributes the largest fraction of particles in the neighbor list, only particle i will be removed from the sorted list. This scheme is repeated until all particles are removed from the sorted list. If all particles within one density level are assigned, then the procedure is repeated at the next level, down to the lowest one. Finally all SPH particles in the system are assigned to individual clumps (see Fig. A.1).

As described here, the scheme is free of assumptions about the geometrical shape of the clumps[1]. This is of great advantage when dealing with highly irregular and filamen-

[1] An alternative approach to determine clump properties in (observed) molecular clouds was introduced by Stutzki & Güsten (1990). These autors explicitely assume clumps of Gaussian shape and decompose

tary structure as in the numerical simulations of gravitational fragmentation and collapse performed for this dissertation. However, the scheme by which neighboring clumps are distinguished is important: two clumps that may at a high level of density be well separated entities, may at lower levels have common contour lines. In our scheme, they are still separated even at these lower levels by introducing an artificial 'interface' between the two clouds. Individual particles are *always* assigned to the clump that contributes most neighbors. This sets a clear division line between two competing clumps and enables their separation. Besides this basic separation criterion, the method is free of independent parameters and uses only intrinsic properties of the SPH scheme.

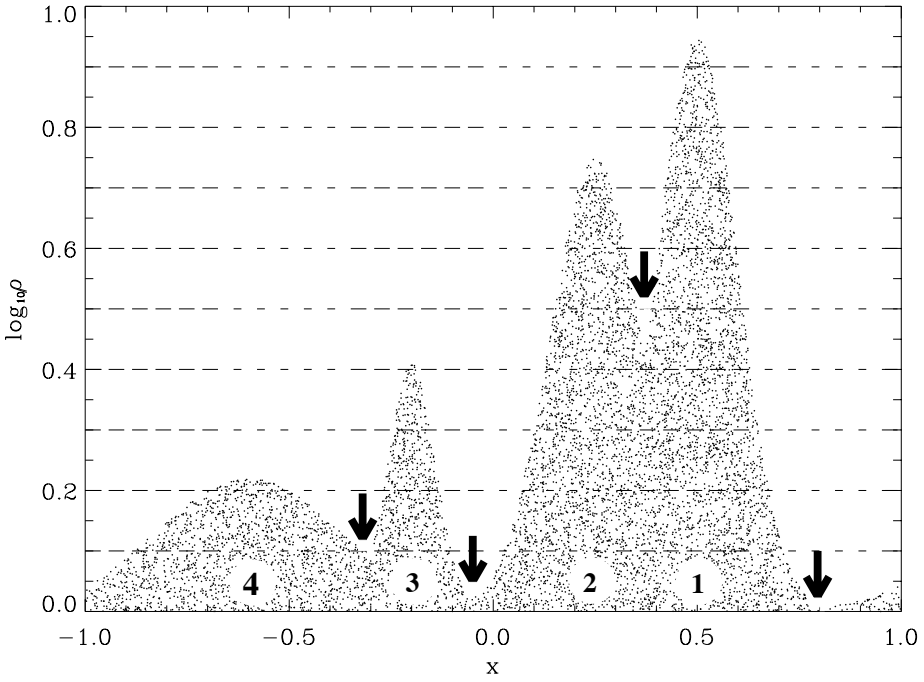

Figure A.1: Illustration of the clump finding algorithm in a 1-dimensional sample case: At the highest contour level one clump is identified and all particles get assigned to it. At the third level a new separate clump is detected. At the sixth highest level, a third new clump is identified. Clumps #1 and #2 now have overlapping contour lines and are separated as described above. This is indicated by an arrow. At level eight the last clump is detected and separeted from the other at the lowest level (again indicated by arrows).

the density field into peaks of this shape by minimizing the residual

Appendix B

Physical Units and Constants

The physical unit system applied throughout this dissertation work is a combination of the 'cgs'-system and 'astrophysical' units. In the 'cgs'-convention, the basic units for length, mass and time are centimeter, gramm and second. Other physical units are expressed as combination of these primary ones. The 'astrophysical' unit system is derived from properties of our solar system. The conversion between both systems is

Length:	$1\,\mathrm{pc}$	$\widehat{=}$	3.085678×10^{18} cm	(parsec)
	$1\,\mathrm{AU}$	$\widehat{=}$	1.495979×10^{13} cm	(astronomical unit)
Mass:	$1\,\mathrm{M}_\odot$	$\widehat{=}$	1.989×10^{33} g	(solar mass)
Time:	$1\,\mathrm{a}$	$\widehat{=}$	3.155815×10^{7} s	(year)
Luminosity:	$1\,\mathrm{L}_\odot$	$\widehat{=}$	3.826×10^{33} erg s^{-1}	(solar luminosity)

The conversion between the two commonly used length units is 1 pc = 206265 AU. Velocities in the interstellar medium are typically given in km s^{-1}.

The physical constants relevant for the dynamics of self-gravitating gas are

Grav. constant:	G	$\widehat{=}$	$6\ .\ 672\ \ 59 \times 10^{-8}$ cm^3 g^{-1} s^{-2}
Gas constant:	$\mathcal{R}$	$\widehat{=}$	8.314510×10^{7} erg K^{-1} g^{-1}
Boltzmann constant:	k	$\widehat{=}$	1.380658×10^{-16} erg K^{-1} .

The mass of a hydrogen atom is

$$m_\mathrm{p} \ \widehat{=}\ 1.672623 \times 10^{-24}\ \mathrm{g}\ .$$

Bibliography

Abergel, A., Bernard, J. P., Boulanger, F., Cesarsky, C., Desert, F. X., Falgarone, E., Lagache, G., Perault, M., Puget, J. L., Reach, W. T., Nordh, L., Olofsson, G., Huldtgren, M., Kaas, A. A., Andre, P., Bontemps, S., Burgdorf, M., Copet, E., Davies, J., Montmerle, T., Persi, P.,, Sibille, F.: 1996. ISOCAM Mapping of the ρ Ophiuchi Main Cloud. *A&A*, **315**, L329–L332.

Abraham, P., Dobashi, K., Mizuno, A.,, Fukui, Y.: 1995. Molecular Material and Young Stellar Objects in the L1188 Dark Cloud Complex. *A&A*, **300**, 525.

Adams, F. C., Fatuzzo, M.: 1996. A Theory of the Initial Mass Function for Star Formation in Molecular Clouds. *ApJ*, **464**, 256–271.

Bally, J., Langer, W. D., Stark, A. A.,, Wilson, R. W.: 1987. Filamentary Structure in the Orion Molecular Cloud . *ApJ*, **312**, L45–L49.

Balsara, D. S.: 1995. von Neumann Stability Analysis of Smoothed Particle Hydrodynamics — Suggestions for Optimal Algorithms. *Journ. Comp. Phys.*, **121**, 357–372.

Barnes, J. E., Hut, P.: 1986. A Hierarchical $\mathcal{O}(N \log N)$ Force-Calculation Algorithm. *Nature*, **324**, 446–449.

Basu, S.: 1997. A Semianalytic Model for Supercritical Core Collapse: Self-similar Evolution and the Approach to Protostar Formation. *ApJ*, **485**, 240–253.

Basu, S., Mouschovias, T. C.: 1995. Magnetic Braking, Ambipolar Diffusion, and the Formation of Cloud Cores and Protostars. II. A Parameter Study. *ApJ*, **452**, 386–400.

Bate, M. R.: 1995. *The Role of Accretion in Binary Star Formation*. PhD thesis, Institute of Astronomy, Cambridge, U.K.

Bate, M. R., Bonnell, I. A.,, Price, N. M.: 1995. Modelling accretion in protobinary systems. *MNRAS*, **277**, 362–376.

Bate, M. R., Burkert, A.: 1997. Resolution Requirements for Smoothed Particle Hydrodynamics Calculations with Self-Gravity. *MNRAS*, **288**, 1060–1072.

Bate, M. R., Clarke, C. J.,, McCaughrean, M. J.: 1998. Interpreting the Mean Surface Density of Companions in Star-Forming Regions . *MNRAS*. in press.

Beichman, C. A., Myers, P. C., Emerson, J. P., Harris, S., Mathieu, R., Benson, P. J.,, Jennings, R. E.: 1986. Candidate Solar-Type Protostars in Nearby Molecular Cloud Cores. *ApJ*, **307**, 337–349.

BENSON, P. J., MYERS, P. C.: 1989. A Survey for Dense Cores in Dark Clouds. *ApJSS*, **71**, 89–108.

BENZ, W.: 1990. Smoothed Particle Hydrodynamics: A Review. In Buchler, J. R., editor, *The Numerical Modelling of nonlinear Stellar Pulsations*, pages 269–288, The Netherlands. Kluwer Academic Publishers.

BENZ, W., MAYOR, M.: 1984. Photoelectric Rotational Velocities of Late-Type Dwarfs . *A&A*, **138**, 183–188.

BERGER, M. J., COLELLA, P.: 1989. Local Adaptive Mesh Refinement for Shock Hydrodynamics. *Journ. Comp. Phys.*, **82**, 64–84.

BERGIN, E. A., UNGERECHTS, H., GOLDSMITH, P. F., SNELL, R. L., IRVINE, W. M.,, SCHLOERB, F. P.: 1997. A Survey of the Chemical Properties of the M17 and Cepheus A Cloud Cores. *ApJ*, **482**, 267–284.

BERTOLDI, F., MCKEE, C. F.: 1996. Self-Regulated Star Formation in Molecular Clouds. In Chiao, R., editor, *Amazing Light: A Volume Dedicated to C.H. Townes on his 80th Birthday*, page 41, New York. Springer.

BINNEY, J., TREMAINE, S.: 1987. *Galactic Dynamics*. Princeton University Press, Princeton, NJ.

BLITZ, L.: 1993. Giant molecular clouds . In Levy, E. H., Lunine, J. I., editors, *Protostars and Planets III* , pages 125–161, Tucson. University of Arizona Press.

BLITZ, L., SHU, F. H.: 1980. The Origin and Lifetime of Giant Molecular Cloud Complexes. *ApJ*, **238**, 148–157.

BLITZ, L., STARK, A. A.: 1986. Detection of Clump and Interclump Gas in the Rosette Molecular Cloud Complex. *ApJ*, **300**, L89–L93.

BONNELL, I., BASTIEN, P.: 1993. Fragmentation of elongated cylindrical clouds. VI - Comparison with observations. *ApJ*, **406**, 614–628.

BONNELL, I. A.: 1994. A New Binary Formation Mechanism. *MNRAS*, **269**, 837–848.

BONNELL, I. A., BATE, M. R., CLARKE, C. J.,, PRINGLE, J. E.: 1997. Accretion and the Stellar Mass Spectrum in Small Clusters. *MNRAS*, **285**, 201–208.

BOSS, A. P.: 1993. Collapse and Fragmentation of Molecular Cloud Cores. I - Moderately Centrally Condensed Cores. *ApJ*, **410**, 157–167.

BOSS, A. P.: 1996. Collapse and Fragmentation of Molecular Cloud Cores. IV. Oblate Clouds and Small Cluster Formation. *ApJ*, **468**, 231–240.

BRIEU, P. P., SUMMERS, F. J.,, OSTRIKER, J. P.: 1995. Cosmological Simulations Using Special Purpose Computers: Implementing P^3M on GRAPE . *ApJ*, **453**, 566–573.

BRONSTEIN, I. N., SEMENDJAJEW, K. A.: 1987. *Taschenbuch der Mathematik*. Verlag Harri Deutsch, Thun & Frankfurt a. Main.

BURKERT, A., BATE, M. R.,, BODENHEIMER, P.: 1997. Protostellar Fragmentation in a Power-Law Density Distribution . *MNRAS*, **289**, 497–504.

BURKERT, A., BODENHEIMER, P.: 1996. Fragmentation in a Centrally Condensed Protostar. *MNRAS*, **280**, 1190–1200.

BURKERT, A., KLESSEN, R. S.,, BODENHEIMER, P.: 1998. Fragmentation in Molecular Clouds and Protostars . In McCaughrean, M., Burkert, A., editors, *The Orion Complex Revisited* . ASP Conference Series. in press.

BURROWS, A., HUBBARD, W. B., SAUMON, D.,, LUNINE, J. I.: 1993. An Expanded Set of Brown Dwarf and very Low-Mass Star Models. *ApJ*, **406**, 158–171.

BUTNER, H. M., LADA, E. A.,, LOREN, R. B.: 1995. Physical Properties of Dense Cores: DCO + Observations. *ApJ*, **448**, 207–225. Provided by the NASA Astrophysics Data System.

CARPENTER, J. M., MEYER, M. R., DOUGADOS, C., STROM, S. E.,, HILLENBRAND, L. A.: 1997. Properties of the Monoceros R2 Stellar Cluster. *AJ*, **114**, 198–221.

CARR, J. S.: 1987. A Study of Clumping in the Cepheus OB 3 Molecular Cloud. *ApJ*, **323**, 170–178.

CASELLI, P., MYERS, P. C.: 1995. The Line Width-Size Relation in Massive Cloud Cores. *ApJ*, **446**, 665–686.

CERNICHARO, J.: 1991. The Physical Conditions of Low Mass Star-Forming Regions . In Lada, C. J., D, K. N., editors, *The Physics of StarFormation and Early Stellar Evolution* , pages 287–328, Dordrecht. Kluwer Academic Publishers.

CLEMENS, D. P.: 1985. Massachusetts-Stony Brook Galactic plane CO survey - The Galactic Disk Rotation Curve. *ApJ*, **295**, 422–428.

COURANT, R., FRIEDRICHS, K.,, LEWY, H.: 1928. *Math. Ann.* , **100**, 32.

CRUTCHER, R. M., TROLAND, T. H., GOODMAN, A. A., HEILES, C., KAZES, I.,, MYERS, P. C.: 1993. OH Zeeman Observations of Dark Clouds . *ApJ*, **407**, 175–184.

CRUTCHER, R. M., TROLAND, T. H., LAZAREFF, B.,, KAZES, I.: 1996. CN Zeeman Observations of Molecular Cloud Cores . *ApJ*, **456**, 217.

DAME, T. M., ELMEGREEN, B. G., COHEN, R. S.,, THADDEUS, P.: 1986. The Largest Molecular Cloud Complexes in the First Galactic Quadrant. *ApJ*, **305**, 892–908.

DAVÉ, R., DUBINSKI, J.,, HERNQUIST, L.: 1997. Parallel TreeSPH . *New Ast.*, **2**, 277–297.

DE VEGA, H. J., SANCHEZ, N.,, COMBES, F.: 1996a. Fractal Dimensions and Scaling Laws in the Interstellar Medium: A new Field Theory Approach. *Phys. Rev. D*, **54**, 6008–6020.

DE VEGA, H. J., SANCHEZ, N.,, COMBES, F.: 1996b. Self-gravity as an Explanation of the Fractal Structure of the Interstellar Medium. *Nature*, **383**, 139.

DEISS, B. M., JUST, A.,, KEGEL, W. H.: 1990. Fluctuations of the Interstellar Medium Induced by the Stellar System – Mechanical Heating and Dynamical Friction. *A&A*, **240**, 123–136.

DI SIGALOTTI, L., KLAPP, J.: 1996. Multiple fragmentation models of centrally condensed molecular cloud cores. *MNRAS*, **281**, 449–462.

DICKMAN, R. L., SNELL, R. L.,, SCHLOERB, F. P.: 1986. Carbon Monoxide as an Extragalactic Mass Tracer. *ApJ*, **309**, 326–330.

DIGEL, S., THADDEUS, P.,, BALLY, J.: 1990. Giant Molecular Clouds in the Outer Arm of the Galaxy. *ApJ*, **357**, L29–L33.

DOBASHI, K., BERNARD, J.-P.,, FUKUI, Y.: 1996. Molecular Clouds in Cygnus. II. Statistical Studies of Star-forming Regions. *ApJ*, **466**, 282–295.

DOBASHI, K., BERNARD, J.-P., YONEKURA, Y.,, FUKUI, Y.: 1994. Molecular Clouds in Cygnus. 1: A Large-Scale ^{13}CO Survey. *ApJSS*, **95**, 419–456.

DOBASHI, K., ONISHI, T., IWATA, T., NAGAHAMA, T., PATEL, N., SNELL, R. L.,, FUKUI, Y.: 1993. Four CO Outflows and Dense Gas in the Dark Cloud Complex near IC 5146. *AJ*, **105**, 1487–1494.

DOBASHI, K., YONEKURA, Y., MIZUNO, A.,, FUKUI, Y.: 1992. ^{12}CO and ^{13}CO Observations of the Dark Cloud Complex near IC5146. *AJ*, **104**, 1525–1532.

DUQUENNOY, A., MAYOR, M.: 1991. Multiplicity among Solar-Type Stars in the Solar Neighbourhood. II - Distribution of the Orbital Elements in an Unbiased Sample. *A&A*, **248**, 485–524.

EBISUZAKI, T., MAKINO, J., FUKUSHIGE, T., TAIJI, M., SUGIMOTO, D., ITO, T.,, OKUMURA, S. K.: 1993. GRAPE Project: An Overview . *PASJ*, **45**, 269–278.

ELMEGREEN, B. G., LADA, C. J.,, DICKINSON, D. F.: 1979. The Structure and Extent of the Giant Molecular Cloud near M17. *ApJ*, **230**, 415.

ELMEGREEN, D. M.: 1997. The Initial Mass Function from Random Sampling in a Turbulent Fractal Cloud. *ApJ*, **486**, 944–954.

EVRARD, A. E.: 1988. Beyond N-body – 3D Cosmological Gas Dynamics . *MNRAS*, **235**, 911–934.

EWALD, P. P.: 1921. Die Berechnung optischer und elektrostatischer Gitterpotentiale. *Ann. Physik*, **64**, 253–287.

FALCONER, K. J.: 1990. *Fractal Geometry: Mathematical Foundations and Applications*. John Wiley & Sons Ltd., Chichester.

FALGARONE, E., PHILLIPS, T. G.: 1996. Small-Scale Density and Velocity Structure of a Molecular Cloud Edge. *ApJ*, **472**, 191.

FALGARONE, E., PHILLIPS, T. G.,, WALKER, C. K.: 1991. The edges of Molecular Clouds - Fractal Boundaries and Density Structure. *ApJ*, **378**, 186–201.

FALGARONE, E., PUGET, J. L.,, PERAULT, M.: 1992. The Small-Scale Sensity and Velocity Structure of Quiescent Molecular Clouds. *A&A*, **257**, 715–730.

FLECK, R. C., J.: 1981. On the Generation and Maintenance of Turbulence in the Interstellar Medium. *ApJ*, **246**, L151–L154.

FLECK, ROBERT C., J.: 1996. Scaling Relations for the Turbulent, Non–Self-gravitating, Neutral Component of the Interstellar Medium. *ApJ*, **458**, 739–741.

FOSTER, P. N., CHEVALIER, R. A.: 1993. Gravitational Collapse of an Isothermal Sphere. *ApJ*, **416**, 303–311.

FRINK, S., RÖSER, S., NEUHÄUSER, R.,, STERZIK, M. F.: 1997. New Proper Motions of Pre-Main Sequence Stars in Taurus-Auriga. *A&A*, **325**, 613–622.

FUKUSHIGE, T., MAKINO, J., ITO, T., OKUMURA, S. K., EBISUZAKI, T.,, SUGIMOTO, D.: 1993. WINE-1: Special-Purpose Computer for N-Body Simulations with a Periodic Boundary Condition . *PASJ*, **45**, 361–375.

FUKUSHIGE, T., TAIJI, M., MAKINO, J., EBISUZAKI, T.,, SUGIMOTO, D.: 1996. A Highly Parallelized Special-Purpose Computer for Many-Body Simulations with an Arbitrary Central Force: MD-GRAPE . *ApJ*, **468**, 51–61.

FULLER, G. A., MYERS, P. C.: 1992. Dense Cores in Dark Clouds. VII - Line Width-Size Relations. *ApJ*, **384**, 523–527.

GENZEL, R.: 1991. Physical Conditions and Heating/Cooling Processes in High-Mass Star-Forming Regions . In Lada, C. J., D, K. N., editors, *The Physics of StarFormation and Early Stellar Evolution* , pages 155–219, Dordrecht. Kluwer Academic Publishers.

GINGOLD, R. A., MONAGHAN, J. J.: 1977. Smoothed Particle Hydrodynamics - Theory and Application to Non-Spherical Stars . *MNRAS*, **181**, 375–389.

GINGOLD, R. A., MONAGHAN, J. J.: 1982. *J. Comp. Phys.* , **46**, 429.

GOLDSMITH, P. F.: 1988. Temperatures and Densities in Interstellar Molecular Clouds. In Chiao, R., editor, *Molecular Clouds in the Milky Way and External Galaxies*, pages 1–25, New York. Springer.

GOLDSMITH, P. F., LANGER, W. D.: 1978. Molecular Cooling and Thermal Balance of Dense Interstellar Clouds. *ApJ*, **222**, 881–895.

GOMEZ, M., HARTMANN, L., KENYON, S. J.,, HEWETT, R.: 1993. On the Spatial Distribution of Pre-Main-Sequence Stars in Taurus. *AJ*, **105**, 1927–1937.

GOMEZ, M., JONES, B. F., HARTMANN, L., KENYON, S. J., STAUFFER, J. R., HEWETT, R.,, REID, I. N.: 1992. On the Ages of Pre-Main-Sequence Stars in Taurus. *AJ*, **104**, 762–773.

GOODMAN, A. A., CRUTCHER, R. M., HEILES, C., MYERS, P. C.,, TROLAND, T. H.: 1989. Measurement of Magnetic Field Strength in the Dark Cloud Barnard 1 . *ApJ*, **338**, L61–L64.

GOODMAN, A. A., HEILES, C.: 1994. The Magnetic Field in the Ophiuchus Dark Cloud Complex . *ApJ*, **424**, 208–221.

GREENE, T. P., MEYER, M. R.: 1995. An Infrared Spectroscopic Survey of the ρ-Ophiuchi Young Stellar Cluster: Masses and Ages from the H-R Diagram. *ApJ*, **450**, 233–244.

GRENIER, I. A., LEBRUN, F., ARNAUD, M., DAME, T. M.,, THADDEUS, P.: 1989. CO Observations of the Cepheus Flare. I - Molecular Clouds Associated with a Nearby Bubble. *ApJ*, **347**, 231–239.

GUETH, F., GUILLOTEAU, S., DUTREY, A.,, BACHILLER, R.: 1997. Structure and Kinematics of a Protostar: mm-Interferometry of L1157. *A&A*, **323**, 943–952.

HAYASHI, M., HASEGAWA, T., OHASHI, N.,, SUNADA, K.: 1994. A $C^{18}O$ (J = 1 – 0) Survey of Protostellar Candidates Embedded in the Taurus Molecular Cloud. *ApJ*, **426**, 234–239.

HEITHAUSEN, A.: 1996. On the Dynamical State of High-Latitude Molecular Clouds. *A&A*, **314**, 251–257.

HEITHAUSEN, A., STACY, J. G., DE VRIES, H. W., MEBOLD, U.,, THADDEUS, P.: 1993. A Composite Large-Scale CO Survey at High Galactic Latitudes in the Second Quadrant. *A&A*, **268**, 265–275.

HERNQUIST, L., BOUCHET, F. R.,, SUTO, Y.: 1991. Application of the Ewald Method to Cosmological N-Body Simulations . *ApJSS*, **75**, 231–240.

HERNQUIST, L., KATZ, N.: 1989. TREESPH – A Unification of SPH with the Hierarchical Tree Method . *ApJSS*, **70**, 419–446.

HERRMANN, F., MADDEN, S. C., NIKOLA, T., POGLITSCH, A., TIMMERMANN, R., GEIS, N., TOWNES, C. H.,, STACEY, G. J.: 1997. The Orion Molecular Clouds OMC-1 and OMC-2 Mapped in the Far-Infrared Fine-Structure Line Emission of C+ and CO. *ApJ*, **481**, 343.

HILLENBRAND, L. A.: 1997. On the Stellar Population and Star-Forming History of the Orion Nebula Cluster. *AJ*, **113**, 1733–1768.

HIRAHARA, Y., SUZUKI, H., YAMAMOTO, S., KAWAGUCHI, K., KAIFU, N., OHISHI, M., TAKANO, S., ISHIKAWA, S.-I.,, MASUDA, A.: 1992. Mapping Observations of Sulfur-Containing Carbon-Chain Molecules in Taurus Molecular Cloud 1 (TMC-1). *ApJ*, **394**, 539–551.

HOCKNEY, R. W., EASTWOOD, J. W.: 1988. *Computer Simulation using Particles* . IOP Publishing Ltd., Bristol and Philadelphia.

HOYLE, F.: 1953. On the Fragmentation of Gas Clouds into Galaxies and Stars. *ApJ*, **118**, 513.

HUNTER, C.: 1977. The Collapse of Unstable Isothermal Spheres. *ApJ*, **218**, 834–845.

HUSS, A., JAIN, B.,, STEINMETZ, M.: 1997. The Formation and Evolution of Clusters of Galaxies in Differnt Cosmogonies. *MNRAS*. submitted.

JONES, B., WALKER, M.: 1988. Proper Motions and Variabilities of Stars Near the Orion Nebula. *AJ*, **95**, 1755–1782.

KATZ, N., WEINBERG, D. H.,, HERNQUIST, L.: 1996. Cosmological Simulations with TREESPH . *ApJSS*, **105**, 19.

KEGEL, W. H.: 1989. The Interpretation of Correlations between Observed Parameters of Molecular Clouds. *A&A*, **225**, 517–520.

KESSEL, O., BURKERT, A.: 1998. Ionizing Radiation from Point Sources in Smoothed Particle Hydrodynamics.

KETO, E. R., LATTANZIO, J. C.,, MONAGHAN, J. J.: 1991. Gravitational Fragmentation – A Comparison with W49A. *ApJ*, **383**, 639–644.

KRAMER, C., STUTZKI, J., ROHRIG, R.,, CORNELIUSSEN, U.: 1998. Clump Mass Spectra of Molecular Clouds. *A&A*, **329**, 249–264.

KRAMER, C., STUTZKI, J.,, WINNEWISSER, G.: 1996. Structure and Excitation Conditions of the Southern Part of the Orion B Molecular Cloud: a CO Multiline Study. *A&A*, **307**, 915–935.

KRAMER, C., WINNEWISSER, G.: 1991. A Molecular Survey of the Dark Cloud L1495 in Taurus. *A&ASS*, **89**, 421–428.

KRAUTTER, J., WICHMANN, R., SCHMITT, J. H. M. M., ALCALA, J. M., NEUHÄUSER, R.,, TERRANEGRA, L.: 1997. New 'weak-line'–T Tauri stars in Lupus. *A&ASS*, **123**, 329–352.

KROUPA, P., TOUT, C. A.,, GILMORE, G.: 1990. The Low-Luminosity Stellar Mass Function. *MNRAS*, **244**, 76–85.

KROUPA, P., TOUT, C. A.,, GILMORE, G.: 1993. The Distribution of Low-Mass Stars in the Galactic Disc. *MNRAS*, **262**, 545–587.

KUTNER, M. L., TUCKER, K. D., CHIN, G.,, THADDEUS, P.: 1977. The Molecular Complexes in Orion. *ApJ*, **215**, 521–528.

LADA, C. J., LADA, E. A., CLEMENS, D. P.,, BALLY, J.: 1994. Dust Extinction and Molecular Gas in the Dark Cloud IC5146. *ApJ*, **429**, 694–709.

LADA, E. A.: 1992. Global Star Formation in the L1630 Molecular Cloud. *ApJ*, **393**, L25–L28.

LADA, E. A., BALLY, J.,, STARK, A. A.: 1991a. An Unbiased Survey for Dense Cores in the Lynds 1630 Molecular Cloud. *ApJ*, **368**, 432–444.

LADA, E. A., EVANS, NEAL J., I., DEPOY, D. L.,, GATLEY, I.: 1991b. A 2.2 Micron Survey in the L1630 Molecular Cloud. *ApJ*, **371**, 171–182.

LANDAU, L. D., LIFSHITZ, E. M.: 1966. *Lehrbuch der Theoretischen Physik VI: Hydrodynamik*. Akademie-Verlag, Berlin.

LANDAU, L. D., LIFSHITZ, E. M.: 1983. *Lehrbuch der Theoretischen Physik X: Physikalische Kinetik*. Akademie-Verlag, Berlin.

LANGER, W. D., VELUSAMY, T., KUIPER, T. B. H., LEVIN, S., OLSEN, E.,, MIGENES, V.: 1995. Study of Structure and Small-Scale Fragmentation in TMC-1. *ApJ*, **453**, 293–307.

LARSON, R. B.: 1969. Numerical Calculations of the Dynamics of a Collapsing Proto-Star. *MNRAS*, **145**, 271.

LARSON, R. B.: 1973. A Simple Probabilistic Theory of Fragmentation. *MNRAS*, **161**, 133.

LARSON, R. B.: 1978. Calculations of Three-Dimensional Collapse and Fragmentation. *MNRAS*, **184**, 69–85.

LARSON, R. B.: 1981. Turbulence and Star Formation in Molecular Clouds. *MNRAS*, **194**, 809–826.

LARSON, R. B.: 1992. Towards Understanding the Stellar Initial Mass Function. *MNRAS*, **256**, 641–646.

LARSON, R. B.: 1995. Star Formation in Groups. *MNRAS*, **272**, 213–220.

LAUGHLIN, G., BODENHEIMER, P.: 1993. Luminosity Functions for very Low-Mass Stars and Brown Dwarfs. *ApJ*, **403**, 303–314.

LI, W., EVANS, NEAL J., I.,, LADA, E. A.: 1997. Looking for Distributed Star Formation in L1630: A Near-Infrared (J, H, K) Survey. *ApJ*, **488**, 277–285.

LOREN, R. B.: 1989a. The Cobwebs of Ophiuchus. I - Strands of the ^{13}CO Mass Distribution. *ApJ*, **338**, 902–924.

LOREN, R. B.: 1989b. The Cobwebs of Ophiuchus. II - ^{13}CO Filament Kinematics. *ApJ*, **338**, 925–944.

LUCY, L. B.: 1977. A Numerical Approach to the Testing of the Fission Hypothesis . *AJ*, **82**, 1013–1024.

MAC LOW, M.-M.: 1998. Structure and Dynamics of Magnetized Interstellar Clouds: Super-Alfvénic Turbulence? In McCaughrean, M. J., Burkert, A., editors, *The Orion Nebula Revisited*, San Francisco. Astron. Soc. Pacific. in press.

MAC LOW, M.-M., KLESSEN, R. S., BURKERT, A.,, SMITH, M. D.: 1998. Kinetic Energy Decay Rates of Supersonic and Super-Alfvénic Turbulence in Star-Forming Clouds. *Phys. Rev. Letter*, **in press**.

MADDALENA, R. J., MOSCOWITZ, J., THADDEUS, P.,, MORRIS, M.: 1986. The large system of Molecular Clouds in Orion and Monoceros. *ApJ*, **303**, 375–391.

MADDALENA, R. J., THADDEUS, P.: 1985. A Large, Cold, and Unusual Molecular Cloud in Monoceros. *ApJ*, **294**, 231–237.

MAGNANI, L., BLITZ, L.,, MUNDY, L.: 1985. Molecular Gas at High Galactic Latitudes. *ApJ*, **295**, 402–421.

MAKINO, J., FUKUSHIGE, T., OKUMURA, S. K.,, EBISUZAKI, T.: 1993a. The Evolution of Massive Black-Hole Binaries in Merging Galaxies. – Evolution of a Binary in a Spherical Galaxy . *PASJ*, **45**, 303–310.

MAKINO, J., FUNATO, Y.: 1993. The GRAPE Software System . *PASJ*, **45**, 279–288.

MAKINO, J., KOKUBO, E.,, TAIJI, M.: 1993b. HARP: A Special-Purpose Computer for N-Body Problem . *PASJ*, **45**, 349–360.

MATSUMOTO, T., HANAWA, T.,, NAKAMURA, F.: 1997. Gravitational Contraction of Rotating Clouds: Formation of Self-similarly Collapsing Disks. *ApJ*, **478**, 569–584.

MILLER, G. E., SCALO, J.: 1979. The Initial Mass Function and the Stellar Birthrate in the Solar Neighborhood. */apjs*, **41**, 513–547.

MIZUNO, A., ONISHI, T., YONEKURA, Y., NAGAHAMA, T., OGAWA, H.,, FUKUI, Y.: 1995. Overall Distribution of Dense Molecular Gas and Star Formation in th Taurus Cloud Complex. *ApJ*, **445**, L161–L165.

MONAGHAN, J. J.: 1985. Particle Methods for Hydrodynamics. *Comp. Phys. J.*, **3**, 71–124.

MONAGHAN, J. J.: 1992. Smoothed Particle Hydrodynamics . *ARAA*, **30**, 543–574.

MONAGHAN, J. J.: 1994. Vorticity, Angular Momentum and Cloud Sragmentation. *ApJ*, **420**, 692–704.

MONAGHAN, J. J., GINGOLD, R. A.: 1983. *Journ. Comp. Phys.* , **52**, 135.

MONAGHAN, J. J., LATTANZIO, J. C.: 1985. A Refined Particle Method for Astrophysical Problems . *A&A*, **149**, 135–143.

MONAGHAN, J. J., LATTANZIO, J. C.: 1991. A Simulation of the Collapse and Fragmentation of Cooling Molecular Clouds. *ApJ*, **375**, 177–189.

MOONEY, T. J., SOLOMON, P. M.: 1988. Star Formation Rates and the Far-Infrared Luminosity of Galactic Molecular Clouds. *ApJ*, **334**, L51–L54.

MOTTE, F., ANDRÉ, P.,, NERI, R.: 1998. The Initial Conditions of Star Formation in the ρ-Ophiuchi Main Cloud: Wide-Field Millimeter Continuum Mapping. *A&A*, **accepted for publication.**

MOUSCHOVIAS, T. C.: 1991. Cosmic Magnetism and the Basic Physics of the Early Stages of Star Formation. In Lada, C. J., Kylafis, N. D., editors, *The Physics of Star Formation and Early Stellar Evolution*, volume 342 of *NASA ASI Series*, The Netherlands. Kluwer Academic Publishers.

MURRAY, S. D., LIN, D. N. C.: 1996. Coalescence, Star Formation, and the Cluster Initial Mass Function. *ApJ*, **467**, 728–748.

MYERS, P. C.: 1983. Dense Cores in Dark Clouds. III – Subsonic Turbulence. *ApJ*, **270**, 105–118.

MYERS, P. C., FULLER, G. A., GOODMAN, A. A.,, BENSON, P. J.: 1991. Dense Cores in Dark Clouds. VI – Shapes. *ApJ*, **376**, 561–572.

MYERS, P. C., GOODMAN, A. A.: 1988. Evidence for Magnetic and VirialEequilibrium in Molecular Clouds. *ApJ*, **326**, L27–L30.

MYHILL, E. A., KAULA, W. M.: 1992. Numerical Models for the Collapse and Fragmentation of Centrally Condensed Molecular Cloud Cores. *ApJ*, **386**, 578–586.

NAKANO, T., HASEGAWA, T.,, NORMAN, C.: 1995. The Mass of the Star Formed in a Cloud Core. *Astrophysics and Space Science*, **224**, 523–524.

NAVARRO, J., WHITE, S.: 1993. Simulations of Dissipative Galaxy Formation in Hierarchically Clustering Universes. I – Tests of the Code . *MNRAS*, **265**, 271.

NELSON, R. P., PAPALOIZOU, J. C. B.: 1993. Three-Dimensional Hydrodynamic Simulations of Collapsing Prolate Clouds. *MNRAS*, **265**, 905–920.

NELSON, R. P., PAPALOIZOU, J. C. B.: 1994. Variable Smoothing Lengths and Energy Conservation in Smoothed Particle Hydrodynamics. *MNRAS*, **270**, 1–20.

NERCESSIAN, E., CASTETS, A., BENAYOUN, J. J.,, CERNICHARO, J.: 1988. A Molecular Study of the Dark Clouds L1506 and L1529 in Taurus. *A&A*, **189**, 207–220.

NEUHÄUSER, R., STERZIK, M. F., TORRES, G.,, MARTIN, E. L.: 1995. Weak-Line T-Tauri Stars South of Taurus. *A&A*, **299**, L13–L16.

NORMAN, C., SILK, J.: 1980. Clumpy Molecular Clouds - A Dynamic Model Self-Consistently Regulated by T Tauri Star Formation. *ApJ*, **238**, 158–174.

NOZAWA, S., MIZUNO, A., TESHIMA, Y., OGAWA, H.,, FUKUI, Y.: 1991. A Study of ^{13}CO Cloud Cores in Ophiuchus. *ApJSS*, **77**, 647–675.

NYMAN, L. A., THADDEUS, P., BRONFMAN, L.,, COHEN, R. S.: 1987. A Large Molecular Cloud in Lupus far from the Galactic Plane. *ApJ*, **314**, 374–379.

OKUMURA, S. K., MAKINO, J., EBISUZAKI, T., FUKUSHIGE, T., ITO, T., SUGIMOTO, D., HASHIMOTO, E., TOMIDA, K.,, MIYAKAWA, N.: 1993. Highly Parallelized Special-Purpose Computer, GRAPE-3 . *PASJ*, **45**, 329–338.

ONISHI, T., MIZUNO, A., KAWAMURA, A., OGAWA, H.,, FUKUI, Y.: 1996. A C^{18}O Survey of Dense Cloud Cores in Taurus: Core Properties. *ApJ*, **465**, 815–824.

PEEBLES, P. J. E.: 1993. *Principles of Physical Cosmology*. Princeton University Press, Princeton, NJ.

PENSTON, M. V.: 1969. Dynamics of Self-Gravitating Gaseous Spheres — III. *MNRAS*, **144**, 425.

PERAULT, M., FALGARONE, E.,, PUGET, J. L.: 1985. ^{13}CO Observations of Cool Giant Molecular Clouds. *A&A*, **152**, 371–386.

PHILLIPS, A. C.: 1994. *The Physics of Stars*. Wiley, Chichester, New York.

PLUME, R., JAFFE, D. T., EVANS, NEAL J., I., MARTIN-PINTADO, J.,, GOMEZ-GONZALEZ, J.: 1997. Dense Gas and Star Formation: Characteristics of Cloud Cores Associated with Water Masers. *ApJ*, **476**, 730.

PRESS, W. H., FLANNERY, B. P., TEUKOLSKY, S. A.,, VETTERLING, W. T.: 1989. *Numerical Recipes. The Art of Scientific Computing* . Cambridge University Press, Cambridge.

PRICE, N. M., PODSIADLOWSKI, P.: 1995. Dynamical Interactions between Young Stellar Objects and a Collisional Model for the Origin of the Stellar Mass Spectrum. *MNRAS*, **273**, 1041–1068.

PRINGLE, J. E.: 1981. Accretion Disks in Astrophysics. *ARA&A*, **19**, 137–162.

REICHL, L. E.: 1991. *A Modern Course in Statistical Physics*. Arnold, London.

REIPURTH, B.: 1989. Observations of Herbig-Haro Objects. In Reipurth, B., editor, *Low-Mass Star Formation and Pre-Main Sequence Objects*, volume 33 of *ESO Conference Proceedings*, pages 247–279, Garching, Germany. European Southern Observatory.

REMY, G. P., GRENIER, I. A., DUVERT, G.,, THADDEUS, P.: 1997. The Cepheus Molecular Cloud. I. Multi-Transition Observations in CO and ^{13}CO. *A&ASS*, **125**, 303.

SAFIER, P. N., MCKEE, C. F.,, STAHLER, S. W.: 1997. Star Formation in Cold, Spherical, Magnetized Molecular Clouds. *ApJ*, **485**, 660–679.

SAKAMOTO, S., HAYASHI, M., HASEGAWA, T., HANDA, T.,, OKA, T.: 1994. A Large Area CO (J = 2 – 1) Mapping of the Giant Molecular Clouds in Orion. *ApJ*, **425**, 641–652.

SALPETER, E. E.: 1955. The Luminosity Function and Stellar Evolution. *ApJ*, **121**, 161–167.

SCALO, J.: 1986. The Stellar Initial Mass Function. *Fund. of Cosmic Physics*, **11**, 1–278.

SCALO, J.: 1990. Perception of Interstellar Structure - Facing Complexity. In Capuzzo-Dolcetta, R., Chiosi, C., editors, *Physical Processes in Fragmentation and Star Formation*, pages 151–176, Dordrecht, Netherlands. Kluwer Academic Publishers.

SCALO, J.: 1998. The IMF Revisited: A Case for Variations. In Gilmore, G., Parry, I.,, Ryan, S., editors, *The Stellar Initial Mass Function*. in press.

SHAPIRO, P. R., MARTEL, H., VILLUMSEN, J. V.,, OWEN, J. M.: 1996. Adaptive Smoothed Particle Hydrodynamics, with Application to Cosmology: Methodology . *ApJSS*, **103**, 269–330.

SHU, F.: 1992. *Gas Dynamics*. University Science Books, California.

SHU, F. H.: 1977. Self-Similar Collapse of Isothermal Spheres and Star Formation. *ApJ*, **214**, 488–497.

SHU, F. H., ADAMS, F. C.,, LIZANO, S.: 1987. Star Formation in Molecular Clouds – Observation and Theory. *ARA&A*, **25**, 23–81.

SILK, J.: 1995. A Theory for the Initial Mass Function. *ApJ*, **438**, L41–L44.

SIMON, M.: 1997. Clustering of Young Stars in Taurus, Ophiuchus, and the Orion Trapezium. *ApJ*, **482**, L81–L84.

STARK, A. A., BLITZ, L.: 1978. On the Masses of Giant Molecular Cloud Complexes. *ApJ*, **225**, L15–L19.

STEINMETZ, M.: 1996. GRAPESPH: Cosmological Smoothed Particle Hydrodynamics Simulations with the Special-Purpose Hardware GRAPE . *MNRAS*, **278**, 1005–1017.

STEINMETZ, M., MÜLLER, E.: 1993. On the Capabilities and Limits of Smoothed Particle Hydrodynamics . *A&A*, **268**, 391–410.

STERZIK, M. F., ALCALA, J. M., NEUHÄUSER, R.,, SCHMITT, J. H. M. M.: 1995. The Spatial Distribution of X-ray Selected T-Tauri Stars: I. Orion. *A&A*, **297**, 418+.

STROM, K. M., STROM, S. E.,, MERRILL, K. M.: 1993. Infrared Luminosity Functions for the Young Stellar Population Associated with the L1641 Molecular Cloud. *ApJ*, **412**, 233–253.

STUTZKI, J., GÜSTEN, R.: 1990. High Spatial Resolution Isotopic CO and CS Observations of M17 SW – The Clumpy Structure of the Molecular Cloud Core. *ApJ*, **356**, 513–533.

SUGIMOTO, D., CHIKADA, Y., MAKINO, J., ITO, T., EBISUZAKI, T.,, UMEMURA, M.: 1990. A Special-Purpose Computer for Gravitational Many-Body Problems . *Nature*, **345**, 33.

TACHIHARA, K., DOBASHI, K., MIZUNO, A., OGAWA, H.,, FUKUI, Y.: 1996. ^{13}CO (J= 1–0) Observations of the Lupus Molecular Clouds. *PASJ*, **48**, 489–502.

TATEMATSU, K., UMEMOTO, T., KAMEYA, O., HIRANO, N., HASEGAWA, T., HAYASHI, M., IWATA, T., KAIFU, N., MIKAMI, H., MURATA, Y., NAKANO, M., NAKANO, T., OHASHI, N., SUNADA, K., TAKABA, H.,, YAMAMOTO, S.: 1993. Molecular Cloud Cores in the Orion A Cloud. I - Nobeyama CS (1-0) Survey. *ApJ*, **404**, 643–662.

TOHLINE, J. E.: 1982. Hydrodynamic Collapse. *Fundamentals of Cosmic Physics*, **8**, 1–81.

TOMISAKA, K.: 1996. Collapse and Fragmentation of Cylindrical Magnetized Clouds: Simulation with Nested Grid Scheme. *PASJ*, **48**, 701–717.

TROLAND, T. H., CRUTCHER, R. M., GOODMAN, A. A., HEILES, C., KAZES, I.,, MYERS, P. C.: 1996. The Magnetic Fields in the Ophiuchus and Taurus Molecular Clouds . *ApJ*, **471**, 302.

TRUELOVE, J. K., KLEIN, R. I., MCKEE, C. F., HOLLIMAN, JOHN H., I., HOWELL, L. H., GREENOUGH, J. A.,, WOODS, D. T.: 1998. Self-Gravitational Hydrodynamics with Three-Dimensional Adaptive Mesh Refinement: Methodology and Applications to Molecular Cloud Collapse and Fragmentation. *ApJ*, **495**, 821–852.

TURNER, J. A., CHAPMAN, S. J., BHATTAL, A. S., DISNEY, M. J., PONGRACIC, H.,, WHITWORTH, A. P.: 1995. Binary star formation: gravitational fragmentation followed by capture. *MNRAS*, **277**, 705–726. Provided by the NASA Astrophysics Data System.

UMEMURA, M., FUKUSHIGE, T., MAKINO, J., EBISUZAKI, T., SUGIMOTO, D., TURNER, E. L.,, LOEB, A.: 1993. Smoothed Particle Hydrodynamics with GRAPE-1A . *PASJ*, **45**, 311–320.

UNGERECHTS, H., THADDEUS, P.: 1987. A CO Survey of the Dark Nebulae in Perseus, Taurus, and Auriga. *ApJSS*, **63**, 645–660.

VAN DISHOECK, E. F., BLAKE, G. A., DRAINE, B. T.,, LUNINE, J. I.: 1993. The Chemical Evolution of Protostellar and Protoplanetary Matter . In Levy, E. H., Lunine, J. I., editors, *Protostars and Planets III* , pages 163–241, Tucson. University of Arizona Press.

VAZQUEZ-SEMADENI, E., BALLESTEROS-PAREDES, J.,, RODRIGUEZ, L. F.: 1997. A Search for Larson-Type Relations in Numerical Simulations of the ISM: Evidence for Nonconstant Column Densities. *ApJ*, **474**, 292–307.

VAZQUEZ-SEMADENI, E., GAZOL, A.: 1995. Gravitational Instability in Turbulent, Non-Uniform Media. *A&A*, **303**, 204.

VERSCHUUR, G. L.: 1995a. Zeeman Effect Observations of H i Emission Profiles. I. Magnetic Field Limits for Three Regions Based on Observations Corrected for Polarized Beam Structure. *ApJ*, **451**, 624–644.

VERSCHUUR, G. L.: 1995b. Zeeman Effect Observations of H i Emission Profiles. II. Results of an Attempt to Confirm Previous Claims of Field Detections. *ApJ*, **451**, 645–659.

WARD-THOMPSON, D., SCOTT, P. F., HILLS, R. E.,, ANDRE, P.: 1994. A Submillimeter Continuum Survay of Pre-Protostellar Cores. *MNRAS*, **268**, 276–290.

WHITWORTH, A., SUMMERS, D.: 1985. Self-Similar Condensation of Spherically Symmetric Self-Gravitating Isothermal Gas Clouds. *MNRAS*, **214**, 1–25.

WHITWORTH, A. P., BHATTAL, A. S., FRANCIS, N.,, WATKINS, S. J.: 1996. Star Formation and the Singular Isothermal Sphere. *MNRAS*, **283**, 1061–1070.

WHITWORTH, A. P., CHAPMAN, S. J., BHATTAL, A. S., DISNEY, M. J., PONGRACIC, H.,, TURNER, J. A.: 1995. Binary star formation: accretion-induced rotational fragmentation. *MNRAS*, **277**, 727–746. Provided by the NASA Astrophysics Data System.

WICHMANN, R., KRAUTTER, J., COVINO, E., ALCALA, J. M., NEUHÄUSER, R.,, SCHMITT, J. H. M. M.: 1997. The T-Tauri Star Population in the Lupus Star Forming Region. *A&A*, **320**, 185–195.

WICHMANN, R., KRAUTTER, J., SCHMITT, J. H. M. M., NEUHÄUSER, R., ALCALA, J. M., ZINNECKER, H., WAGNER, R. M., MUNDT, R.,, STERZIK, M. F.: 1996. New weak-line T-Tauri Stars in Taurus-Auriga. *A&A*, **312**, 439–454.

WIESEMEYER, H., GUESTEN, R., WINK, J. E.,, YORKE, H. W.: 1997. High Resolution Studies of Protostellar Condensations in NGC2024. *A&A*, **320**, 287–299.

WILLIAMS, J. P., BLITZ, L.,, STARK, A. A.: 1995. The Density Structure in the Rosette Molecular Cloud: Signposts of Evolution. *ApJ*, **451**, 252.

WILLIAMS, J. P., DE GEUS, E. J.,, BLITZ, L.: 1994. Determining Structure in Molecular Clouds. *ApJ*, **428**, 693–712.

WISEMAN, J. J., HO, P. T. P.: 1996. Heated Gaseous Streamers and Star Formation in the Orion Molecular Cloud . *Nature*, **382**, 139–141.

WOOD, D. O. S., MYERS, P. C.,, DAUGHERTY, D. A.: 1994. IRAS Images of Nearby Dark Clouds. *ApJSS*, **95**, 457–501.

YANG, J., FUKUI, Y., UMEMOTO, T., OGAWA, H.,, CHEN, H.: 1990. A Newly Discovered Molecular Cloud in Cepheus OB4. *ApJ*, **362**, 538–544.

YONEKURA, Y., DOBASHI, K., MIZUNO, A., OGAWA, H.,, FUKUI, Y.: 1997. Molecular Clouds in Cepheus and Cassiopeia. *ApJSS*, **110**, 21.

YU, Z.-Y., NAGAHAMA, T.,, FUKUI, Y.: 1996. The New Observation of $C^{18}O$ (J=1–0) Molecular Emission in the Cepheus OB3 Molecular Cloud. *ApJ*, **471**, 867.

ZEL'DOVICH, Y. B.: 1970. Gravitational Instability: An approximate theory for large density perturbations. *A&A*, **5**, 84.

ZINNECKER, H.: 1984. Star Formation from Hierarchical Cloud Fragmentation - A Statistical Theory of the Log-Normal Initial Mass Function. *MNRAS*, **210**, 43–56.

ZINNECKER, H.: 1990. In Capuzzo-Dolcetta, R., Chiosi, C., editors, *Physical Processes in Fragmentation and Star Formation*, page 201, Dordrecht, Netherlands. Kluwer Academic Publishers.

This work had been impossible without the help and friendship of a very large number of people. Thanks to all...

Special thanks to Dr. Andreas Burkert who introduced me to the subject of star formation and molecular cloud dynamics. His ideas and physical knowledge are the fundament of this thesis — and are the reason why I traded a beautiful view of the Alps by a beautiful (though often foggy) view of the Rhine valley.

Very important (in many aspects) for the success of this dissertation project was the help and advice by Dr. Matthew Bate and Dr. Mordecai Mac Low. Joint discussions have been equally challenging, instructive and funny.

Thanks to Dr. Rainer Spurzem for his help with GRAPE-related problems and his astrophysical insight.

Thanks to Dr. Pavel Kroupa for many discussions about the IMF and about dwarf galaxies.

The reason why I very much enjoyed being at the MPIA is the 'extended' theory group: We had lots of fun together and the daily lunch and coffee sessions became an integral part of the social life at the institute. Thanks to my office mates Massimo Robberto and Mike Meyer (from whom I learned many strange noises), thanks to Panos Patsis, Thorsten Naab, Olaf Kessel, Peter Marx, JiaSheng Huang, Irene Porro, Paul Kalas, Ralph Andersen, Hélène Di Nella and to the non coffee drinkers Matthew Bate, Andi Burkert and Mordecai Mac Low. Also, thanks to many occasional coffee drinkers for stepping by but never washing up.

Thanks...

...to Walter Rauh for the initial voice training and for his support concerning GRAPE and the computer system.

...to Mike Meyer, Massimo Robberto, Thorsten Naab, Mordecai Mac Low, and Ralph Andersen for many exciting non-scientific discussions.

...to the poker gang for good food and thrilling evenings.

...to the other PhD students for advice on common problems.

...to my apartment mates.

Beyond all others, I am thanking my mother and Sibylle Eggers for love and faith and everything.

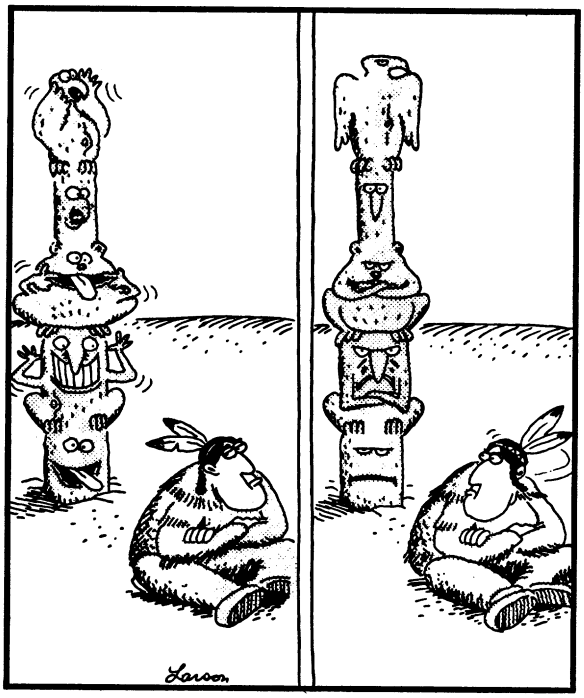
Larson